function $u = u(x, y)$ can be represented as

$$u(x, y) = c_x^T \vec{B} c_y. \tag{12.67}$$

where $\vec{B}$ is now a matrix of unknowns, and $c(x)$, $c(y)$ are Chebyshev bases with respect to x and y respectively.

Operators for the co-ordinate directions x and y now pre- and post-multiply onto the unknown coefficients; for instance the mixed derivative $\frac{\partial^2}{\partial x \partial y}$ operating on u becomes, in the Chebyshev basis,

$$\frac{\partial^2}{\partial x \partial y} u \Rightarrow c_x^T \eta^T \vec{B} \hat{\eta} c_y. \tag{12.68}$$

For any given differential equation $A_1 \vec{B} A_2 = C$, the boundary conditions are augmented for x by shifting the resulting operator matrices A_1 and C down a numbe of rows, and for y by shifting A_2 and C over by a number of columns. A conflict arises at the top left corner of the matrix C, where the conditions 'interfere' with one another. The upshot of this is that only really simple conditions can be accommodated with ease; for instance, velocity everywhere around the perimeter zero can be accommodated, but any more complicated conditions cause a problem.

This problem occurs primarily because the boundary constraints in the Chebyshev basis concern all the expansion coefficients. The collocation approach on the other hand simply asserts the relevant boundary condition at the respective node (like a finite-difference approach), with the result that no compatibility conflicts arise.

12.9 Summary

This chapter has been concerned with developing the tools and basic principles that will be needed to apply the operational approach to the problems of fluid mechanics. A limitation of the standard operational-Tau method was removed, allowing accurate solution to be carried out at high orders of solution. The collocation approach was also shown to be uniformly understandable under the operational methodology. The best means of description of a principle is usually by illustration, and to this end, proper explanation of the method's application to real problems is given in the following chapter, by means of examples pertinent to the study.

Using relations (12.63) and (12.64), any matrix operator (for example $\hat{\eta}$) in the Chebyshev basis can be transformed via a similarity transformation into the Lagrange basis as

$$\tilde{A} = C^{-1}\hat{A}C. \tag{12.65}$$

Thus the operator D given in algorithm 12.7 above can be alternatively generated by transforming the differentiation matrix $\hat{\eta}$ into the physical domain; that is D can be redefined as

$$D \equiv C\hat{\eta}C^{-1}. \tag{12.66}$$

The similarity transform (12.66) is well behaved numerically, in that both C and C^{-1} are explicitly derivable, and are both well conditioned. Thus the problem with the similarity transform apparent in the Tau method is not present here.

One fundamental difference between the Lagrange and Chebyshev bases concerns their behaviour as their order is extended. With both systems, the basis $\hat{c}$ or $\tilde{\psi}$ each span the space of polynomials P_N. Furthermore, the truncated bases c_N and $\tilde{\psi}$ each spans the space of polynomials P_N of order less than or equal to N. However, in the case of the Chebyshev basis $\hat{c}$, each restricted basis vector $\hat{c}_{N-k}$ is completely contained by its higher order bases. This is in contrast to the Lagrange system: here each restricted basis $\tilde{\psi}_N$ is unique and not necessarily contained within the larger bases. In other words, for each order N, there is a unique basis vector $\tilde{\psi}_N$ of Lagrange polynomials that spans the space P_N of polynomials in an optimum way. Thus, unlike the Chebyshev system, the operators in the Lagrange basis at a certain order are *not* simply the truncation of an infinite system, but must be generated explicitly for a certain N. For a particular N, this results in the projection matrices C and C^{-1} being unique and not simply a chosen truncation of infinite matrices. This restriction of the Lagrange basis defines the fundamental difference between the collocation and Tau methods.

12.8.5 Advantages of the collocation method

The major reason for preferring the collocation method over a Tau approach for the axial discretisation was its ease of handling the inlet boundary conditions. While one-dimensional Tau approaches readily admit unusual boundary values, their two-dimensional counterparts are severely restricted in this regard.

To illustrate this, consider a two-dimensional Tau approach. Here the unknowns form a matrix of coefficients, and the two sets of basis vectors (one for each coordinate direction) pre- and post-multiply onto these coefficients. That is, the

$$\Pi_i(x) = (x - x_0)(x - x_1)\cdots(x - x_{i-1})(x - x_{i+1})\cdots \\ \cdots(x - x_{N-2})(x - x_{N-1}). \tag{12.59}$$

These functions can be defined to correspond to any set of collocation nodes. However, it is shown by Fox & Parker (1968) that in order to minimise the maximum value of $|\Pi_i(x)|$, these nodes should be taken as the zeroes of the Chebyshev polynomial T_{N+1} - the nodes of maximum quadrature as defined by equation (12.55). In other words, the correct choice of grid enforces minimax behaviour on the Lagrange polynomials, and will produce uniform convergence of the solution with increasing N. In fact an inappropriate choice of nodes (for instance equi-spaced) can ensure that the interpolating series does not converge at all[10]. Using the Lagrange basis, the function u can be represented in the physical domain as

$$u = \tilde{u}\tilde{\psi} \tag{12.60}$$

with the row vector $\tilde{\psi}$ given by

$$\tilde{\psi} = [\hat{\Pi}_0\, \hat{\Pi}_1 \cdots \hat{\Pi}_{N-2}\, \hat{\Pi}_{N-1}]^T, \tag{12.61}$$

where $\hat{\Pi}_i$ is the ith Lagrange polynomial, corresponding to the ith collocation node x_i, and normalised such that $|\hat{\Pi}_i(x_i)| = 1$:

$$\hat{\Pi}_i(x) = \frac{\Pi_i(x)}{\Pi_i(x_i)}. \tag{12.62}$$

Equation (12.57) defines a direct mapping between the coefficient vector in the Tau system and the vector in the physical (Lagrange) basis. Immediately obvious is a direct analogy between the matrix C and the transformation matrix V from the operational-Tau method [See section 12.7], in that they both primarily define a mapping between two polynomial bases. Thus the function u can be defined equivalently in both the Chebyshev and Lagrange bases as

$$u = \tilde{a}\tilde{\sigma} = \tilde{u}\tilde{\psi}. \tag{12.63}$$

By the substitution of the relation (12.57) into the above equality, a relation between the bases can be inferred; this relation is

$$C\tilde{\sigma} = \tilde{\psi}. \tag{12.64}$$

[10]This phenomenon will hamper any attempt to use a high order differentiation matrix in a finite-difference system with equi-spaced nodes, because of instability.

For the Chebyshev polynomials of the second kind, evaluated at the Gauss-Lobatto points, the differentiation matrix is given by algorithm (12.7) that follows.

Algorithm 12.7: D

```
for l = 1 : N − 1 {
    x_l = cos(π ∗ l/(N − 1))
    if (l == 0 or l == N − 1) { c_l = 2 } else { c_l = 1 }
    for j = 0 : N − 1 {
        x_j = cos(π ∗ j/(N − 1))
        if (j == 0 or j == N − 1) { c_j = 2 } else { c_j = 1 }
        if (l ≠ j) {
            e_{j,l} = (c_l/c_j) ∗ ((−1)^{j+l}/(x_l − x_j))
        } elseif (l == j and l == 0) {
            e_{j,l} = (2 ∗ (N − 1)^2 + 1)/6
        } elseif (l == j and l == N − 1) {
            e_{j,l} = −(2 ∗ (N − 1)^2 + 1)/6
        } else {e_{j,l} = −x_j/(2 ∗ (1 − x_j^2))
        }
    }
}
D = 2D.
```

It is primarily the structure of the operator D that distinguishes the method from a difference approach. Using D as defined by (12.7) above, differentiation in the physical domain can be represented as

$$\frac{d}{dx}u \Rightarrow \hat{u}D. \tag{12.58}$$

12.8.4 The collocation approach as an operational system

The above explanation essentially follows the 'traditional' description of the collocation method, albeit using a more terse matrix notation. It is, however, possible to describe the entire collocation approach completely uniformly as with the Tau method. This novel method of considering the collocation approach is outlined below.

In contrast to the Tau method, the matrix representation of the function in the collocation approach is given with no associated basis vector. However, there *is* an implicit basis vector, namely a vector of Lagrange polynomials - polynomials that are zero at all the collocation nodes except one; that is polynomials whose roots coincide with all the nodes except one. These polynomials can be defined as [Fox & Parker (1968)]

Algorithm 12.6: C^{-1}

```
for k := 0 : N - 1 {
    for j := 0 : N - 1 {
        C^{-1}_{k,j} := cos(πjk / (N - 1))
    }
}.
```

Algorithms (12.5) and (12.6) are given as Matlab functions in appendix D. Alternatively, the fast Fourier transform (FFT) can be employed to the same effect. Canuto *et al* (1988) contains detailed descriptions of how an FFT algorithm can be most economically employed for this purpose, and thus it will be taken no further here. The two approaches (Matrix transform or FFT) are equivalent and yield identical results the sole advantage of the FFT approach is a relatively modest gain in speed[8]. Thus for the current description, the matrix transformations given by the algorithms (12.5) and (12.6) will be used to project the discrete function between the physical space and Chebyshev space.

12.8.3 Differentiation

The simple transformation of the data to and from the physical domain as described above is useful in evaluating efficiently the convolution sums arising from the non-linear terms in the base-flow equation. The method of achieving this will be described later; however, the primary concern now is with differentiation of the function in the physical space. The effect of differentiation on the function $\hat{u}$ can be deduced either by considering the derivatives of the Lagrange polynomials - which are zero at all the collocation nodes except one - or by transforming the differentiation matrix η of the operational-Tau method into the physical space using C. Using the former approach, the first derivative matrix has been given by Canuto *et al* (1988), and this is a full matrix representing differentiation[9]. It will however be shown later that treating the collocation method as just a particular case of the operational paradigm results in the natural use of the latter option for generating operators.

[8] The cost in terms of floating-point operations of the matrix transform for a one dimensional vector $\hat{u}$ of order N is approximately N^2, whereas a well designed FFT, if to operate on many real-valued vectors at the same time, can take advantage of the full complex FFT (by packing the vectors together as real-complex pairs) and perform the same operation at a cost of $\frac{5}{2}N\log_2 N + 4N$ per transform. The advantage at an order of approximately $N = 60$ (the approximate value for the entrance calculations) is to speed up the calculation time by ≈ 3.2 times.

[9] Note that the derivative matrix is not derived from difference formulae: rather from the global coefficient operators projected into the physical basis.

the grid points (12.55) are evenly spaced in θ. Furthermore, the polynomials simply become a cosine series with respect to θ. Thus it is possible to define a simple Fourier transform between the physical values at the collocation nodes, and the expansion coefficients. This is important because is allows the requisite operators to be transformed from the Chebyshev basis into the physical system. It will be shown a little later that the choice of points (12.55) is optimal for representing the system as a Lagrange polynomial expansion.

12.8.2 General description

To describe the collocation approach, consider the variation of a variable $u = u(x)$ in the one-dimensional range $x \in [0, 1]$. Let the space values at the N collocation points in this range be defined as

$$u \equiv [u_{x_0}\, u_{x_1}\, u_{x_2} \cdots u_{x_{N-3}}\, u_{x_{N-2}}\, u_{x_{N-1}}], \tag{12.56}$$

where the term u_{x_i} represents the space values at the ith collocation node as defined by (12.55). Using the fact that the Chebyshev system is simply a cosine series with a change in variable, a matrix transformation can be generated such that the vector (12.56) can be transformed into the equivalent expansion coefficient representation $\vec{a}$ according to

$$\vec{a} = \vec{u}C', \tag{12.57}$$

where the matrix C' is defined by algorithm (12.5) below.

Algorithm 12.5: C'

```
for k = 0 : N - 1 {
    for j = 0 : N - 1 {
        if  (k == 0 or k == N - 1) { c_k = 2 } else { c_k = 1 }
        if  (j == 0 or j == N - 1) { c_j = 2 } else { c_j = 1 }

                    c_{j,k} = 2/((N-1) c_j c_k) cos(πjk/(N-1))

    }
}.
```

The inverse transform is obtainable simply by inverting C', or can be directly calculated from the even simpler algorithm which follows.

12.8 Collocation

As already mentioned, in the collocation method, the unknowns are physical values at node points within a compact domain. Thus the method has a finite difference-like quality to it. It is very much unlike the finite difference method in that it is subject to the property of infinite-order accuracy. The reason for this behaviour is best explained by carefully considering the method.

12.8.1 Collocation grid

The appropriate collocation grid is dependent upon the method chosen to derive the operator matrices. When using the Chebyshev polynomials, the correct mesh is the Gauss-Lobatto grid. For the purpose of the current investigation, the grid was adapted to the restricted range $[0, 1]$ from the more usual $[-1, 1]$. This restriction is in accordance with the restriction of the range for the earlier Tau derivations. The Gauss-Lobatto grid is shown in figure 12.1, and is given by equation (12.55) [Canuto *et al* (1988)] below.

$$x_j = \frac{1}{2}\left(\cos\frac{\pi j}{N-1} + 1\right), \quad j \in [0, N-1]. \tag{12.55}$$

Important to note is that this grid is reversed, that is $x_0 = 1$ and $x_{N-1} = 0$. Re-orientation of the grid to the more intuitive, reversed, sense can be done, but this unnecessarily complicates the mathematics. Practically it is far simpler to 'flip' the resultant vector after calculation (if at all necessary), for the sake of convenient presentation.

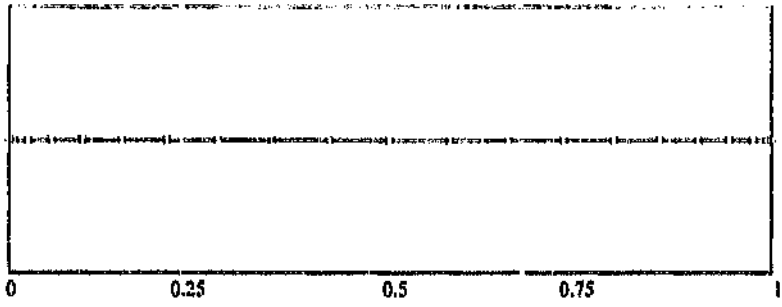

Figure 12.1: The Gauss-Lobatto grid points, shown for $N = 20$.

While representing the function at the nodal points of this grid might seem much like a finite-difference philosophy, some important features distinguish it from a normal difference grid. To begin with, the points defined by (12.55) are nodes of maximum quadrature for the Chebyshev polynomials. If the Chebyshev polynomials are subjected to a change of independent variable as $\theta = \cos^{-1} x$, then

Table 12.1: Variation most unstable eigenvalue with order in plane Poiseuille flow, for $\alpha = 1$, $Re = 3\,000$, compared to results generated by explicit transformation of operators into the orthogonal basis. Only the imaginary component is shown.

Order	Imaginary component of first eigenvalue ($\times 10^2$)	
	Current method	Explicit transform
20	−5.196 545 582	−5.196 545 582
30	−5.197 312 873	−5.197 312 873
32	−5.197 312 311	−5.197 312 311
34	−5.197 312 289	−5.197 312 289
36	−5.197 312 270	−5.197 312 270
38	−5.197 312 319	−5.197 312 319
40	−5.197 312 203	175.049 274 0
50	−5.197 313 602	
60	−5.197 309 190	
70	−5.197 310 993	
80	−5.197 266 519	
90	−5.197 227 359	
100	−5.197 396 441	
120	−5.196 395 536	

data on the left-hand side was generated by implementing the matrix operators given in section 12.7, while the data on the right-hand side was calculated using the explicitly transformed matrices of the Ortiz approach.

For low orders, both approaches give identical results - as would be expected, since the basic numerical construction of each is identical. In both data up to $N = 38$, the answer can be seen to converge with order to the level of the round-off error. However, increasing N by just 2, from 38 to 40 causes the Ortiz method to collapse. This phenomenon is entirely due to the badly scaled behaviour of the matrix construction transform matrix $\mathbf{I}$, resulting in *incorrect* operator matrices $\hat{\eta}$ and $\hat{\mu}$, and not due to the solution process[7].

That the catastrophic behaviour is not innate to the Tau system is further demonstrated by considering the behaviour of the present results above $N = 40$. What is seen is only a gradual decrease in the decimal precision of the solution, resulting from the gradual increase in the round-off error of the Q-Z solution algorithm as the order increases. At the very high order of $N = 120$, the solution is still correct to three significant figures.

[7] The only difference between the two methods was where they got their operator matrices from. Thus by inference the problem could not have been with the numerical formulation of the Orr-Sommerfeld system since this step was identical in both cases, as was the solution of the subsequent algebraic eigenvalue problem. The entire limitation of the Ortiz approach was thus simply the calculation of incorrect operators at higher orders.

yields the following:

The integral matrix operator evaluates to

$$\hat{J} = \begin{bmatrix} 1 & 0 & 0 & 0 & \cdots & 0 & \cdots \\ 0 & 0 & & & & & \\ -\frac{1}{1\cdot 3} & 0 & & & & & \\ 0 & 0 & & & & & \\ -\frac{1}{3\cdot 5} & 0 & & & & & \\ 0 & 0 & & & & & \\ -\frac{1}{5\cdot 7} & 0 & & & & 0 & \\ \vdots & & & & & & \ddots \end{bmatrix} , \tag{12.52}$$

the limit operator at $r = 1$ is

$$\hat{L}_1 = \begin{bmatrix} 1 & 0 & 0 & 0 & \cdots \\ 1 & 0 & & & \\ 1 & 0 & & & \\ 1 & 0 & & 0 & \\ \vdots & & & & \ddots \end{bmatrix} , \tag{12.53}$$

while for the condition $r = 0$ the correct limit operator is

$$\hat{L}_0 = \begin{bmatrix} 1 & 0 & 0 & 0 & \cdots \\ -1 & 0 & & & \\ 1 & 0 & & & \\ -1 & 0 & & 0 & \\ \vdots & & & & \ddots \end{bmatrix} . \tag{12.54}$$

12.7.2 Verification of operator transformation

To show the effect of the removal of the similarity transform, it is perhaps best to present some results. Table 12.1 shows stability data from the application of the Orr-Sommerfeld stability equation to the parabolic Poiseuille profile. The numerical method used was the spectral formulation given later in chapter 13. Although premature, the presentation of these simple results here is necessary to illustrate the dramatic effect that the elimination of the transformation has on the convergent behaviour of the system.

The data in table 12.1 was generated for a Reynolds number $Re = 3\,000$ and spatial wavenumber $\alpha = 1$, by increasing the order of solution N while noting the behaviour of the imaginary component of the most unstable eigenvalue. The

Algorithm 12.3: $\tilde{\eta}$

```
for  i = 1 : 2 : ∞ {
     e_{i,0} = 2 * i
     for  j = 2 : 2 : i {
          e_{i,j} = 4 * i
     }
}
for  i = 2 : 2 : ∞ {
     for  j = 1 : 2 : i {
          e_{i,j} = 4 * i
     }
}  ;
```

Algorithm 12.4: $\hat{\eta}$

```
e_{0,0} = 2
e_{0,1} = 2
for  i = 1 : ∞ {
     e_{i,i-1} = 1
     e_{i,i}   = 2
     e_{i,i+1} = 1
}
η̂ = ∫_{-1}^{1} ·  .
```

The most notable thing about $\tilde{\eta}$ and $\hat{\eta}$ is that their terms are rational. This allows assembly of numerically *exact* operators, regardless of the order of the problem. The matrices (12.51) are not particularly badly scaled, despite the transformation matrix V being so. This ability to assemble the operators without any round-off error for any reasonable N, is in stark contrast to the standard approach of Ortiz [Liu & Ortiz (1987)] where a 'numerical catastrophe' limits the value of N severely, even before solution is attempted: the incorrect algebraic system is solved for any N exceeding this value. In the current approach, accuracy is limited by the ability to solve the *correct* algebraic system within a fixed-precision system. The 'highly stressed' nature attributed to the operational-Tau method by Wright (1993) has been shown by numerical experiment (see section 13.1.6) to be due to the similarity transformation. The true effect of precision-limited error has proved to be a constant 'noise' at a fixed level of precision in the result - regardless of order, and not a catastrophic decline in accuracy. Similar catastrophic (mis)behaviour of spectral methods has been noted by Gaster (1989), but this observation is quite possibly made of a poor formulation analogous to that of Ortiz, and is not a valid criticism of the spectral approach itself.

The limit and integral operators are far easier to formulate. Evaluation of the matrices (12.20) and (12.25) for the Chebyshev polynomials of the second kind

fact, a 'numerical catastrophe' occurs above a certain order N, where the result of the transformation becomes nonsensical within a fixed-precision system.

As shown in the proof (12.1), the transformation (12.11) is distributive. Thus the transformation sum and product of individual operators is equal to the sum and product of the transformed operators, or

$$V\left[AB + C\right]V^{-1} = \left[(VAV^{-1})(VBV^{-1}) + (VCV^{-1})\right] \quad . \tag{12.50}$$

As a result of this there is no need to transform the final operators into the orthogonal basis (along with the error associated with poor scaling this entails) if it is possible to generate the operators $\hat{\eta}$ and $\hat{\mu}$ (and of course the limit and integral operators, $\hat{L}$ and $\hat{J}$ respectively) directly by other means.

12.7.1 Transformed operators

It is possible to infer $\hat{\eta}$ by direct differentiation of the Chebyshev series representation, and similarly to obtain the structure of $\hat{\mu}$ by pre-multiplying the series by x and rearranging. The relations in Fox & Parker (1968) or Rivlin (1990) are singularly useful in this regard. However, the simplest route was simply to perform numerically the transformations $V\eta V^{-1}$ and $V\mu V^{-1}$ for small matrix orders, and induce the underlying algorithm (if any). This course of action proved to be successful. Using Matlab, these matrices were found to be, for the Chebyshev polynomials of the second kind;

$$\hat{\eta} = \begin{bmatrix} 0 & & & & \\ 2 & 0 & & & \\ 0 & 8 & 0 & & \\ 6 & 0 & 12 & 0 & \\ 0 & 16 & 0 & 16 & 0 \\ & & \cdots & & \end{bmatrix} \; ; \quad \hat{\mu} = \frac{1}{4}\begin{bmatrix} 2 & 2 & & & \\ 1 & 2 & 1 & & \\ & 1 & 2 & 1 & \\ & & 1 & 2 & 1 \\ & & & 1 & 2 \\ & & \cdots & & \end{bmatrix} \quad . \tag{12.51}$$

The underlying generative algorithms for the matrices (12.51) are:

Algorithm 12.2: V^*

$v_{0,0} = 1$
$v_{1,0} = -1$
$v_{1,1} = 2$
for $i = 2 : \infty$ {
  $v_{i,0} = -2 * v_{i-1,0} - v_{i-2,0}$
  for $j = 1 : i$ {
    $v_{i,j} = 4 * v_{i-1,j-1} - 2v_{i-1,j} - v_{i-2,j}$
  }
}.

Thus the first few terms of the matrix V^* are

$$V^* = \begin{bmatrix} 1 & & & & & \cdots \\ -1 & 2 & & & & \\ 1 & -8 & 8 & & & \\ -1 & 18 & -48 & 32 & & \\ 1 & -32 & 160 & -256 & 128 & \\ & & & & & \ddots \end{bmatrix}. \tag{12.49}$$

The reverse mapping can be derived from equation (12.44), or by inverting V^*. However, as will be shown in the next section, neither of the matrices V^* or V^{*-1} is ever needed explicitly because, unlike the operational-Tau method of Ortiz, the current approach formulates the operator matrices *directly* in the orthogonal basis.

From here on, it will be assumed that the orthogonal basis is the set of Chebyshev polynomials of the second kind, on the interval $[0, 1]$. These polynomials are given by equation (12.47), and the basis vector is $\vec{e} = [T_0^*(r)\ T_1^*(r)\ T_2^*(r)\ \cdots]^T$.

The notation for the mapping V will be as such, and the asterisk will be dropped, although V will from here on denote the matrix (12.49).

12.7 Direct formulation of operators

The standard operational-Tau method as advocated by Ortiz and his school entails formulating the differential operator using the function operators η and μ, in the canonical basis, and then transforming it to the orthogonal basis via the similarity transformation (12.11)[6]. The operator V is, however, badly scaled, so that errors are inevitable when large matrices are transformed under (12.11). In

[6] Later papers by Ortiz [cf. Liu & Ortiz (1987)] do not generate the canonical operator from the operators η and μ, but do so directly using a simple algorithm. However, the result of this is still an operator in the canonical basis which must be transformed.

the point of lowest Re on this curve is termed the minimum critical Reynolds number. This is the Reynolds number below which no infinitesimal disturbances are amplified.

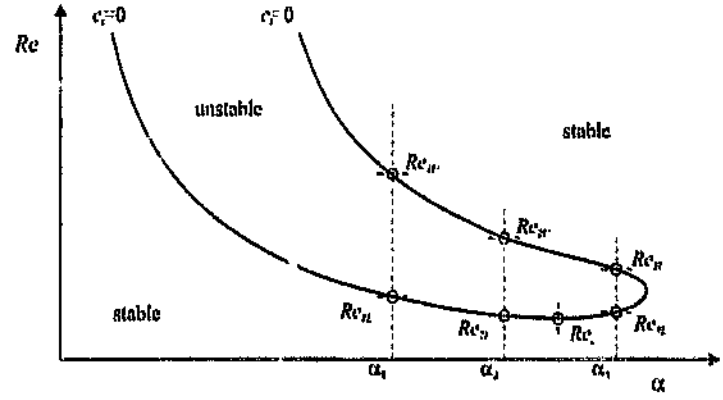

Figure 13.3: A schematic representation of the neutral stability curve for temporal disturbances in plane-Poiseuille flow.

A vertical cross-section through the stability curve in figure 13.3 is given in figure 13.4, showing the prominence of the various eigenvalues. In order to reconstruct the neutral stability curve, a search can be conducted at various values of $\alpha = \alpha_i$ to find the Reynolds numbers Re_{1L} and Re_{1U} at which $c_i = 0$. This is achieved as follows: consider figure 13.4 to be a cross-section taken at $\alpha = \alpha_1$. The two cutting points Re_{1L} and Re_{1U} can easily be determined by using a simple Regula Falsi algorithm, combined every now and then by a half-interval method [Carnahan *et al* (1969)], the combination being necessary because of the non-smooth nature of the c_i vs. Re curve[4]. Rapid convergence with just the Regula Falsi algorithm can be ensured by restricting the range of eigenvalues to be considered, thus only generating the locus of a single eigenvalue. The latter approach must be followed with caution, as it may eliminate the actual eigenvalue that exhibits the largest imaginary component.

The minimum critical Reynolds number may be determined from the results obtained from the above determination of the neutral curve. Considering only the lower values of critical Reynolds number Re_{iL} as shown on figure 13.3, a method to find the minimum Re_c can proceed as follows:

(1) Choose three values of Re_{iL} near the lower side of the curve; for instance, take Re_{1L}, Re_{2L} and Re_{3L}.

(2) Fit a quadratic function through the three points, and find the value of

[4]The mixing of algorithms is important in order to achieve rapid convergence. The non-smooth nature of the c_i vs. Re curve is due to it being defined as the value of the most unstable eigenvalue, and the eigenvalues do change position. With such data, a simple Regula Falsi algorithm may converge very slowly indeed.

development only, with final algorithms to be developed in C or FORTRAN for speed and flexibility. However, after implementation, it was realised that Matlab offered *no* significant speed, size or accuracy impediment over the traditional numerical languages (C, FORTRAN). Furthermore, Matlab is platform independent (identical code can be run on fast UNIX computers, or IBM PC's), and offers a symbolic matrix environment. In this environment, the construction and solution of the Orr-Sommerfeld problem can be carried out *exactly* as derived above. The symbolic nature of the package shields the user from the mundane matrix manipulations[3]. The package also works with complex algebra, so the solution of problems such as equation (13.29) with general complex terms can be treated in a uniform manner.

The computer platform used for the solution of the Orr-Sommerfeld equation under Matlab was an IBM-80486 computer running at 50 Mhz. The operating system was Windows NT. The ability to solve such problems as the Orr-Sommerfeld equation quickly on an ordinary *desktop* computer highlights the rapid development in both numerical methods and computer platforms in recent years. For instance da Silva's (1990) results for plane-Poiseuille flow were obtained using finite-difference methods on an IBM 3081k mainframe computer (with computational speed roughly equal to the current 50 Mhz 80486). In order to attain reasonable accuracy, he had to solve matrices of order 300×300. For equivalent accuracy, the present system required the solution of a system with order 25×25. Results for the current formulation are shown and discussed in the next section.

13.1.0 Numerical results for plane-Poiseuille flow

Numerical tests were conducted using the Orr-Sommerfeld equation for plane-Poiseuille flow. Firstly, generation of the neutral stability curve in the α-Re plane for this flow was investigated, and resulting from this, the minimum critical Reynolds number was extracted for different orders N, using a simple search algorithm. Secondly, the full eigenspectrum for the case of $\alpha = 1$ and $Re = 10\,000$ was obtained for varying N, and the first few eigenvalues were compared to existing results.

The neutral stability curve

The neutral stability curve defines a region in the α-Re plane within which small disturbances are amplified. The neutral stability curve given by Shen (1954) for this problem was already shown in figure 13.1, and is repeated schematically in figure 13.3 below. The boundary of the region is defined by $c_i = 0$, and

[3]For instance, inverting a matrix M is simply the operation `inv(M)`. Matlab utilises up-to-date optimised algorithms for such functions as inversion and eigenvalue and eigenfunction determination.

A numerical solution is now sought to the algebraic eigenvalue problem

$$\vec{b}\left[\hat{\Pi} - c\hat{\Psi}\right] = 0 \quad , \tag{13.29}$$

which is the subject of the next section.

13.1.5 Solution procedure

The formulation of an eigenvalue problem in a suitable numerical framework is one part of the procedure. Regardless of the formulation (finite-difference, spectral), a system of the form (13.29) has to be solved. Once the matrices $\hat{\Pi}$ and $\hat{\Psi}$ are set up, there remains the daunting task of extracting the correct eigenvalue and eigenfunctions from systems exhibiting what is termed 'pathological' behaviour. By this is implied that the systems are extremely ill-conditioned, and perhaps nearly singular.[3]

There are two main approaches to the problem. Firstly, a 'shooting method' can be employed, where an initial guess for the eigenvalue is supplied, and then a search is conducted by varying the eigenvalue in a way so as to reduce the residual of the equation until convergence is attained. This method is useful if an initial approximate guess of a relevant eigenvalue is available. For instance Ng & Reid (1979) employed such a method for the solution of stiff ordinary differential equations, including the Orr-Sommerfeld equation, by using a technique of compound matrices.

If the entire eigenspectrum is desired and if initial guesses are not available, then the standard approach is to use a 'black-box' general complex eigenvalue solver. The standard algorithm employed in this case is the QR [Wilkinson (1965), Wilkinson & Reinsch (1971)] or related algorithms. da Silva (1990) employed a modification of the QR algorithm - the QZ algorithm - for his finite-difference studies of the stability of pipe entrance flow. This method, as suggested by Moler & Stewart (1973), Ward (1975), and Wilkinson (1979), is very effective at extracting the eigenvalues from ill conditioned problems.

The advent of powerful numerical toolboxes for most programming languages (e.g. NAG subroutines for C and FORTRAN), and further, the development of fourth generation mathematical packages such as Matlab, has rendered obsolete any need to develop from scratch solution algorithms for solving these problems. For instance Matlab has the QZ algorithm already available as a standard function call, as do the NAG routines.

The construction and solution of the Orr-Sommerfeld problem was conducted in Matlab. The Matlab environment was initially intended to be for prototype

[3] The distinction between singular and nearly singular systems becomes blurred in a numerical application, due to the finite representation of the matrix values in such applications.

and

$$[c]_{N\times 1} = [1,\ 1,\ 1,\ 1,\ \cdots]^T \quad . \tag{13.22}$$

The individual boundary operators f_i from (13.20) can be calculated and then augmented into a matrix as

$$K_1 = \left[f_1 | f_2 | f_3 | f_4\right] = \begin{bmatrix} 0 & 0 & 1 & 0 \\ 2 & 0 & 1 & 2 \\ -8 & 0 & 1 & 8 \\ 18 & 192 & 1 & 18 \\ -32 & -1536 & 1 & 32 \\ 50 & 6720 & 1 & 50 \\ \vdots & & & \end{bmatrix} \quad . \tag{13.23}$$

The boundary conditions can be stated in the Tau system as

$$\vec{b}K_1 = [0\ 0\ 0\ 0] \quad . \tag{13.24}$$

or via a simple revision of the right-hand side of (13.24), a form ready for augmentation can be developed, namely

$$\vec{b}K_1 = c\vec{0}K_2 \quad . \tag{13.25}$$

Here K_2 is an $N\times 4$ matrix of zeroes, thus making the right-hand side of (13.24) equivalent to the right-hand side of (13.25).

The boundary conditions (13.25) are now augmented to the system (13.5). This leads to

$$\vec{b}\Pi = c\vec{0}\Psi, \quad \Pi = \left[K_1 | (A_1 + iA_2)\right], \quad \Psi = \left[K_2 | B\right]. \tag{13.26}$$

The shifting right of the inner problem matrices can be simply accomplished by using the canonical multiplication matrix - post-multiplication by μ^m shifts the columns of a matrix to the right m places. Thus, if K_1 and K_2 are both made of size $N\times N$ by adding zeroes, then the augmented matrices Π and Ψ can be written equivalently as

$$\Pi = [A_1 + iA_2]\mu^4 + K_1, \tag{13.27}$$

$$\Psi = [B]\mu^4 + K_2. \tag{13.28}$$

13.1.4 Boundary conditions

The boundary conditions must be augmented to the system (13.3) before solution can proceed. As this is an eigenvalue problem, the structure of the matrices is slightly different from those used in the general description of the operational-Tau method at the beginning of this chapter. For the linear problem described there, the boundary conditions had to be augmented to a system

$$\vec{b}L = \vec{k}$$

where L is a square matrix, and $\vec{k}$ is a row vector; thus for ν boundary conditions, the boundary operators were of the form

$$\vec{b}K = \vec{d} \quad ,$$

with K an $N \times \nu$ matrix, and $\vec{d}$ a row vector with ν elements.

For this case, the boundary conditions need to be of a similar form to equation (13.5), that is, in the form of

$$\vec{b}K_1 = c\vec{b}K_2 \quad .$$

Before proceeding ,the form of the boundary operators (13.3) in the Tau system must be considered. In turn these are

$$\begin{aligned}
D\phi|_{\eta=0} = 0 \quad &\Rightarrow \quad \vec{b}_i\,[c]_{\eta=0} = 0 \\
&\text{or:} \quad \vec{b}f_1 = 0, \\
D^3\phi|_{\eta=0} = 0 \quad &\Rightarrow \quad \vec{b}\hat{\eta}^3\,[c]_{\eta=0} = 0 \\
&\text{or:} \quad \vec{b}f_2 = 0, \\
\phi|_{\eta=0} = 0 \quad &\Rightarrow \quad \vec{b}[c]_{\eta=1} = 0 \\
&\text{or:} \quad \vec{b}f_3 = 0, \\
D\phi|_{\eta=1} = 0 \quad &\Rightarrow \quad \vec{b}\hat{\eta}\,[c]_{\eta=1} = 0 \\
&\text{or:} \quad \vec{b}f_4 = 0.
\end{aligned} \tag{13.20}$$

The terms $[c]_{\eta=0}$ and $[c]_{\eta=1}$ evaluate to

$$[c]_{\eta=0} = [1, -1, 1, -1, \cdots]^T \tag{13.21}$$

Thus for a general velocity profile, given as $u = \vec{a}^T c$ in the Chebyshev basis, the matrix (13.6) can now be generalised to

$$\hat{A}_r = \left[\hat{\eta}^2 - \alpha^2 I\right] \hat{R}(\vec{a}^T) - \hat{R}(\vec{a}^T \hat{\eta}^2) \tag{13.19}$$

where the operator $\hat{R}$ is defined by (13.17).

13.1.3 Construction

Returning to the more restrictive case of plane-Poiseuille flow, the matrices (13.9), (13.10), (13.11) and (13.12) must be developed for the chosen order N. As was discussed in section 12.5, the operators should be constructed as infinite matrices. However, in this case it will suffice if the operators $\hat{\eta}$ and $\hat{\mu}$ are matrices of size $(N+1) \times (N+1)$, because the largest power of the polynomial operator $\hat{\mu}$ is 2. Once $\hat{A}_r$, $\hat{A}_i$ and $\hat{B}$ are constructed at the hi order, they can be truncated to $N \times N$.

In reality, only the matrix $\hat{A}_r$ needs to be constructed at the larger dimension. It is only the operation of raising $\hat{\mu}$ to a power that causes a disparity between the truncated and infinite result before and after the operation[1]. Thus matrix (13.9) can be first developed at order $(N+1) \times (N+1)$ then truncated at $N \times N$. All the other matrices (because they contain only the terms $\hat{\eta}$, I) can be constructed at order $N \times N$.

For the more general case of an arbitrary velocity profile given in the canonical basis, the construction of $\hat{A}_r$, then given by equation (13.16), must be conducted at order $(N+p-1) \times (N+p-1)$, where p is the dimension of the coefficient vector $\vec{a}$, of the base velocity profile. If the general profile is applied in the orthogonal basis, then $\hat{A}_r$, now given by equation (13.19), can be constructed at $N \times N$, because no matrices are raised to a power here.

The best method of checking whether the matrix truncation has been carried out at a sufficient order is to generate two sets of matrices; one set constructed at the order to be tested, and one at a much higher order [say $(2N) \times (2N)$]. The point of truncation can be said to be correct if the large and small operators, when both truncated at $N \times N$, are identical. If they are not, then some order-dependent numerical 'reflection' has occurred.

[1] Raising a finite sized $\hat{\mu}$ to a power causes the 'reflection' of numerical values at the lowest rows of the matrix - the higher the power, the more rows affected. In an infinite system, such 'end-effects' in the multiplication would occur at infinity. If the raised power is m, then the number of 'bad' rows is $m-1$. Thus if the highest polynomial power in the system is k, then to be safe, the matrices should be developed at order $(N+k-1) \times (N+k-1)$.

Thus for a general velocity profile, the matrix (13.6) can be generalised to

$$\hat{A}_r = \left[\hat{\eta}^2 - \alpha^2 I\right] \hat{P}(\vec{u}) - \hat{P}(\vec{u}\eta^2) \quad . \tag{13.16}$$

The operator (13.13) accepts a coefficient vector in the canonical basis. Of more use would be an analogous operator that would construct the matrix from the coefficient vector in the Chebyshev basis. Again, consider the representation of a known function $u = u(y) = \vec{u}c$, but with c the orthogonal basis vector. The effect of multiplication by u on the unknown function ϕ is equivalent in the Tau system, of post-multiplication by the matrix

$$\hat{R}(\vec{u}) = \sum_{i=0}^{N-1} u_i \zeta_i \tag{13.17}$$

where ζ_i is defined by algorithm (13.1) below.

Algorithm 13.1: ζ_k

```
for  i = 0 : k − 1 {
     v_{i,k−i} = 1
}
v_{0,k} = 2
for  i = 1 : ∞ {
     v_{i+k,i} = 1
}
for  i = 1 : ∞ {
     v_{i,i+k} = v_{i,i+k} + 1
}
ζ_k = ζ_k/2    .
```

The form of algorithm (13.1) can be derived by considering the relations of Fox & Parker (1968), for the product of two Chebyshev polynomials.

For example, $k = 3$ would give

$$\zeta_3 = \frac{1}{2}\begin{bmatrix} 0 & & 2 & & 0 & \\ & 1 & & 1 & & \\ 1 & & & & 1 & \\ & 1 & & & & \\ & & 1 & & & \\ 0 & & & \ddots & & \end{bmatrix} . \tag{13.18}$$

The operators (13.6), (13.7) and (13.8) can now be replaced by their Tau analogues. For this case, the base flow is $u = 1 - y^2$, simply a polynomial multiplier.

Thus u becomes

$$\hat{U} = I - \hat{\eta}^2 \tag{13.9}$$

and $D^2 u$ is simply $-2I$. The other operators are then

$$\hat{\mathrm{A}}_r = \left[\hat{\eta}^2 - \alpha^2 I\right]\hat{U} + 2I \tag{13.10}$$

$$\hat{\mathrm{A}}_i = \frac{1}{\alpha Re}\left[\hat{\eta}^2 - \alpha^2 I\right]^2 \tag{13.11}$$

$$\hat{B} = \hat{\eta}^2 - \alpha^2 I \tag{13.12}$$

where I is the identity matrix. For chosen values of N, Re and α - respectively, the order of solution, the Reynolds number, and the wavenumber - the matrices (13.10), (13.11) and (13.12) can be assembled.

13.1.2 Treatment of general velocity profiles

The above derivation has been strictly for Poiseuille flow with mean velocity $u = 1 - y^2$. Before solution is attempted, a diversion will be made to explain how a general velocity profile is accommodated. This is useful in that such a generalisation is necessary for the later solution of the Sexl equation for arbitrary velocity profiles.

For a more general velocity profile given as $u = \vec{u}y$, where y is the canonical basis vector, the terms u and $D^2 u$ can be evaluated easily by first defining the function $\hat{P}(\vec{u})$ as

$$\hat{P}(\vec{u}) = \sum_{i=0}^{N-1} u_i \hat{\eta}^i \tag{13.13}$$

where u_i is the i'th term of the coefficient vector $\vec{u}$ in the canonical basis. For some given variation $u = u(y) = \vec{u}y$, the terms u and $D^2 u$, as multipliers onto the unknown function ϕ become, in the Tau system, the operator matrices:

$$u \Rightarrow \hat{P}(\vec{u}) \tag{13.14}$$

$$D^2 u \Rightarrow \hat{P}(\vec{u}\hat{\eta}^2) \quad . \tag{13.15}$$

13.1.1 Analytical and numerical formulation

The flat plate system has a central plane of symmetry, therefore two sorts of disturbance mode can exist within it; the modes can be either symmetric and antisymmetric, or in more mathematical terms, even and odd. If the full domain $y \in [-1, 1]$ were taken as the region of solution, then the results obtained would consist of all the eigenfunctions, both even and odd. As only half the solution domain is considered here, suitable boundary conditions must be implemented at the centreline. Dependent on these conditions, a solution can be obtained for either the even or the odd modes. Since the odd modes for parallel channel flow are always stable, the even-mode boundary conditions are implemented at the centre. The full set of boundary conditions are [Drazin & Reid (1981)] as follows:

$$\begin{aligned} D\phi|_{y=0} &= 0, \\ D^3\phi|_{y=0} &= 0, \\ \phi|_{y=1} &= 0, \\ D\phi|_{y=1} &= 0. \end{aligned} \tag{13.3}$$

The solution can now proceed. First equation (13.1) must be rearranged to the general form

$$A\phi = cB\phi \quad ,$$

which is amenable to numerical solution. Equation (13.1) becomes

$$\left\{ \frac{i}{\alpha Re} \left[D^2 - \alpha^2 \right]^2 + u \left[D^2 - \alpha^2 \right] - \left[D^2 u \right] \right\} \phi = c \left[D^2 - \alpha^2 \right] \phi \quad , \tag{13.4}$$

and further grouping of the left- and right-hand sides gives

$$[\mathcal{A}_r + i\mathcal{A}_i] = cB \tag{13.5}$$

where

$$\mathcal{A}_r = u \left[D^2 - \alpha^2 \right] - \left[D^2 u \right] \tag{13.6}$$

$$\mathcal{A}_i = \frac{1}{\alpha Re} \left[D^2 - \alpha^2 \right]^2 \tag{13.7}$$

$$B = \left[D^2 - \alpha^2 \right] \quad . \tag{13.8}$$

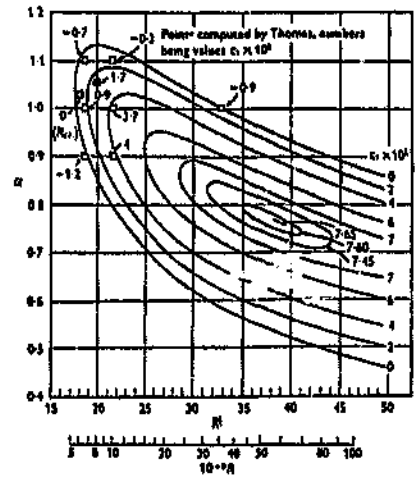

Figure 13.1: The curves of constant temporal amplification for plane-Poiseuille flow [Shen (1954), after Lin (1955)].

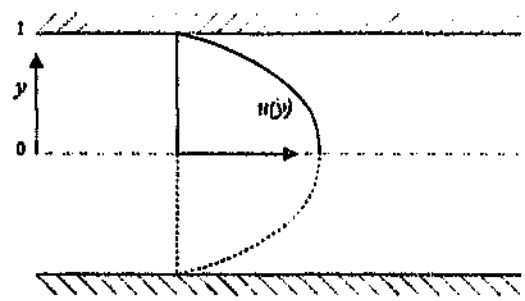

Figure 13.2: The solution domain for the stability of flow between parallel plates.

Stability for a certain velocity profile u is determined, for a given value of Re and α, by whether the imaginary component of c is less than zero. If $c_i < 0$ for all α, then the profile is stable, whereas if for $c_i \geq 0$ for any α, then a small disturbance in the flow will grow in time.

As a further simplification, only the solution for plane-Poiseuille flow will be considered here, although it is a trivial task to extend this Tau formulation to accept any general velocity profile $u(y)$ - as long as it is expressible as a polynomial series expansion. Although it is not directly used here, the more general formulation is presented below, because of its necessity later for solving the Sexl stability equation for general velocity profiles.

13.1 The Orr-Sommerfeld stability problem

The first system considered is the Orr-Sommerfeld equation for the stability of planar flow. The solution is formulated generally for flow between parallel plates. While this might seem like tackling a hard problem first, it will be shown that this method allows a simple formulation for such high-order systems.

Early investigations of the stability of plane-Poiseuille flow were carried out by Heisenberg (1924) and Lin (1945) using asymptotic methods. Thomas (1953) first implemented a numerical method of solution to this problem, and his solution showed that this flow was indeed unstable. Lin (1944) gave the curve of neutral stability for plane-Poiseuille flow. Later Shen (1954), extended these results by giving the contours of constant temporal amplification as well as the curve of neutral stability. Shen obtained these contours by using a perturbation from Lin's curve. The stability curves of Shen are shown in figure 13.1. His results, although qualitatively correct, do deviate from the more accurate calculations of later authors [da Silva (1990)]. Most other investigations into this system were concerned only with the minimum critical Reynolds number, and thus did not present values for the entire neutral stability curve. Orszag (1971a) was the first to accurately predict the minimum critical Reynolds number for this flow, using a Chebyshev-Tau method. His result of $Re = 5\,772.22$, $\alpha = 1.020\,56$ and $c = 0.264002$ is generally accepted as being the *exact* answer to this problem. Recently, Liu & Ortiz (1987), using their operational-Tau method, extended Orszag's results to $Re = 5\,772.221\,2$, $\alpha = 1.020\,547$ and $c = 0.264\,000\,2$, substantially agreeing with unpublished results of Davey and as given in Drazin & Reid (1981), ($Re = 5\,772.221\,8$, $\alpha = 1.020\,547$ and $c = 0.264\,000\,3$) obtained using a shooting method.

The Orr-Sommerfeld equation [Drazin & Reid (1981), Lin (1955)] is given by

$$\frac{-i}{\alpha Re}\left[D^2 - \alpha^2\right]^2 \phi = (u - c)\left[D^2 - \alpha^2\right]\phi - \left[D^2 u\right]\phi \tag{13.1}$$

where α is the wavenumber, Re is the Reynolds number based on channel cross-section, c is the phase-speed or celerity, $\phi(y)$ is the disturbance shape and u is the undisturbed velocity profile. The solution domain is taken as $y \in [0, 1]$, where $y = 0$ corresponds to the centre plane of the system, and $y = 1$ to the wall. The base velocity $u = u(y)$ is given as a polynomial function in y. Figure 13.2 shows the solution domain and undisturbed velocity profile.

Equation (13.1) is a differential eigenvalue problem of the form

$$\mathcal{F}(\alpha, c, Re) = 0. \tag{13.2}$$

For this problem, the simpler case of temporal stability is considered, yielding a linear complex differential eigenvalue problem, with c the complex eigenvalue.

Chapter 13

Verification

The modified operational-Tau method is perhaps better illustrated further by means of example. This chapter demonstrates its application to standard problems whose results are relevant to this study.

The first example considers the classic Orr-Sommerfeld stability equation, for the case of plane-Poiseuille flow. Comparison is made between the present study and other results for both the case of the minimum critical Reynolds number, and for eigenspectra at various Reynolds numbers. The relevance of this example is twofold. Firstly, it is a high-order differential eigenvalue problem, and thus an ideal vessel for verifying the accuracy of the method. Secondly, its similarity to the Sexl equation, in the context of pipe stability, allows for the introduction of formulation and solution techniques that will be used to later solve the pipe stability problem. The second example is concerned with a simple linear initial value problem in a single space variable - the temporal development of an impulsively started pipe flow far from the inlet. This problem is used to introduce the temporal discretisation, which will be used later in the non-linear pipe inlet flow calculations. Further to this, the parameters that will be used to characterise the unsteady pipe flow are introduced. The final problem concerns the solution of a non-linear ordinary differential equation - the Blasius boundary layer similarity equation for the spatial development of a flat-plate boundary layer in the absence of a pressure gradient. This solution demonstrates the iterative procedure needed for an exact solution to such a system, in addition to illustrating the method of dealing with the convolution sums arising from the use of a Chebyshev method.

The formulation of the problems in this chapter is by necessity full, in order that the details of the process be evident. The numerical solutions presented in subsequent chapters will be more brief, but frequent reference will be made to these prototypical examples below.

If the matrix (13.50) is extended to order $N \times N$, and the vector (13.51) to length N, then the augmentation carried out in equations (13.53) and (13.54) can be accomplished equivalently by use of the canonical shift matrix μ as

$$\Pi = C\mu^2 + G, \quad \Psi_n = \vec{D}_n\mu^2 + \vec{E}. \tag{13.55}$$

As discussed in section 13.1.3, the construction of the matrices should be carried out at an order slightly bigger than the order N at which solution will proceed. In this case, all matrices can be constructed directly at order $N \times N$, because the matrix μ is not raised to any power here. The matrix Π is non-singular, and can be readily inverted to allow explicit solution for the unknown coefficient vector $\vec{b}_{n+1}$. Solution of system (13.52) is the subject of the next section.

13.2.4 Initial conditions and solution procedure

The solution approach for an initial value problem is to start with some starting or *initial* value u_0 to the system at time $t = 0$, and to allow the solution to develop through time by application of the governing differential equation. For this particular problem, the starting value is taken as $u_0 = 1$, or the velocity constant everywhere.

In the Chebyshev basis, this condition can be represented by the coefficient vector

$$\vec{b}_0 = [1\ 0\ 0\ \cdots], \tag{13.56}$$

The solution is initiated by using this value to generate $\vec{D}_0$, using initially a low-order temporal scheme (because only one level of solution exists at this point). The matrices Π and Ψ are then generated. The matrix Π is then inverted and a solution is sought for the next time level as

$$\vec{b}_1 = \Psi_0[\Pi]^{-1}. \tag{13.57}$$

If a higher-order time scheme is to be used, the matrix Π can now be recalculated for new values of the constants a_i [see table (13.5)]. The vector Ψ_1 is now generated using the velocity data from the time-steps zero and one. By inverting Π again, the solution $\vec{b}_2$ at time-step two, can be generated.

If the temporal discretisation remains fixed, then Π is a constant. Thus it need only be inverted once and then stored. Solutions to each subsequent time-step $t+1$ are then sought by calculating Ψ_t and post-multiplying it by the inverted Π, or

$$\vec{b}_{t+1} = \Psi_t[\Pi]^{-1}. \tag{13.58}$$

$$\begin{aligned} u|_{r=1} = 0 \quad &\Rightarrow \quad \vec{b}_{n+1} c|_{r=1} = 0 \\ &\text{or:} \quad \vec{b}_{n+1} f_1 = 0 \qquad (13.47) \\ \left.\frac{\partial u}{\partial r}\right|_{r=0} = 0 \quad &\Rightarrow \quad \vec{b}_{n+1} q c|_{r=0} = 0 \\ &\text{or:} \quad \vec{b}_{n+1} f_2 = 0 \quad . \qquad (13.48) \end{aligned}$$

These conditions can be augmented into a single system as

$$\vec{b}_{n+1} \hat{G} = \vec{k}, \qquad (13.49)$$

where $\hat{G}$ is defined as

$$\hat{G} = \left[f_1 \vdots f_2 \right] = \begin{bmatrix} 1 & 0 \\ 1 & 2 \\ 1 & -8 \\ 1 & 18 \\ 1 & -32 \\ 1 & 50 \\ \vdots & \vdots \end{bmatrix}, \qquad (13.50)$$

and $\vec{k}$ is simply

$$\vec{k} = [0 \; 0] \quad . \qquad (13.51)$$

The solution for the time-step $n+1$ is now generated by solving the system

$$\vec{b}_{n+1} \hat{\Pi} = \vec{\Psi}_n \qquad (13.52)$$

where $\hat{\Pi}$ is defined as

$$\hat{\Pi} = \left[\hat{G} \vdots \hat{C} \right] \qquad (13.53)$$

and $\vec{\Psi}_n$ is given by

$$\vec{\Psi}_n = \left[\vec{k} \vdots \vec{b}_n \right]. \qquad (13.54)$$

conditions) can in a numerical scheme be inverted to yield an explicit solution for the unknown u^{n+1}.

13.2.3 Numerical formulation

Equation (13.39) is analogous to the general form (12.26), which, as was shown, is simply solved using the operational-Tau method. Returning now to the more specific problem, equation (13.34), a statement in the form of (13.39) can be made simply by multiplying this equation through by r:

$$\mathcal{C}u^{n+1} = D(u^n, u^{n-1}, \cdots) \quad , \tag{13.40}$$

with the operator $\mathcal{C}$ and function D now defined as

$$\mathcal{C} = [r - a_0 \Delta t \mathcal{M}] \tag{13.41}$$

$$D = ru^n + \Delta t \mathcal{M}\left[a_1 u^n + a_2 u^{n-1} + a_3 u^{n-2} + \cdots\right], \tag{13.42}$$

and the term $\mathcal{M}$ given by equation (13.35).

The equation (13.40), along with the boundary conditions (13.31), can now be formulated in the Tau system: consider first the operator $\mathcal{C}$ and functional D. If the function u^k is represented in Tau form as $\vec{b}_k c$, then these operators respectively become in the Tau system:

$$\hat{C} = \left[\hat{\mu} - (a_0 \Delta t)\hat{M}\right], \tag{13.43}$$

$$\vec{D}_n = \vec{b}_n \left[\hat{\mu} + (a_1 \Delta t)\hat{M}\right] + \Delta t \left[a_2 \vec{b}_{n-1} + a_3 \vec{b}_{n-2} + \cdots\right] \hat{M}, \tag{13.44}$$

$$\hat{M} = -2\hat{L}_1 \hat{\mu} + \hat{\eta}\hat{\mu}\hat{\eta}, \tag{13.45}$$

where the limit operator $\hat{L}_1$ is defined in the canonical basis as equation (12.19) and in the current Chebyshev system directly as (12.53). The operators $\hat{\mu}$ and $\hat{\eta}$ are defined as usual directly in the Chebyshev basis by the matrices (12.51). Solution for the time step $n+1$ entails solving the inner problem

$$\vec{b}_{n+1} \hat{C} = \vec{D}_n \tag{13.46}$$

along with the boundary conditions (13.31). The spatial boundary conditions become, in the Tau system, the following matrix operators:

Table 13.5: The values for the constants a_i for the the various temporal discretisation schemes.

Scheme	a_0	a_1	a_2	a_3
Explicit				
Forward-Euler	0	1	0	0
Adams-Bashforth (2nd order)	0	$\frac{3}{2}$	$-\frac{1}{2}$	0
Adams-Bashforth (3rd order)	0	$\frac{23}{12}$	$-\frac{16}{12}$	$\frac{5}{12}$
Implicit				
Backward-Euler	1	0	0	0
Crank-Nicholson	$\frac{1}{2}$	$\frac{1}{2}$	0	0
Adams-Moulton	$\frac{5}{12}$	$\frac{8}{12}$	$-\frac{1}{12}$	0

approaches can be constructed by making a_0 non-zero. Table (13.5) gives the values of the constants a_i that define the various schemes.

Such schemes as the leap-frog discretisation are not representable exactly in this form; however such a scheme is only really appropriate for problems with temporal periodicity [Canuto *et al* (1988)], and even here are subject to an aliasing effect. Thus they will not be considered further here. Other approaches not encompassed by the above formulation are Runge-Kutta methods. Although these show better temporal accuracy than the simpler schemes above, they may be more prone to suffer from stability problems in long-term time integration. Furthermore, their accuracy gain over the simpler methods is not of infinite-order, so a simple decrease in time step Δt of a simple method is sufficient to match the accuracy of a Runge-Kutta approach at a coarser time-step. Thus only the set of schemes given by equation (13.37) will be considered here. The stability and convergence properties of all these schemes are discussed in detail in Canuto *et al* (1988). These convergence criteria given in this reference are only an indication, however, so the current method was formulated generally as in (13.37) and numerical experimentation was undertaken to determine the stability of the various approaches.

Considering equation (13.37), the unknown quantity is represented by the term u^{n+1}. As such, this equation can be rearranged to make u^{n+1} the subject of the left-hand side alone. Further, the linearity of $\mathcal{L}$ allows substantial simplification of the right-hand side. This results in

$$[1 - a_0 \Delta t \mathcal{L}]\, u^{n+1} = u^n + \Delta t \mathcal{L} \left[a_1 u^n + a_2 u^{n-1} + a_3 u^{n-2} + \cdots \right] \qquad (13.38)$$

which is an equation of the form

$$\mathcal{A} u^{n+1} = B(u^n, u^{n-1}, \cdots) \quad . \qquad (13.39)$$

The right-hand side B contains only known quantities (the u's from the previous time steps) and the left-hand operator $\mathcal{A}$ (after incorporation of the boundary

As was shown in section 12.2.2, the limit term in (13.33) can be represented uniformly in the operational-Tau system. The operator $\mathcal{L}$ does however contain fractions in r, which are not directly representable in the numerical system. This is simply resolved by multiplying through by r in equation (13.30). This results in the initial-value formulation

$$r\frac{\partial u}{\partial t} = \mathcal{M}u \tag{13.34}$$

with the linear operator $\mathcal{M}$ defined as

$$\mathcal{M} = -2r\frac{\partial}{\partial r}\bigg|_{r=1} + \frac{\partial}{\partial r}\left(r\frac{\partial}{\partial r}\right). \tag{13.35}$$

The operator (13.35) is directly representable in the Tau system.

13.2.2 Temporal discretisation

The spatial operator (13.35) is suitable for implementation under the operational-Tau system. Equation (13.30) is however an initial value problem, thus the temporal discretisation must be considered. In this section a simple discrete temporal method is used, but this is formulated generally such that it embraces all common temporal discretisations.

Consider for now equation (13.32). The left-hand side of this equation can be discretised using a finite-difference methodology as

$$\frac{\partial u}{\partial t} = \frac{1}{\Delta t}\left[u^{n+1} - u^{n}\right] \tag{13.36}$$

where the superscript ^{n} represents the solution at the time-level n, and Δt is the time step. In general, the temporal variation (13.36) can be said to depend on the solution at different time-levels; this can be stated as

$$\frac{1}{\Delta t}\left[u^{n+1} - u^{n}\right] = a_0\mathcal{L}u^{n+1} + a_1\mathcal{L}u^{n} + a_2\mathcal{L}u^{n-1} + \cdots \quad . \tag{13.37}$$

where the terms a_i are constants. It can be shown simply that the judicious choice of constants can determine a broad range of temporal discretisations. For instance a range of explicit schemes including all the Adams-Bashforth methods is generated by setting $a_0 = 0$ and choosing various values for the other constants. Implicit schemes such as the Crank-Nicholson and Adams-Moulton

13.2 Impulsively started laminar pipe flow far from the inlet

The solution of equations (10.33) and (10.34) determine the laminar behaviour of high Reynolds number flow in the entrance region of a pipe. This pair form a coupled, non-linear system in u and v, the axial and radial velocities respe tively. Of interest in this system is the behaviour of the fluid far downstream of the pipe inlet. In this limit, the radial component of velocity v becomes zero, and the system (10.33) and (10.34) reduces t single simple linear initial-value equation, with $u = \bar{u}(\bar{r},t)$ only. Further, only the impulsive case is considered here. For this the term $\Omega = 0$, and equation (10.33) simplifies somewhat. The solution of this system is the subject of this chapter.

13.2.1 Analytical formulation

The neglecting of the radial component of velocity and the acceleration term in equations (10.33) and (10.34) leads directly to the formulation

$$\frac{\partial \bar{u}}{\partial \bar{t}} = -2\left.\frac{\partial \bar{u}}{\partial \bar{r}}\right|_{\bar{r}=1} + \frac{1}{\bar{r}}\frac{\partial}{\partial \bar{r}}\left(\bar{r}\frac{\partial \bar{u}}{\partial \bar{r}}\right) \tag{13.30}$$

with boundary conditions

$$\begin{aligned} \bar{u}|_{\bar{r}=1} &= 0, \\ \left.\frac{\partial \bar{u}}{\partial \bar{r}}\right|_{\bar{r}=0} &= 0, \\ \bar{u}|_{\bar{t}=0} &= \bar{u}_0. \end{aligned} \tag{13.31}$$

the wall no-slip condition, the centreline symmetry condition and the initial velocity distribution respectively.

The system (13.30) and (13.31) describes fully the parallel development of flow in a pipe. Equation (13.30) is a linear system of the form

$$\frac{\partial u}{\partial t} = \mathcal{L}u \tag{13.32}$$

where the linear operator $\mathcal{L}$ is defined as

$$\mathcal{L} = -2\left.\frac{\partial}{\partial r}\right|_{r=1} + \frac{1}{r}\frac{\partial}{\partial r}\left(r\frac{\partial}{\partial r}\right), \tag{13.33}$$

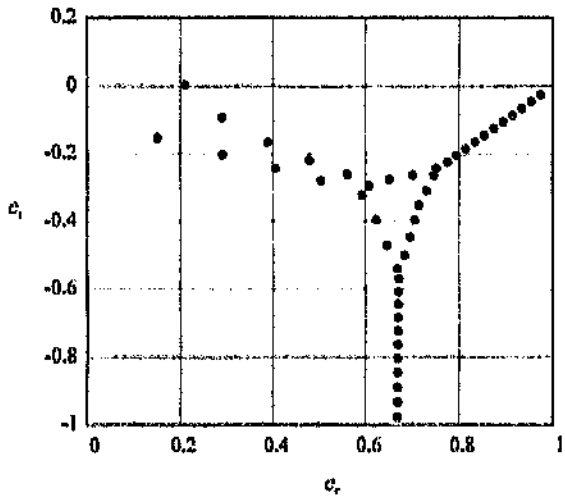

Figure 13.6: The eigenspectrum for the even modes for plane-Poiseuille flow with $\alpha = 1$ and $Re = 50\,000$.

result represents a computer operation-count saving of 60 times, with an improvement in accuracy of 4 significant figures. For the approach of da Silva to have attained comparable accuracy, his order would have had to be inconceivably high, because of the algebraic convergence rates given by a finite-difference approach. For comparable accuracy to da Silva at this Reynolds number, the current scheme needed to be solved at only $N = 52$, resulting in a real operation-count ratio of approximately 1/260.

The operational-Tau approach is thus capable of solving ill-conditioned problems highly accurately. The level of accuracy attainable at high values of Re renders comparison with other (finite-difference) methods meaningless. The simplicity of the method (*no* use of improvement techniques, second-guessing the eigenfunction shapes, or extrapolation to infinite mesh density.) yields the solution of this traditionally difficult system trivial. Furthermore, it exceeds the accuracy of the traditional Tau approach [Orszag (1971a)] while avoiding the use of the MWR formulation altogether. Its operational nature allows simple algorithmic assembly of *any general system* and its analogy to analytic operator notation allows for ready understanding of the method.

The improvement over the original operational-Tau method, of assembling the operators directly, removes one of the major impediments of this approach, allowing extension of problems to extremely high orders of solution (hence allowing the solution of badly scaled problems) with no catastrophic decay in accuracy as is usually noted in the standard operational-Tau method. The approach thus shows itself to be highly optimum for the solution of badly conditioned eigenvalue problems such as the Orr-Sommerfeld equation. As will be shown in the next example, the method is ideal for initial-value problems as well.

Table 13.4: The variation of the most unstable eigenvalue for plane-Poiseuille flow with $\alpha = 1$ and increasing Re, compared to the results of Gersting (1981) and da Silva (1990).

Reynolds number	Present results		Gersting (1981)	da Silva (1990)
	order	value		
10 000	38	0.237 526 49 +0.003 739 67i	0.237 52 +0.003 74i	0.237 52 +0.003 74i
50 000	46	0.175 258 8 −0.005 312i	0.175 25 −0.005 3i	0.175 25 −0.005 3i
100 000	62	0.145 924 79 −0.015 042 0i	0.145 0 −0.015 i	0.145 9 −0.015 i
500 000	84	0.084 329 0 −0.016 353 71i	0.084 −0.016 3i	0.084 3 +0.016i

(ii) The mode A_1 is unstable at moderate Reynolds numbers, but becomes stable again with increasing Re. At the higher Re, it is not the most unstable mode at all, that role being assumed by the first few eigenvalues of the P family, although none of these ever actually become unstable.

(iii) The eigenspectrum for the highest value of Re, namely $Re = 500\,000$ is given in figure 13.6. As can be seen, it is very similar to the spectrum shown in figure 13.5. The emergence of the triangular central feature is interesting. A similar feature is evident in Davey & Drazin's (1969) spectrum for $Re = 10000$, but the feature there was due to poor numerical representation[6]. The eigenvalues in figure 13.6 are well converged, thus the 'triangle' represents a real feature of the eigenvalue spectrum at this Reynolds number.

(iv) The current results were produced to the greatest precision possible - order was increased until the decimal representation was fixed to the level of the round-off 'noise'. As can be seen, the effect of the finite decimal representation (round-off) on the result is at an approximately constant level, irrespective of order N. This indicates that the maximum accuracy attainable is fixed by the numerical precision (for a particular problem, that is) and not by the order of the matrices. This further vindicates the approach of directly evaluating the operator matrices (see section 12.7) directly in the orthogonal domain. The round-off problem of a standard operational Tau approach would have been limited in order here to approximately $N = 40$: at this order, for the case of $Re = 500\,000$, the result would have been accurate to only 1 significant figure - far inferior to both da Silva's and Gersting's results.

(v) For the case of $Re = 500\,000$, da Silva's calculations were extrapolated from $N = 100$, $N = 200$, and $N = 300$ to infinite order. Assuming an operation-count of approximately N^3 for the eigenvalue solver, the current

[6] The accurately determined spectrum for $\alpha = 1$, $Re = 10\,000$ is given in figure 13.5.

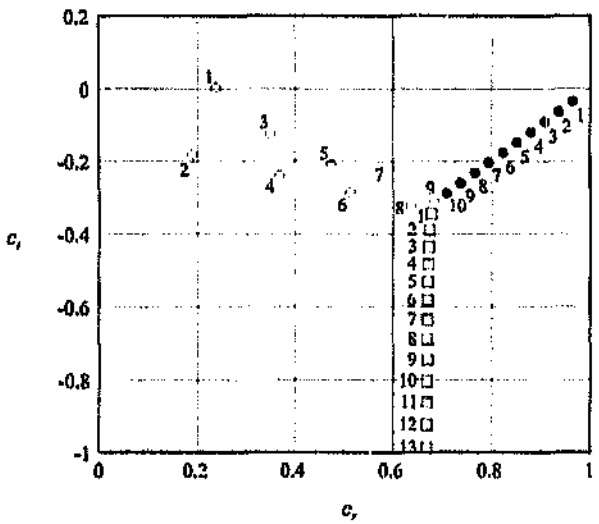

Figure 13.5: The eigenspectrum for the even modes for plane-Poiseuille flow with $\alpha = 1$ and $Re = 10000$. Modes numbered according to the scheme of Mack (1976). ○, A family; •, P family; □, S family.

Accuracy with increasing Reynolds number

The variation in accuracy of the system with increasing Reynolds number is an important consideration in stability calculations. As Reynolds number is increased, the left-hand side of the Orr-Sommerfeld equation (13.1) becomes increasingly smaller with respect to the right-hand side. This leads to the system becoming increasingly badly scaled, with the resultant introduction of inaccuracies. Numerical experimentation was conducted at $\alpha = 1$, ascertaining the most unstable eigenvalue for increasing Re. This was done in accordance with the results of Gersting (1981) and da Silva (1990). For Reynolds numbers of 10 000, 50 000, 100 000 and 500 000, answers from the present methods were obtained to the maximum attainable decimal precision. Table (13.1) shows the results obtained, their precision, and the order of solution. Only the correct (converged) digits are given for each case. A comparison is also made with the values of both Gersting and da Silva.

By increasing N at each Reynolds number while considering the behaviour of the most unstable eigenvalue (λ_1 in figure 13.5), it was possible to ascertain which decimal digits in the answer were invariant. da Silva's and Gersting's results have also been truncated to show only the digits that they determined correctly. A number of issues arise from these results:

(i) As the Reynolds number increases, the order of the system must be increased to represent the eigenvalues correctly. This is primarily because the numerical problem becomes badly scaled with increasing Re.

to his $N = 58$. Such vast gains in accuracy over the finite-difference approach allowed solution times to be decreased by orders of magnitude for comparable results to da Silva.

Table 13.3: Comparison between present results for the most unstable eigenvalue with $\alpha = 1$, $Re = 10000$, and those from Orszag (1971a), with N varied to show the rate of convergence.

Orszag (1971a)			Present		
order	value		order	value	
28	0.237	$+0.0i$	20	0.237	$+0.00i$
30	0.237	$+0.003\,7i$	22	0.237	$+0.003i$
34	0.237	$+0.003\,7i$	24	0.237	$+0.003\,7i$
40	0.237 52	$+0.003\,73i$	30	0.237 52	$+0.003\,7i$
46	0.237 52	$+0.003\,739i$	32	0.237 526	$+0.003\,739i$
52	0.237 526 4	$+0.003\,739\,67i$	34	0.237 526 4	$+0.003\,739\,6i$
58	0.237 526 49	$+0.003\,739\,67i$	38	0.237 526 49	$+0.003\,739\,67i$

It is interesting to note that the current method is more accurate for a chosen order of solution then Orszag's approach. This can be easily explained by considering the problem domain in each case. Orszag solved the problem over the full interval $[-1, 1]$ but only used the even Chebyshev polynomials whereas the current method used the full Chebyshev set over the sub-range $[0, 1]$. Both methods returned only the even modes, but the restriction in domain allowed better accuracy of interpolation [see Fox & Parker (1968), Rivlin (1990)]. If Orszag had applied his method to the sub-range $[0, 1]$, then the results of the two methods would be identical. This refutes a suggestion made by Liu & Ortiz (1987) that their method is innately better than that of Orszag. In fact the two yield identical matrices when applied identically to a problem, and the only benefit of the current formulation over Orszag's method is that it avoids the confusing and difficult formulation of his MWR approach.

The first 16 symmetrical and asymmetrical eigenvalues for $\alpha = 1$ and $Re = 10\,000$ are shown plotted in figure 13.5. The asymmetrical modes were obtained by replacing the centreline boundary conditions from (13.3) with their asymmetrical equivalents, namely

$$\begin{aligned} \phi|_{y=0} &= 0 \\ D^2\phi|_{y=0} &= 0. \end{aligned}$$

The eigenvalues are here grouped into the A, P and S families according to the classification by Mack (1976). These modes have been equivalently named the wall, centre and median modes due in part to their asymptotic behaviour in the inviscid limit (as $Re \to \infty$) [see Drazin & Reid (1981), Schmid & Henningson (1994)].

the order is raised to $N = 60$, no significant decrease in precision occurs. When the Tau method was originally implemented for this system, the standard Ortiz approach was used, and the numerical system became inaccurate above $N \approx 40$.

Table 13.1: The convergence of the minimum critical Reynolds number with order for the present investigation.

N	Re	α	c_r
20	5 [illegible]	1.02	0.26
30	5 772.2	1.020 547	0.264 000
40	5 772.221 8	1.020 547 0	0.264 000 208 17
44	5 772.221 80	1.020 547 0	0.264 000 20 1
60	5 772.221 8	1.020 547	0.264 000 2

The eigenvalues for $\alpha = 1$, $Re = 10\,000$

While the minimum critical Reynolds number might serve as the best point of comparison for the most unstable eigenvalue, the natural framework for the verification of the full eigenspectrum has become, by virtue of its historical precedent, the case of $\alpha = 1$ and $Re = 10\,000$.

da Silva (1990) [table 4.3, p90] compared the convergence of his finite-difference scheme to other results, for the most unstable eigenvalue of the above test case. He indicated the error in the various solutions as a percentage deviation from the *exact* result of Orszag (1971a). The maximum accuracy attained for his and other authors' results are represented in table (13.2).

Table 13.2: Maximum accuracy attained for the most unstable eigenvalue at $\alpha = 1$, $Re = 10\,000$, as compared to the results of Orszag (1971a).

Author	Error %
Thomas (1953)	0.02
Gary & Helgason (1971)	0.0005
Grosch & Salwen (1968)	1.57
Davey (1973)	0.008
Gersting (1981)	0.06
da Silva (1990)	0.008

By extrapolating to [illegible] mesh density, da Silva was able to reduce his error to 0.008%. In contrast, [illegible] present results attain the same accuracy of Orszag's results at $N = 38$. Thus a comparison of the present data to the results presented in table (13.2) is meaningless. As would be expected, the current method does report identical convergent behaviour to the similar approach by Liu & Ortiz (1987). The convergence with order of the most unstable eigenvalue for this case is shown in table (13.3). Here the respective order for the same level of accuracy for each method is shown on the same line of the table. As mentioned, the present method reaches the accuracy of Orszag at $N = 38$, corresponding

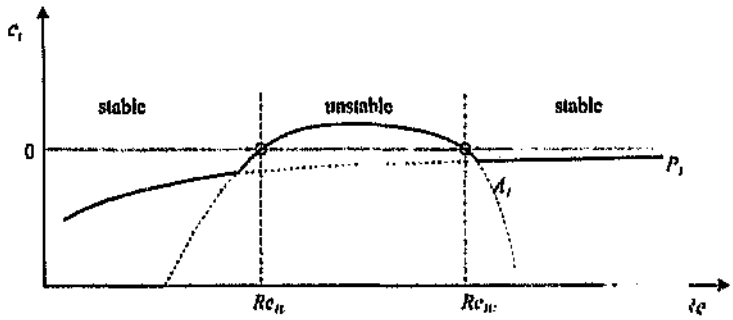

Figure 13.4: The variation of c_i with Reynolds number [illegible]cular value of the wavenumber α.

α corresponding to the minimum of this fitted curve. Find the critical Reynolds number at this point, and call this value Re_{4L}.

(3) Choose the three of the four points Re_{1L}, Re_{2L}, Re_{3L} and Re_{4L} that have the lowest Reynolds number. Rename these three points Re_{1L}, Re_{2L} and Re_{3L}.

(4) If the Reynolds numbers of the three points are sufficiently close (within a given tolerance), then stop the process and take the point with the median value of α as the minimum critical point, else go to step 2.

For suitable initial guesses, the above algorithm will give the minimum critical Reynolds number to within the given tolerance.

The current results for the minimum critical Reynolds number are shown in table (13.1). Only figures invariant with order are shown here. As can be seen, the results of Davey are duplicated, suggesting that the last decimal place of Liu & Ortiz's values is wrong. This is a strong indication that explicit use of the mapping V (see section 12.1) causes numerical round-off problems. Liu & Ortiz did not extend their results past $N = 41$, but it is conceivable that they were limited to this value by the transformation (12.11). The present results do not show any catastrophic round-off limit, but round-off error seems to be present in the solution, rendering it accurate to approximately 8 significant figures in Reynolds number, *regardless of* N. The effect of the fixed decimal precision is manifest in the stability curve being jagged at the magnitude of the truncation error. By this is meant that there is uncertainty in the position of the actual stability curve itself within a finite decimal representation, and not inaccuracy in the determination of the numerical system. In other words, the perturbation of a parameter (say α) needed to discriminate between two distinct points on the curve is so small, that the effect of the variation is non-uniform[5], effectively producing 'noise' in the algebraic matrix system. As shown in the table, when

[5]In some multiplications the factor 'falls off' the finite decimal representation, leaving the value unchanged, while in other cases it does not.

transformations and their limitations is contained in Canuto *et al* (1988). For the present system, it was decided to use a simple linear transform, because the more sophisticated transforms were found to complicate the structure of the equation unnecessarily. As will be shown, the simpler choice did not preclude the attainment of a highly accurate solution.

The Blasius equation (13.71) is applicable to a flat plate situated along the x axis (figure 13.12). For the current investigation, it was required that the solution be for a plate situated at $\zeta = k$, and with the solution domain extending in the direction of decreasing ζ towards zero. This rather unusual requirement was so that the solution be compatible with the pipe base-flow models and stability schemes (whose solution domains extend from a wall at $r = 1$ to the centreline of the pipe/flat-plate-system at $r = 0$). A suitable mapping encompassing both the stretching and boundary reversal was achieved by use of the simple algebraic equation

$$\zeta = k(1 - \tilde{\zeta}), \tag{13.74}$$

Using (13.74), the differential $\partial\zeta$ can be related to its transformed counterpart as

$$\partial\zeta = -k\partial\tilde{\zeta}, \tag{13.75}$$

then, using (13.74), (13.75) and the chain rule of differentiation, the Blasius equation in terms of $\tilde{\zeta}$ becomes

$$2f_{\tilde{\zeta}\tilde{\zeta}\tilde{\zeta}} + k^2 f f_{\tilde{\zeta}\tilde{\zeta}} = 0, \tag{13.7}$$

where the subscript $_{\tilde{\zeta}}$ indicates differentiation with respect to $\tilde{\zeta}$. The boundary conditions must also be transformed, and these become

$$\begin{aligned} f(1) &= 0, \\ f_{\tilde{\zeta}}(1) &= 0, \\ f_{\tilde{\zeta}}(0) &= 1. \end{aligned} \tag{13.77}$$

Although the system (13.76), (13.77) is reversed, the solution thereto can be related back to the traditional solution simply by transforming the ordinate back to the standard ζ using equation (13.74).

where $f = f(\zeta)$, and the prime denotes differentiation with respect to ζ. The boundary conditions under the transformation become

$$\begin{aligned} f(0) &= 0 \\ f'(0) &= 0, \\ f'(\infty) &= 1. \end{aligned} \tag{13.72}$$

The solution of (13.71) with conditions (13.72) describe the shape of velocity profiles on a flat plate boundary layer with no pressure gradient. The lack of an axial co-ordinate implies that the shapes of subsequent profiles in x are self-similar; thus a single solution encompasses the entire plate[10].

Domain truncation & co-ordinate transformation

Although the solution for (13.71) is only strictly valid for $\zeta \in [0, \infty]$, a numerical system cannot easily obtain a solution on such an infinite domain. However, if the solution is taken over a restricted part of the domain, say $[0, k]$, then, providing k is large enough, the solution to the problem in the truncated domain should be a good approximation of the proper solution. The truncated-domain solution will converge to the exact result at a rate greater than any power of k as k is increased, because all the higher derivatives of the Blasius solution decay to zero a short way from the edge of the boundary layer. This rapid convergence of the solution with an increase of domain allows a spectral method to be successfully used here.

In order to solve the Blasius equation (13.71) using an operational-Tau approach, the domain must be transformed analytically such that $[0, k]$ maps to the unit domain $[0, 1]$. Such a co-ordinate transformation can be implemented in a number of ways, but all approaches involve defining a transformation between the current independent variable ζ and a new variable ζ as

$$\zeta = \mathcal{Z}(\zeta). \tag{13.73}$$

The form of the functional $\mathcal{Z}$ defines the nature of the transform: at the simplest level, $\mathcal{Z}$ can simply be a linear mapping; here $\mathcal{Z}$ would simply 'stretch' the domain linearly. More sophisticated methods might involve distorting the domain so as to emphasise certain areas: an algebraic, logarithmic or exponential mapping might be applicable in such a case. A detailed listing of applicable

[10] The equation (13.67) breaks down at the very leading edge of the plate; therefore the Blasius solution becomes invalid there. A recent paper by McLachlan (1991) addresses this issue exactly. This author does however show that the Blasius solution is valid for an intermediate range of axial positions.

$$\begin{aligned} u(x,0) &= v(x,0) = 0, \quad x \in [0,\infty] \\ v(x,\infty) &= U_\infty \end{aligned} \tag{13.68}$$

The flow domain is shown schematically in figure 13.12. This figure shows also the expected qualitative boundary layer development along the plate (the vertical scale has been exaggerated and no scale is given), and the approximate shape of the velocity profile at a selected positions along the plate.

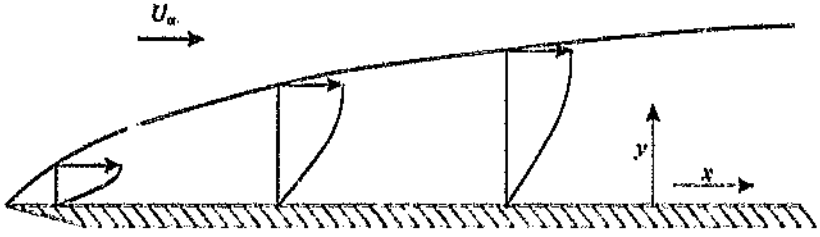

Figure 13.12: The development of the laminar boundary layer over a flat plate at zero incidence.

A similarity solution exists to the above equations (13.66) and (13.67) with auxiliary conditions (13.68), which reduces them to a single (non-linear) ordinary differential equation. This problem was considered by Blasius in his doctoral thesis, and is summarised and described in Schlichting (1979).

Derivation of the Blasius equation

Briefly, if a dimensionless co-ordinate[9]

$$\zeta = y\sqrt{\frac{U_\infty}{\nu x}} \tag{13.69}$$

and dimensionless streamfunction $f(\zeta)$, defined by

$$\psi = \sqrt{\nu x U_\infty} f(\zeta), \tag{13.70}$$

are introduced into the above equations, then they can be rearranged to yield the Blasius equation

$$f f'' + 2f''' = 0 \tag{13.71}$$

[9]Schlichting (1979) uses η to denote this co-ordinate. Here the symbol ζ is substituted, in order to avoid confusion with the differentiation matrix η.

13.3 The Blasius problem - base flow and stability

The developing boundary-layer flow over a flat plate, under conditions of no pressure gradient, is of direct interest to the current study because it represents the asymptotic limiting behaviour for pipe inlet flow (this is shown in chapter 14). This problem is described analytically by the well-known Blasius similarity solution, the solution of which is described below.

Solutions to the Blasius equation have been produced by other authors: Blasius (1908) obtained a solution as a matched series expansion. Subsequent workers [for instance, Bairstow (1925), Goldstein (1930)] used a similar technique. Töpfer (1912) was the first to solve this problem using a Runge-Kutta integration technique, and later Howarth (1938) achieved even more accurate results by use of this method. The most accurate results to date were obtained by Davey [unpublished, but presented in Drazin & Reid (1981)], although he never presented his Blasius solution technique, but only the linear stability solution to this profile.

This classical problem is reconsidered here for a number of reasons. Firstly, the Blasius solution is needed in terms of the Chebyshev coefficients, in order that it can be treated uniformly with the other velocity profiles considered in this work. Secondly, it presents an ideal vehicle to demonstrate the treatment of the non-linear terms under the operational-Tau approach. Lastly, the velocity profiles can be used to further verify the stability formulation of section 13.1, for higher order profiles. The last point of verification deserves further mention; good agreement with the results of Davey [Drazin & Reid (1981)] for the minimum critical Reynolds number for this system immediately would vindicate both the Blasius and Orr-Sommerfeld algorithms simultaneously.

13.3.1 Analytical formulation

The steady, spatially developing boundary layer flow over a flat plate with no pressure gradient is described by the simplified boundary-layer equations:

$$\frac{\partial u}{\partial x} + \frac{\partial v}{\partial y} = 0, \tag{13.66}$$

$$u\frac{\partial u}{\partial x} + v\frac{\partial v}{\partial y} = \nu\frac{\partial^2 u}{\partial y^2}, \tag{13.67}$$

where $u = u(x, y)$, $v = v(x, y)$, and there exists a flat plate along the positive x axis. The free-stream velocity is U_∞, and is taken as being from left to right. The above two equations are thus subject to the boundary conditions

normalised shape parameter and dimensionless centreline velocity is given here for different values of the dimensionless time, from the point of flow inception $\bar{t} = 0$ until steady-state ($\bar{t} \to \infty$).

Table 13.7: Variation of parameters in impulsively started pipe flow far from the inlet.

$\bar{t}$ $\times 10^3$	u_c/U_m	$\delta^*/R\bar{t}$ $\times 10^2$	S	S_{δ^*}
0	1	0	∞	1.273 2
1	1.074 4	3.461 0	38.954	1.254 9
2	1.107 1	4.837 9	28.476	1.241 3
3	1.133 0	5.870 8	23.870	1.236 8
4	1.155 4	6.726 1	21.141	1.230 7
5	1.175 6	7.467 9	19.288	1.225 3
6	1.194 2	8.129 3	17.927	1.220 4
7	1.211 5	8.729 8	16.875	1.215 9
10	1.258 7	10.275	14.750	1.204 1
15	1.327 0	12.321	12.792	1.187 7
20	1.387 9	13.974	11.657	1.173 7
25	1.444 1	15.376	10.905	1.161 1
30	1.496 8	16.595	10.367	1.149 4
40	1.592 7	18.607	9.647 1	1.127 0
50	1.675 6	20.159	9.190 8	1.105 8
60	1.744 7	21.341	8.880 3	1.086 3
70	1.800 8	22.234	8.659 9	1.069 2
100	1.907 8	23.792	8.289 6	1.033 8
150	1.975 2	24.686	8.076 7	1.009 4
200	1.993 4	24.917	8.020 5	1.002 6
300	1.999 5	24.994	8.001 5	1.000 2
400	2.000 0	25.000	8.000 1	1.000 0
∞	2	25	8	1

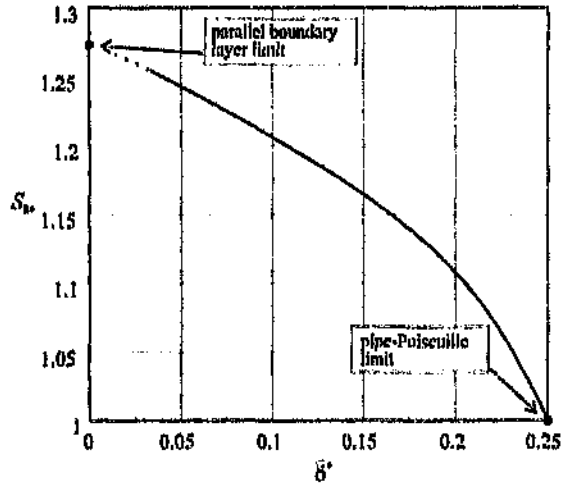

Figure 13.11: The variation of the normalised shape parameter S_{δ^*} with displacement thickness δ^* in an impulsively started pipe flow far from the inlet.

is shifted to the plate, then the velocity shape is given by

$$u(\eta) = U\mathrm{erf}(\eta). \tag{13.64}$$

The value of S_{δ^*} for this profile was accurately determined by generating the Chebyshev series for $\mathrm{erf}(\eta)$, and then manipulating it using the operational-Tau matrices. This was done as follows: a mathematical software package (Matlab) was used to generate the values for $\mathrm{erf}(\eta)$ at the Gauss-Lobatto collocation points in the range $\eta \in [0, \eta_{max}]$, for a particular order N. The values at the grid points were then transformed directly into the Chebyshev-coefficient space by using a Chebyshev transform [see Canuto *et al* (1988) for a fast-cosine transform applicable to this process, and section 12.8 for the equivalent matrix transform] and the value of S_{δ^*} was then calculated using elementary operational-Tau matrix functions. By varying η_{max}, N in the ranges $6 \leq \eta_{max} \leq 10$ and $40 \leq N \leq 100$ respectively, the value of S_{δ^*} for this profile was determined to be

$$S_{\delta^*[\mathrm{erf}]} = 1.273\,239\,544\,7, \tag{13.65}$$

exact to 10 significant figures.

13.2.8 Tabulated results

The results for the various parameters, for selected values of time t, are presented in table 13.7. The variation of the shape parameter, displacement thickness,

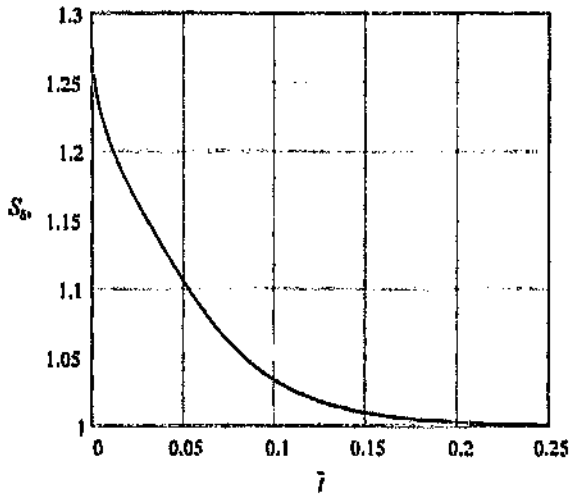

Figure 13.10: The temporal variation of the normalised wall shear stress S_{δ^*} in impulsively started pipe flow far from the inlet.

13.2.7 Limiting behaviour of S_{δ^*}

As was shown above the parameter S_{δ^*} tends to a definite limit as the displacement thickness of the profiles decreases to zero. This limiting system is given by a similarity solution to the Navier-Stokes equations, first discovered by Stokes [Schlichting (1979)]. The problem is for a infinite flat plate suddenly accelerated from rest to a velocity U, and is described by the simplified equation

$$\frac{\partial u}{\partial t} = \nu \frac{\partial^2 u}{\partial y^2}. \tag{13.63}$$

That this equation is the limiting case for the current system is easily demonstrable by an order of magnitude analysis; if the fuller equation is scaled with respect to δ^*, and the system is transformed to a wall co-ordinate, then equation (13.30) will formally reduce to equation (13.63).

The solution of equation (13.63) is straightforward - the problem is termed Stokes' first problem, which he solved in 1851. If the independent variable y is made dimensionless according to

$$\eta = \frac{y}{2\sqrt{\nu t}}$$

then the solution to equation (13.63) is self-similar and the resultant boundary layer shape is the complimentary error function $\mathrm{erfc}(\eta)$. If the reference frame

S is as useful a parameter as δ^* described above, except for its boundedness problem for vanishingly thin boundary layers.

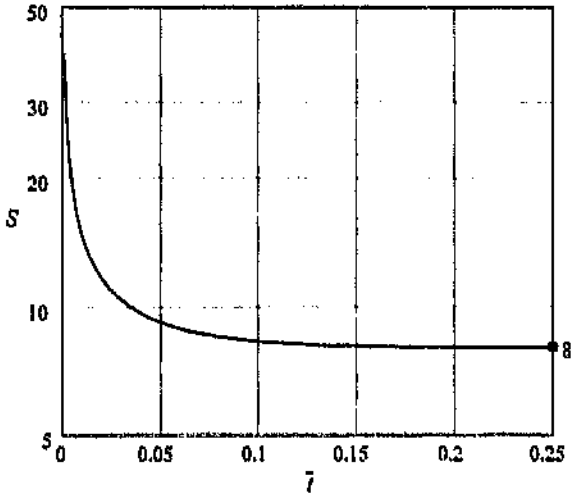

Figure 13.9: The variation of the shape parameter S with time in an impulsively started pipe flow far from the inlet.

The scaled shape parameter

Arising from the unbounded behaviour of S as $\bar{t} \to 0$, a shape parameter normalised with respect to δ^* and centreline velocity u_c is introduced as

$$S_{\delta^*} = \frac{U_m}{u_c}\frac{\delta^*}{R}S \quad = 2\frac{\tau_w \delta^*}{\mu u_c}. \tag{13.62}$$

This parameter refers directly to the geometrical *shape* of the boundary layer. Moss' (1985) definition of S - equation (13.61) - did not take this geometrical conformality into account. The variation of S_{δ^*} with $\bar{t}$ is given in figure 13.10. The bounded limiting behaviour is apparent as $\bar{t} \to 0$, and S_{δ^*} remains finite here.

The parameter S_{δ^*} together with the displacement thickness describe a velocity profile in a more natural framework than S and δ^* do. The parameter δ^* can be used to give a measure of the 'thickness' of the layer, and the term S_{δ^*} its form. The variation of S_{δ^*} with δ^* is shown in figure 13.11. The notable issue about this figure is that both the ordinate and abscissa are bounded. Thus as $\bar{t} \to \infty$, $\delta^* \to 1.75$, and as $\bar{t} \to 0$ (corresponding to $\delta^* \to 0$), the scaled shape S_{δ^*} converges on a fixed point. This point is labelled in this figure as the parallel boundary layer limit. The value of this point is calculated in the next section.

dimensionless displacement thickness can be defined as a ratio of the radius according to

$$\bar{\delta}^* \equiv \frac{\delta^*}{R}. \tag{13.60}$$

Use of the dimensionless parameter allows comparison independent of the pipe radius. The value at $t = 0$ is $\bar{\delta}^* = 0$ - corresponding to a boundary layer of zero thickness. At far times, $\bar{\delta}^* \to 0.25$: although the boundary layers have in fact merged at this point, the parameter still describes uniquely these velocity profiles.

This parameter is bounded and monotonic for an entire range of profiles, from top-hat to parabolic. Thus for a particular variation of profiles (either temporal as here, or spatial as in steady-state pipe inlet flow), it offers a unique alternative method of identifying a velocity profile. For instance, instead of referring to a profile's spatial position (or time), one can equally validly refer to its displacement thickness.

Velocity profile shape parameter

The dimensionless wall shear stress or velocity profile shape parameter [Moss (1985)] is defined as

$$S = \frac{2\tau_w R}{\mu U_m}. \tag{13.61}$$

The variation of S with t is shown in figure 13.9. This was the parameter used by both Moss and da Silva [Moss (1985), da Silva (1990)] to uniquely define pipe inlet velocity profiles. The parameter converges to the value of $S = 8$ in the far-time limit, corresponding to a parabolic profile. However, $S \to \infty$, as $t \to 0$, because the velocity gradient at the wall becomes infinite. It is an analogous parameter to the displacement thickness described above, in that it is a scalar quantity that varies monotonically for the range of profiles of interest. It does however encode different information to δ^*[8].

da Silva (1990) implied that this parameter was sufficient to uniquely describe *all* impulsively started pipe profiles, both in the inlet and far downstream. This assumption is equivalent to stating that all impulsive pipe velocity profiles belong to a one-parameter group with S that parameter. This has been shown to be fallacious, and it is later clearly demonstrated in chapter 14 that inlet and downstream profiles - for the same value of S - are very different indeed. However, for a *particular* flow situation (for example, steady-state pipe inlet flow),

[8]The term S concerns the profile slope at the wall, while δ^* is an integral property of the profile.

the same level, the infinite-order accuracy of the spatial operator ensures that the profiles are infinitely smooth: this makes the temporal error behave like a small random time shift alone - the error does not propagate as random 'wiggles' in the profiles at all, rather, it is embodied uniformly in the entire profile. This is in contradistinction to the finite-difference method. Here the error at 4 significant figures is embodied spatially as well as temporally. It takes on the form of a random uncertainty at every node point, and thus this error will significantly affect a stability analysis, because the profile is 'wavy' at the level of the error.

13.2.6 Derived parameters

Various integral or limit terms derivable for the velocity profiles are useful to describe their variation. These are discussed in turn below.

Displacement thickness

The variation of displacement thickness δ^* with time is given in figure 13.8. The value of δ^* is directly derivable from the centreline velocity as

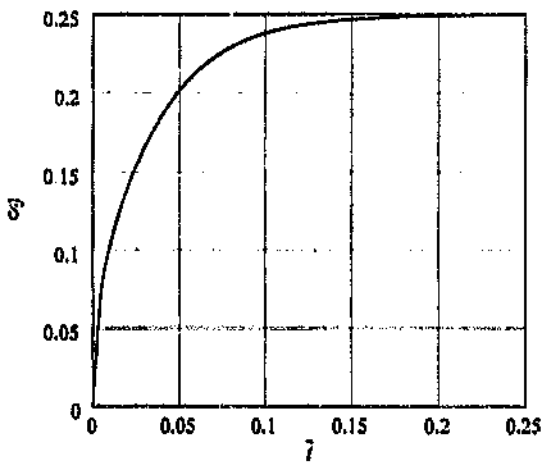

igure 13.8: The variation of the displacement thickness δ^* with time in an impulsively started pipe flow far from the inlet.

$$\frac{\delta^*}{R} = \frac{1}{2}\left(1 - \frac{U_m}{u_c}\right) \tag{13.59}$$

where U_m is the cross-sectional mean velocity - equal to unity in this case, u_c is the centreline velocity, and R is the pipe radius. For convenience sake, a

Table 13.6: Variation of centreline velocity in impulsively started pipe flow far from the inlet, showing also the values obtained using da Silva's (1990) finite-difference algorithm.

$\bar{t}$	u_c/U_m	
($\times 10^3$)	Present	da Silva (1990)
0	1	1
1	1.074 367	1.073 882
2	1.107 123	1.106 747
3	1.133 038	1.132 709
5	1.175 583	1.175 300
7	1.211 528	1.211 267
10	1.258 663	1.258 421
20	1.387 887	1.387 668
30	1.497 763	1.496 564
40	1.592 717	1.592 555
50	1.675 551	1.675 438
60	1.744 669	1.744 603
70	1.800 752	1.800 726
100	1.907 779	1.907 821
150	1.975 165	1.975 237
200	1.993 351	1.993 426
300	1.999 524	1.999 598
∞	2	2

The methods show agreement with each other consistently to three decimal places. The Tau method was shown to be correct to approximately 4 decimal places by decreasing Δt and observing the variation in the numerical representation. In the Tau results, the errors originate overwhelmingly from the temporal discretisation[7], thus increasing N will have no effect on long-term accuracy. The results of the finite-difference formulation are probably equally affected by errors from both temporal and spatial discretisations. The only way to improve the accuracy in the scheme would be to employ a high order time-discretisation. For the sake of robustness however, it was decided to remain with the simple techniques, because of stability problems with more exotic methods.

The current scheme is A stable in the sense of Canuto *et al* (1988), in that all small numerical perturbations are damped and the solution remains bounded, even for an indefinite number of iterations. This is so despite the fully *implicit* nature of the method, along with no explicit enforcement of mass flow conservation between time steps. da Silva's method is fully time-explicit; this, and his means of applying the boundary conditions, explains its comparable numerical stability behaviour.

Although it may seem that the method is no more accurate than the finite-difference approach because of both being limited in accuracy at approximately

[7]This is because the spatial variation is more than properly represented at $N = 60$.

Each time step consists primarily of a matrix-vector multiplication (the matrix assembly is mostly vector-scalar multiplication and addition) and the time taken is thus of order N^2 for an implicit scheme. Thus as well as being accurate (by virtue of its implicit nature) the method is also fast.

13.2.5 Convergence and accuracy

Results were obtained for impulsively started flow by setting $\bar{\Omega} = 0$. The more general results for exponential accelerations, with varying values of $\bar{\Omega}$ are contained in chapter 15. The only point of comparison for the impulsive results are the studies by Moss (1985) and da Silva (1990), in which they present the centreline variation of velocity with time. Moss used a simple momentum-integral scheme, and da Silva employed a vorticity-transport finite-difference method. The centreline variation of velocity with time for the present study is shown in figure 13.7. These results are visually identical to da Silva's values.

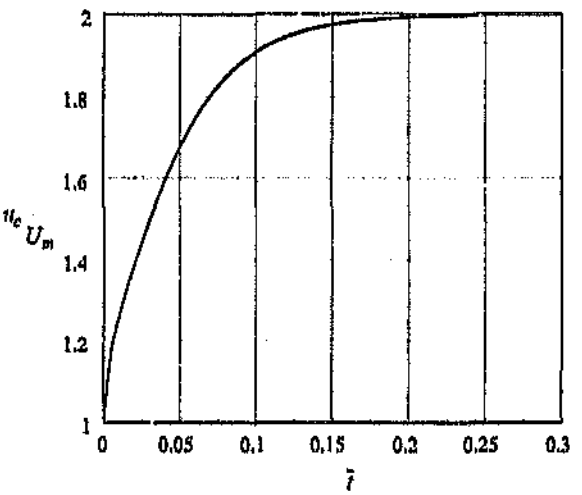

Figure 13.7: The temporal development of the centreline velocity in an impulsively started pipe flow far from the inlet.

Table 13.6 lists values for the the dimensionless centre-line velocities at selected times $\bar{t}$ for the present scheme. Also shown are the values attained by rerunning da Silva's (1990) finite-difference algorithm. The present results were solved at order $N = 60$, with $\Delta t = 1 \times 10^{-5}$. The order of 60 was excessive for most of the calculation, except initially, where the thin boundary-layer like nature of the flow necessitated the retention of more coefficients. Results for the da Silva calculation were obtained at $N = 200$. The time-step used here was the same as that used in the spectral calculation. Both sets of results are shown to 6 significant figures.

(vi) The determination of a highly accurate solution to the Blasius equation demonstrated the convergence behaviour and accuracy of the method when applied to general velocity profiles. Using the iterative Blasius solver in conjunction with the Orr-Sommerfeld algorithm, the results for the minimum critical Reynolds number for this system obtained by Davey [Drazin & Reid (1981)] were extended by one significant figure. Further to this, an indication of the solution order needed to calculate correctly the stability of these higher order profiles was determined.

The current chapter has given broad demonstration of the modified operational Tau method to problems directly relevant to the current study. As such it serves as a good starting point for the following chapters. The second example (temporally developing pipe flow) leads naturally to the consideration of pipe inlet flow under general accelerations - the subject of the next two chapters - while the stability analysis here allows a natural progression to the pipe-flow stability study of chapter 16.

Difficult equation terms and boundary conditions were shown to be handled in a completely uniform manner. The universality of the philosophy of application in all cases allowed focus to be placed on the more important parts of the problem at hand, namely the analytic method of solution. In fact this approach allows most problems to be pursued in an uniform and almost fully analytic way. This is in strong contrast to the finite-difference approach, where the primary concerns are almost always numerical (discretisation schemes, etc.).

(ii) For the solution of the Orr-Sommerfeld equation for plane-Poiseuille flow, results obtained from the present scheme was shown to exceed the accuracy of *both* that of Orszag (1971a) and the later investigation by Liu & Ortiz (1987). Using the verification of the minimum critical Reynolds number, namely $Re_c = 5\,772.221\,8$, as a test case, the present method duplicated the reputedly highly accurate but unpublished results of Davey [contained in Drazin & Reid (1981)], obtained using a shooting method. Liu & Ortiz' result, obtained using a similar scheme to the present one but using a badly-scaled similarity transform, was incorrect in the final decimal place.

(iii) The current scheme did not show any 'catastrophic' decay in accuracy above a certain order of solution. This was due to the elimination of the similarity transform in the standard method of Ortiz. It is this effect that is thought to have limited Liu & Ortiz' results in their determination of the minimum critical Reynolds number for plane-Poiseuille flow. Certainly their standard approach would not have been able to duplicate the highly accurate stability results obtained in the third example. In all cases, the current method could be extended to extremely high orders ($N > 120$), with only a gradual increase in the round-off error.

(iv) The initial value problem for parallel pipe flow was solved in a extremely straightforward way, regardless of the 'difficult' terms contained in the equation. The method allowed this problem to be discretised temporally in a most general sense. The present method duplicated the results of da Silva (1990), obtained using a large grid finite-difference method. The error in the current solution resulted primarily from the temporal discretisation. Although this was of the same level as the error in da Silva's results, the current results' uncertainty was manifest as a random temporal shift, thus the velocity profiles were in effect far more accurate than the finite-difference ones.

(v) The investigation into the temporal development of pipe flow proved an ideal way of introducing relevant parameters to quantify the boundary layer in a pipe. The normalised shape parameter S_{k^*} and displacement thickness δ^*, were in combination shown to be appropriate parameters for describing pipe flow profiles. Use of the parameter S_{k^*} showed that the boundary layer for impulsively started flow far downstream in a pipe behaved like a parallel impulsively started flat-plate boundary layer with zero pressure gradient, in the limit of vanishing boundary layer thickness.

$$\begin{aligned} Re_{\delta^*} &= 519.060\,1, \\ \alpha_{\delta^*} &= 0.303\,771, \\ c &= 0.396\,637, \end{aligned}$$

in agreement with the unpublished results of Davey [Drazin & Reid (1981)] but extending them by one significant figure. The decimal representation could possibly have been pursued to further significant figures, but a more sophisticated procedure for finding the minimum critical Reynolds number (see section 13.1) would have had to be employed. Furthermore the increase in k necessary to achieve this would have resulted in a much larger order of stability solution being necessary, with a commensurate decay in accuracy due to round-off. Thus at the current level of numerical precision (IEEE double precision), it is possible that only one further correct decimal digit would be obtainable.

The results from table 13.9 are useful in that they give an indication of the order of stability solution necessary to achieve accurate results as the boundary layer thins. Calculating the stability of pipe entrance flows entails determining the stability characteristics of profiles with successively thinner boundary layers as the inlet plane is approached. The highest order profile here considered is that for $k = 90$: this corresponds to a velocity profile with a dimensionless displacement thickness of $\delta^* = 0.019$ and shape parameter of $S = 60.9$. This profile is of the same order as the highest order profile considered later in the pipe entrance stability analysis of chapter 17. Thus the results presented here give an indication of the order needed to obtain accurate results in the later analysis[13].

13.4 Summary

The application of the modified operational-Tau method has been explained in this chapter by means of pertinent examples, these being: the solution of the Orr-Sommerfeld equation for plane-Poiseuille flow, the temporal development of an impulsively started pipe flow far from the inlet, and the determination of the Blasius solution (and the stability thereof). The following points arise from the results obtained this chapter

(i) In all cases, the method was shown to be extremely simple to implement, with construction of the problem proceeding as in D operator notation.

[13] Of course, the pipe inlet analysis concerns the use of the Sexl - bility equation - the axisymmetric analogue of the Orr-Sommerfeld equation - the numerical formulation of which results in a worse-conditioned system than the present one. However, this bad conditioning can be shown to affect substantially only the round-off error, not the rate of convergence with order. Thus the axisymmetric solution will behave similarly to the one above, and only the numerical precision to which the results can be given will be affected.

number for this system is one based on the far-field velocity and the displacement thickness, namely $Re_{\delta^*} \equiv U_\infty \delta^* / \nu$. Table 13.9 shows the value of the minimum critical Reynolds number for various values of k, N. All the results are here presented to six decimal places, because that was the accuracy to which the minimum point on the critical curve was ascertained.

Table 13.9: The value for the minimum critical Reynolds number based on displacement thickness Re_{δ^*} for various orders of solution and domain truncation, for the Blasius boundary layer.

	Minimum critical Re_{δ^*}			
N	$k = 60$	$k = 70$	$k = 80$	$k = 90$
80	519.059 147	519.074 489	519.016 733	461.348 225
84	519.060 330	519.055 704	519.067 592	519.033 737
88	519.060 136	519.061 397	519.060 074	519.053 359
94	519.060 132	519.059 907	519.061 480	519.050 503
100	519.060 150	519.060 097	519.059 891	519.061 525
106	519.060 151	519.060 125	519.060 092	519.059 926
110	519.060 151	519.060 122	519.060 108	519.060 213
116		519.060 122	519.060 105	519.060 123
120		519.060 122	519.060 107	519.060 128
126			519.060 107	519.060 126
130				519.060 126

The variation of the domain size k was in the range $60 \leq k \leq 90$; these values of k gave profiles with very thin boundary layers relative to the domain extent, namely $0.043 \leq \delta^* \leq 0.019$. Such a large solution domain was necessary to allow the imposed perturbations to decay to zero properly away from the boundary layer, thus allowing an accurate approximation of the system to the proper case of infinite domain.

For each value of k, the Orr-Sommerfeld order was increased until a solution invariant to six decimal places in Re was obtained. Apparent is the increase in N needed to obtain a solution to a certain precision as k is increased. This trend is consistent with the results from the base flow, as given in table 13.8: more coefficients need to be retained as the boundary layer thickness decreases, in order that a velocity profile be properly represented. In the same way, a higher order stability analysis needs to be used as k increases, to capture the full manner in which the eigenfunctions vary.

The highest order of solution was $N = 130$. Accurate solutions at this order again shows that elimination of the similarity transform V (see chapter 12) from the operational-Tau method removes completely the major obstacle of the standard approach - namely its catastrophic decay in accuracy above a certain (low) order of solution.

By observing the convergence of the present results with k, the present Blasius profile minimum critical stability point was found to be

As a check of the validity of the criterion $|f_{N-1}|$ as an accurate indicator of the accuracy of the series, the values of the function itself at arbitrary discrete points was calculated for selected values of N, k. These comparisons showed that, above an accuracy of approximately 10^{-6}, this criterion was a reliable indicator of convergence. Thus the solutions stated above to be determined to the level of the round-off yielded results fixed to approximately 13 significant figures.

To demonstrate the significant difference between the Blasius boundary layer and the error-function profile calculated in section 13.2 above, it is useful to consider the scaled shape parameter S_{b^*} for each of these profiles. For the error function profile, the value of this parameter was given by equation (13.65) as 1.273 239. For the current Blasius profile, this term was determined to be

$$S_{b^*[\text{Blasius}]} = 1.142\,800\,6, \tag{13.98}$$

exact to 8 significant figures. This indicates a substantial difference between the boundary layer structure of the two systems. This issue will be addressed further in a later chapter.

Stability results

Subsequent results were all calculated at order $N = 100$; these were then used in a stability analysis using the Orr-Sommerfeld equation (section 13.1), in order to ascertain the various parameters concerning the stability of the Blasius profile. This process provided an ideal vessel for verifying the accuracy of the entire system (both Blasius and Orr-Sommerfeld solver). A small modification was made to the boundary conditions of the above mentioned analysis: conditions commensurate with the domain truncation were used in place of the 'centreline' conditions in (13.3), and these were [Drazin & Reid (1981)]

$$\begin{aligned} \phi'(0) + \alpha\phi(0) &= 0 \\ \phi''(0) - \alpha^2\phi(0) &= 0. \end{aligned} \tag{13.99}$$

The conditions (13.99) are equivalent, on the truncated domain, to the formal condition $\phi(z) \simeq B\exp(-\alpha z)$ as $z \to \infty$. However, the choice of these conditions or the ones (13.3) practically makes little difference to the solution as k is increased.

Blasius profiles for different values of k were calculated, and for each of these the order N of the stability analysis was varied while the convergence of the value for the minimum critical Reynolds number was noted. The relevant Reynolds

was the smallest value possible; values of $|\Lambda|$ smaller than this could not be achieved because the round-off error produced numerical 'noise' in the system at 10^{-11}, stopping the deterministic nature of the iterative algorithm at this level.

As can be seen, a greater order is needed to represent the solution as the domain size increases. The [illegible] most entry in each row of the table (marked with an asterisk) represents the order at which the respective solutions had converged to the level of the round-off error. For the largest domain considered ($k = 80$), an order of $N = 100$ was sufficient to determine the solution to the maximum accuracy possible. This value of k corresponds to a dimensionless displacement thickness of $\delta^* \simeq \delta^*/k = 2.151 \times 10^{-2}$. The respective dimensionless displacement thickness for the various domain sizes can be directly calculated via the relation

$$\delta^* \simeq 1.720\,787\,6/k. \tag{13.97}$$

The bracketed numbers in table 13.8 represent orders for which the truncated series was insufficient to resolve even the coarser features of the system. Visually, these solutions were characterised by large oscillations (with a deviation of > 0.1 from the proper solution) and thus the truncation error was not accurately indicated by the magnitude of the highest order coefficient. Numerically, for such low order solutions, the truncated solution is not 'close' to the projection of the infinite series onto the truncated numerical basis. In other words, the low-order vector in Chebyshev space represented by this solution is not a good approximation to the infinite vector representing the true solution - effectively, not enough degrees of freedom have been admitted to give a proper representation of the system.

Table 13.8: The truncation error for the Blasius solution, for various values of the domain size k and order N. *, to the level of the round-off error; (), not yet properly representative of the solution.

	Truncation Error ($-\log_{10}$)						
k	$N = 20$	$N = 30$	$N = 40$	$N = 50$	$N = 60$	$N = 80$	$N = 100$
6	−9.61	−14.16*					
10	−7.29	−11.39	−14.61*				
15	−5.87	−10.75	−11.99	−14.31*			
20	−5.17	−7.84	−10.47	−12.89	−13.66	−14.05*	
30	−5.18	−6.54	−8.58	−10.64	−12.62	−14.03*	
40	−4.32	−5.85	−7.12	−9.23	−11.32	−13.05*	
50	(−4.91)	−5.71	−6.91	−8.31	−9.86	−13.45	−14.34*
60	(−4.76)	−5.22	−7.08	−7.37	−9.09	−13.34	−15.33*
70	(−3.84)	(−5.81)	−6.14	−7.51	−8.83	−11.68	−14.81*
80	(−3.73)	(−5.02)	−6.09	−7.04	−8.23	−10.58	−13.57

of the low-order result to the higher order is done simply by appending zeroes to the former. The final result of this process will approach an invariant solution.

The convolution sums in equation (13.88) take the major portion of time in the solution. A quicker method of calculating these will be given in chapter 14; however, because a single solution is required here, speed is not a concern. As before, the algorithms were implemented using Matlab, and a listing of the pertinent functions are contained in appendix D.2. Solutions were developed for various scaling factors k, and these solutions are the subject of the next section.

13.3.4 Numerical results

Laminar velocity profile

Tabulated solutions of the Blasius velocity profile are available [see Schlichting (1979)], and thus the present results could be directly compared. The present results agreed substantially with the results of Howarth (1938), as reproduced in Schlichting (1979). Unfortunately, Howarth's results were only presented to five decimal places, and thus the level of accuracy to which he calculated his figures could not be ascertained directly. The present results did however show a small deviation from Howarth's values in the final decimal digit of several of his tabulated numbers, and this seemed to indicate that his results were correct to only four decimal figures.

For the sake of comparison, the order N of the present system was decreased until the present values were accurate to the same level of precision as Howarth's. For a scaling factor of $k = 10$, agreement with this decimal precision was obtained at $N = 17$, corresponding to a total solution time of approximately 27 seconds on an IBM 80486 - 50 MHz desktop computer.

Absolute convergence was assessed by increasing both order N and solution domain k and observing the invariance of the decimal representation of the solution. Because of the minimax properties of the Chebyshev polynomials[11], and the uniform convergence of the series to the exact result, the magnitude of the error in the interpolating series is the same order as the magnitude of the last terms in the series; thus the criterion $|f_{N-1}|$ was taken[12] as an appropriate indication of the effect of truncation. For various domain sizes k, the order was increased and the truncation error determined. The results of this process are contained in table 13.8. The convergence criterion was set to $|\delta| = 10^{-11}$, which

[11] By minimax behaviour is meant that the maximum absolute magnitude of these polynomials is unity everywhere in the range; thus the maximum magnitude of a Chebyshev polynomial is always the value of its coefficient.

[12] The term f_i is taken to denote the ith expansion coefficient, or in other words, the ith member of the row vector $\boldsymbol{f}$ of unknown coefficients; thus $|f_{N-1}|$ is simply the magnitude of the last expansion coefficient.

The evolution equation

With the perturbation calculated as above, the next iterand needs to be developed; equation (13.84) thus needs to be formulated in the operational-Tau system. This simple system merely becomes

$$\bar{f}^{(j+1)}{}_{\bar{r}} = \bar{f}^{(j)}{}_{\bar{r}} + \omega \bar{g}^{(j)}{}_{\bar{r}} \tag{13.94}$$

where the superscript $^{(j)}$ denotes the most recent value of the iterand $\bar{f}$ and $\bar{g}^{(j)}$ is the value of the perturbation calculated using equation (13.93) with the iterand $\bar{f}^{(j)}$. The identity matrix I is introduced in to the left-hand side of (13.94) to facilitate the augmentation of the boundary conditions. These conditions are derived from (13.77), and in the operational-Tau system are

$$\begin{aligned} \bar{g}B_1 &= B_3; \\ B_3 &= [0\,0\,1]. \end{aligned} \tag{13.95}$$

The matrix B_1 is identical to the matrix B_1 from (13.92). Augmentation of the boundary conditions (13.95) to the inner problem (13.94) is simple and the resultant system becomes

$$\begin{aligned} \bar{f}^{(j+1)}\hat{\Pi}_1 &= \hat{\Psi}(\bar{f}^{(j)})_1, \\ \hat{\Pi}_1 &= \Big[B_1 \,\Big|\, I\Big], \\ \hat{\Psi}(\bar{f}^{(j)})_1 &= \Big[B_3 \,\Big|\, \bar{f}^{(j)} + \omega \bar{g}^{(j)}\Big], \end{aligned} \tag{13.96}$$

The solution for the new iterand $\bar{f}^{(j+1)}$ can be obtained from (13.96) by the inversion of $\hat{\Pi}_1$.

13.3.3 Solution procedure

Suitable values for a starting guess and the iteration relaxation factor are: $\bar{f}^{(0)} = [1, 0, 0, 0, \cdots]$ and $\omega = 0.9$ respectively. The most expedient way to achieve a high order accurate solution for a certain scaling factor k is by solving the system at a low order (say $N \approx 16$), letting the system converge, and then using this result as a starting guess for a slightly higher order ($N \approx N + 10$) system. This process can be repeated until the desired order is achieved, and is substantially quicker than proceeding directly from the coarse initial guess at a high order. Extension

This equation can be rearranged to make the unknown $\vec{g}$ the subject, and after elimination of the coefficient vector $\vec{c}$ becomes

$$\vec{g}\hat{L}(\vec{f}) = \vec{f}\left[2\hat{\eta}^3 + k^2\hat{R}(\vec{f}\hat{\eta}^2)\right]. \tag{13.90}$$

Equation (13.90) is of the form

$$\vec{g}[\text{LHS}]_{(\vec{f})} = [\text{RHS}]_{(\vec{f})} \tag{13.91}$$

where the matrix $[\text{LHS}]_{(\vec{f})}$ and the row vector $[\text{RHS}]_{(\vec{f})}$ are functions of $\vec{f}$, the known coefficient vector from the previous iteration. Equation (13.91) is in a form amenable to the augmentation of the boundary conditions. As stated before, the boundary conditions are implemented in the solution for both f and Δf. The relevant conditions here are (13.85), and under the operational-Tau system become

$$\begin{aligned} \vec{g}B_1 &= B_2(\vec{f}); \\ B_1 &= \left[\hat{\tau}|_{\hat{\zeta}=1} \,\vdots\, \hat{\eta}\hat{c}|_{\hat{\zeta}=1} \,\vdots\, \hat{\eta}\hat{c}|_{\hat{\zeta}=0}\right] \\ B_2(\vec{f}) &= \left[-\vec{f}\hat{c}|_{\hat{\zeta}=1} \,\vdots\, -\vec{f}\hat{\eta}\hat{c}|_{\hat{\zeta}=1} \,\vdots\, -\vec{f}\hat{\eta}\hat{c}|_{\hat{\zeta}=0} + 1\right]. \end{aligned} \tag{13.92}$$

Thus the system to be solved for the unknown $\vec{g}$ is

$$\begin{aligned} \vec{g}\hat{\Pi}(\vec{f}) &= \hat{\Psi}(\vec{f}), \\ \hat{\Pi}(\vec{f}) &= \left[B_1 \,\vdots\, [\text{LHS}]_{(\vec{f})}\right], \\ \hat{\Psi}(\vec{f}) &= \left[B_2(\vec{f}) \,\vdots\, [\text{RHS}]_{(\vec{f})}\right], \end{aligned} \tag{13.93}$$

where both the matrix $\hat{\Pi}(\vec{f})$ and row vector $\hat{\Psi}(\vec{f})$ depend on the previous iterand $\vec{f}$. Solution is straightforward by means of inversion of $\hat{\Pi}(\vec{f})$.

Thus, given some iterand $\vec{f}^{(j)}$, the Fréchet perturbation $\vec{g}^{(j)}$ can be calculated using equation (13.93).

Each of the above conditions is compatible with the condition that the perturbation quantity Δf and its derivatives be zero everywhere in the limit as $\|\Delta f\| \to 0$. More importantly, the use of conditions (13.85) ensure that *every* iterand $f^{(j)}$ satisfies the boundary conditions (13.77) at all times.

13.3.2 Numerical formulation

The equations to be solved are (13.83) and (13.84), which form a coupled pair of non-linear partial differential equations. The 'evolution' equation is (13.84), and (13.83) is linear in Δf (and f in this equation is a known). Solution is thus straightforward, except for the evaluation of the convolution sums occurring in (13.83).

Basic discretisation

Under the operational-Tau system, the functions f and Δf are represented by their series expansion counterparts as

$$f \Rightarrow \vec{f}c \tag{13.86}$$

$$\Delta f \Rightarrow \vec{g}c \tag{13.87}$$

which, as before, are simply infinite polynomial expansions denoted in vector form.

Considering first the convolutions, it was shown in section 13.2 that a known polynomial multiplied onto a function becomes, in the operational-Tau system, post-multiplication by the matrix operator (13.17). Using this operator, the iterative method in the operational-Tau system can be simply defined.

The equation (13.82) is linear with regard to the unknown function f; thus it can be represented in the operational-Tau system as

$$\vec{g}\hat{L}(\vec{f})c \quad \vec{g}\left[2\hat{\eta}^3 + k^2\left(\hat{\eta}^2\hat{R}(\vec{f}) + \hat{R}(\vec{f}\hat{\eta}^2)\right)\right]c \tag{13.88}$$

where $\hat{R}()$ is defined by (13.17). The analogue of equation (13.83) can then be shown to be

$$\vec{f}\left[2\hat{\eta}^3 + k^2\hat{R}(\vec{f}\hat{\eta}^2)\right]c + \vec{g}\hat{L}(\vec{f})c = 0. \tag{13.89}$$

and the perturbation Δf must be calculated as the solution to

$$2f_{\zeta\zeta\zeta} + k^2(ff_{\zeta\zeta}) + L\Delta f = 0. \tag{13.83}$$

An iterative algorithm to equation (13.76) can then be defined as follows:

(1) Make an initial guess $f^{(0)}$ to the unknown function f. This guess need not satisfy the boundary conditions, but should be 'relatively' close to the final solution. A simple yet sufficient guess for the current problem would be $f = 1$.

(2) Determine the solution for the perturbation Δf using equation (13.82) and the current guess for f. Simultaneous to this the boundary conditions must be enforced such that the perturbation is compatible with the system. Suitable conditions to achieve this will be given later.

(3) If the criterion $||\Delta f|| < |\delta|$ is satisfied (with $||\Delta f||$ a suitable norm of Δf, and $|\delta|$ the convergence criterion), then stop the iteration and return the current value of f as the solution. Otherwise, calculate the new iterand $f^{(j+1)}$ from the current value $f^{(j)}$ using

$$f^{(j+1)} = f^{(j)} + \omega\Delta f. \tag{13.84}$$

The boundary conditions (13.77) must also be applied such that the new iterand satisfies them exactly. The new solution is now made the current solution, and the algorithm returns to step 2 above.

The method then proceeds using the above algorithm, until Δf has approached zero uniformly to the required tolerance $|\delta|$.

The boundary conditions were briefly mentioned above; the most robust way to enforce them is to make both the function f and perturbed function $f + \Delta f$ satisfy them. Thus boundary conditions are applied during the solution of both (13.83) and (13.84). The specific application of the conditions (13.77) is dependent on the equation being solved. When solving the 'evolution' equation (13.84) the conditions must be enforced exactly as stated in (13.77); however, when the system (13.83) is solved, boundary conditions pertinent to the perturbation function Δf must be used. Such conditions can be easily derived by considering the original conditions (13.77), but with the term $f + \Delta f$ substituted everywhere for f; the conditions in Δf can then be found by rearranging the resulting relations, leading to

$$\begin{aligned} \Delta f(1) &= -f(1) \\ \Delta f_\zeta(1) &= -f_\zeta(1), \\ \Delta f_\zeta(0) &= -f_\zeta(0) + 1. \end{aligned} \tag{13.85}$$

The iterative algorithm

Although the equation (13.76) is a differential equation in a single variable, and thus ideal for solution under the operational-Tau approach, it is non-linear; therefore either linearisation or iteration have to be employed in its solution.

Linearising the equation will yield only an approximate solution, and for this reason, an iterative scheme was adopted. In general terms this proceeds as follows: the equation is reformulated to represent an initial-value problem; an initial guess is supplied, and this supplied function is fed recursively through the algorithm until the solution has converged to a stationary value (to within a certain tolerance). A simple scheme involves taking the Fréchet derivative of the analytic function (13.71), and defining the next iteration through this derivative. A definition of the Fréchet derivative is contained in Canuto *et al* (1988) [in appendix A.4].

The Fréchet derivative $\mathcal{L}(f)$ of a general function $A(f)$, $f = f(y)$, can be defined as

$$\mathcal{L}(f) \equiv \lim_{\Delta f \to 0} A(f + \Delta f) - A(f) \tag{13.78}$$

where Δf is a general perturbation of the function. For a smooth function f, the Fréchet derivative should approach zero uniformly as the perturbation Δf diminishes. Dropping the limit constraint, an approximate estimate of the Fréchet derivative for a non-zero Δf becomes

$$L\Delta f = A(f + \Delta f) - A(f). \tag{13.79}$$

Using (13.79), a general iterative procedure to determine a solution $f = f(y)$ to a general non-linear equation $A(f) = 0$ can be defined as

$$f \leftarrow f + \omega \Delta f, \tag{13.80}$$

where the term Δf is the solution of the equation

$$A(f) + L\Delta f = 0 \tag{13.81}$$

and ω is a relaxation factor. Specifically, the approximate Fréchet derivative of equation (13.76) is

$$L\Delta f = 2\Delta f_{ccc} + k^2(f\Delta f_{cc} + \Delta f f_{cc}), \tag{13.82}$$

the super-computer). Appendix D contains a listing of the Matlab functions. The script used to solve the problem was the function `base2d.m`, given in section D.4.1. The spatial order of solution was 60×60, although this was extended to 80×80 to verify the convergence of the system. The time-step was taken to be $\Delta t = 7 \times 10^{-6}$. Steps any bigger than 10^{-4} made the system unstable. The final (steady-state) accuracy of the system was unaffected by the time-step (as long as stability was maintained). Since the steady-state solutions are used predominantly for comparison to the experiment, it was unimportant that the temporal discretisation was highly accurate, as long as the steady state solution was exact. The current method of discretisation ensured that this was so, and the high order of spatial discretisation made spatial errors vanishingly small. However, the above time step was also sufficiently small for good temporal accuracy, as adjudged by the parallel system solved in section 13.2. A small systematic error in the mass flow (due to the explicit nature of the non-linear terms) was corrected every few time steps by simply dividing each row of the axial velocity by the mass flow rate calculated for that particular row.

The axial solution domain was taken to be $x \in [0, 0.02]$ in that this region embraced adequately the portion of pipe inlet flow that exhibits linear instability. Although it is not explicitly evident in the formulation, a variation of the axial domain is easily achieved by simply dividing the collocation derivative operator D by the domain extent. This is because the collocation derivative operator embraces the domain $[0, 1]$; if the domain length is required to be say, d units, then the operator D can be simply multiplied by the scalar factor d as $D' = (1/d)D$ and the new matrix D' used in place of D. For example, to achieve the present domain extent of $[0, 0.02]$, the factor d was taken as $d = 1/50$, and the operator $D' = 50D$ was used in place of D.

Solutions were generated both for impulsively started flow, and then for flows with increasing values of exponential acceleration. The results for the impulsive case are contained in the following section of this chapter, while the results for the more general exponential acceleration are deferred until the next section. The impulsive case is given here separately because it represents the only point of comparison to studies contained in the literature. The remainder of this chapter is thus devoted to the impulsive system, with an emphasis on comparison with existing results.

14.4 Numerical results

Impulsively started flow can be modelled using the numerical system described above, simply by setting the acceleration parameter Ω to zero. The impulsive system provides the only framework of comparison for the present results; thus a detailed investigation of the limiting behaviour and comparisons with existing data is carried out in this section. Detailed results obtained for the steady-state pipe entrance flow calculations are then presented; in particular the parameters

and this is simply achieved by the inversion of the constant $\hat{\Pi}_c$. The boundary matrices $\hat{B}_3$ and $\hat{B}_1$, of dimension $N \times 2$ and $M \times 2$ respectively, are given as

$$\hat{B}_3 = \begin{bmatrix} 1 & 1 \\ -1 & 1 \\ 1 & 1 \\ -1 & 1 \\ \vdots & \vdots \end{bmatrix}, \quad \hat{B}_1 = \begin{bmatrix} 0 & 0 \\ 0 & 0 \\ 0 & 0 \\ 0 & 0 \\ \vdots & \vdots \end{bmatrix}. \tag{14.36}$$

There is no need to assert any radial inflow boundary. If however it is desired to restrict the inlet radial component to zero, then the last row of the resultant matrix $\hat{\Gamma}^1$ can be made zero.

14.3 Method of solution

The non-linear terms in the final formulation (14.27) add a fair deal of complication to the system. If these are removed, then the resultant system is exactly that developed in section 13.2, but with the acceleration retained.

Numerically, the non-linear terms are the most expensive at N^3, because the linear system can be solved implicitly at a cost of N^2. Although the discretised equation needs the calculation of the non-linear operator at many time steps (if a higher-order discretisation is used), it is only necessary to calculate the non-linear product $\hat{N}(\vec{\Gamma}, \vec{\Gamma})$ once per time-step, and then to store it. When advancing to the next step, the last few convolution matrices (from previous times) can be stored. The oldest matrices can be simply discarded at each new time-step.

The choice of discretisation was the simple forward-Euler for the non-linear terms, and Crank-Nicholson for the linear ones. This explicit-implicit approach is optimum for this system as it retains the highest accuracy possible (by making as much of the equation as possible implicit) without having to resort to iterative techniques (which would be necessary if the non-linear terms were implicit), or linearisation and the subsequent decay in accuracy. The constants a_i, b_i for these time discretisations are: $a_0 = 1/2$, $a_1 = 1/2$, $a_2 = 0$, $b_1 = 1$, and $b_2 = 0$. Later, (and to obtain the solutions presented in this chapter), a modification of the Crank-Nicholson method - the θ method [Canuto *et al* (1988)]- was employed to avoid the lack of damping of high-frequency components inherent in the former approach. This method is simply implemented by making $a_0 = \theta$ and $a_1 = (1 - \theta)$, where $\theta = 1/2 + \alpha\Delta t$ and α is a small positive constant.

The numerical solution was done using Matlab. All the functions, for instance, calculating the non-linear terms, were written as Matlab functions. The computer platform used was firstly a Convex C210, and then later a 50Mhz IBM 80486 under Windows NT (which in real terms only ran at half the speed of

The conditions (14.30) and (14.31) must, as before, be augmented to the inner problem (14.29) as

$$\begin{aligned} \hat{\Gamma}^{(k+1)}\hat{\Pi} &= \hat{\Psi}, \\ \hat{\Pi} &= \left[\hat{B}_1 \vdots [\mathrm{LHS}]\right], \\ \hat{\Psi} &= \left[\hat{B}_2 \vdots [\mathrm{RHS}]\right], \end{aligned} \tag{14.32}$$

where the matrixes $\hat{B}_1$ and $\hat{B}_2$ are the augmented boundary conditions; namely

$$\hat{B}_1 = \begin{bmatrix} 0 & 1 \\ 2 & 1 \\ -8 & 1 \\ 18 & 1 \\ \vdots & \vdots \end{bmatrix}, \quad \hat{B}_2 = \begin{bmatrix} 0 & 0 \\ 0 & 0 \\ 0 & 0 \\ 0 & 0 \\ \vdots & \vdots \end{bmatrix}. \tag{14.33}$$

The left-hand boundary matrix $\hat{B}_1$ is of dimension $N \times 2$, and $\hat{B}_2$ is of size $M \times 2$. Equation (14.32) can be solved by inversion of the matrix $\hat{\Pi}$. For a set discretisation, $\hat{\Pi}$ is a constant, therefore the inversion needs be done only once.

The inlet condition is imposed by replacing the entire last row of the newly calculated velocity $\hat{\Gamma}^{(k+1)}$ by that condition. This allows for a lot of flexibility, in that *any* velocity profile can be used as an inlet condition. In fact, the actual solutions generated used a very thin boundary layer inlet profile with $\delta^*/R < 10^{-2}$ as the inlet condition in order to avoid oscillations in the solution caused by the singularity inherent in the simplified 'top-hat' profile. The continuity requirement (14.28) determines the radial coefficients from the axial ones, and thus the radial boundary conditions must be implemented for this system. These conditions are simply $v = 0$ at both the centreline and wall. Again for clarity, (14.28) is written as

$$\Gamma^1[\mathrm{LHS}_r] = [\mathrm{RHS}_r] \tag{14.34}$$

where $[\mathrm{LHS}_r]$ is constant and the matrix $[\mathrm{RHS}_r]$ depends on Γ^1. The system with boundary conditions to be solved is

$$\begin{aligned} \Gamma^1\Pi_r &= \Psi_r, \\ \Pi_r &= \left[B_3 \vdots [\mathrm{LHS}_r]\right], \\ \Psi_r &= \left[B_4 \vdots [\mathrm{RHS}_r]\right], \end{aligned} \tag{14.35}$$

$$\begin{aligned}\tilde{U}^{(k+1)}\left[\hat{\mu} - a_0\Delta t\hat{L}\right] &= \tilde{U}^{(k)}\left[\hat{\mu} + a_1\Delta t\hat{L}\right] \\ &+ a_2\Delta t\tilde{U}^{(k-1)}\hat{L} \\ &+ b_1\Delta t\hat{N}(\tilde{U}^{(k)},\tilde{V}^{(k)}) \\ &+ b_2\Delta t\hat{N}(\tilde{U}^{(k-1)},\tilde{V}^{(k-1)}) \\ &+ \Delta t\hat{K}.\end{aligned} \tag{14.27}$$

Equation (14.27) needs the implementation of the boundary conditions before solution is attempted.

The continuity requirement (14.2) is used to determine the radial velocity field coefficients $\tilde{V}^i$ from a given axial velocity field coefficients $\tilde{U}^i$. In the Tau system it can be written as

$$\tilde{V}^i\hat{\mu}\hat{q} = -D^T\tilde{U}^i\hat{\mu} \quad , \tag{14.28}$$

The two equations (14.27) and (14.28) form a coupled pair of equations for the unknown coefficients $\tilde{U}^i$ and $\tilde{V}^i$. As the radial coefficient matrix $\tilde{V}^i$ only appears in the non-linear part of the equation, the solution is straightforward. Equation (14.27) is used to generate the axial velocity coefficients $\tilde{U}^i$ at the new time-step $(k+1)$ using the known radial and axial coefficients from the previous time-steps. The continuity requirement (14.28) is then implemented to calculate the radial coefficients $\tilde{V}^i$ at the new time-step.

Obviously, boundary conditions need to be implemented at each step. To show the implementation of these boundary conditions, it is useful to summarise (14.27) as

$$\tilde{U}^{(k+1)}[\mathrm{LHS}] = [\mathrm{RHS}] \tag{14.29}$$

where the matrix [LHS] is a constant (dependent on the choice of temporal discretisation) $N \times N$ matrix. The matrix [RHS] is constructed from the known coefficients from the previous time steps, and is of dimension $M \times N$. The boundary conditions relevant to this equation are those concerning the axial velocity component u: thus symmetry at the centreline and the no-slip condition at the wall must be appended. In the Tau system these are

$$\tilde{U}^i\hat{\eta}[r]_{r=0} = 0, \tag{14.30}$$

$$\tilde{U}^i[r]_{r=1} = 0. \tag{14.31}$$

14.2.3 Operators

All the operators defined by the relations (14.4) to (14.6) can now be translated into the operational-Tau basis. These become in turn

$$\hat{L} = -2L_1\hat{\mu} + \hat{\eta}\hat{\mu}\hat{\eta} - \Omega\hat{\mu}, \tag{14.22}$$

$$\hat{N}(\vec{W}_1, \vec{W}_2) = \vec{P}(\vec{W}_1, D^T\vec{W}_1)\hat{\mu}\left(4\hat{J}\mu - I\right) - \vec{P}(\vec{W}_2, \vec{W}_1\hat{\eta})\hat{\mu}, \tag{14.23}$$

$$\hat{K} = \Omega K_1\hat{\mu}, \tag{14.24}$$

where the terms are defined as follows: I is the identity matrix; $\hat{L}_1$ is the limit operator defined by (12.53); $\hat{J}$ is the definite integral matrix given by (12.52); D is the collocation derivative matrix given by algorithm (12.7); μ and $\hat{\eta}$ are the pre-multiplication and derivative matrices respectively, defined by (12.51); and K_1 is defined by

$$K_1 = \begin{bmatrix} 1 & 0 & 0 & \cdots \\ 1 & & & \\ 1 & & & \\ \vdots & & & \end{bmatrix}. \tag{14.25}$$

14.2.4 Discretisation

The spatially and temporally discretised analogue of equation (14.3) can now be written in a manner analogous to the linear system from the example in section 13.2, as

$$\begin{aligned} \frac{1}{\Delta t}\left[\vec{f}^{(k+1)} - \vec{f}^{(k)}\right]\hat{\mu} = {} & \left[a_0\vec{f}^{(k+1)} + a_1\vec{f}^{(k)} + a_2\vec{f}^{(k-1)} + \cdots\right]\hat{L} \\ & + b_1\hat{N}(\vec{f}^{(k)}, \vec{\gamma}^{(k)}) \\ & + b_2\hat{N}(\vec{f}^{(k-1)}, \vec{\gamma}^{(k-1)}) + \cdots \\ & + \hat{K} \end{aligned} \tag{14.26}$$

where the superscripts $^{(k)}$ indicate coefficients from the kth time step, and the values of the constants a_i, b_i define the temporal discretisations for the linear and non-linear terms respectively, and their values for various schemes are given in table 13.5. The non-linear terms can only be treated explicitly (hence the omission of the b_0 term). Equation (14.26) can be rearranged to make the unknown $\vec{f}^{(k+1)}$ the subject of the left-hand side. This results in

can be written as

$$\vec{s} = \left\{ \left[\vec{a}_1 C^{-1} \right] \circ \left[\vec{a}_2 C^{-1} \right] \right\} C, \tag{14.19}$$

where $\circ$ represents the term-wise (or scalar) multiplication of the two vectors. Equation (14.19) can be evaluated at a cost of $4N^2$ operations if the matrices C and C^{-1} are calculated first and then stored. For a two-dimensional system like the present one, the vectors $\vec{a}_i$ in equation (14.19) can simply be replaced by the unknown coefficient matrices $\vec{W}_i$ with no loss of generality. The cost of the full two-dimensional calculation is now $4N^2M$, or $4N^3$ for a square system. If one ignores the factor of 4, the saving in calculation time is N times.

The quicker FFT between the coefficients and the physical values can be achieved at a reduced operation count cost; from approximately N^3 to approximately $\frac{5}{2}N^2 \log_2 N$ operations. For the present system, the matrix-transform method was used because of its simplicity of formulation. However, the modest speed gains did not justify the implementation of the FFT approach.

Aliasing

Pseudo-spectrally performed convolutions produce aliasing in the resultant vector if the transform is performed at the order of the system N [Canuto *et al* (1988)]; that is, spurious high-frequency modes are introduced. The way around this is to extend the input vectors $\vec{a}_i$ to order $3N/2$ simply by adding zeroes to the end of these vectors. The transform is then conducted at the higher order, and the result *after* transforming back to the Tau basis is truncated at order N. A detailed account of why this aliasing occurs is contained in the above reference. However the aliasing is so slight as to be negligible, as long as the system is properly represented at the order N; that is, the error produced by aliasing *also* decays at infinite-order. The present convolution calculations were performed in both aliased and non-aliased forms, but no difference to the level of the round-off noise was found between the calculations.

Definition of $P(\vec{W}_1, \vec{W}_2)$

Considering the above, the product of two functions can be defined for the present system as

$$P(\vec{W}_1, \vec{W}_2) = \left\{ \left[\vec{W}_1 C^{-1} \right] \circ \left[\vec{W}_2 C^{-1} \right] \right\} C, \tag{14.20}$$

Thus under the operational-Tau system, the product of two functions is

$$w_1 w_2 \Rightarrow P(\vec{W}_1, \vec{W}_2)c. \tag{14.21}$$

out at order $2 \times N - 1$ and *then* truncated. This means that the smaller (and hence quicker) calculation does not *alias* the result. This is in contrast with the pseudo-spectral method for calculating the product (described below), where aliasing does occur.

Extension of the above method to a two-dimensional system, where the second discretisation is collocation (the present problem), results in a convolution having to be performed between each row of the two matrices. The cost of a single convolution is however high; of order N^3 when performed at order N - making a two-dimensional convolution prohibitive at $N^3 \times M$ or N^4 for a square system.

This problem of cost, and hence speed, of a product under the spectral system is inherent when dealing with the coefficients in the transformed system. If the system were represented at discrete nodes (as in a finite-difference method), then the price of a two-dimensional product would only be N^2 for a square system of order N. Performing the convolution by considering the product at discrete nodes is the essence of the pseudo-spectral approach described below.

The Pseudo-spectral approach

This approach entails transforming the coefficients $\vec{a}_i$ into the physical (Lagrangian) domain via the transformation C, representing the function here at the collocation points, performing a multiplication between the two functions at these nodes, and then transforming the result back into the Chebyshev basis. As mentioned, transformation between the Chebyshev and Lagrange bases can be achieved in two ways: firstly by using a matrix transform [C, given by algorithm (12.6)], and secondly (and more quickly) by utilising a fast-Fourier type transform.

Convolution via the first option is simpler to explain, but is mathematically equivalent to the second. Consider again the two one-dimensional functions x_1, x_2, with their operational-Tau forms given as before. Each coefficient vector, if of order N, can be equivalently transformed to physical values at the N Gauss-Lobatto collocation points by the matrix C^{-1}, defined by the algorithm (12.6):

$$\begin{aligned} \check{x}_1 &= \vec{a}_1 C^{-1}, \\ \check{x}_2 &= \vec{a}_2 C^{-1}, \end{aligned} \tag{14.18}$$

where as before the check ($\check{x}$) indicates that the vector represents the physical values at the collocation nodes. In the physical space, $\check{x}_1$ can be multiplied element-wise with $\check{x}_2$, and the result transformed back to the Tau basis by employing the inverse transformation C, resulting in the answer z. This process

scheme allows the flexibility of introduction of an arbitrary inlet condition. The variables $\vec{U}^t$ and $\vec{V}^t$ can, however, be rendered as two-dimensional Chebyshev coefficient matrices U and V via the transformation C^{-1} [C^{-1} is given by (12.5) on page 251], as

$$\begin{aligned} U &= [C^{-1}]^T \vec{U}^t \\ V &= [C^{-1}]^T \vec{V}^t. \end{aligned} \tag{14.15}$$

14.2.2 Non-linear terms

The non-linear terms defined by the operator $\mathcal{N}(w_1, w_2)$ cannot be accommodated uniformly into an implicit scheme such as that given in the example in section 13.2. The terms can, however, be stated as a polynomial function of τ (see section 13.3). Thus, they can be accommodated explicitly in an initial-value problem.

The method of including these non-linearities can be shown by considering two general functions of τ alone under the operational-Tau system, $w_1 = \vec{w}_1 e$ and $w_2 = \vec{w}_2 e$. For the current problem, all the non-linearities consist of products of linear terms. The product of the above two functions become, in the Tau basis, a convolution between the respective coefficient vectors $\vec{w}_1$, $\vec{w}_2$, or

$$w_1 w_2 = [\vec{w}_1 * \vec{w}_2]\, e. \tag{14.16}$$

This convolution is given by

$$[\vec{w}_1 * \vec{w}_2] = \vec{w}_1 \hat{\mathcal{R}}(\vec{w}_2) = \vec{w}_2 \hat{\mathcal{R}}(\vec{w}_1) \tag{14.17}$$

where $\hat{\mathcal{R}}$ is simply the multiplication operator (13.17) defined in section 13.1. Equation (14.17) is valid because the product of the two functions is equivalent simply to the one function (w_1) pre-multiplied by a polynomial (w_2, the other function).

Due to the fact that the convolution is a product between polynomials, the resultant vector will have magnitude $2 \times N - 1$ if all the terms are to be retained. However, truncation of the product at N terms is acceptable as long as the vectors $\vec{w}_1$ and $\vec{w}_2$ are sufficiently representative of their respective functions, implying that their higher coefficients are very small. As stated before, this is always the case for a smooth function if the interpolating series is taken to sufficient terms, because of the infinite-order convergence to zero of the higher coefficients. An important point is that the result calculated at a truncation level N using (14.16) will be identical to the result of the convolution carried

14.2.1 Axial discretisation

The discretisation of the unknowns $\bar{u}$ and $\bar{v}$ in the axial direction was by means of collocation. This method was discussed in detail in section 12.8, where an operational approach was developed. In general under a mixed operational-Tau - collocation approach, these variables can be given as

$$\bar{u} = \vec{U}\vec{c}, \tag{14.11}$$

$$\bar{v} = \vec{V}\vec{c} \tag{14.12}$$

where $\vec{U}$ and $\vec{V}$ for an Mth order collocation discretisation and an Nth order operational-Tau formulation are $M \times N$ matrices of unknowns. The column vector $\vec{c}$ represents the Chebyshev basis vector in r. Operations in the radial direction are carried out in the usual way. For instance differentiation with respect to $\bar{r}$ is simply

$$\frac{\partial \bar{u}}{\partial \bar{r}} = \vec{U}\hat{\eta}\vec{c}, \tag{14.13}$$

while in the axial direction, differentiation is

$$\frac{\partial \bar{u}}{\partial \bar{x}} = D^T\vec{U}c. \tag{14.14}$$

The matrix D is the standard Chebyshev Gauss-Lobatto collocation derivative matrix, defined by the algorithm (12.7). Each row of the coefficient matrix $\vec{U}$ represents the Tau coefficients at a particular collocation point, thus slices through the coefficient matrix form discrete profiles at fixed $\bar{x}$ stations. The case of implementation of the inlet boundary condition arises because of the discrete nature of the collocation system. For instance, to assert the inflow boundary condition, the last[1] row of the coefficient matrix is just replaced with the given inlet condition.

While the mixing of schemes might seem unusual, it is common practice to do this in a spectral approach. Furthermore, the current mixture uses the optimum properties of each scheme for each direction. The radial Tau discretisation is optimum in that it accommodates the symmetry conditions at the centreline, can be extended quickly to any order (by simply augmenting zeroes to the coefficient matrices), and, as will be seen later, is compatible with the highly accurate stability formulation to be developed in the next chapter. The axial collocation

[1] Remember that the collocation grid (12.55) is reversed in x; thus the inflow condition at $x = 0$ corresponds to the last ($N - 1$'th) collocation node.

(i) Symmetry at the pipe centreline, given by the two relations below.

$$\begin{aligned} \frac{\partial}{\partial \bar{r}} \bar{u}(\bar{x}, 0, \bar{t}) &= 0, \\ \bar{v}(\bar{x}, 0, \bar{t}) &= 0. \end{aligned} \tag{14.7}$$

(ii) The no-slip condition at the wall, described by the following constraints:

$$\begin{aligned} \bar{u}(\bar{x}, 1, \bar{t}) &= 0, \\ \bar{v}(\bar{x}, 1, \bar{t}) &= 0. \end{aligned} \tag{14.8}$$

(iii) The initial conditions, that is the state of the system at $\bar{t} = 0$:

$$\begin{aligned} \bar{u}(\bar{x}, \bar{r}, 0) &= 1, \\ \bar{v}(\bar{x}, \bar{r}, 0) &= 0. \end{aligned} \tag{14.9}$$

(iv) The axial inlet or inflow conditions persisting at the inlet plane, given by

$$\bar{u}(0, \bar{r}, \bar{t}) = 1, \tag{14.10}$$

while the inlet radial component is left to be determined from continuity.

Both the evolution equation (14.3) and the continuity requirement (14.2) have to be applied with consideration of these boundary condition; that is, their solutions must be compatible with the boundary conditions. The above operators (14.4), (14.5) and (14.6) can be formulated radially in the operational-Tau system.

14.2 Numerical formulation

The radial Tau formulation has been covered in some detail in previous chapters, the discretisation of the axial operators $\frac{\partial}{\partial \bar{x}}$ has not been defined. This section discusses the axial discretisation scheme, furthermore, the method of treatment of non-linearities, which was introduced in the solution of the Blasius equation (section 13.3), is given detailed consideration below.

14.1 Analytical formulation

The equations (10.33) and (10.34) are the basis for the pipe entrance model to be developed. These equations are repeated below for convenience. They consist of a coupled pair of non-linear partial-differential equations in two variables $\bar{u} = \bar{u}(\bar{x}, \bar{r}, \bar{t})$ and $\bar{v} = \bar{v}(\bar{x}, \bar{r}, \bar{t})$, while the pressure has been formally eliminated.

$$\frac{\partial \bar{u}}{\partial \bar{t}} + \bar{\Omega}(\bar{u}-1) + \bar{u}\frac{\partial \bar{u}}{\partial \bar{x}} + \bar{v}\frac{\partial \bar{u}}{\partial \bar{r}} = 2\frac{\partial}{\partial \bar{x}}\int_0^1 \bar{r}\bar{u}^2 d\bar{r} - 2\left.\frac{\partial \bar{u}}{\partial \bar{r}}\right|_{\bar{r}=1} + \frac{1}{\bar{r}}\frac{\partial}{\partial \bar{r}}\left(\bar{r}\frac{\partial \bar{u}}{\partial \bar{r}}\right), \quad (14.1)$$

$$\frac{1}{\bar{r}}\frac{\partial}{\partial \bar{r}}(\bar{r}\bar{v}) + \frac{\partial \bar{u}}{\partial \bar{x}} = 0. \quad (14.2)$$

The system given by (14.1) and (14.2) is an initial-value problem with an evolution term in $\bar{u}$.

The equations (14.1) and (14.2) need to be arranged in a form amenable to solution by the operational-Tau method. The only problematic aspect of these equations in that regard is that they contain terms in $\frac{1}{\bar{r}}$. Thus a simple multiplication through by $\bar{r}$ will result in operators that can be formulated directly in the Tau basis.

After multiplication through by $\bar{r}$, the evolution equation (14.1) can be rewritten in the form

$$\bar{r}\frac{\partial \bar{u}}{\partial \bar{t}} = \mathcal{L}\bar{u} + \mathcal{N}(\bar{u}, \bar{v}) + \mathcal{K}. \quad (14.3)$$

The continuity relation will be considered later.

The linear operator $\mathcal{L}$ for non-accelerating ($\bar{\Omega} = 0$) flow was given by (13.33). The more general operator of equation (14.3) contains an extra term, but as before is a function of $\bar{u}$ alone. The non-linear operator $\mathcal{N}(\bar{u}, \bar{v})$ describes the non-linear terms, and is a function of both $\bar{u}$ and $\bar{v}$. The remaining constant term $\mathcal{K}$ encapsulates the constant (non-functional) terms in the equation. The relationship between $\bar{u}$ and $\bar{v}$ is given by the continuity constraint (14.2). These operators and constant factor are given as

$$\mathcal{L} = -2\bar{r}\left[\frac{\partial}{\partial \bar{r}}\right]_{\bar{r}=1} + \frac{\partial}{\partial \bar{r}}\left(\bar{r}\frac{\partial}{\partial \bar{r}}\right) - \bar{r}\bar{\Omega}, \quad (14.4)$$

$$\mathcal{N}(w_1, w_2) = 2\bar{r}\frac{\partial}{\partial \bar{x}}\int_0^1 \bar{r}w_1^2 d\bar{r} - \bar{r}w_1\frac{\partial w_1}{\partial \bar{x}} - \bar{r}w_2\frac{\partial w_1}{\partial \bar{r}}, \quad (14.5)$$

$$\mathcal{K} = \bar{r}\bar{\Omega}. \quad (14.6)$$

Boundary conditions for the current system are:

Chapter 14

Impulsive laminar pipe entrance flow

A suitable tool for the accurate solution of differential equations has been developed in chapter 12, and in chapter 13 was applied to various simple problems of relevance to the current study. The means of discretising the non-linear terms was given, as was a generally applicable form of temporal discretisation. However, the problems there all had only one spatial dimension, and the means of discretisation for a second spatial co-ordinate needs to be considered before a solution for the accelerating base-flow in the pipe entrance can be generated.

A sensible problem in which to introduce the relevant two-dimensional formulation is that of the impulsively started pipe entrance flow. Some work has been done in this area, and thus comparisons can be drawn. Further to this, the extension of the impulsive case to the more general accelerating system involves the incorporation of a single additional term into the steady equations.

Due to the numerical similarity between the two systems, the more general set of equations is actually discretised here; but a solution is only presented for the impulsive flow, which is the formal limiting case as $\tilde{\Omega} \to 0$. The full results for non-zero $\tilde{\Omega}$ are given in the following chapter. This break was chosen because it allowed separation of the numerical issues from the fluid dynamics considerations. Thus the current chapter concentrates on the axial discretisation and the presentation of the impulsive data in suitable parametric frameworks, which leaves the following chapter to be concerned with the more general results alone. The break between this chapter and the next also falls along the line between the known and unknown. This chapter can draw comparisons to existing results, whereas the subsequent one presents novel results.

14.5 Exclusion of the inlet plane

In the case of the flat-plate boundary layer, the simplifying assumptions used to derive the Blasius equation are no longer valid as the front of the plate is approached. This has been investigated by McLachlan (1991) whose paper showed that the leading edge does not conform to the Blasius solution, but that the simple Blasius solution does become valid a short way downstream of this point. At the front edge, the full Navier-Stokes equations must be applied to describe the flow properly. The same is true for pipe inlet flow. Although the system tends to the Blasius limit as the inlet is approached, this limit itself becomes invalid, and the full Navier-Stokes equations should be invoked here. This is, however, a rather academic point, because in reality, a pipe inlet is usually fed from some sort of contraction on which there exists a boundary layer already. Thus the limit of zero displacement thickness at the inlet is merely a convenient simplification. In the present analysis, the inlet condition was *not* taken as this simple limit, but rather as a velocity profile with a small boundary layer, more in keeping with the physical system. In fact the result of using the simple condition (the 'top-hat' profile) caused oscillations to arise in the solution, highlighting this breakdown in the equations at this point[5]. This was because the simplified boundary layer relations could not properly describe the solution in this limit. Regardless of this, whatever inlet profile was taken, the solution a short way downstream behaved as if it were originating from the simplified Blasius limit.

Thus, although the inlet plane must strictly be excluded from the analysis, the Blasius boundary layer-like description of this limit is valid, regardless of the details of the thin inlet boundary layer. In simpler words, the flow behaves as though it originated from a Blasius-like form, even though the actual inlet conditions were not so. This is substantiated by the work of McLachlan (1991), which states that a boundary layer becomes Blasius-like a short way downstream, regardless of the nature of its origin.

14.6 Summary

The behaviour of steady-state pipe entrance flow has been investigated thoroughly, and comparisons made to the natural asymptotic limits. A number of important issues have been introduced in this chapter which deserve mention:

(i) A general numerical scheme is presented, for pipe inlet flows under general accelerations using the operational-Tau method. The present scheme uses the same philosophy as applied to the linear systems in the previous

[5]The spectral approach is very sensitive to analytic properties of the system - the oscillation indicated a breakdown in the smooth functional nature of the solution at the inlet wall, indicating the non-applicability of the simplified equations here.

pipe entrance, and since the effects of the non-parallel nature of the flow on the stability of this profile is known, it is important to evaluate the value of the parallel parameter for the Blasius system. For this profile, the parallel parameter is given by $\kappa = 0.8604 Re_x^{1/2}$, while $Re_{\delta^*} = 1.7208 Re_x^{1/2}$. The value of the parallel parameter for the Blasius profile is $\kappa = 1.48 Re_{\delta^*}^1$, or, in terms of the boundary layer parameter, $\kappa_{\delta^*} = 1.48$.

In the case of the Blasius system, 1.48 is much smaller than the critical Reynolds number of $Re_{\delta^*[\mathrm{crit}]} = 519$, indicating that the non-parallel effects for this flow are insignificant. Boundary layers with a displacement thickness-based parallel parameter much less than the Blasius value will thus be *even less* prone to non-parallel effects than the Blasius profile. Figure 14.9 shows the variation of κ_{δ^*} with δ^* for the pipe entrance system, with the limiting value of $\kappa_{[\mathrm{Blas}]}$ shown on the left-hand axis.

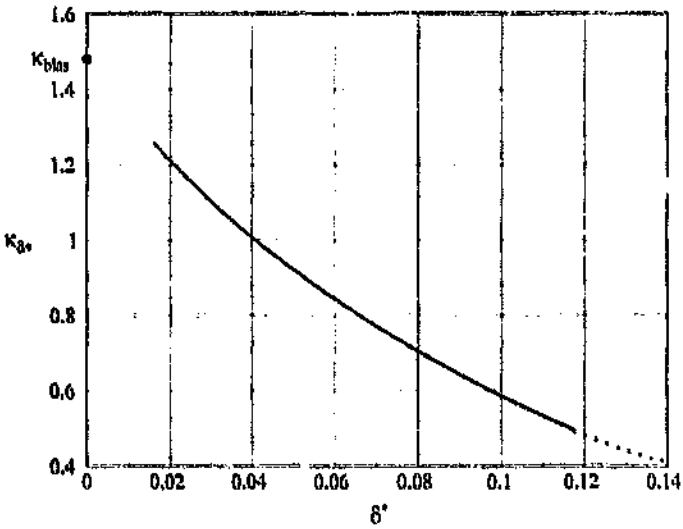

Figure 14.9: The variation of the parallel parameter scaled with respect to displacement thickness κ_{δ^*}, with displacement thickness δ^*, in a steady-state pipe entrance flow, showing the Blasius limit at the inlet.

This figure immediately shows the diminishing nature of the non-parallel effects away from the pipe inlet. At the inlet, the parameter approaches the Blasius value of $\kappa_{[\mathrm{Blas}]} = 1.48$. The value of the parameter diminishes away from this limit, indicating that the pipe entrance flow becomes increasingly more parallel away from the inlet plane. The maximum discrepancy between the parallel and non-parallel stability analyses for the pipe entrance would thus be expected to diminish from the Blasius difference of about 8% [Abbot & Moss (1994)] near the inlet plane to an insignificant quantity a short distance downstream. The stability analysis of this system will be addressed in chapter 16.

measure of the non-parallel nature of the pipe inlet flow. A sufficient criterion to determine the non-parallel*ness* of the pipe system will be taken as

$$\kappa \equiv \max\left[\frac{\bar{v}}{u}\right] \ll Re. \tag{14.44}$$

The variation of the *parallel parameter* κ, given by (14.44), with displacement thickness δ^* for pipe entrance flow is shown in figure 14.8. Near the point of minimum critical Reynolds number, $\kappa \ll 11667$, and so the flow is most certainly nearly-parallel. However, as the inlet plane is approached, both κ and $Re_{[crit]}$ increase without bound, making it unclear whether the parallel assumption is valid as the inlet plane is approached.

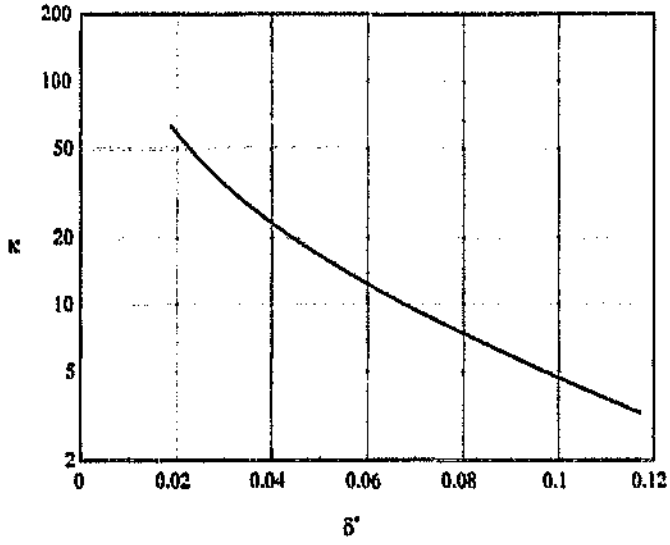

Figure 14.8: The variation of the parallel parameter κ with displacement thickness δ^* in a steady-state pipe entrance flow.

Due to the unbounded nature of κ towards the inlet, it is as before appropriate to scale the parameter with respect to the boundary layer dimension in this limit. A parallel criterion scaled according to the boundary layer parameters can be simply defined as

$$\kappa_{\delta^*} \equiv \frac{\delta^*}{R}\frac{u_e}{\bar{v}_m}\kappa \ll Re_{\delta^*}. \tag{14.45}$$

Thus when considering the pipe entrance region as a boundary layer flow, the boundary layer parallel parameter κ_{δ^*} must be much less than the displacement thickness critical Reynolds number for non-parallel effects to be unimportant. Since the Blasius boundary layer is the limiting boundary layer shape for the

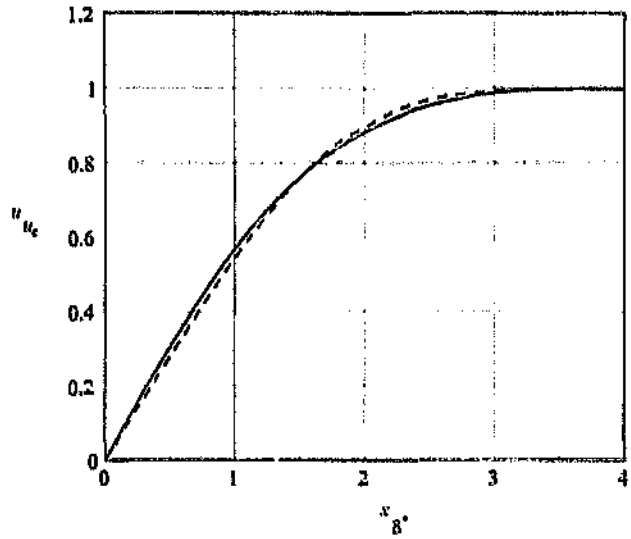

Figure 14.7: A comparison between the parallel and Blasius boundary layers for identical displacement thickness δ^*: , parallel boundary layer; - - -, Blasius profile.

one, the latter possessing a high value for the second derivative throughout the boundary layer. It will be shown later in the stability analysis that these two profiles have very different critical Reynolds numbers.

14.4.6 The nearly-parallel nature of the flow

The above discussion raises some questions regarding the non-parallel nature of the inlet flow. This topic was addressed in some detail in Abbot & Moss (1994). The magnitude of non-parallelness of the entrance flow can be shown directly by considering the ratio between the axial and radial components of velocity, and by observing the magnitude of the term $\frac{\partial v}{\partial r}$. Drazin & Reid (1981) define a *nearly-parallel* flow as one in which $v \ll u$ and $\frac{\partial v}{\partial x} \ll 1$. The current variables are dimensionless; thus for the present case, the flow can be judged nearly-parallel if

$$\frac{v}{u} \ll Re, \tag{14.42}$$

$$\frac{\partial u}{\partial x} \ll \frac{R^2}{r}. \tag{14.43}$$

It can be easily shown via continuity that the criterion (14.43) for pipe flow is of the same order of magnitude as (14.42), therefore (14.42) will be used as the

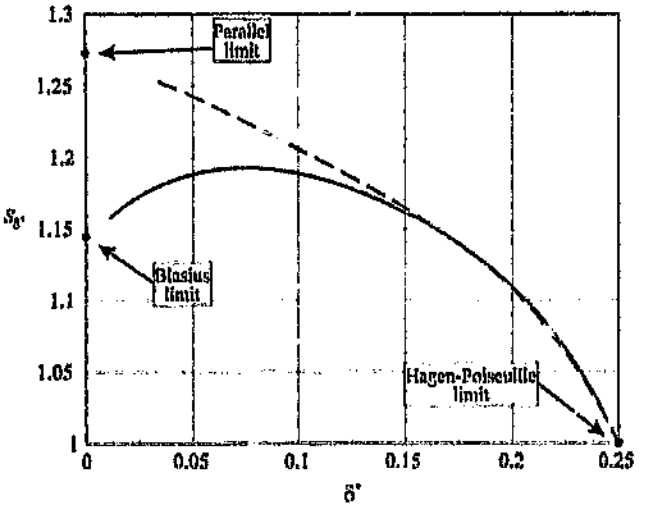

Figure 14.6 The variation of the scaled shape parameter S_δ with displacement thickness δ^*, for the two cases of parallel impulsive pipe flow (- - -), and steady-state pipe entrance flow ( ).

The two curves in figure 14.6 converge at $\delta^* \approx 0.15$, and from then on are virtually indistinguishable towards the Hagen-Poiseuille limit. This seems to indicate that the non-parallel influence has become negligible in the entrance flow for $\delta^* > 0.15$. From figure 14.3, it can be seen that the portion of the inlet corresponding to $\delta^* \in [0, 0.15]$ is only the very small region $x \in [0, 0.02]$; thus only a small region of the total pipe entrance deviates markedly from the parallel system; however, the portion of the pipe within which instability can occur is well within this region[4].

Figure 14.6 shows that, for the same displacement thickness δ^*, profiles from the pipe entrance and from far downstream have *very* different structures, especially in the limit of decreasing boundary-layer thickness, convincingly demonstrating that velocity profiles do not form a single-parameter group with S as parameter. The limiting behaviour of the pipe inlet flow can be shown analytically by considering equations (10.8) and (10.9) - the full boundary layer equations for pipe flow. If these equations are non-dimensionalised with respect to δ^*, and the radial co-ordinate is transformed to a wall co-ordinate as $y = R - r$, then as $\delta^* \to 0$, these equations will reduce to the flat plate boundary layer equations with *no* pressure gradient, for which the Blasius system yields an exact solution.

Figure 14.7 shows, for the same value of displacement thickness, the comparison between the Blasius and error-function (parallel) profiles. Immediately apparent on this plot is the large discrepancy between these two types of profile. The Blasius boundary layer is much less 'convex' near the wall than the parallel

[4]The axial station at which the minimum critical Reynolds number occurs is approximately $x = 0.003\,59$.

14.4.5 Scaled shape parameter

This parameter was defined in section 13.2.6 [equation (13.62) on page 285] as

$$S_{\delta^*} = \frac{U_m}{u_c}\frac{\delta^*}{R}S \quad = 2\frac{\tau_w \delta^*}{\mu u_c}. \tag{14.41}$$

It is thus simply the shape parameter scaled according to the boundary layer dimension and centreline velocity. The variation of S_{δ^*} with x is given in figure 14.5. As in temporally developing flow, this parameter remains bounded as the pipe inlet is approached, converging to a finite asymptotic limit. Far downstream it approaches unity, corresponding to the parabolic Hagen-Poiseuille profile.

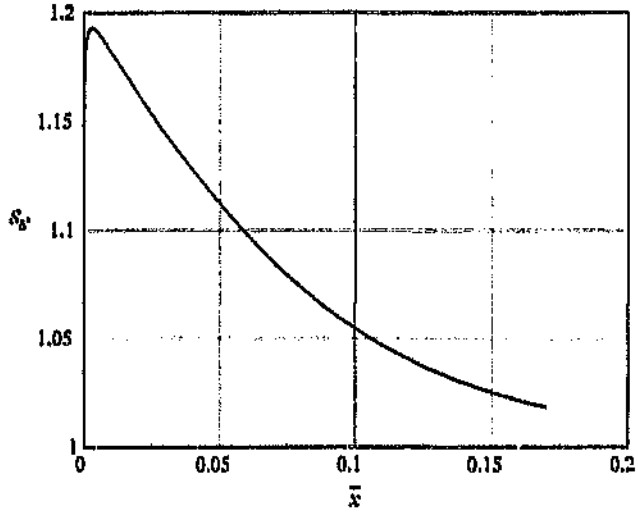

Figure 14.5: The variation of the scaled shape parameter S_{δ^*} with axial station $\bar{x}$ in a steady-state pipe entrance flow.

If this figure is compared to the analogous one for temporally developing flows - figure 13.10 - it is immediately apparent that the current curve approaches a different, lower, limit at the inlet. While the parallel system approaches the parallel boundary layer limit $S_{\delta^*[\mathrm{prl}]}$ given by (13.65), the current curve seems to be asymptotically convergent to $S_{\delta^*} = 1.143$, the Blasius limit, given by (13.98). If, as in figure 13.11, S_{δ^*} is plotted against δ^*, this limiting behaviour becomes immediately apparent. Figure 14.6 shows this variation, along with the results from figure 13.11 superimposed for comparison. The values of $S_{\delta^*[\mathrm{Blasius}]}$ and $S_{\delta^*[\mathrm{prl}]}$, for the Blasius and parallel boundary layer calculations respectively, are shown plotted on the left-hand axis. The entrance system can be seen to converge to the Blasius boundary layer limit.

far-downstream end S reduces to the parabolic limit of $S = 8$. The similarity of this figure to the one presented for temporally developing flow - figure 13.9 - is possibly what led da Silva (1990) to erroneously conclude that the parameter S uniquely quantifies a profile (that is, profiles from anywhere in a pipe flow with identical values of S are identical).

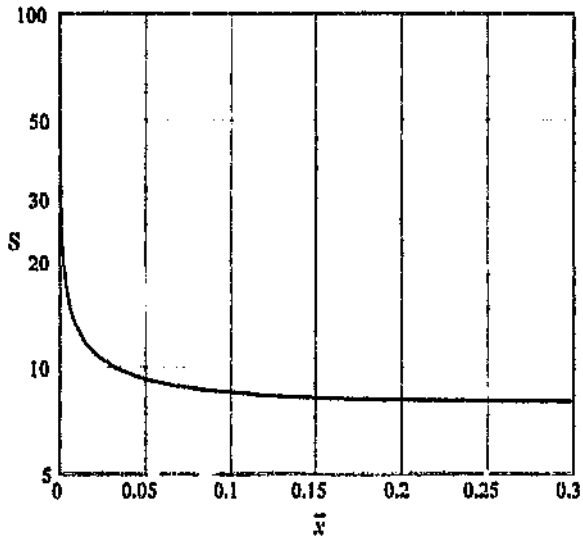

Figure 14.4: The variation of the shape parameter S with axial station $\bar{x}$ in a steady-state pipe entrance flow.

Both figures 14.4 and 13.9 show the same two asymptotic limits. This is *not* however sufficient to allow one to conclude that the parameter uniquely defines a profile, in that there is no other point of comparison between the two figures[3]. In fact, starting with the assumption of the universality of S, and the two figures, a temporal-spatial equivalence between different profiles can be erroneously derived. As will be shown, the use of the shape parameter scaled with respect to δ^*, S_δ, immediately highlights the discrepancy between the spatial and temporal velocity profiles.

[3]A small amount of reflection on the problem - one of quantifying the shape of a profile that consists of a boundary layer followed by a central core - will show that at least two parameters would be necessary to describe the profile adequately in the case where the shape (structure) of the boundary layer is subject to variation. In such a case, one parameter would be needed to describe the extent (size) of the boundary layer, and at least one would be necessary to encapsulate the shape of this region. That only one parameter were sufficient would infer that the boundary layer were *always* of the same shape, i.e. self-similar. The consideration of the structure of various boundary layers, especially in the pipe system, will show this to be false.

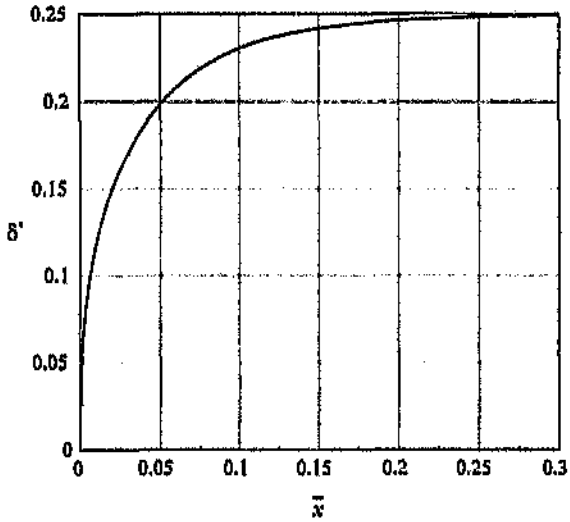

Figure 14.3: The variation of the displacement thickness δ^* with axial station $\bar{x}$ in a steady-state pipe entrance flow.

parameter in its own right, as it characterises the system.

14.4.4 Velocity profile shape parameter

This parameter was defined by Moss (1985) as

$$S = \frac{2\tau_w R}{\mu \bar{U}}, \tag{14.39}$$

In the context of the normalised variables $\bar{u}$ and $\bar{r}$, it is given by

$$S = -2 \left. \frac{d\bar{u}}{d\bar{r}} \right|_{\bar{r}=1} \tag{14.40}$$

and is thus simply ($-2\times$) the dimensionless velocity derivative at the wall. The centreline velocity and displacement thickness discussed above are integral quantities in that they contain information from the entire boundary flow. The shape parameter on the other hand is concerned with the radial derivative of axial velocity at the pipe wall. It is thus an independent measure from the previous two parameters.

Figure 14.4 shows the variation of the shape parameter S with axial position $\bar{x}$. The unbounded behaviour $S \to \infty$ as $\bar{x} \to 0$ is immediately apparent. At the

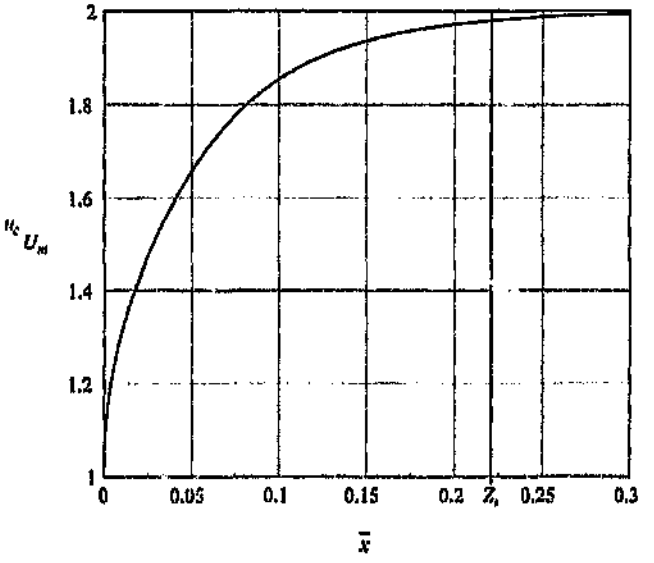

Figure 14.2: The variation of the normalised centreline velocity u_c/U_m with axial station $\bar{x}$ in a steady-state pipe entrance flow, showing the entrance length Z_c.

The dimensionless centreline variation of velocity is a simple measure of the velocity profile shape and can be extracted readily from numerical or even experimental data.

14.4.3 Displacement thickness

The dimensionless centreline velocity and the boundary layer displacement thickness are directly related through the relation (13.59) from the previous chapter, which is repeated as (14.38) below:

$$\frac{\delta^*}{R} = \frac{1}{2}\left(1 - \frac{U_m}{u_c}\right) \quad . \tag{14.38}$$

The variation in displacement thickness δ^* with $\bar{x}$ is shown in figure 14.3. Analogous to the centreline variation, the two limiting values of δ^* at the inlet and far downstream are: $\delta^* = 0$ at $\bar{x} = 0$, corresponding to the 'top-hat' inlet profile, and $\delta^* \to 0.25$ as $\bar{x} \to \infty$, the parabolic limit. Although no new information is encoded in the displacement thickness, this term is more physically meaningful than the centreline velocity variation in that is gives a direct indication of the boundary layer dimension.

The equation (13.59) is not the exact definition of δ^* for pipe flow (see the discussion on page 283) in that it is linearised, but it does serve as a valid

and this is reinforced by the longer entrance length that he obtained (see table 14.1). This cannot however be verified, without the data for his entrance length calculation (with its much larger axial domain).

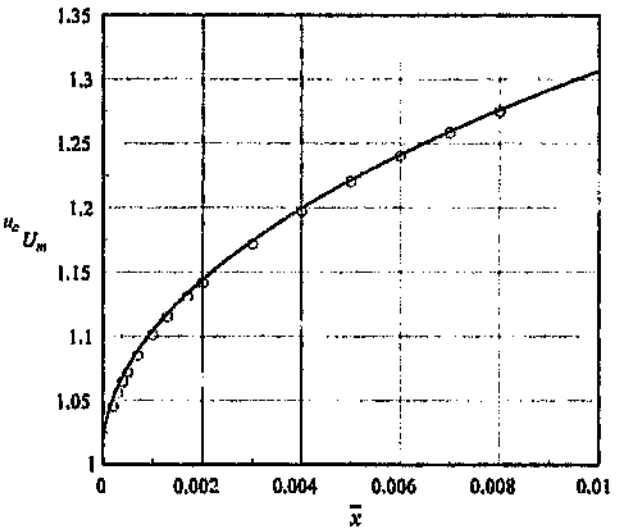

Figure 14.1: The normalised centreline velocity u_c/U_m, compared to the results of da Silva (1990): ∘, da Silva; —, present.

The temporal development of pipe flow

Pipe flow sufficiently far from the entrance is parallel, and the non-linear system (14.3) simplifies to a linear one. The example in section 13.2 solved exactly this problem for impulsively started pipe flow, and the results are presented there. The only points of comparison were the momentum-integral technique of Moss (1985) and the results of da Silva (1990). The present results and da Silva's showed remarkable agreement, due to the upwinding being absent from his simplified one-dimensional calculation. The present results were dominated by temporal errors, and the invariance to only 4 decimal places of the present results shown in table 13.6 confirms this. However, as discussed there, the current error is manifest as a temporal uncertainty, and thus the accuracy of determination of the profiles was much higher than 10^{-4}.

14.4.2 Centreline velocity

The centreline velocity variation normalised with respect to the mean velocity, u_c/U_m, with $\bar{x}$ is shown in figure 14.2. As expected, u_c/U_m varies from a value of unity at the inlet plane, and becomes asymptotic to $u_c/U_m = 2$ far downstream. Also shown on this plot is the inlet length Z_r as given by (14.37).

70 × 70 and comparing the results. The current inlet calculation used a very thin boundary layer profile as inlet boundary condition, not the top-hat, and an extrapolation to the inlet was done to correct this. The shape of the inflow profile boundary layer was the Blasius profile. This choice of condition was made on physical grounds. However, the solution a short distance downstream from the inlet was invariant, *regardless* of the particular form of the inlet condition[2]. The inlet offset was found to be $1.6099 \times 10^{-4} \pm 3 \times 10^{-9}$; thus the inlet length, exact to 6 decimal places, is

$$Z_e = 0.220\,779. \tag{14.37}$$

Due to the fact that no simplifying assumptions were made except that the Reynolds number was high, the present answer can be adjudged exact to at least the 6 decimal places given in (14.37). da Silva's (1990) model, although using the correct equations, used the (physically highly dubious) upwinding technique, allowing a bias to enter the calculations. Thus, although his results may have converged to an invariant solution, this value would have been wrong. The Hornbeck (1963) model yields the closest results to the present system; therefore Hornbeck's model seems to be the most valid choice if a simplified inlet system is needed, at least when adjudged by the Z_e criterion.

Unfortunately, the entrance length criterion for inlet flow is the only universal point of comparison; b[illegible]e of this the validity of the various simplified models in terms of profile shape, etc., could not be validated. Agreement on Z_e does not guarantee the correctness of a model. However, the present model is the most natural in that no non-physical simplifying assumptions are made, and because the numerical model solves the proper equations accurately.

Centreline variation

The study by da Silva (1990) gives tabulated values for the centreline velocity variation with $\bar{x}$ in the restricted range $\bar{x} \in [0, 0.02]$, and these are compared with the present results in figure 14.1. The results of da Silva show a small lag near the pipe inlet, where the centreline velocities are slightly depressed. Further downstream, his values approach the current curve, and become visually indistinguishable from the present results. The slight suppression of the centreline velocity is thought to be due to a bias introduced by the upwinding technique,

[2]The inlet profile was taken sequentially as 'top-hat', the Blasius profile, and the parallel boundary layer limit, and the results compared. For all three cases, the solution three collocation nodes downstream was visually identical, and one or two nodes further downstream had converged to the level of the round-off error. The problem with the 'top-hat' profile was that it caused oscillations in the solution unless an extremely high radial order of solution was used, due to the presence of a singularity at the wall. The Blasius profile was thus chosen because that was the natural limit for this system.

shown are the centreline velocity u_c, the displacement thickness δ^*, the shape parameter S, and the scaled shape parameter S_{δ^*}. The introduction of these terms is covered fully in section 13.2, where these parameters' temporal variation is presented for parallel, impulsively started pipe flow far from the inlet

14.4.1 Comparisons with previous results

A number of analytical and numerical studies of impulsive pipe inlet flow have been carried out by workers in the field of fluid dynamics. However, the only universal means of comparison with these results is via a single parameter, the entrance length.

Entrance length

The entrance length of the pipe is defined as Z_e, the axial location at which the centreline velocity attains 99% of the parabolic centreline value. The values of Z_e for the various entrance flow investigations is shown in table 14.1.

Table 14.1: The entrance length for a pipe inlet Z_e as determined by various authors.

Author	Z_e
Boussinesq (1891)	0.26
Schiller (1922)	0.115
Atkinson & Goldstein (1938)	0.260
Langhaar (1942)	0.227
Hornbeck (1963)	0.226
Campbell & Slattery (1963)	0.244
Mohanty & Asthana (1978)	0.184
da Silva (1990)	0.233
Present	0.221

The authors shown in the table all made various simplifying assumptions about the pipe inlet flow, and this is reflected in the discrepancies shown between their results. For instance, Schiller (1922) and Mohanty & Asthana (1978) both restricted the profile shape, and this probably resulted in their results both showing a shorter inlet length. In contrast, the greater length of Campbell & Slattery (1963) reflects the suppression of boundary layer development caused by their flat-core assumption. The closeness of the well-accepted Hornbeck (1963) analysis to the present analysis a good indication of the accuracy of his inlet model.

The entrance length for the current investigation was obtained at a solution order of 60×60. The solution was found to be invariant at this order to 9 significant figures. This was ascertained by increasing the solution order to

15.2.4 Velocity profile shape parameter

The variation of Moss' (1985) shape parameter S with time is shown for the various values of acceleration parameter in figure 15.7. This relation is given as

$$S = 2\frac{\tau_w R}{\mu U_m} = -2\left.\frac{du}{dr}\right|_{r=1}. \tag{15.5}$$

At $t = 0$ the shape parameter for each value of the acceleration parameter is infinite (the 'top-hat' limit). As time increases, the value of S for each run successively diminishes until each reaches a fixed value which it maintains for all time. In keeping with the observation made for the velocity profiles, this final value of $S = S_\infty$ increases with Ω. However, the *rate* of increase of S_∞ decreases as the acceleration parameter goes up, raising the possibility that the behaviour of the system might be bounded in some way as $\Omega \to \infty$. Unfortunately, the final value of $\Omega = 70$ is too low to infer the value of any such limit if it does exist. It is also unlikely that S has a finite limit for an infinite acceleration, in that this parameter generally shows unbounded behaviour, for instance as $t \to 0$. Discussion of limiting behaviour will thus be deferred until the next section, when the more useful scaled shape parameter is considered.

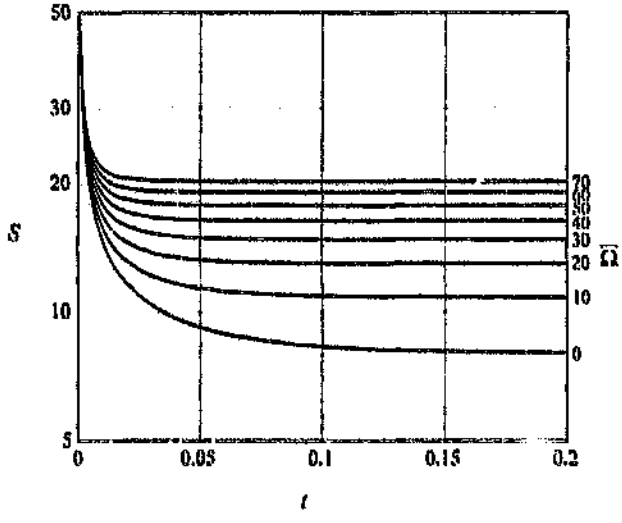

Figure 15.7: The variation of shape parameter S with time t in parallel exponentially accelerating pipe flow, for varying values of the acceleration parameter Ω.

Table 15.1: The variation of the final displacement thickness δ_∞^*/R with acceleration parameter Ω, given to 9 significant figures.

Ω	δ_∞^*/R	Ω	δ_∞^*/R
0	0.250 000 000	40	0.141 042 691
10	0.207 158 883	50	0.128 940 358
20	0.177 773 361	60	0.119 323 508
30	0.156 727 933	70	0.111 489 926

final value to the exact result was then determined by increasing the solution order N, and observing which figures of the decimal representation remained invariant. In this way, the values in the table were determined to be correct to the 9 significant figures given there.

15.2.3 Velocity profiles

The extrapolation to $t = \infty$ resulted in a series of final velocity profiles - one for each value of Ω, and these are given in figure 15.6. Immediately evident is the reduction in the centreline velocity as the acceleration parameter is increased, consistent with the decrease in displacement thickness. For the highest acceleration considered ($\Omega = 70$), the flow can be well approximated by a core-flow/boundary layer type system. These velocity profiles also show an increase in the wall shear stress with increasing acceleration, qualitatively explainable from a simple Newtonian force balance consideration.

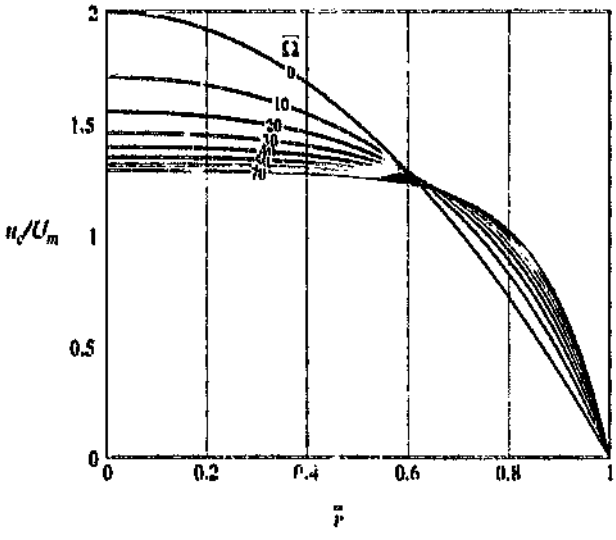

Figure 15.6: The variation of velocity profiles at $t = \infty$, with acceleration parameter Ω in parallel exponentially accelerating pipe flow.

the displacement thickness. This is consistent with the decrease in centreline velocity shown in figure 15.2, and is also in agreement with the results of Moss (1991), who observed the same trend.

The particular value of acceleration parameter at which the boundary layers fall to merge could not be determined in the present study, primarily because the boundary layer thickness is a meaningless criterion in pipe flows[3]. The change in behaviour observed by Moss (1991) at this 'critical' acceleration was in fact an artefact of the very assumption of a well defined value for δ. The more mathematically rigorous nature of the current numerical system shows only a smooth change in the flow as the acceleration increases, without any discontinuous behaviour. Arising from the variation of the displacement thickness δ^*/R with time, a relationship can be given between the value of δ^*/R as $t \to \infty$, and the acceleration parameter. This variation is shown in figure 15.5, and in table 15.1.

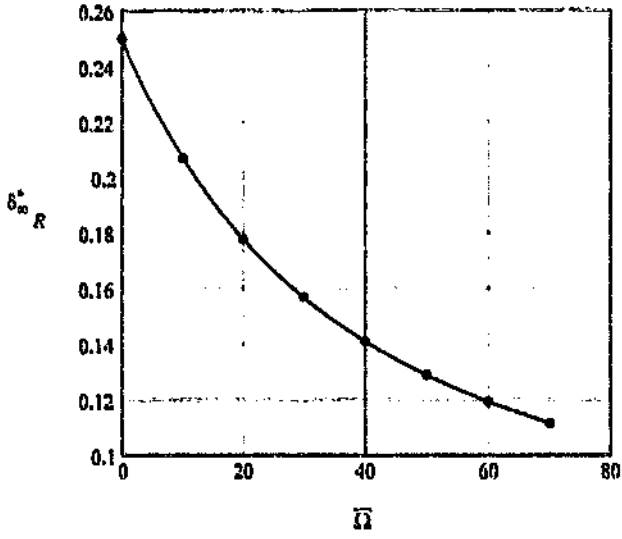

Figure 15.5: The variation of displacement thickness as $t \to \infty$, δ^*_∞/R, with acceleration parameter Ω in a parallel exponentially accelerating pipe flow.

The values for this parameter were generated by allowing the models to run toward $t \to \infty$ by successively increasing the time step in the numerical system. The resultant velocity profiles were thus ascertained (for a particular N) to the level of the round-off error ($\approx 10^{-11}$). The absolute convergence of the

[3]The boundary layer thickness δ is usually taken as that distance away from a surface at which the local velocity attains 99% of the free-stream value. In pipe flows, there is no proper way in which any part of the velocity field can be designated as free-stream flow, except in the limit as the boundary layer is very thin (and the centreline velocity can be meaningfully understood as the mean velocity of the core flow). For this reason, use is made in the current study of the mathematically precise criterion - the displacement thickness - as a measurement of the boundary-layer dimension.

Figure 15.3 shows a clear reduction in T_t with increasing exponential acceleration; thus, for the higher accelerations, the flow development time is reduced substantially when compared to the impulsive case. For the highest acceleration considered here ($\Omega = 70$), the development time is approximately 5 times shorter than for impulsive flow. This ratio of time scales is also reflected exactly in the physical system, because the dimensionless time parameter t_0 does not scale with the Reynolds number.

15.2.2 Displacement thickness

The dimensionless displacement thickness δ^*/R is directly derivable from the dimensionless centreline velocity u_c/U_m. Its definition - equation (13.59) - is repeated below for clarity:

$$\frac{\delta^*}{R} = \frac{1}{2}\left(1 - \frac{U_m}{u_c}\right). \tag{15.4}$$

The variation of δ^*/R with t is shown in figure 15.4 for the various values of the acceleration parameter Ω.

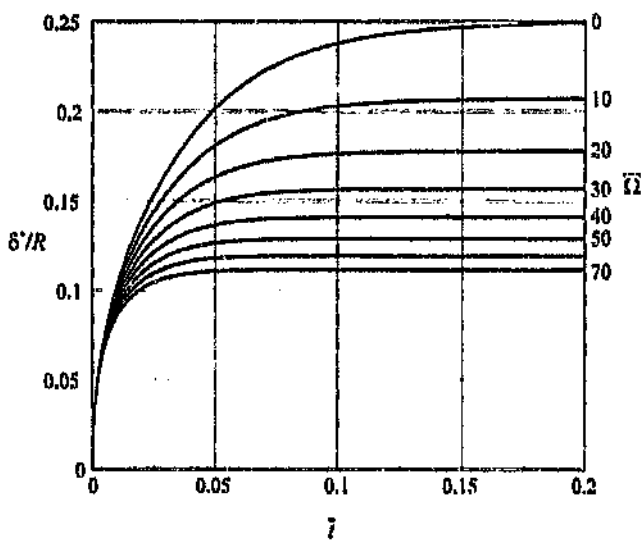

Figure 15.4: The variation of displacement thickness with time in parallel exponentially accelerating pipe flow, for various values of the acceleration parameter Ω.

For all the accelerative cases, this parameter starts at zero, corresponding to the initial 'top-hat' velocity profile. However, for increasing values of Ω, the value of δ^*/R in the far-time limit asymptotes to successively lower values of

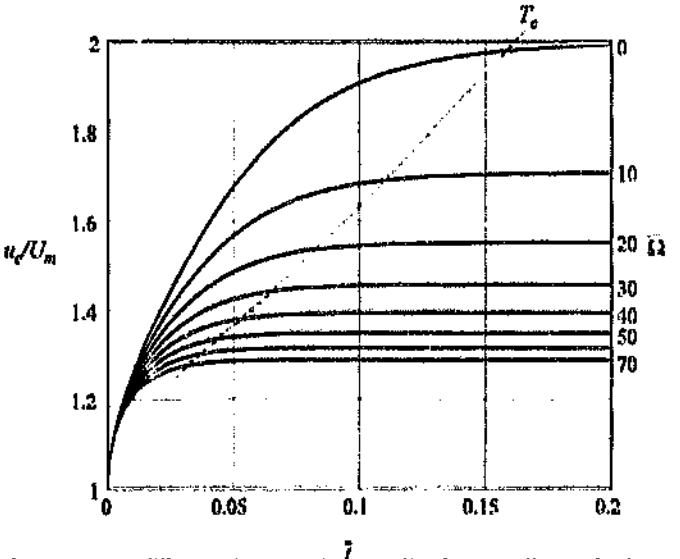

Figure 15.2: The variation of normalised centreline velocity u_c/U_m with time in parallel exponentially accelerating pipe flow, for various values of $\bar{\Omega}$. Also shown is the entrance-time T_e for each acceleration.

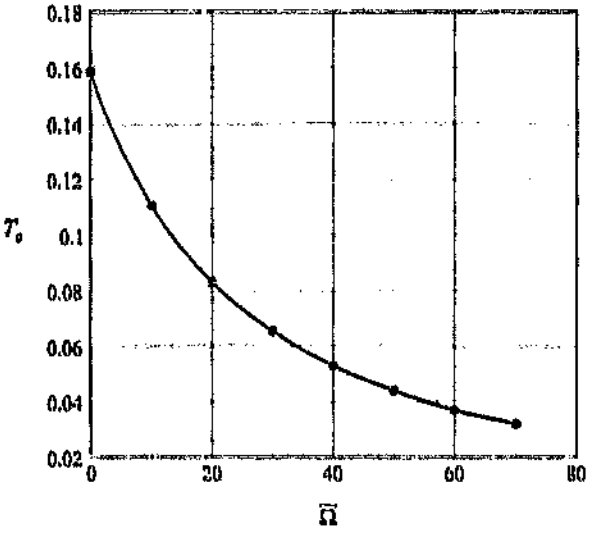

Figure 15.3: The variation of the entrance time T_e for parallel exponentially accelerating pipe flow, for various values of the acceleration parameter $\bar{\Omega}$.

and quantified the acceleration using a pressure-gradient parameter, which he denoted λ. The form of this term is identical to the acceleration parameter Ω. Moss showed that above a certain rate of acceleration the boundary layers in the system would not merge at all, and the flow would retain a 'core' region for all time. For increasing acceleration parameter, he showed a successive decrease in both the final centreline velocity and boundary layer thickness, and an increase in the shape parameter, all consistent with the presence of the acceleration. However, his characterisation using the boundary-layer thickness δ, led to the artificial distinction between flows in which the boundary layer had merged and flows in which it had not. In reality, the boundary layer thickness is only valid as a parameter in pipe flow in the limit as $\delta \to 0$). As a result of this, he falsely identified two modes of behaviour, separated by that value of the acceleration parameter where the edge of the boundary layer coincides with the centreline. The present solution was obtained using the full algorithm from the previous chapter, by simply setting the non-linear terms to zero. An optimised Matlab script for this was developed, `base1d.m`, and this can be found in appendix D (section D.3). The time-step and order here were identical to those used to obtain the results in section 13.2, namely $\Delta t = 1 \times 10^{-5}$ and $N = 60$; however, for the very high accelerations, the order of discretisation was increased to $N = 100$. A presentation of the data for the parallel temporal case follows.

15.2.1 Centreline velocity and entrance time

The variation of the centreline velocity with time t within the parallel flow, for the various values of acceleration parameter, is shown in figure 15.2 below. Also shown on this figure is the dimensionless entrance time. The entrance time is analogous to the inlet length [given as (14.37)], and is defined as the time taken for the centreline velocity to develop to 99% of its steady-state value; in other words with $u = \bar{u}(\bar{r},\bar{t})$,

$$T_e = [t \mid \bar{u}(0,t) = 0.99\,\bar{u}(0,\infty)]. \tag{15.3}$$

In all cases, the flow is started impulsively from rest. Therefore at $t = 0$ the velocity profiles for each acceleration reduce to 'top-hat', with $u_c/U_m = 1$. In the limit as $\bar{t} \to \infty$, the centreline variations for the different accelerations converge to successively lower values of u_c/U_m as the acceleration is increased. Thus the direct effect of the acceleration is to lower the normalised centreline velocity, implying a thinning of the boundary layer with increasing Ω. This is in agreement qualitatively with the simplified model of Moss (1991). As can be seen, the entrance time decreases markedly with increasing acceleration parameter, indicating that the flow develops more rapidly for increasing values of the acceleration parameter. In order to quantify this effect, the variation of the entrance time T_e with Ω is given in figure 15.3.

approximations, thus the acceleration parameter could have arbitrary temporal dependence. It so happens that the chosen form of flow to be investigated was the exponential case. These specific types of flows are described by maintaining a constant value for Ω. Thus equation (15.1) does *not* define the acceleration parameter in general: it is only valid for exponential flows. A less confusing way of stating the flow variation is rather to give it as

$$Q = Q_0 \exp kt,$$

where the constant k happens to assume the value of Ω (also constant) in this particular case of exponentially varying flows.

15.2 The far-downstream flow

The far-downstream flow is that flow which occurs at axial positions a sufficiently distance downstream of the pipe inlet. It is characterised by its parallel nature, that is, its lack of axial dependence. Because the flow is strictly parallel, the radial component of velocity is zero, and the non-linear terms of the of the governing equation (14.3) vanish. The continuity requirement becomes redundant, and the system reduces to a linear initial value problem. The parallel flow shows no axial dependence; thus the resulting axial velocity is a function of r and t alone. This simplified form of the equation is as follows:

$$\frac{\partial \bar{u}}{\partial t} + \bar{\Omega}(\bar{u} - 1) = -2 \left.\frac{\partial \bar{u}}{\partial \bar{r}}\right|_{r=1} + \frac{1}{r}\frac{\partial}{\partial r}\left(r\frac{\partial \bar{u}}{\partial r}\right). \tag{15.2}$$

This exact system was solved in section 13.2 for the limiting case of zero acceleration parameter (impulsive flow), but the more general exponentially increasing flow is considered here. The value of Ω was increased in steps of 10 from 0 to 70, in order to generate data describing the effect of increasing exponential acceleration. Of primary interest here is the limiting behaviour of this flow system, both at early times, and as $t \to \infty$. The parallel far-downstream flow is considered here first because its lack of x dependence eliminates the Reynolds number dependent axial scaling that occurs between the dimensionless and physical coordinate systems, and thus allows a simpler interpretation of results.

The only existing work of direct relevance is that by Moss (1991). He solved a similar accelerating system for parallel pipe flow, using a simple momentum-integral approach. His formulation was, however, flawed in that the treatment of the pressure term was incorrect. Despite this, and regardless of the simplicity of the approach, the results yielded were qualitatively correct and of considerable interest. He concluded that an exponential acceleration would cause the flow system to converge to a limit other than the well known Poiseuille flow,

The development of the displacement thickness both for the parallel temporally developing system, and for the steady state entrance flow, are presented in the final section of this chapter. The current chapter is concerned with the laminar development of the pipe flow, and consideration of its instability is deferred to the following two chapters.

15.1 Flowrate variation

All the exponential accelerations considered here are generalisations of the steady impulsively started flow. In all cases the flow is started from rest impulsively and then accelerated exponentially. Figure 15.1 shows the various flowrate variations for the different tests.

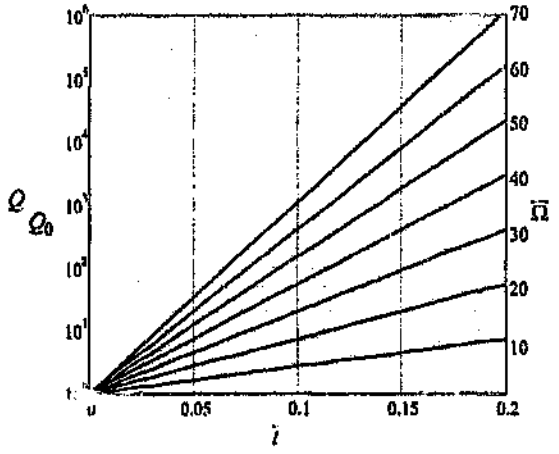

Figure 15.1: The variation of normalised flowrate Q/Q_0 with time in exponentially accelerating pipe flow, for various values of the acceleration parameter Ω.

Eight different flows (including the impulsive limit) were considered in all. The vertical axis in this graph denotes the flowrate, normalised with respect to its initial value[1]. The curves in figure 15.1 are each of the form

$$Q = Q_0 \exp \Omega_i t, \tag{15.1}$$

where Ω_i is simply the particular value of the acceleration parameter for each test. A point of potential confusion needs to be cleared up here. Throughout the earlier analysis, no restriction whatsoever was placed on the temporal dependence of Ω. All derivations - base flow and stability - contained no steady

[1]The governing equation (15.2) is Reynolds number independent; therefore the numerical model represents a system with any chosen flowrate. It is rather the nature of the flowrate change with time that is important.

Chapter 15

Exponentially accelerating pipe flows

A spectral numerical method was formulated in chapter 14 for generally accelerating pipe entrance flows, but was used there only to obtain results for the limiting steady flow case. In this chapter, the identical formulation is used to generate results for exponentially accelerating flows both far downstream and in the entrance. The exponential acceleration is modelled by making the acceleration parameter Ω a constant, and results are presented for eight different cases, namely, $\Omega \in \{0, 10, 20, \cdots, 70\}$. This range of acceleration parameters was chosen because it adequately embraced the accelerations used in the experimental measurements.

Results for this numerical system are presented directly, for the reason that both the numerical method and mathematical derivation of the system are adequately covered in previous chapters. The reader is referred both to section 14.1 and to chapter 13 for comprehensive descriptions of both the method of formulation and solution. The flows here are all impulsively started at time $\tilde{t} = 0$; thereafter they are allowed to develop exponentially in time. The following aspects of these flows are addressed in the sections that follow:

(i) The initial temporal development of the flow far downstream of the inlet.

(ii) The spatial structure of the flow field in the entrance region of the pipe, in the limit as $\tilde{t} \to \infty$.

(iii) The full temporal and spatial development of the flow away from the initial conditions, and the comparison of these results to the simpler two limiting cases mentioned above.

(iv) The relationship between the data in the non-dimensional system and the dimensional (physical) system, and the effect of the Reynolds number dependent mapping between the two.

(v) The large discrepancy between the temporal and spatial profiles towards the limit of decreasing boundary-layer thickness does *not* allow them both to be quantified using a single parameter as was stated by da Silva (1990); especially for the range of displacement thickness where the flow is most unstable. At least a two-parameter classification - using the displacement thickness δ^* and scaled shape parameter S_{δ^*} - is necessary to classify the full system. As the Hagen-Poiseuille limit is approached, the two sets of profiles become similar.

(vi) The spatial accuracy of the system has been computed to at least 8 significant figures, while temporal invariance was significantly lower at 4 significant figures, as demonstrated by the parallel system in section 13.2. However the spatial results presented here are unaffected by the lower temporal accuracy because they are taken as the limit as $\bar{t} \to \infty$.

This chapter concludes the comparison of the present data with known results. The following chapter presents the novel solutions for the exponentially accelerating pipe entrance system.

chapter, namely an matrix assembly approach. The operational approach is successfully applied to the collocation method, allowing it to be incorporated uniformly into the scheme. The temporal discretisation of the system is given in an as general a way as possible, and is implemented as implicit for the linear terms and explicit for the non-linear ones.

(ii) Results are generated for the case of steady pipe inlet flow. The present entrance model shows fair agreement with existing results when compared on the strength of the entrance length, but the large deviation between the existing values is taken as an indication of the inadequacy of that parameter as a point of comparison. The present results are quite close to the simplified but accepted results of Hornbe (1963). Comparison to the values of da Silva (1990) show a slight disparity that is thought to be due to his use of the invalid upwinding methodology in his finite-difference calculations. The comparison to da Silva's parallel temporally developing (far downstream) model shows better agreement, due to the absence of upwinding here.

(iii) The pipe flow is shown to approach the Blasius boundary layer limit toward the inlet, which allows some very important conclusions to be drawn regarding the non-parallel nature of pipe entrance flow. As the axial station $\bar{x}$ increases from zero, the boundary layer flow becomes less like a flat-plate boundary layer, until a parabolic profile is eventually attained. In the same way, the non-parallel nature of the entrance flow decreases monotonically from the *most* non-parallel Blasius limit at the inlet, to completely parallel flow far downstream. Thus the flow is never any *more* non-parallel than a flat plate boundary layer, and quickly becomes less so. This infers that a parallel stability analysis is a valid method of approximating the initiation of instability in pipe entrance flows. It has been shown that non-parallel effects do *not* play an important role in flat plate boundary layer stability [Fasel & Konzelmann (1990), Gaster (1974), Abbot & Moss (1994)][6]. Pipe entrance flows are more parallel than flat plate flows. This implies that a parallel stability analysis is valid for such flows. A direct measure of the non-parallel nature of the pipe inlet showed this conclusion to be valid. This is consistent with the conclusions of da Silva & Moss (1994), who also argued that non-parallel effects in a pipe inlet are negligible.

(iv) In the limit of decr boundary layer thickness, both the entrance and the parallel sys ave asymptotically as boundary layers with zero pressure gradient. ough the actual pressure gradient increases with decreasing boundar -layer thickness in each case, this gradient scaled with respect to the boundary layer parameters diminishes as the boundary layer thins.

[6]Fasel & Konzelmann, by direct numerical experiment, discredit the many analyses that show non-parallel effects to be dominant in boundary layer flows, giving the work of Gaster (1974) as the only valid analysis. Gaster obtained a non-parallel minimum critical Reynolds number of only 480, a small reduction when compared to $Re = 520$ of the parallel system.

chapter, namely an matrix assembly approach. The operational approach is successfully applied to the collocation method, allowing it to be incorporated uniformly into the scheme. The temporal discretisation of the system is given in an as general a way as possible, and is implemented as implicit for the linear terms and explicit for the non-linear ones.

(ii) Results are generated for the case of steady pipe inlet flow. The present entrance model shows fair agreement with existing results when compared on the strength of the entrance length, but the large d[illegible] between the existing values is taken as an indication of the in[illegible]qu[illegible] of that parameter as a point of comparison. The present resul[illegible]e close to the simplified but accepted results of Hornbeck (1963). Comparison to the values of da Silva (1990) show a slight disparity that is thought to be due to his use of the invalid upwinding methodology in his finite-difference calculations. The comparison to da Silva's parallel temporally developing (far downstream) model shows better agreement, due to the absence of upwinding here.

(iii) The pipe flow is shown to approach the Blasius boundary layer limit toward the inlet, which allows some very important conclusions to be drawn regarding the non-parallel nature of pipe entrance flow. As the axial station $\bar{x}$ increases from zero, the boundary layer flow becomes less like a flat-plate boundary layer, until a parabolic profile is eventually attained. In the same way, the non-parallel nature of the entrance flow decreases monotonically from the *most* non-parallel Blasius limit at the inlet, to completely parallel flow far downstream. Thus the flow is never any *more* non-parallel than a flat plate boundary layer, and quickly becomes less so. This infers that a parallel stability analysis is a valid method of approximating the initiation of instability in pipe entrance flows. It has been shown that non-parallel effects do *not* play an important role in flat plate boundary layer stability [Fasel & Konzelmann (1990), Gaster (1974), Abbot & Moss (1994)][6]. Pipe entrance flows are more parallel than flat plate flows. This implies that a parallel stability analysis is valid for such flows. A direct measure of the non-parallel nature of the pipe inlet showed this conclusion to be valid. This is consistent with the conclusions of da Silva & Moss (1994), who also argued that non-parallel effects in a pipe inlet are negligible.

(iv) In the limit of decreasing boundary layer thickness, both the entrance and the parallel systems behave asymptotically as boundary layers with zero pressure gradient. Although the actual pressure gradient increases with decreasing boundary-layer thickness in each case, this gradient scaled with respect to the boundary layer parameters diminishes as the boundary layer thins.

[6] Fasel & Konzelmann, by direct numerical experiment, discredit the many analyses that show non-parallel effects to be dominant in boundary layer flows, giving the work of Gaster (1974) as the only valid analysis. Gaster obtained a non-parallel minimum critical Reynolds number of only 480, a small reduction when compared to $Re = 520$ of the parallel system.

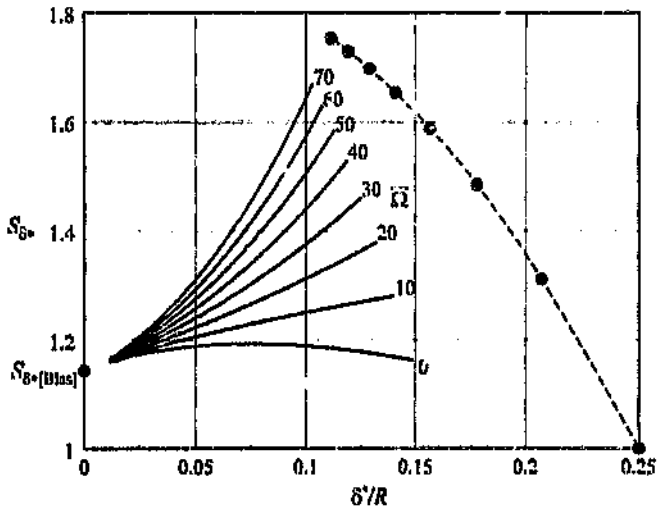

Figure 15.15: The variation of scaled shape parameter S_{δ^*} with displacement thickness δ^*/R in the entrance region of a pipe, for various values of the acceleration parameter $\bar{\Omega}$. The dashed line indicates the locus of limiting values for $\bar{x} = \infty$.

of final points ($\bar{x} \to \infty$), while the dots on this line are the specific limiting points corresponding to successive values of the acceleration parameter. Due to the limited range taken for $\bar{x}$, the trajectories for each Ω stop a short way from their final limit; however as mentioned in the preamble to this section, it is trivial to demonstrate that these points are in fact the true limits of the system[7].

15.3.6 Comparison between the limiting temporal and spatial results

The similarities and discrepancies evident between the temporal and spatial systems are of major interest. Both systems, for the same value of acceleration parameter, have the same steady-state limits, that is, as $x \to \infty$ and $t \to \infty$. Furthermore, the developing (early time) entrance flow will consist of two regions: a non-parallel upstream regime where there is spatial development of the boundary layer, and a downstream portion where the influence of the inlet has not yet been felt. The ideal framework for the comparison between the parallel and entrance results is again the δ^*/R - S_{δ^*} plane. Figure 15.16 shows the full temporal and spatial results and their limiting values for all the accelerations given.

[7]These points correspond to $x = \infty$, where the flow is formally parallel; therefore the parallel steady-state limit is appropriate here.

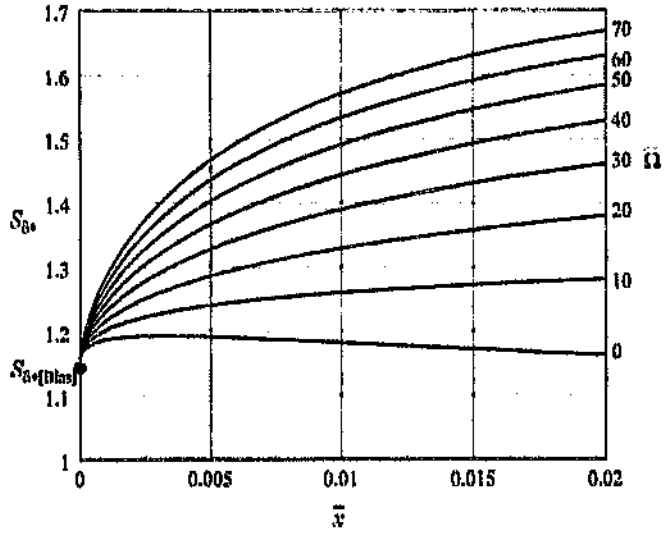

Figure 15.14: The variation of scaled shape parameter S_{δ^*} with axial position $\bar{x}$ in the entrance region of a pipe, for various values of the acceleration parameter $\bar{\Omega}$.

accelerations. The data in the far limit again approach their far-time values, but due to the restricted axial solution domain are not extensive enough to reach this limit. Despite this, the data does show much of the behaviour for increasing $\bar{x}$. As in the parallel data, the impulsive ($\bar{\Omega} = 0$) case is inflexional, with S_{δ^*} first increasing and then decreasing with $\bar{x}$. For the larger accelerations considered, however, S_{δ^*} increases monotonically from the Blasius limit to the higher steady-state value. The $\bar{x}$ ordinate is rather inappropriate for the demonstration of downstream behaviour (because this limit is only truly reached as $\bar{x} \to \infty$). To eliminate the unboundedness, the data is now considered in the δ^*/R - S_{δ^*} plane; this is given in figure 15.15.

The data for the impulsive case given in chapter 14, combined with the parallel developing flow section earlier in this chapter both showed the δ^*/R - S_{δ^*} framework to be optimal in that *both* upstream and downstream behaviours map to discrete points on this plane. Therefore the entire flow variation (for a particular set of parameters) is described by a single line leading from the start point to the point corresponding to the final state of the flow. Further to this, the data shown in this way is strongly distinguished from data generated with other values of the parameters; for instance, the lines for different acceleration parameters $\bar{\Omega}$ are clearly distinct.

As in the previous figure, all of the curves are unambiguously directed towards the point $[0, S_{\delta^*[\mathrm{erf}]}]$. This trend is far clearer here than previously, due to the advantageous scaling effect that the ordinate δ^*/R shows. The dotted line in figure 15.15, as in the impulsive case of the previous section, indicates the locus

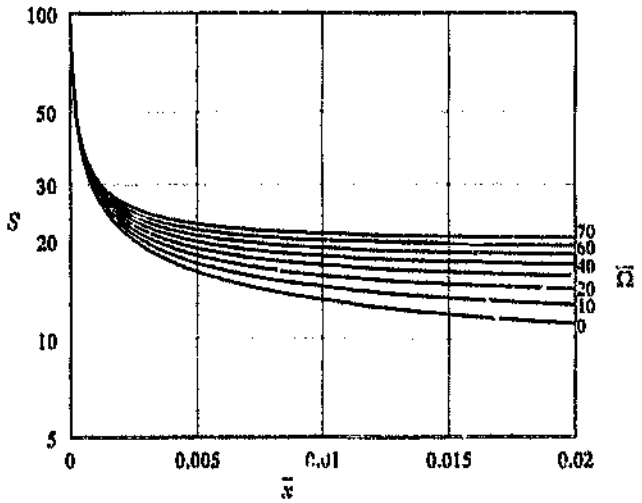

Figure 15.13: The variation of shape parameter S with axial position x in the entrance region of a pipe, for various values of the acceleration parameter $\bar{\Omega}$.

As before, the downstream limiting values are described by the data from the previous section. The final value of S increases with increasing acceleration. All the data approach $S = \infty$ at the inlet, because the wall shear stress approaches infinity here. This figure again emphasises the deficiency in S as a parameter towards the inlet, because of its unbounded behaviour as $\bar{x} \to 0$. However, away from the inlet plane it becomes a useful for the quantification of velocity profile behaviour.

15.3.5 Scaled shape parameter

The scaled shape parameter has been defined in section 13.2 of chapter 13, and is given there by the equation (13.62), namely

$$S_{\delta^*} = \frac{\delta^*}{R}\frac{U_m}{u_c}S, \tag{15.13}$$

Its variation with axial position x in the range $[0, 0.02]$ is shown in figure 15.14.

This parameter is the first to highlight any structure in the flow as $x \to 0$. It was shown in the impulsive solution of chapter 14 that the limiting behaviour towards the inlet of the steady-state pipe entrance flow was the Blasius boundary layer-like. To this end, the value of $S_{\delta^*[\mathrm{Blas}]} = 1.143$ [first given in (13.98)] is shown on the figure. Immediately evident here is that all the data are convergent on this point. Thus as in the temporal case, the effect of the acceleration diminishes as the boundary layer thins, and a single upstream asymptote is present for all

The variation of this parameter with axial displacement $\bar{x}$, for the chosen values of $\bar{\Omega}$, is shown in figure 15.12.

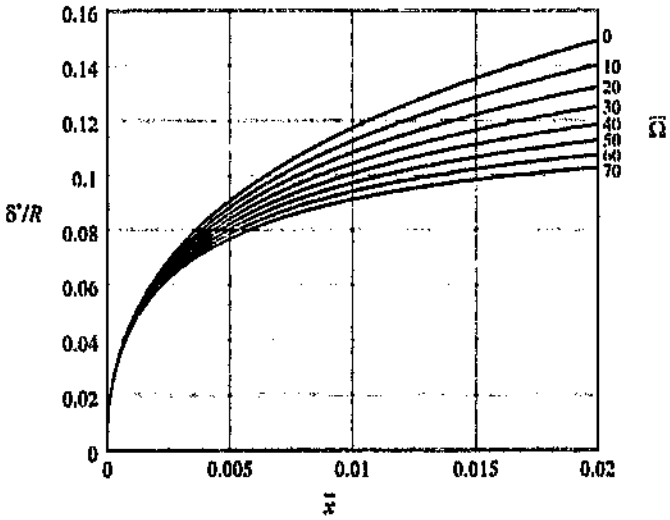

Figure 15.12: The variation of displacement thickness δ^*/R with axial position $\bar{x}$ in the entrance region of a pipe, for the chosen values of $\bar{\Omega}$.

As with the impulsive case, the boundary layer displacement thickness is zero at $\bar{x} = 0$ corresponding to the 'top-hat' profile there. As $\bar{x}$ increases, the value of δ^*/R for the various accelerations $\bar{\Omega}$ increase towards their respective far-time asymptotic limits as given in the previous section [see figure 15.4]. Again, the current axial solution domain is too short to indicate properly the downstream behaviour. As can be seen, the effect of the acceleration is to reduce everywhere the displacement thickness from that of its impulsive value. This result is in keeping with the behaviour of δ^*/R shown in the parallel flow. As has been mentioned before, the displacement thickness is used as a quantification of the boundary layer dimension in the system. This term is preferred because the simpler boundary layer thickness term δ is meaningless in a pipe system with any significant boundary layer size. The definition of the displacement thickness is given by equation (15.12). Although the strict physical interpretation of this term may diminish with increasing boundary layer thickness in a pipe, it maintains a mathematically exact meaning throughout the system, in its evolution from 'top-hat' to parabolic.

15.3.4 Velocity profile shape parameter

Figure 15.13 represents the variation of velocity profile shape parameter with axial distance. For all the accelerations, this parameter decreases from infinity at the inlet to some fixed value far downstream.

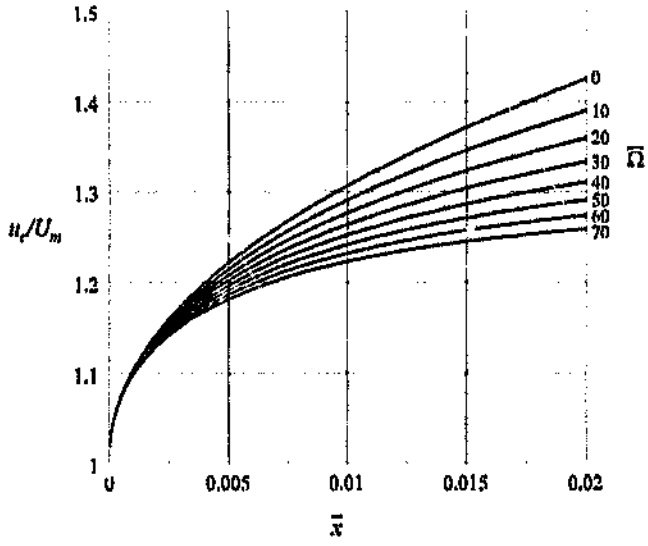

Figure 15.11: The variation of normalised centreline velocity u_c/U_m with axial distance $\bar{x}$, in the entrance region of a pipe, for various values of the acceleration parameter $\bar{\Omega}$.

time was defined, which diminished with increasing acceleration. An entrance length could be defined for each exponential data set given here. However, such a parameter in reality has little meaning. It cannot be used as before as a point of comparison (no other data exists), neither is it really useful in itself, because in dimensional physical terms, the entrance continues extending downstream anyway. The rate at which this extension occurs is linked to the Reynolds number, which in turn is a function of time. Thus the only real bounding parameter of use in the accelerative case is the entrance time. A calculation of the entrance length for the general case will, however, show a reduction in length (in the normalised framework) with increasing acceleration parameter. The short axial extent of the present model (optimised for the linear stability analysis later) prevented the direct determination of the entrance length for the non-zero accelerations. Calculations would have to be conducted over a larger domain to determine this parameter.

15.3.3 Displacement thickness

As before, the displacement thickness depends directly on the dimensionless centreline velocity; its definition is given by equation (13.59), repeated below:

$$\frac{\delta^*}{R} = \frac{1}{2}\left(1 - \frac{U_m}{u_c}\right). \tag{15.12}$$

step Δt used was initially $\Delta t = 2 \times 10^{-7}$, but this was increased as the steady-state limit was approached. Solution was continued until the solution remained invariant to the level of the round-off and truncation errors (approximately 10^{-14}). The solution became independent of Δt in the far limit; thus its accuracy was unaffected by the low order temporal discretisation.

The solution domain $x \in [0, 0.02]$ concerns only a small portion of the pipe entrance in comparison to the definition of *entrance length* [equation (14.37)]; however this small region embraces the entire portion of the pipe inlet that can show infinitesimal instabilities [see Abbot & Moss (1991) for the case of steady entrance flow]. It was for this reason that the calculations were not extended further downstream. Beyond this region the temporal and spatial systems approach each other closely, and this equivalence obviously becomes exact at $x = \infty$ in the steady-state. The current data is thus not extensive enough to demonstrate formally the limiting behaviour as $x \to \infty$. However, this behaviour has been properly given for the impulsive case in chapter 14, and the extension of these results to the exponential case is trivial. The unqualified far downstream limits for the flows here are thus taken as being the far-time solutions of the parallel flows in the previous section (section 15.2), and these values are shown in the various figures that follow.

As with the impulsive pipe inlet solution of chapter 14, the inlet boundary conditions are not taken as being 'top-hat', but rather a very thin boundary layer velocity profile (the same profile as was used there) is implemented. The reason for this, as described in detail in that chapter, is to prevent oscillations in the solution introduced by the presence of the singularity in the 'top-hat' condition. It was shown that the solution becomes rapidly independent of the choice of inlet condition only a short distance downstream of the inlet plane.

15.3.2 Centreline variation

The variation of the dimensionless centreline velocity u_c/U'_m with axial distance x is a simple means of describing an entrance flow, and this is shown for all the different values of Ω in figure 15.11. The value of u_c/U'_m in each case develops from a value of unity at $x = 0$ to its far-downstream steady-state value - determined in the parallel analysis of the previous section. Due to the short axial solution domain, the downstream limiting behaviour is not evident in this figure. See section 15.3.1 above for more detail on this point.

A factor concerned with the centreline velocity variation in x is the entrance length - that distance taken for the centreline velocity to approach 99% of its far-downstream value. This quantity was calculated in chapter 14 for the impulsive flow, and was compared to the results of other researchers. Its value for the impulsive case is given by the relation (14.37), and was $Z_e = 0.221$. The concept of the entrance length was also extended in the previous section of this chapter, in the context of the results for the parallel flow. Here an analogous *entrance*

shape, and subsequent axial profiles evolve from this profile to the parabolic Hagen-Poiseuille limit as $\tilde{x} \to \infty$. The equivalent occurs in exponential pipe flows in the far time limit (considered of course in the normalised framework). Here, for a particular value of Ω, the flow field develops from a 'top-hat' profile at the inlet plane, to an invariant profile sufficiently far downstream. However, in this case, the far downstream limit is *not* the simple Hagen-Poiseuille profile, but rather the corresponding limiting parallel velocity profile, as shown in figure 15.6.

Of course the far-time limit defines only the final state of the flow. An initially impulsively started exponential flow will pass through a number of intermediate phases as the influence of the inlet convects and diffuses downstream. It will, however, be shown in the following section (section 15.4) that the two asymptotic limiting behaviours - parallel temporal development, as described in section 15.2, and steady-state non-parallel flow, as described here - are extremely good approximations to most portions of the generally developing entrance flow; that is, these simpler solutions together embody most of the flow description for $\tilde{u}(\tilde{x},\tilde{r},t)$ and $\tilde{v}(\tilde{x},\tilde{r},t)$.

15.3.1 Method of solution

The current presentation of the data for steady-state exponentially accelerating pipe entrance flow is similar to that given in chapter 14 and in section 15.2 above. As before, the data is presented in successive states of interpretation. Results were generated for the range of acceleration parameters $\Omega \in \{0, 10, 20, 30, 40, 50, 60, 70\}$, with the impulsive flow included as a limiting value. The relevant equations for the present system are (10.33) and (10.34), which are repeated below:

$$\frac{\partial \tilde{u}}{\partial t} + \Omega(u-1) + \tilde{u}\frac{\partial \tilde{u}}{\partial \tilde{x}} + \tilde{v}\frac{\partial \tilde{u}}{\partial \tilde{r}} = 2\frac{\partial}{\partial \tilde{x}}\int_0^1 r\tilde{u}^2 dr - 2\left.\frac{\partial \tilde{u}}{\partial \tilde{r}}\right|_{\tilde{r}=1} + \frac{1}{\tilde{r}}\frac{\partial}{\partial \tilde{r}}\left(\tilde{r}\frac{\partial \tilde{u}}{\partial \tilde{r}}\right) \quad (15.10)$$

$$\frac{1}{\tilde{r}}\frac{\partial}{\partial \tilde{r}}(\tilde{r}\tilde{v}) + \frac{\partial \tilde{u}}{\partial \tilde{x}} = 0. \quad (15.11)$$

The numerical formulation of these equations was presented in chapter[6] 14. Solutions were generated here simply by choosing Ω to have successive values from the range chosen. That which follows is a systematic presentation of the results obtained.

The calculations were implemented for the axial domain $\tilde{x} \in [0, 0.02]$. The discretisations used to obtain these results were $N = 80$ for the radial Tau discretisation and $M = 80$ for the collocation axial implementation. The time

[6] The general, accelerative, numerical system was developed in that chapter, but only the impulsive case was solved there.

at the wall, or $S \to 2U/\delta = 2/\delta$, thus the scaled shape parameter is in this case given by

$$S_{\delta^*} = S \times \delta^* = 2\frac{\delta^*}{\delta} \to 2.$$

Numerically, the value seemed to be approaching 2 unambiguously. The highest acceleration investigated before numerical instability occurred was $\Omega = 500\,000$, for which the final value of S_{δ^*} was 1.9972.

The asymptotic bounds of the system, although primarily of academic interest, do allow important verification of the results obtained. Both limits require high precision for their accurate solution. Considering the error-function limit, the system converges to the correct value of S_{δ^*} at this point. Accurate determination of the data near this point implies that the data far from this limit is very accurate, since in general a far lower order system is required to solve the data away from the numerically 'highly stressed' limiting point. The high-acceleration asymptote is of a different nature in that it is more extrapolatory. Unlike the error-function limit for the flow at early times, the implied limiting value of 2 as $\Omega \to \infty$ had no rigorous theoretical basis.

15.3 The far-time entrance flow

An important limiting case for pipe flows near the inlet is the far-time limit - that is, the flow that persists after all the transients have died away. The far-time solution for impulsively started flow was obtained in chapter 14. The current section is concerned with the invariant limit of exponentially accelerating entrance flow. Invariance in this context has a different meaning to that in the impulsive case; whereas the impulsive entrance flow attains invariance in the physical co-ordinate system[5], the exponential flow appears to be constantly changing when viewed in the physical axial ordinate. However, this change is contained solely in the mapping between the physical and normalised systems; thus invariance in the exponential case means simply that the flow in the normalised co-ordinate system attains steady-state. The mapping between physical and normalised co-ordinate systems was introduced in chapter 10, and its effect in the context of the current system is given later in section 15.5.

Viewed from the normalised co-ordinate system, the exponential accelerating flow behaves in a manner analogous to the impulsive one of chapter 14, except for the normal effects of acceleration, such as suppression of boundary layer growth. In the steady impulsive, 'orter' case, the entrance flow converges to a steady-state configuration, in which the most upstream station has a 'top-hat'

[5]Remember there is a constant mapping between the dimensionless and physical co-ordinate systems for impulsive flows.

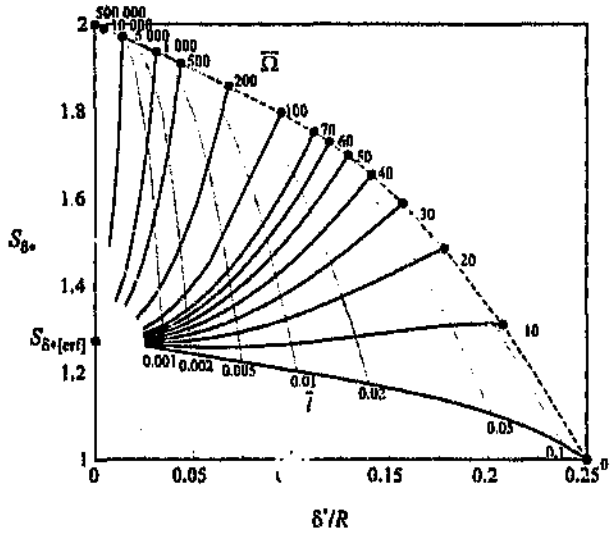

Figure 15.10: The variation of scaled shape parameter S_{δ^*} with displacement thickness δ^*/R in parallel exponentially accelerating pipe flow, for varying values of the acceleration parameter $\bar{\Omega}$: – – –, locus of limiting values as $\bar{t} \to \infty$ of $(\delta^*/R,\ S_{\delta^*})$; $S_{\delta^*[\mathrm{erf}]}$, parallel boundary-layer limit as $\bar{t} \to 0$; lines of constant-time are shown superimposed.

the acceleration term $\bar{\Omega}(\bar{u}-1)$, resulting in this limit being described by

$$\bar{u} = 1, \tag{15.8}$$

along with the no-slip wall conditions. The solution to this system is simply

$$\bar{u} = \begin{cases} 0 & \bar{r} = 1 \\ 1 & 0 \le \bar{r} < 1 \end{cases} \tag{15.9}$$

Since there is a discontinuity at the wall, the slope there is infinite. However, the scaled shape parameter can remain bounded, since the boundary layer displacement thickness also is zero. That the limiting value of S_{δ^*} is 2 can be shown by considering the velocity profile given by (15.9). The boundary layer thickness in this case is $\delta \to 0$. The displacement thickness is defined as that distance the boundary must be displaced to compensate for the presence of the wall; in this case[1], $\delta^* \to \delta$. The velocity profile shape parameter is given by twice the slope

[1]This assumption is subject to dispute, but is commensurate with the boundary line being described by a vertical line at the wall. The entire argument given here is rather informal, and a more rigorous proof is necessary.

The limit $S_{\delta^*[\mathrm{erf}]}$ is clearly shown on the left-hand side of this figure; the other limits ($\bar{t} \to \infty$) for the various values of $\bar{\Omega}$ constitute a locus [the dotted line] originating at the impulsive limit, and moving up and to the left for increasing values of acceleration. The usefulness of the δ^*/R - S_{δ^*} representation is again evident in this figure, in that it transforms all the data into a finite domain, while discriminating strongly between the different accelerative cases. Again, the points defining the $\bar{t} \to \infty$ locus seem to be approaching some finite value as the acceleration is increased. Leading from this inference, flows with substantially higher values of $\bar{\Omega}$ were investigated to deduce this limiting behaviour.

15.2.6 Limiting behaviour as $\bar{\Omega} \to \infty$

A simple extension of the data in figure 15.9 was made by increasing the value of $\bar{\Omega}$ to values of 500 000; these results are shown in figure 15.10. Also reproduced in this figure are lines of constant $\bar{t}$. In order to obtain the results for the very high acceleration cases, the order of solution had to be extended from the $N = 60$ used for the results below $\bar{\Omega} = 100$, to as high as $N = 120$ for $\bar{\Omega} = 500\,000$. Furthermore, the time step Δt of the solution had to be reduced to 10^{-5} (from the value of 5×10^{-4} used for the lower acceleration tests) in order to capture the extremely short time scale behaviour at the higher accelerations. For the highest acceleration case of $\bar{\Omega} = 500\,000$, only the final limiting point was stored, due to of the extremely quick development times at this acceleration.

It is clearly evident from the figure that the locus of the final values of the $(\delta^*/R, S_{\delta^*})$ pair with increasing $\bar{\Omega}$ are convergent on the point $(0, 2)$, while the time taken for the system to reach the far-time asymptote becomes rapidly shorter. Thus the limiting behaviour of the system as $\bar{\Omega} \to \infty$ can be inferred to be the *straight line segment* extending from $(0, S_{\delta^*[\mathrm{erf}]})$ to $(0, 2)$. The behaviour of S was, as anticipated, unbounded for increasing $\bar{\Omega}$. This limiting behaviour is evident in the differential governing equation (15.2). The behaviour as $\bar{t} \to 0$ is described by the relation

$$\frac{\partial \bar{u}}{\partial \bar{t}} = \frac{\partial^2 \bar{u}}{\partial \bar{y}^2}. \tag{15.7}$$

This can be formally shown by transforming the radial co-ordinate to a wall co-ordinate system and scaling it according to the displacement thickness, as $\bar{y} = (1 - \bar{r})R/\delta^*$. By neglecting all small terms, i.e. those containing coefficients of δ^*/R in the limit as $\delta^* \to 0$, the equation (15.7) results. This equation, along with the no-slip boundary conditions (as given in section 13.2) describes the flow field next to a flat plate impulsively started and moving parallel to its plane. This problem is self-similar and yields the error function solution [Schlichting (1979)]. The limiting equation applicable as $\bar{\Omega} \to \infty$ is even simpler to derive. Here all terms in equation (15.2) become negligible in comparison to

value diminishes. Interesting to note is that for accelerations above $\bar{\Omega} \approx 10$, the value of S_{δ^*} *increases* with time, while at a value of slightly below 10, it remains approximately constant[3]. Thus for the higher acceleration flows, the wall shear stress normalised to the boundary layer displacement thickness increases with time (unlike the impulsive case). Another interesting aspect shown is the rate of increase in $S_{\delta^*\infty}$ with $\bar{\Omega}$. As with S_{∞}, this value seems to not be increasing without bound, but rather approaching some finite value in the high acceleration limit. As mentioned previously, the highest value of $\bar{\Omega}$ for this set of data is only 70, not sufficient to determine limiting behaviour. Extended data is, however, presented in the next section, in order that this upper bounding value be ascertained.

It was shown in section 13.2 that an optimum, bounded, representation of the data is obtained if the scaled shape S_{δ^*} data is plotted versus the displacement thickness δ^*/R. In the case of impulsive flow, this framework reduces both limits of the data ($\bar{t} = 0$ and $\bar{t} \to \infty$) to finite points on the δ^*/R - S_{δ^*} plane, with $\bar{t} = 0$ corresponding to $(0, S_{\delta^*[\mathrm{erf}]})$ and $\bar{t} \to \infty$ to $(0.25, 1)$. The plot of the current data, for all the values of $\bar{\Omega}$ considered, is shown in figure 15.9.

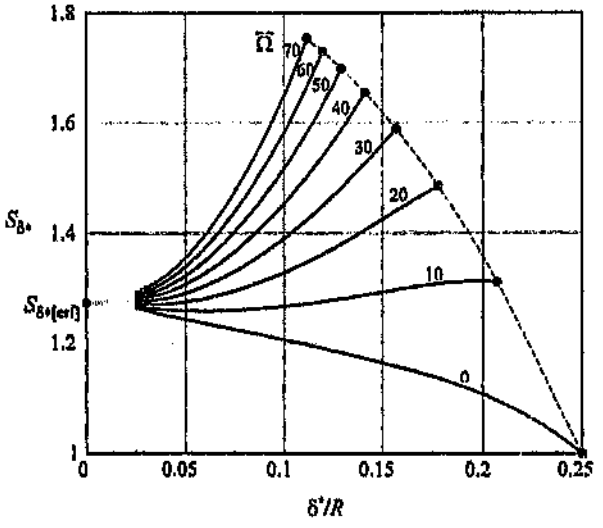

Figure 15.9: The variation of scaled shape parameter S_{δ^*} with displacement thickness δ^*/R in parallel exponentially accelerating pipe flow, for varying values of the acceleration parameter $\bar{\Omega}$: — — —, locus of limiting values as $\bar{t} \to \infty$; $S_{\delta^*[\mathrm{erf}]}$, parallel boundary-layer limit as $\bar{t} \to 0$.

[3]It is unlikely that the curve for any particular exponential acceleration will remain exactly constant for the entire flow development, as all curves show some inflexional behaviour near flow inception. No investigation was carried out to ascertain which value of $\bar{\Omega}$ would generate the curve showing the *most* constant behaviour, but this is likely to be that flow whose final value of S_{δ^*} is also equal to the error-function limit in value.

15.2.5 Scaled shape parameter

The scaled shape parameter S_{δ^*} is defined as S scaled with respect to δ^*/R and u_c; its formal definition is given by (13.62), which is repeated below:

$$\begin{aligned} S_{\delta^*} &= \frac{\tau_w \delta^*}{\mu u_c} \\ &= \frac{\delta^*}{R} \frac{U_m}{u_c} S. \end{aligned} \tag{15.6}$$

The variation of this parameter in time for different values of the acceleration parameter Ω, is shown in figure 15.8.

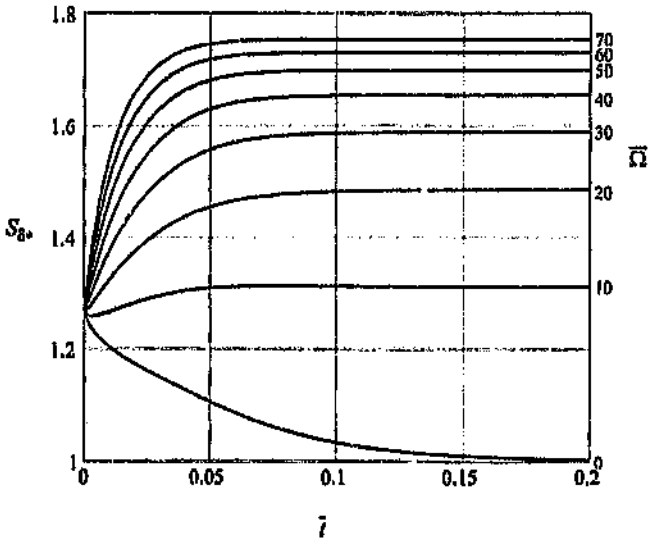

Figure 15.8: The variation of scaled shape parameter S_{δ^*} with time $\bar{t}$ in parallel exponentially accelerating pipe flow, for varying values of the acceleration parameter Ω.

At inception, the value of S_{δ^*} for each value of Ω tends toward the parallel boundary layer limit, namely $S_{\delta^*[\mathrm{erf}]} = 1.273$ as defined by (13.65). This is an important result, in that it shows that in the limit as $\delta^*/R \to 0$, the relative effect of the acceleration becomes insignificant, and that all the flows approach the error function boundary layer in structure, corresponding to the parallel flow over a flat plate instantaneously started from rest (see section 13.2). As time progresses, the values for S_{δ^*} for each Ω diverge from this value, and approach their respective far-time limits. For the impulsive case (the lowest curve), this limit is $S_{\delta^*,\infty} = 1$ as was given in section 13.2. As the acceleration parameter increases from zero, the final value increases, while the time taken to reach this

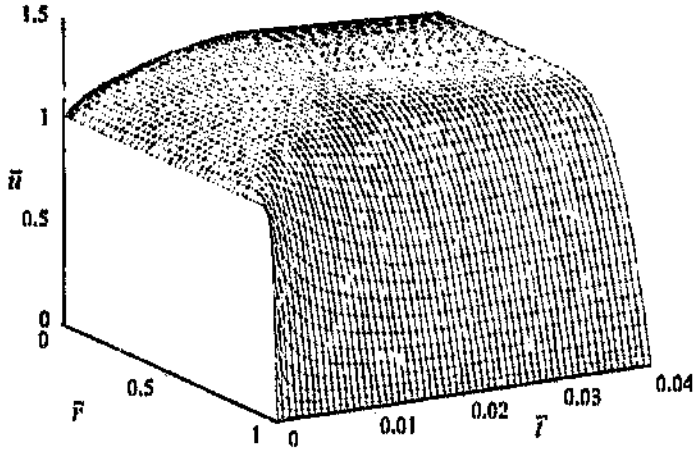

Figure 15.23: The variation of velocity profiles in time for $\Omega = 20$, at the physical station $x' = 0.02$.

The displacement thickness can be extracted directly from the velocity profiles above. The variation of this parameter in time at fixed x' describes the variation that would be seen experimentally at the corresponding point. Presented here is the temporal variation of δ^*/R corresponding to the three stations $x' = 0.002$, 0.01 and 0.02, given in the previous figures. Figure 15.24 shows the variations for these three stations. Also shown is the far-downstream (parallel) variation of displacement thickness.

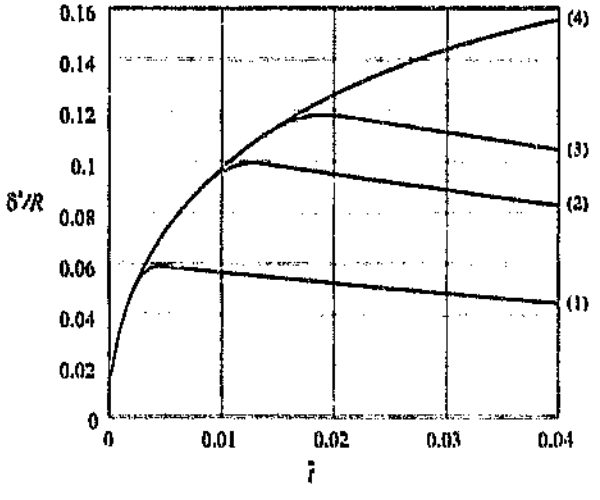

Figure 15.24: The variation of displacement thickness δ^*/R in time for $\Omega = 20$; (1), $x' = 0.002$; (2), $x' = 0.01$; (3), $x' = 0.02$; (4), parallel ($x' = \infty$).

Here it is clearly evident that the early parallel development is identical for all stations. The flow begins to deviate from this line, firstly at the upstream sta-

with figure 15.22 of an intermediate nature. Obviously, the initial (temporal) development regions in all the figures are identical, the temporal development merely being cut short earlier in the upstream flow. These three data have been presented as a qualitative indication of the effects of the co-ordinate stretching on the flow. What follows is a presentation of the variation of the displacement thickness δ^*/R in time.

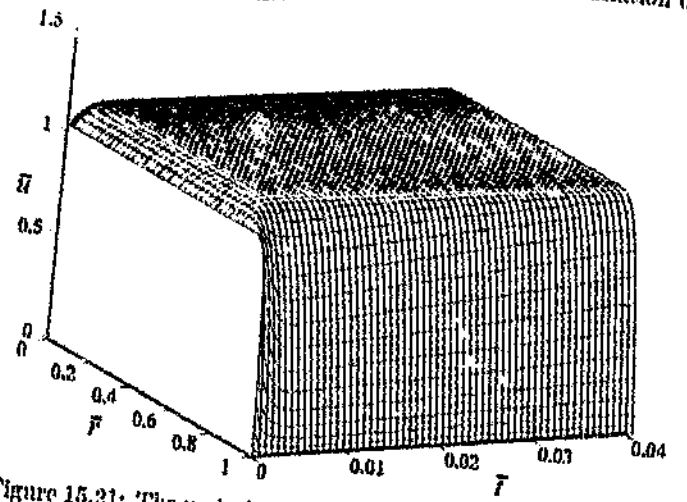

Figure 15.21: The variation of velocity profiles in time for $\Omega = 20$, at the physical station $x' = 0.002$.

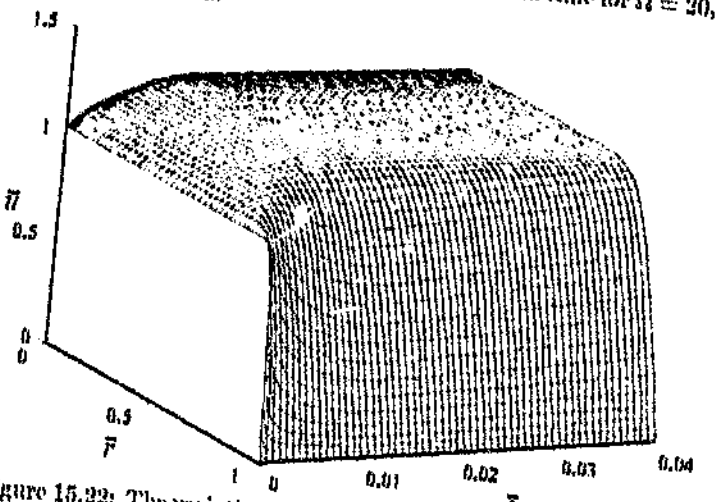

Figure 15.22: The variation of velocity profiles in time for $\Omega = 20$, at the physical station $x' = 0.01$.

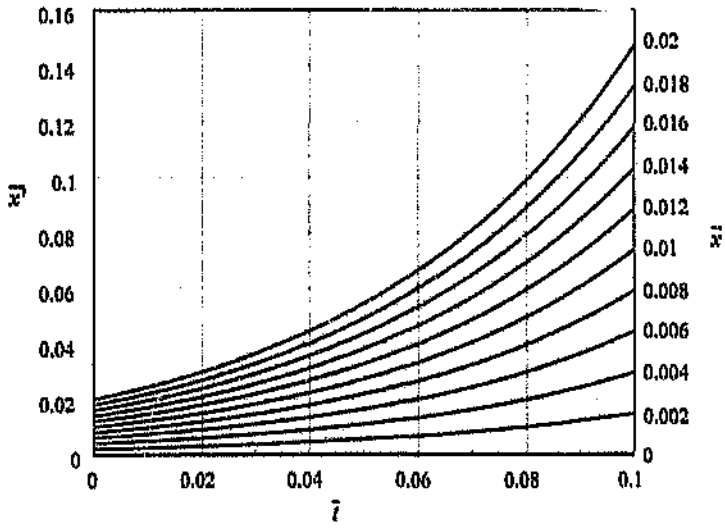

Figure 15.20: Lines of iso-$\bar{x}$ in the $\bar{t}$ - $\bar{x}'$ plane, for $\bar{\Omega} = 20$.

were stored for various times. For each snapshot, the velocity profile information was stored as Chebyshev coefficients in $\bar{r}$ and collocation values in $\bar{x}$. The collocation direction was projected into the Chebyshev-Tau form by the transformation (12.57), resulting in velocity data as a full two-dimensional Chebyshev coefficient matrix. Thereafter, it was simple to extract the appropriate velocity profile (as a one-dimensional vector of coefficients) from the correct $\bar{x}$ station for each corresponding time value. This allowed the construction of a set of velocity profiles (one set for each chosen station in $\bar{x}'$) describing the temporal variation of the flow at a particular physical position. From the sets of velocity profile data, all further information could be extracted.

For the sake of conciseness, only three $\bar{x}'$ stations are shown and discussed for the 'demonstration' acceleration of $\bar{\Omega} = 20$. These are: one close to the inlet plane at $\bar{x}' = 0.002$, one central to the axial solution extent, at $\bar{x}' = 0.01$, and the final one furthermost downstream, at $\bar{x}' = 0.02$. Figure 15.21 shows a three-dimensional surface plot of the variation of the velocity profiles at $\bar{x}' = 0.002$, figure 15.22 the similar variation further downstream at $\bar{x}' = 0.01$, and figure 15.23 gives the furthermost downstream variation. These results clearly show the initial thickening and then thinning of the boundary layer. The most upstream profile - figure 15.21 - shows the sharpest changes in behaviour in time, while further downstream the changes are more gentle.

The striking feature about figures 15.21, 15.22 and 15.23 is the nature of the variation shown. The far upstream flow - figure 15.21 - shows an abrupt change in behaviour when the entrance flow reaches each station. Its temporal development rapidly changes into a reversion towards a thinner boundary layer. The downstream flow in figure 15.23 shows analogous, but more leisurely, features.

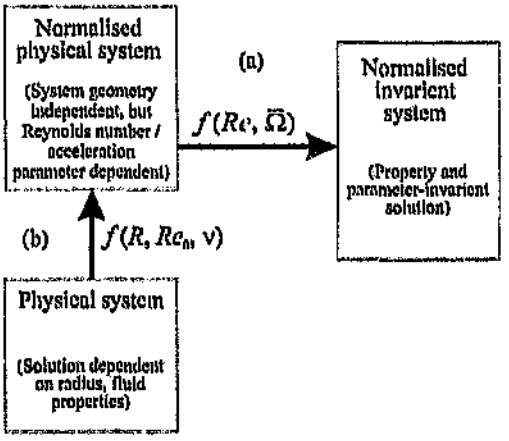

Figure 15.19: The relationship between the dimensionless co-ordinate systems and the physical independent variables.

With the basic co-ordinate transformations defined, it is now possible to extract the physical fluid variation at a point in an exponentially accelerating inlet. As mentioned above, specific use will be made here of the (arbitrarily chosen) data for $\bar{\Omega} = 20$.

15.5.2 Development of the flow for $\bar{\Omega} = 20$

As mentioned in section 15.4, the flow for $\bar{\Omega} = 20$ will be used for a specific example in illustrating the transformed behaviour of exponential flows. The range of interest in the entrance flow case is, as mentioned, $\bar{x} \in [0, 0.02]$. Using the parametric descriptions of sections 15.2 and 15.3, the physical appearance of the flow at equispaced measuring stations in the physical basis $\bar{x}'$ will be examined. For the sake of rigour, the full (temporally and spatially varying) data will be used in this process, but as before, it will be shown that use of the two simple limiting cases will suffice here, too, in describing most of the fluid variation. Consider 11 fixed, equally spaced, measuring stations in $\bar{x}'$ - the dimensionless physical co-ordinate system. For the present range, these points will occur at the axial positions $\bar{x}' = \{0, 0.02, 0.04, \cdots, 0.18, 0.2\}$. At $\bar{t} = 0$, both the $\bar{x}'$ and $\bar{x}$ co-ordinate systems coincide; thereafter, each fixed point on the $\bar{x}'$ ordinate will correspond to an exponentially diminishing axial position in the solution domain $\bar{x}$, according to equation (15.19). Figure 15.20 shows what lines of constant $\bar{x}$ look like in an $\bar{x}' - \bar{t}$ framework.

Using the information contained in figure 15.20 in conjunction with the full inlet flow for $\bar{\Omega} = 20$, the physical variation of fluid properties at stationary points in the physical domain could be ascertained. This was achieved as follows: temporal 'snapshots' of the flow development for the chosen acceleration parameter

15.5.1 A normalised co-ordinate system for the physical domain

The equations (15.16) and (15.17) above unfortunately complicate the mapping, in that the physical x ordinate has dimension. Of far more use would be a normalised (dimensionless) physical reference frame, from which the specifics of the flow (pipe radius, etc.) were excluded. An ideal candidate for normalising the physical system would be the state of the flow at inception; using these conditions, a normalised physical axial co-ordinate $\bar{x}'$ could be formed. Consider the definition

$$\bar{x}' \equiv \frac{x}{RRe_0}, \tag{15.18}$$

where Re_0 is the Reynolds number at inception. Using this new dimensionless ordinate, (15.16) and (15.17) can be redefined in a much simpler way. Firstly, the mapping (15.16) becomes, for a fixed $\bar{x}'$

$$\bar{x}(\bar{t}) = \bar{x}' \exp(-\bar{\Omega}\bar{t}), \tag{15.19}$$

and, secondly the reverse transformation, for fixed $\bar{x}$, is

$$\bar{x}'(\bar{t}) = \bar{x} \exp(\bar{\Omega}\bar{t}). \tag{15.20}$$

The $\bar{x}'$ framework is helpful in that it is a dimensionless and thus pipe geometry independent. The governing equations are Reynolds number independent, thus a co-ordinate system normalised with respect to inception Reynolds number will be universal to flows with arbitrary starting Reynolds number. Moreover, the normalised physical and dimensionless ordinates coincide at $\bar{t} = 0$. The temporal relation between these two systems is defined merely by the parametric groups in the flow, while the normalised physical system, because it is constant in relation to the proper physical variables, has a unique correspondence to the physical flow. This useful interrelationship is depicted in figure 15.19.

Here, for flow with a certain value of Ω and Re, the mapping (a) is a given function of $\bar{t}$ alone, and thus does not concern the pipe and fluid geometry and properties. The mapping between the normalised physical domain and physical system (b) embodies all the physical pipe and fluid properties. Using this system, data can be presented in a uniform and general manner, while the projection of this data to a particular physical system (a pipe with radius R, fluid with viscosity ν, etc.) remains remote from the general description. A fixed point in the normalised physical basis will correspond to a fixed point in the physical system (dependent on the geometry); thus the normalised physical basis is the most general framework from which to describe the physical flow behaviour.

upstream, the point of observation will be in the parallel region of the flow; thus the temporal development will proceed exactly as given in section 15.2, according to the specified value of the acceleration parameter Ω.

(ii) A time will arise when the upstream moving observation point coincides with the downstream moving entrance front. The temporal flow development (as, of course measured from the physical station x_a) will slow as the transition region between parallel and entrance flow traverses the measuring station.

(iii) Once the measuring station is within the steady-state (as seen from the dimensionless co-ordinate system) entrance flow, it will continue to move upstream. The temporal development of the flow in this region would be one in which successive velocity profiles at a fixed x would originate from increasingly upstream stations in the dimensionless system. Thus the flow here would show a *decrease* in boundary layer thickness from this time on.

Considering some physical property of the flow such as displacement thickness, a fixed observer would first see an increase in this quantity in time, exactly as in the simple far-downstream flow of the first section. Thereafter, the displacement thickness would start to decrease again, as the physical measurement station traverses upstream in the dimensionless co-ordinate system. This principle was illustrated in figure 10.5 (page 200).

The above way of perceiving the co-ordinate mapping was concerned with the equivalent behaviour in the dimensionless basis of a fixed point in the physical system. An alternative but equally valid perspective, would be to consider the behaviour of a fixed region in the dimensionless basis in the physical system. For instance, consider the line segment $[0, \bar{x}_{a'}]$ in the dimensionless system. If $\bar{x}_{a'} = 0.02$, then this line segment would encompass the dimensionless solution domain used for the entrance calculations. Of interest now would be the behaviour of this segment in the physical basis. In order to show this, a relation needs to be developed stating how a fixed point in $\bar{x}$ translates to the physical space. Such a relation can be simply developed in a manner analogous to (15.16), from equations (15.14) and (15.15), and is

$$x_{a'}(t) = \bar{x}_{a'} R Re_0 \exp(\Omega t). \tag{15.17}$$

Thus a line segment $[0, \bar{x}_{a'}]$ in the dimensionless co-ordinate system translates into a line segment $[0, x_{a'}(t)]$ which *extends* in time; therefore the reference-frame transformation is equivalent to a stretching of the dimensionless solution in time. If the dimensionless solution were drawn on a rubber sheet, then the transformation would correspond to stretching the sheet exponentially downstream in time.

transformation is

$$x^* = \frac{x}{RRe}. \tag{15.14}$$

This relation indicates that for an increasing Reynolds number, an axial position in the physical domain represents an increasingly diminishing ordinate in the dimensionless basis. What such a transformation means in practice is unclear from such a short explanation, therefore discussion of its effect on the flow will be ventured upon in much greater detail. The description will be developed in a general fashion; however, where specific illustration is to be made, the data of the preceding section, for the case $\Omega = 20$, will be used.

The Reynolds number in the exponential flows discussed increases exponentially, and its variation in time can thus be given as

$$Re = Re_0 \exp(\Omega \tilde{t}) \tag{15.15}$$

with Re_0 the initial impulsively attained Reynolds number. Equation (15.15) affords a relation between Re and $\tilde{t}$; this allows the axial co-ordinate transformation (15.14) to be given as a function of time. The reference frame of greatest importance is the physical, because it is in this framework that experimental results are observed. Measurement of an exponentially accelerating flow experimentally, is usually made from a fixed axial position; for instance, shear stress probes or a laser Doppler velocimeter will measure a flow at a given spatial position. Thus it is important to determine what the observation of the flow from a fixed x (physical) station will mean when transformed to the x^* (dimensionless) framework. Assume that an observer is measuring fluid velocities at a fixed physical station $x = x_a$. The observation starts at $\tilde{t} = 0$ and continues for a suitable time. Using equations (15.14) and (15.15), the equivalent dimensionless axial station will be

$$x_a^*(\tilde{t}) = \frac{x_a}{RRe_0} \exp(-\Omega \tilde{t}). \tag{15.16}$$

Thus the dimensionless axial station corresponding to a fixed point in the physical co-ordinate system is a point that moves *upstream* in the dimensionless basis with increasing time. As has been shown, any exponentially accelerated pipe entrance flow consists of two portions - a parallel downstream flow and a steady-state entrance flow - and that as time develops, the entrance region increases to encompass more and more of the pipe. From a physical vantage point $x = x_a$ a small way downstream (at, say 50% of the entrance length) the flow will behave as follows:

(i) In the initial stages, when both the non-parallel region is short, and the dimensionless x station [as governed by (15.16)] has not moved very far

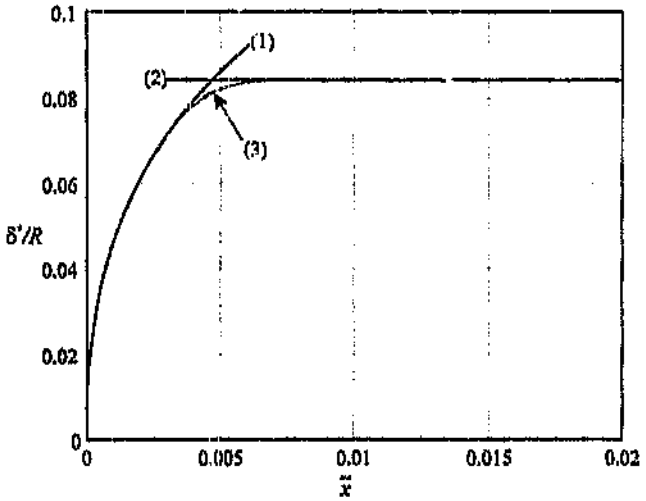

Figure 15.18: The variation of displacement thickness δ^*/R with axial distance $\tilde{x}$ in the developing entrance region of a pipe, for $\Omega = 20$ and $t = 7 \times 10^{-3}$: (1), steady-state entrance flow; (2), temporal developing flow; (3), the actual inlet flow.

the system predominantly in the steady-state entrance portion of the flow, thus the most important base flow results are those from the steady-state entrance calculation - fortuitously, these are also the most accurate.

15.5 Mapping to the physical domain

The exponentially accelerating steady-state entrance flows considered above are only really steady-state in the dimensionless framework. It was shown in chapter 10 that a variable, Reynolds number dependent mapping exists between the physical variables and their dimensionless counterparts. Thus physically, an exponential flow is constantly changing, but this change can be entirely described by using the variable reference-frame transformation from the physical to the dimensionless basis. The role of this section is to describe the effects of the transformation, and thus to make obvious the underlying pattern in the superficially complicated behaviour when viewed from the physical domain. To illustrate this, the full results from the 'test' acceleration $\Omega = 20$ are again used.

The mapping between the physical and normalised variables is given by the set of equations (10.20). The transformations between these two bases for the axial co-ordinate x, the pressure p, and the axial velocity u are all Reynolds number dependent; of these, x is the only independent variable, thus it alone affects the transformation between the two solution domains. The axial co-ordinate

its steady-state value, the entrance flow becomes globally steady-state, with no more temporal development. For this final condition, the flow resembling the entrance region is that within the entrance length of the pipe, while the flow downstream of this is essentially parallel. However, one must bear in mind that the above designation of regions is artificial; information in the pipe flow can in reality propagate at the local speed of sound (in the case of the mathematical model at an infinite rate, commensurate with the assumption of incompressibility) and there is thus no hard interface. However, and quite fortuitously, the flow behaves much as if an interface were propagating downstream at the mean velocity[8].

The flow development is clearly evident in figure 15.17. The subsequent temporal curves 1 to 7 clearly show the two regions. Here the entrance component of the flow rises from the origin to meet the parallel downstream flow, given by the horizontal portion of the data. As the time develops the entrance moves downstream, and an increasingly larger portion of the curves lie on the steady-state entrance curve (curve number 8). What is striking about this system is that, except for a small intermediate part of the flow, most of the inlet at any time can be accurately approximated by a combination of the steady-state entrance - curve number 8 - and parallel temporally developing flow - a horizontal series of lines.

In order to illustrate the good asymptotic matching to the full data, the curve for $\bar{t} = 7 \times 10^{-3}$ from figure 15.17 is reproduced in figure 15.18. Also shown in this figure are the two limiting curves: firstly the steady-state entrance curve, indicated as (1), and the temporally developing parallel flow result for $\bar{t} = 7 \times 10^{-3}$ - curve number (2). Only the portion of the full data that differs from the above curves is visible, and this is denoted (3). The validity of the two simpler limits is immediately apparent here.

The major importance of the applicability of the two limiting cases concerns numerical accuracy. Firstly, the spatial solution (1) is independent of the temporal discretisation in the present model; thus solutions invariant to the machine precision can be attained in this case. Secondly, the much simpler temporal model (2), while limited by its temporal scheme, is so simple and fast to calculate that accurate results can be produced simply by 'brute force'. Furthermore, as argued in chapter 13, the limitation in accuracy for this case was substantially less than was superficially evident. To achieve equivalent accuracy from the full system would become prohibitively expensive; this is because it suffers from the disadvantages of both the simpler schemes, namely slowness and the presence of temporal inaccuracy.

A final point deserves mention concerning the approximations, although it will be covered in more detail later: the observed experimental instability occurs in

[8]One is always quick to imagine a 'lump' of fluid convecting downstream from the inlet, but this intuition is not necessarily correct. However, the physical laws governing fluid motion give a rate of axial diffusion close to the mean velocity; thus the illusion is complete, and a purely 'convected' interface is perceived.

accelerated pipe flow proceeds from the inception conditions to the far-time steady-state solution. Such a flow can be represented as a series of curves, each one representing the flow at an instant. This representation allows the use of the notational and descriptive framework of the previous section. The simplest manner in which to indicate the tempore-spatial development of the inlet is by observing the development of the boundary layer displacement thickness. The development of this parameter with $\bar{x}$ is shown in figure 15.17.

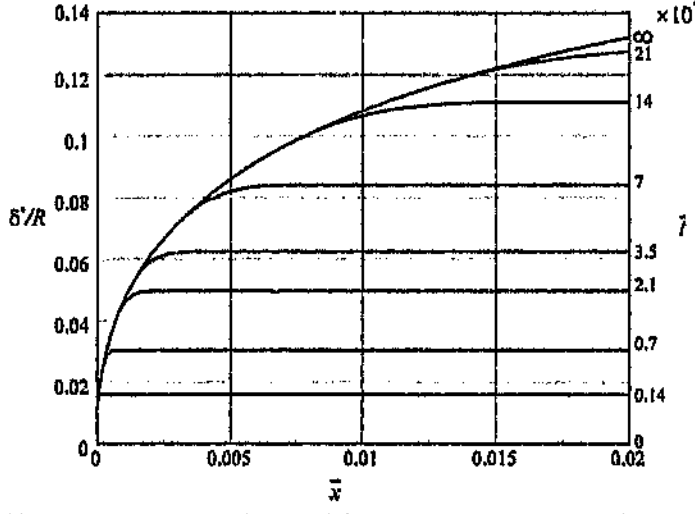

Figure 15.17: The variation of displacement thickness δ^*/R with axial distance $\bar{x}$ in the developing entrance region of a pipe, for $\bar{\Omega} = 20$. The curves represent the value of the parameter at various times.

The flow develops from the initial condition at $\bar{t} = 0$, with the 'top-hat' flow condition assumed everywhere. This state of the system is represented by a line along the positive $\bar{x}$ axis. The system now moves away from this curve as the boundary layer starts growing. The inlet boundary condition, however, maintains the 'top-hat' condition at the inlet plane; thus the flow starts to show two distinct regimes. The first region is near the inlet, and here the boundary layer develops spatially from the zero thickness inflow condition to a value matching the second region. This spatial variation in the flow implies that this region is non-parallel in nature. Another, although perhaps less evident, property of this region is its steady-state behaviour - as the inlet interface propagates downstream, it leaves behind a virtually temporally invariant flow system. The second flow region encompasses the flow regime that extends downstream from the first. In this portion of the pipe, there is no axial variation in the flow, and the system develops only temporally.

The entrance region can be associated with the convection of information about the inlet in the downstream direction: as the flow develops, the interface between this region and the parallel one moves downstream at approximately the mean velocity in the flow. Eventually, when the far downstream flow has approached

any linear instability is well within the region [0, 0.02], and in fact occupies only about 3% of the entire entrance in the steady case [Abbot & Moss (1994)]. This point further enhances the use of the δ^*/R - S_δ framework, because it properly emphasises this region of importance.

15.4 The limiting cases as approximations to the proper solution

It has been indicated above that the two types of flows discussed in this chapter - temporally developing and steady-state entrance - are merely approximations to the actual developing flow in a pipe at any one time.

A heuristic description was forwarded in chapter 10 for the behaviour of a pipe entrance flow started from rest to some fixed Reynolds number. There it was argued that the effect of the pipe entrance would convect downstream with time, and this interface would effectively divide the pipe into two sections - one downstream in which the flow remained strictly parallel, and one at the entrance in which the flow developed spatially (in temporal steady-state) from 'top-hat' at the inlet plane to some more curved profile at the convecting interface. It has been shown that impulsively started exponential flows behave analogously to the impulsive zero-acceleration case, as long as the flow is observed from the viewpoint of the dimensionless variables. Thus, if the above assumption (that the system can be accurately approximated by its respective temporal and spatial limiting cases) is correct, then the full tempero-spatial development for all the exponentially accelerating flow considered can be equally considered as a 'patch' between the two simplified mathematical models solved so far. This section will show that most of the pipe flow can indeed be validly expressed in terms of the simpler models.

In this section, the assumption that the limiting cases provide an adequate description of the general flow is investigated, by direct comparison of the temporal and spatial approximations to a full mathematical model for the development of an exponentially accelerating pipe entrance flow. To illustrate this assertion, an arbitrary selection of the case for $\Omega = 20$ was made, and the data for this case were generated using the full two-dimensional model. Unlike in the investigation of the steady-state results in section 15.3, the interim results between impulsive and steady-state were retained. These data were generated at an order of $M \times N$ of 60×60, while the time discretisation was taken at $\Delta t = 7 \times 10^{-4}$. What follows is the presentation of these results at various times, in comparison to the simpler limiting cases.

Although the discussion until now has led towards the use of the displacement thickness δ^*/R as the ordinate in data representation, for the sake of physical understanding use will again now be made of the axial co-ordinate x for this purpose. The development in the entrance of impulsively started and exponentially

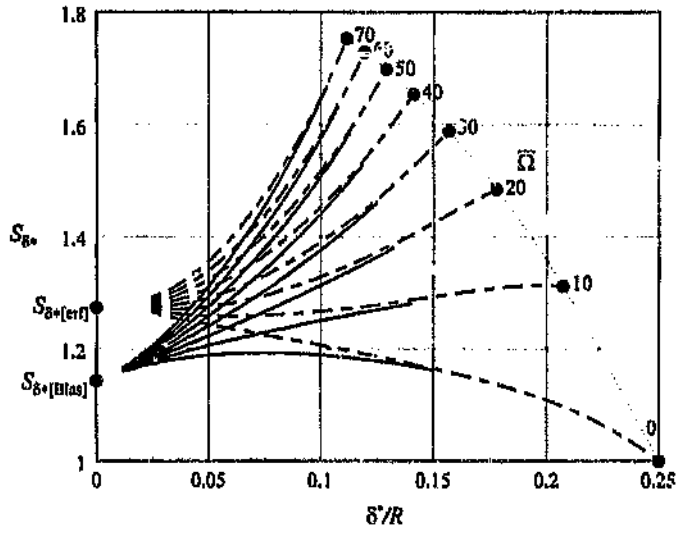

Figure 15.16: The variation of scaled shape parameter $S_{\delta*}$ with displacement thickness δ^*/R in the entrance region of a pipe, for various values of the acceleration parameter $\bar{\Omega}$. The equivalent temporal development curves are superimposed, and are shown dashed. The dotted line indicates the locus of limiting values for $\bar{x} = \infty$.

This figure presents no new results, but meaningfully shows the relationship between the temporal and spatial systems. The first important feature of this plot is the respective asymptotic limit possessed by each system. The distinct nature of each type of flow is immediately apparent in this comparison. This figure is merely the generalisation of figure 1-1.6 (page 324), for non-zero values of $\bar{\Omega}$; the reader is referred to the discussion there for further enlightenment.

As the flow develops, the two results - spatial and temporal - approach each other until they become formally identical at the final asymptotic limit. The two sets of data have effectively become indistinguishable, for each value of $\bar{\Omega}$, at the points corresponding in the spatial data to $\bar{x} = 0.02$. The spatial data was only generated for $\bar{x} \in [0, 0.02]$, but in all cases at its downstream limit, the resulting velocity profiles were virtually identical in shape to the equivalent temporal profiles. Velocity profiles beyond this value of $\bar{x}$ for a chosen value of $\bar{\Omega}$ thus approximate a one-parameter family. This was the relationship incorrectly ascribed to the *entire* pipe flow by da Silva (1990).

While the region over which the temporal and spatial results are divergent seems substantial in figure 15.16, its extent in terms of the axial co-ordinate is relatively insignificant. Considering the case $\bar{\Omega} = 0$, the entrance length was calculated to be $Z_r \approx 0.22$, and thus the domain length of 0.02 indicates that the entrance flow is distinct for only 10% of the formal pipe entrance. However, the insignificant size of this region belies its importance. The area of the pipe which can show

Results for $\bar{\Omega} = 70$

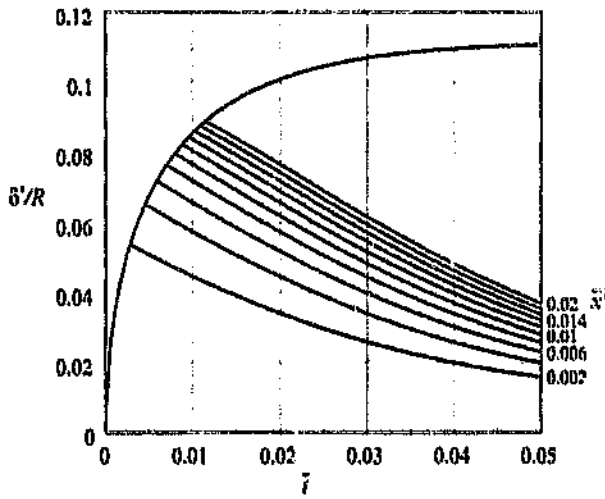

Figure 15.41: The variation of displacement thickness δ^*/R with time t, for various values of the dimensionless physical ordinate x'; $\bar{\Omega} = 70$.

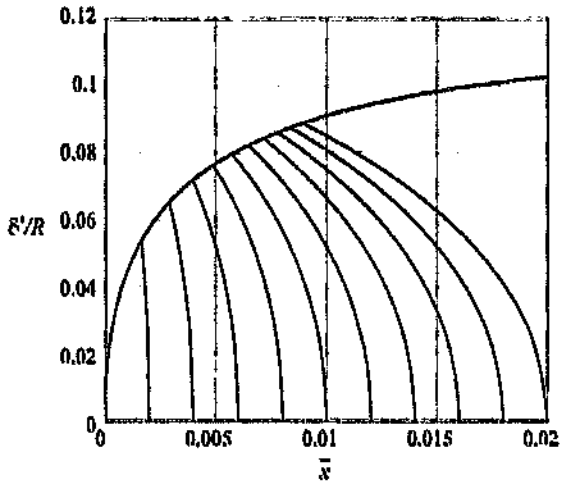

Figure 15.42: The variation of displacement thickness δ^*/R with normalised ordinate x, for various values of the dimensionless physical ordinate x'; $\bar{\Omega} = 70$.

Results for $\hat{\Omega} = 60$

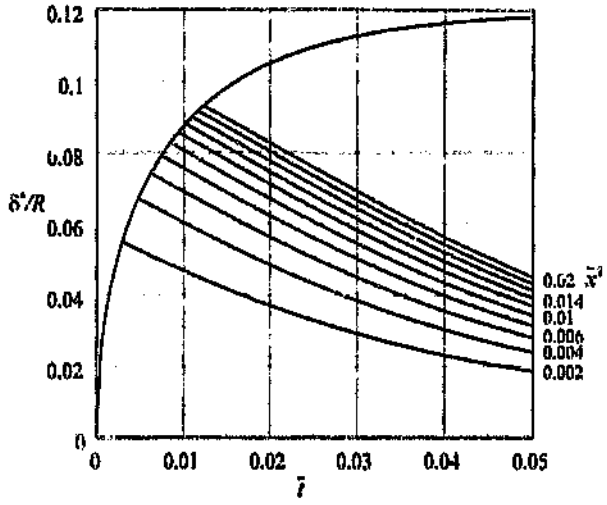

Figure 15.39: The variation of displacement thickness δ^*/R with time $\bar{t}$, for various values of the dimensionless physical ordinate $\bar{x}'$; $\hat{\Omega} = 60$.

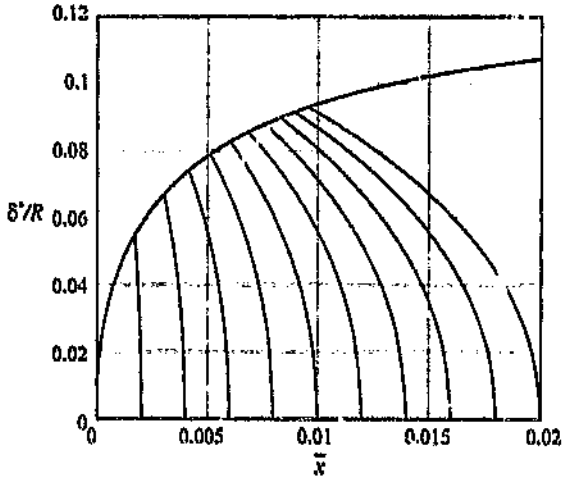

Figure 15.40: The variation of displacement thickness δ^*/R with normalised ordinate $\bar{x}$, for various values of the dimensionless physical ordinate $\bar{x}'$; $\hat{\Omega} = 60$.

Results for $\mathcal{U} = 50$

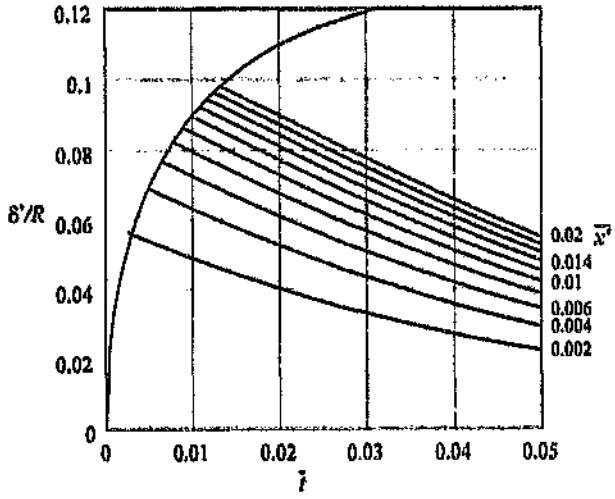

Figure 15.37: The variation of displacement thickness δ^*/R with time t, for various values of the dimensionless physical ordinate x'; $\mathcal{U} = 50$.

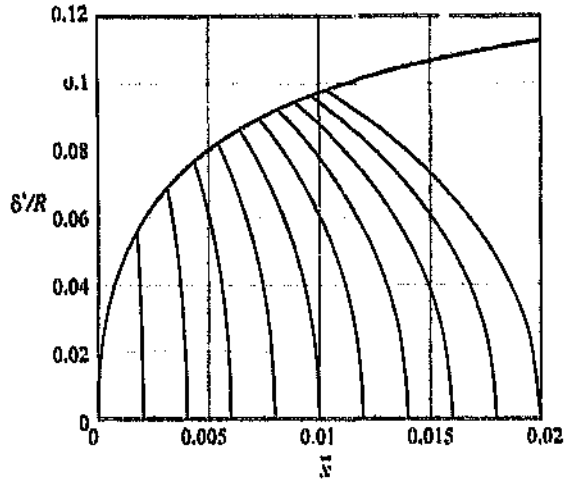

Figure 15.38: The variation of displacement thickness δ^*/R with normalised ordinate $\bar{x}$, for various values of the dimensionless physical ordinate x'; $\mathcal{U} = 50$.

Results for $\Omega = 40$

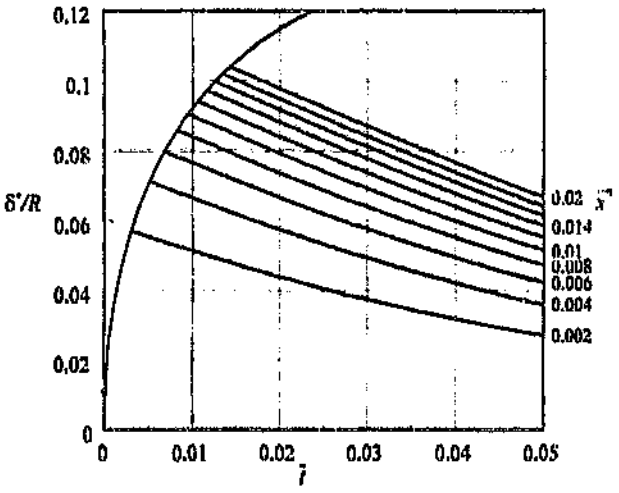

Figure 15.35: The variation of displacement thickness δ^*/R with time t, for various values of the dimensionless physical ordinate x'; $\Omega = 40$.

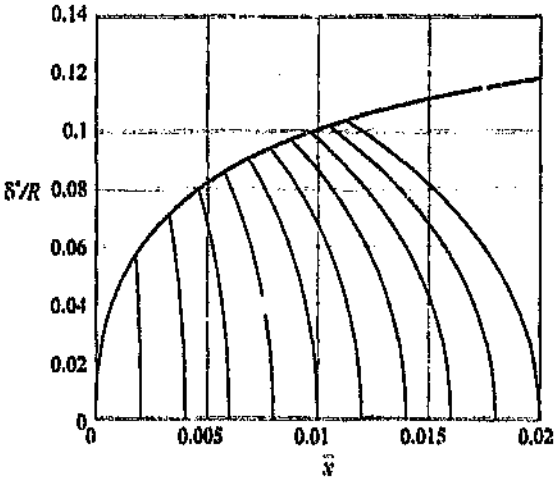

Figure 15.36: The variation of displacement thickness δ^*/R with normalised ordinate $\bar{x}$, for various values of the dimensionless physical ordinate x'; $\Omega = 40$.

Results for $\Omega = 30$

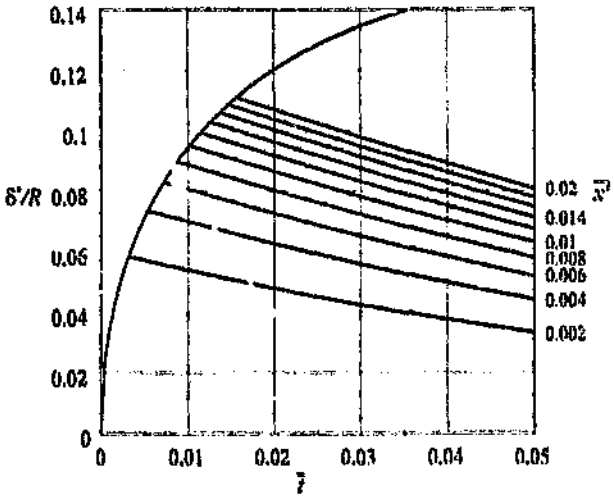

Figure 15.33: The variation of displacement thickness δ^*/R with time t, for various values of the dimensionless physical ordinate x': $\Omega = 30$.

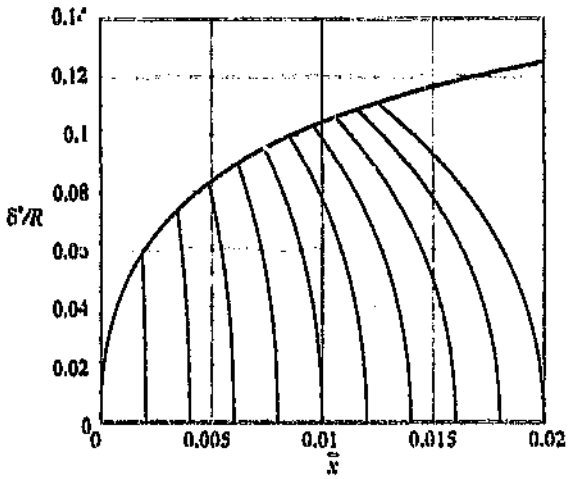

Figure 15.34: The variation of displacement thickness δ^*/R with normalised ordinate x, for various values of the dimensionless physical ordinate x': $\Omega = 30$.

Results for $\Omega = 20$

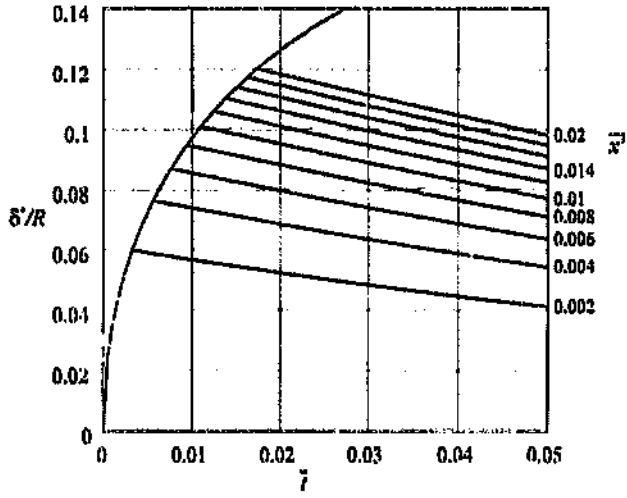

Figure 15.31: The variation of displacement thickness δ^*/R with time t, for various values of the dimensionless physical ordinate x'; $\Omega = 20$.

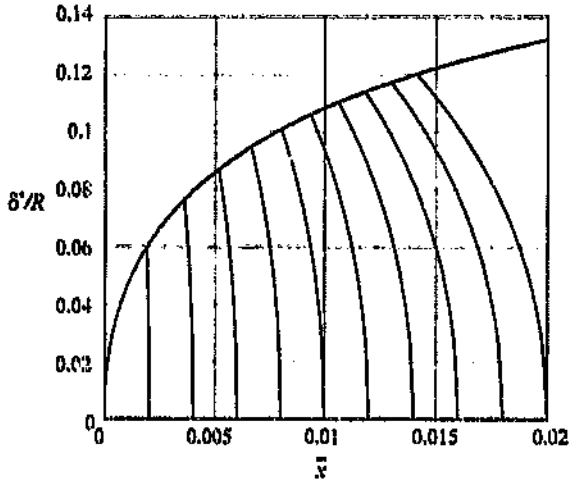

Figure 15.32: The variation of displacement thickness δ^*/R with normalised ordinate x, for various values of the dimensionless physical ordinate x'; $\Omega = 20$.

Results for $\Omega = 10$

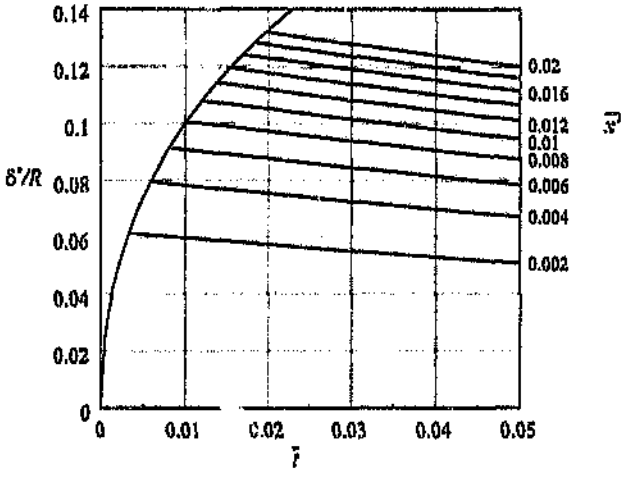

Figure 15.29: The variation of displacement thickness δ^*/R with time $\bar{t}$, for various values of the dimensionless physical ordinate $\bar{x}'$; $\Omega = 10$.

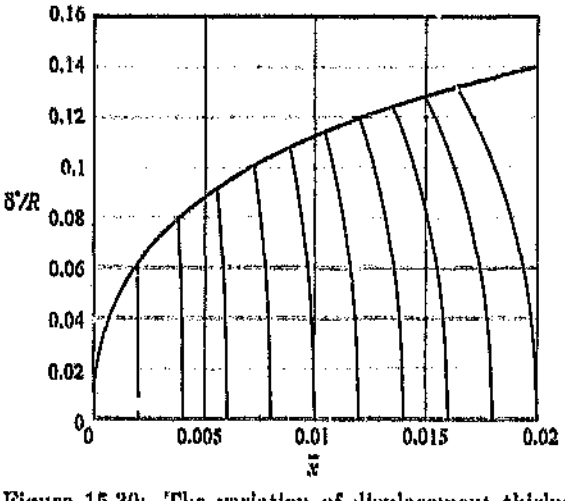

Figure 15.30: The variation of displacement thickness δ^*/R with normalised ordinate $\bar{x}$, for various values of the dimensionless physical ordinate $\bar{x}'$; $\Omega = 10$.

Results for $\tilde{\Omega} = 0$

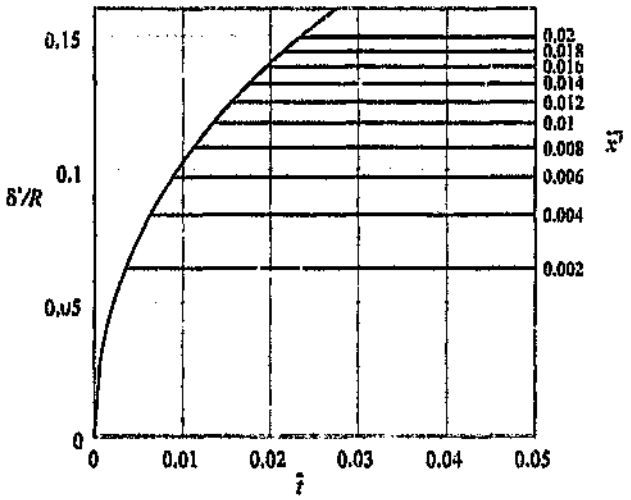

Figure 15.27: The variation of displacement thickness δ^*/R with time $\tilde{t}$, for various values of the dimensionless physical ordinate $\tilde{x}'$; $\tilde{\Omega} = 0$.

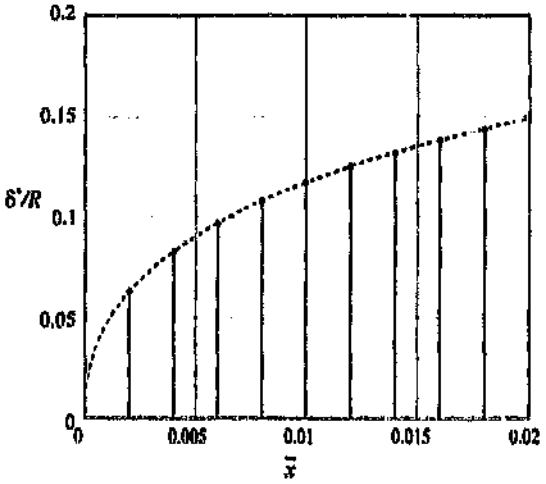

Figure 15.28: The variation of displacement thickness δ^*/R with normalised ordinate $\tilde{x}$, for various values of the dimensionless physical ordinate $\tilde{x}'$; $\tilde{\Omega} = 0$.

15.7 Comprehensive results

Only a few selected results were given in section 15.5.2 - specifically the data for $\Omega = 20$ - in order to illustrate the effects of the co-ordinate transformation, and to describe the general nature of the exponential flow system. This section presents more general results for all the exponential accelerations investigated, from the impulsively started case to $\Omega = 70$. The parameter used for the presentation here is the displacement thickness. Variation of δ^*/R for fixed values of x' is shown in both the temporal and spatial sense. The presentation proceeds from the impulsive case upwards to the highest value of Ω. It was shown in the previous section that the asymptotic limiting curves are properly representative of most of the data; therefore only these curves are given. In both the temporal and spatial representations that follow, ten separate normalised physical stations x'_i have been given, in steps of $\Delta x'_i = 0.002$ in the range $0.002 \leq x' \leq 0.02$.

Figures 15.27 to 15.42 below show the temporal and spatial development of the flow sequentially for increasing values of the acceleration parameter. The impulsive data is also given here (figures 15.27 and 15.28), in a uniform manner to the accelerating cases. Due to the fact that in the impulsive case, the mapping from the physical axial position to the dimensionless ordinate is constant, the entrance flow is given by horizontal lines in figure 15.27. In the case of the spatial representation (figure 15.28), the early parallel flow development at the respective axial stations is shown as a set of vertical lines. In this case the flow at any chosen physical station remains invariant once temporal development has ceased, and it is for this reason that the steady-state curve on this graph is shown as a dotted line. For the remaining accelerating flows, the flow development proceeds in the same way as described in section 15.6 above. As the value of the acceleration parameter increases, the entrance flow lines on the temporal representation (figures 15.29, 15.31, 15.33, 15.35, 15.37, 15.39 and 15.41) increase in slope. In accordance with this, the lines of temporal development on the spatial data (figures 15.30, 15.32, 15.34, 15.36, 15.38, 15.40 and 15.42) move from a vertical orientation and become increasingly curved as the acceleration increases. These data follow below.

physical axial measurement station, a continuous range of dimensionless axial stations to be traversed. This is in strong contrast to impulsive flow, where the physical and normalised ordinates remain in fixed correspondence. Thus exponential flows, if indeed possessing the predicted behaviour, would be in seeming contradiction, a far better framework in which to study economically the steady-state development of a flow. In the chapter on the stability of these flows, a further strong argument will be forwarded as to why these flows are much better to study than ostensibly *simple* steady impulsive flows.

It has been shown previously that the asymptotic spatial and temporal solutions describe substantially the data, with only a small transition region not concurrent with either of these curves. Figure 15.26 shows again the data of figure 15.25, but here with the asymptotic curves superimposed. The close matching of the data at all points except a small transition 'fillet' indicates that the asymptotic curves alone can be successfully used to give the variation of parameters in almost all of the pipe entrance.

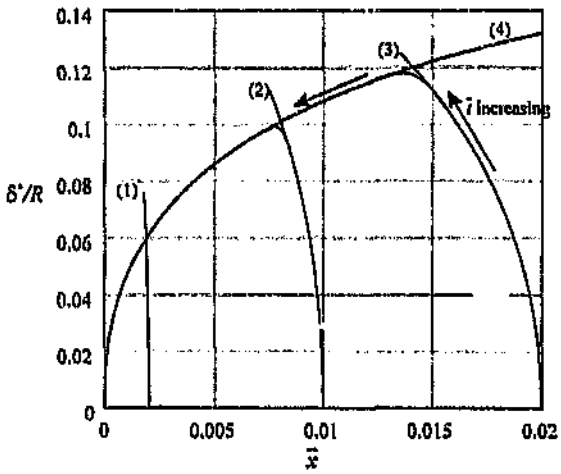

Figure 15.26: The actual variation, for $\bar{\Omega} = 20$, of displacement thickness δ^*/R in $\bar{x}$ (as given in the previous figure), compared to data according to the parallel-temporal and steady-state spatial limits of the system; (1), (2), (3), parallel temporal flow, corresponding to $\bar{x}' = 0.002$, $\bar{x}' = 0.01$, and $\bar{x}' = 0.02$ respectively; (4), steady-state entrance flow.

This section has shown a means whereby experimentally measured data from a fixed physical position in an exponentially accelerating pipe flow can be compared directly to the two asymptotic theoretical data - that for parallel temporally developing flow, and that for the steady entrance system. The following section systematically presents the data in this way for all the accelerations considered.

physical measuring station within the pipe, the time ordinate relates to the dimensionless axial ordinate $\bar{x}$ according to equation (15.19). Thus the $(\bar{t}, \bar{r}, \bar{u})$ data above can be transformed directly into the $(\bar{x}, \bar{r}, \bar{u})$ framework via this relation. In this case, increasing values of the time ordinate $\bar{t}$ will correspond to *decreasing* values of the normalised axial ordinate $\bar{x}$. Since the far-time portions of figures 15.21, 15.22 and 15.23 were obtained by transforming from the invariant entrance solution in the first place, the reverse process - via equation (15.19) - will simply recover the invariant entrance solution for this portion of the flow. In this case, data from different (physical) axial positions in the pipe for the far-time *thinning* portion of the flow will align exactly to the steady entrance solution, while the early-time parallel data from each axial position will be unique. The best way to illustrate this principle is again to consider the variation of the displacement thickness δ^*/R for the flow for $\bar{\Omega} = 20$. Figure 15.25 shows the three curves of figure 15.24 transformed in this way. Also shown in this figure is the steady-state pipe entrance variation of δ^*/R in $\bar{x}$.

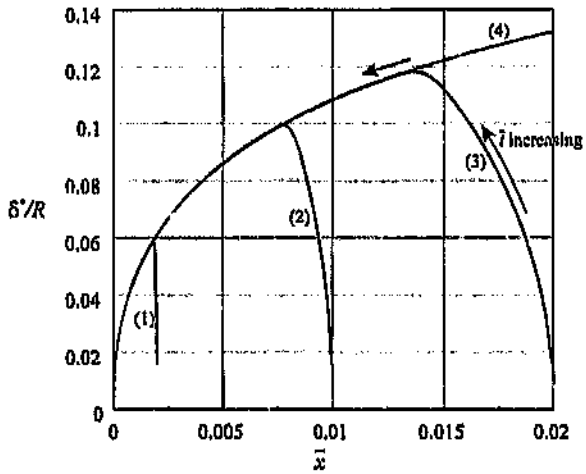

Figure 15.25: The simulated variation of experimentally 'measured' displacement thickness δ^*/R with normalised axial station $\bar{x}$ for $\bar{\Omega} = 20$, corresponding to three dimensionless physical positions; (1), $\bar{x}' = 0.002$; (2), $\bar{x}' = 0.01$; (3), $\bar{x}' = 0.02$; (4), steady-state entrance flow.

Here, the hypothetical experimental data line up exactly with the invariant spatial solution for large times, while the short-time data - which fell onto a single line in the temporal framework - trace unique curves, one for each axial station. Notable here is that the direction of increasing time on this figure is from right to left.

Thus immediately there is a mechanism for comparing experimental data *directly* to the asymptotic results (parallel temporal and steady-state spatial) in such a way that almost all of the experimental data, regardless of point of origin in the pipe, will (if accurate) align to two unique lines. This brings to light a subtle point regarding exponentially accelerated flows. These flows allow, for a single

tion, and then later further downstream. The results for the specific acceleration $\bar{\Omega} = 20$ have been used for illustration only, and the more general results (for all the values of acceleration parameter used) are presented in a later section. Before proceeding to the more general results, a diversion will be made in order to explain another complimentary method of presenting the data, in a form that will be useful for presentation of, and comparison with, the experimentally measured flow results in part IV.

15.6 Physical framework for comparison to experiment

The most natural framework of presentation for the numerical data is the normalised dimensionless co-ordinate system, where the solutions are invariant in the far-time limit, with both their domain and range remaining bounded. Experimentally measured data on the other hand is naturally measured in the physical co-ordinate system; thus in order to compare theory to experiment, one of the sets of results must be transformed into the system of the other. In the previous section, the numerical results in the normalised co-ordinate system were transformed into the physical framework, and the resultant data represented the theoretically predicted variation of parameters (displacement thickness, velocity profiles) in time, at fixed physical positions in the pipe. This section is concerned with the reverse process; the transformation of the experimental data towards the normalised system.

Experimentally measured data were given in part II of this work, and were presented as a series of velocity profiles developing in time at a fixed physical axial station. As such, the experimental data were presented as three-dimensional surface plots in the $(\bar{t}, \bar{r}, \bar{u})$ co-ordinate system, and were similar in form to the numerical data shown in figures 15.21, 15.22 and 15.23 above. The early time, parallel development of the above three figures was identical at any axial station; velocity profile parameters, such as the displacement thickness or shape parameter, followed a single curve for this portion of the flow. Figure 15.24 showed that this was so for the displacement thickness. The universal curve was described exactly by the simplified parallel flow development model as given in section 15.2. This universal alignment for early times, is an ideal framework for verification of data. However, once the entrance effects have passed, and the boundary layer thickness is decreasing in time, each curve from a distinct axial station assumes its own identity in figure 15.24. Due to this, comparison of theory to experiment for the later portion of the flow requires that the experimental data from each axial measuring station be compared to a separate theoretical curve.

There is, however, a method of transforming the measured data such that the far-time portion of the curves will align to a single curve. That this is possible is manifest in the axial co-ordinate transformation (15.14) itself. For any *fixed*

Straightforward substitution of (16.5) into (16.2) and subsequent rearrangement of the terms results in the following non-singular equation:

$$\frac{-i}{\alpha Re}\left[P - 2\alpha^2 Q + \alpha^4 r^2 + \Omega Q\right]\breve{\phi} = (u - c)\left[Q - \alpha^2 r^2\right]\breve{\phi} - [Tu]\breve{\phi}, \quad (16.6)$$

with the operators defined as

$$\begin{aligned} P &= r^2 D^4 + 6rD^3 + 3D^2 - (3/r)D; \\ Q &= r^2 D^2 + 3rD; \\ T &= r^2 D^2 + rD; \\ D &= \frac{d}{dr}. \end{aligned} \quad (16.7)$$

Due to the fact that the centreline constraints are implicit in (16.6), only the wall conditions are relevant; these remain unchanged from (16.3) and are

$$\begin{aligned} \breve{\phi}(1) &= 0 \\ \breve{\phi}_D(1) &= 0. \end{aligned} \quad (16.8)$$

Equation (16.6), the operators (16.7) and the boundary conditions (16.8) define a non-singular, general eigenvalue problem for the stability of general velocity profiles in pipe flow; this is a general complex differential eigenvalue system of the form

$$\mathcal{F}(\alpha, c, Re) = 0, \quad (16.9)$$

where Re is real and positive, and both α and c are generally complex. As such, either α or c can be taken as the eigenvalue and the other (along with Re) as a parameter. The system (16.9) cannot be solved generally; one must usually restrict its use to a simpler situation by respectively setting either α or c to a (real) fixed value, and treating the other parameter as the (complex) characteristic value in the equation. What these restrictions mean physically are discussed in the following section.

16.3 Types of linear instability

The stability equation (16.9) above can as mentioned be used to investigate separately two different modes of stability, these modes each giving the temporal

$$\begin{aligned}
\frac{1}{r^2}\phi(0) &= \text{const.}\\
\frac{1}{r}\phi_r(0) &= \text{const.}\\
\phi(1) &= 0,\\
\phi_r(1) &= 0,
\end{aligned} \tag{16.3}$$

where the subscript indicates differentiation with respect to r. The two conditions at $r = 0$ are traditionally taken to be zero at this point, whereas they need only be bounded at the centre[6].

The range of the independent variable is taken as before as being $r \in [0, 1]$ (the radial co-ordinate scaled with respect to the radius R), and u is the axial velocity of the base flow, scaled with respect to the mean cross-sectional velocity U.

The centreline boundary conditions assert that the function and its first derivative must approach zero at a rate greater than $1/r$. What this implies for the function itself can be deduced by the simple application of L'Hopital's rule to these two conditions. This results in

$$\begin{aligned}
\lim_{r\to 0}\frac{\phi(r)}{r} &= \phi_r(0)\\
\lim_{r\to 0}\frac{\phi_r(r)}{r} &= \phi_{rr}(0).
\end{aligned} \tag{16.4}$$

This shows that both $\phi(0)$ and $\phi_r(0)$ must be zero, while $\phi_{rr}(0)$ needs only be bounded at $r = 0$.

The most straightforward way of ensuring single-valuedness is by introducing the new dependent variable

$$r^2\tilde{\phi}(r) = \phi(r). \tag{16.5}$$

The transformation (16.5), when substituted into the limits (16.4) will automatically satisfy the boundedness criterion, and thus will automatically ensure a smooth function at the centre point. The way forward now is to reformulate (16.2) in terms of $\tilde{\phi}$, thus producing a governing equation that is smooth in all its derivatives everywhere in r.

[6] This was discovered by numerical experimentation. Taking the wall derivatives to be zero, i.e. taking $\phi(0) = \phi_r(0) = \phi_{rr}(0) = 0$, overspecified the problem and collapsed the rate of convergence to algebraic.

series representation of some *smooth* function $f(x)$ in $[-1,1]$ can be given as

$$\hat{f}(x) = \sum_{k=-\infty}^{\infty} a_k \phi_k, \tag{16.1}$$

where $\phi_k(x) = e^{ikx}$, $k \in [-\infty, \infty]$ are the Fourier functions orthogonal on the range $[-1,1]$. If the function f to be represented is smooth, then the k'th coefficient a_k decays at a rate greater than any inverse power in k. Thus, once sufficient coefficients are present to represent the essential features of the function, only a few more need be retained in order that the truncated series be an exceedingly accurate approximation of the function.

If, however, the function contains a discontinuity in the range, for instance a step decrease, then the Fourier series (16.1) near this point will not converge rapidly at all, but rather will suffer from the well-known Gibbs phenomenon whereby the solution converges only algebraically in an oscillatory fashion as the discontinuous point is approached. It is due to this phenomenon that a spectral scheme will show poor accuracy in such a system. Canuto *et al* (1988) contains a relevant discussion of the Gibbs phenomenon.

The presence of other types of discontinuity will have a similar effect. In the present system the centre point is a regular singularity, with the function and first derivative being undefined here. Thus the function is non-unique at this point. Uniqueness is enforced by the imposition of boundary conditions, but their application is not 'strong' enough to ensure smoothness properly. It is for this reason that the current system needs to be *analytically* transformed such that this singular point is entirely absent from the analytic formulation. A spectral solution to the untransformed (singular) problem would be expected to converge to the correct answer, but at an algebraic rate; whereas a transformed (non-singular) problem would exhibit spectral convergence.

16.2.2 Removal of the singularity

The general unsteady stability equation is given by (10.55), which, for convenience is reproduced below:

$$\frac{-i}{\alpha Re}\left[\left(L-\alpha^2\right)^2+\mathfrak{M}L\right]\phi = (u-c)\left[L-\alpha^2\right]\phi - [Lu]\phi, \tag{16.2}$$

with the operator L defined as $L = D^2 - \frac{1}{r}D$, $D \equiv \frac{d}{dr}$. The boundary conditions at the centreline are given as (10.56), or

then a transition study would have to use as initial disturbance the altogether more complicated non-parallel theory; in fact in such a case it would probably be advantageous to simulate the entire process directly. Where non-parallel effects are absent, the linear theory predicts exactly the point at which small disturbances will grow; thus linear instability is a necessary condition for transition in such circumstances. The recent paper by Herbert (1988) serves as a good summary of the current state of thought concerning secondary instability and the transition process.

16.2 Analytical formulation of the unsteady Sexl equation

In order that the stability behaviour of unsteady pipe flow be determined, the unsteady Sexl equation (10.55) needs to be formulated in a manner that is amenable to solution using the operational-Tau methodology. Solution of differential eigenvalue problems using this method was shown to be straightforward in section 13.1; however, the present problem is not as simple mathematically as the Orr-Sommerfeld relation, due to the presence of a singularity in the solution domain at the origin. This section is largely concerned with the removal of this singularity, resulting in a numerical formulation that allows accurate solution of the unsteady Sexl problem.

16.2.1 A singularity as a hindrance to spectral accuracy

Simple finite-difference schemes are usually insensitive to analytic properties of the solution space; for instance a finite-difference scheme can be successfully used to model shock phenomena, even though in terms of the mathematical description, a shock interface is a discontinuity. Global-analytical methods such as the operational-Tau method on the other hand attempt to represent the entire solution in a space where the function and *all* its derivatives are smooth. Where the underlying function *is* smooth, such methods attain infinite-order accuracy; however in the presence of a singular or discontinuous point in the solution domain, convergence rates collapse to algebraic, and the accuracy of solution is no better (and in most cases far worse) than an equivalent finite-difference scheme. The mechanism for the collapse of the convergence rate to algebraic can be illustrated by analogy to the Fourier system[5]. The Fourier

[5]All of the spectral methods represent an unknown function as a series expansion in a suitable orthogonal basis. The behaviour of such series' are analogous to the Fourier system in that the magnitude of the higher-order coefficients decay at a rate greater than any power of order [Canuto *et al* (1988)], and direct comparison can be drawn between a Fourier system and for instance the Chebyshev expansion.

has been made to incorporate non-parallel effects into the analysis of the pipe entrance flow. However the equivalence of the flow near the inlet to the flat-plate boundary layer allows the use of results obtained for that system to be applied to the pipe inlet. In the context of the Blasius boundary layer, the applicability of non-parallel stability has been controversial. Certain authors [Bouthier (1972, 1973), Levchenko & Solovyev (1974), Saric & Nayfeh (1975)] have achieved results using non-parallel approaches that agree substantially with the available experimental data of Schubauer & Skramstad (1947) and Ross *et al* (1970) (and therefore show a large deviation from the results of parallel theory); however other authors [Barry & Ross (1970), Gaster (1974)] gave results where the inclusion of non-parallel effects led only to a small reduction in the minimum critical Reynolds number.

Fortunately some light has lately been brought to bear on the subject. In a recent paper by Fasel & Konzelmann (1990), it was shown by direct numerical simulation in the context of a flat-plate boundary layer, that non-parallel[4] effects account for only a small part of the difference between the experimental results and the unmodified parallel analysis. Notably these authors vindicate the conservative analysis of Gaster (1974), who by means of an asymptotic method achieved results remarkably close to their data. Furthermore, Fasel & Konzelmann discredit the results of authors such as Bouthier (1972, 1973). Bouthier achieved remarkable agreement between his non-parallel analysis of the flat plate system and the experimentally observed transition values; however Fasel & Konzelmann have shown this agreement to be fortuitous, because of Bouthier's use of physically inconsistent assumptions when comparing his theory to experiment. Fasel & Konzelmann conclude that the discrepancies between theory and experiment cannot be accounted for by non-parallel effects, and suggest that adverse pressure gradients, source-disturbance coupling[4], or non-linear effects may be the actual culprits.

In section 14.4.6, and in Abbot & Moss (1994), it was shown that the flow close to the pipe inlet plane approached the structure of the flat plate boundary layer. The parallel criterion [defined in both the above mentioned section and in Abbot & Moss (1994)] was used to demonstrate that the maximum degree of non-parallelness in a pipe is found towards the inlet, where the degree of the non-parallel behaviour was asymptotic to that of the flat-plate boundary layer. Thus by inference it was shown that, towards the position in the pipe at which the minimum critical Reynolds number occurs, non-parallel effects are virtually absent from the system. The unimportance of non-parallel effects in the transition process in pipe entrance flow is an extremely important result, in that it allows the theoretical description of this process to proceed directly from the linear scenario. Transition to turbulence in an environment where the level of background disturbance is small is well described firstly by the standard linear theory, and then by the resultant interaction of the linear perturbations via non-linear finite amplitude effects. If non-parallel effects were important,

[4] This effect occurs when the disturbance source (a vibrating ribbon) is placed too close to the region of interest, thus disrupting the phenomenon to be observed.

of 10 874. da Silva surmised that his lower result indicated the correctness of his data, as it was closer to the experimental study of Sarpkaya (1975) [shown superimposed in figure 16.1]. However the 'gain' in agreement is insignificant, especially considering that the nature of the two data differs fundamentally[3]. It is thus more important to find other mechanisms whereby pipe flow can be destabilised (and thus reconciled with Sarpkaya's results), rather than try to explain these experimental results using the simple linear theory alone.

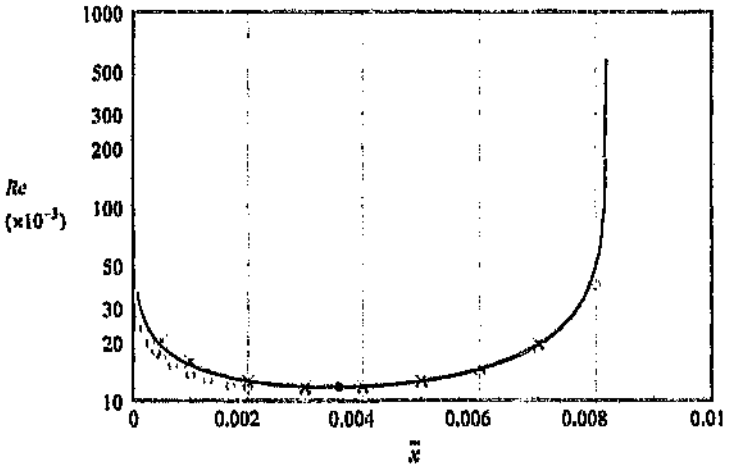

Figure 16.2: The axial variation of the critical Reynolds number for axisymmetric disturbances in steady-state pipe entrance flow: ×, Garg (1981); ○, da Silva (1990); , Abbot & Moss (1994); •, minimum critical Reynolds number.

The Garg data align almost exactly with the present study at the nose of the stability curves, but are slightly higher than the present data both upstream and downstream of this region. This misalignment is, however, small and is biased towards higher Reynolds numbers. The specific details of Garg's calculations are unknown, but this trend indicates either a possible lack of convergence, or insufficient order of discretisation in his eigenvalue solution. Both the above causes would be manifest at higher Reynolds numbers, where the numerical problem requires high precision and increased order to achieve accurate results.

A detailed discussion on the level of non-parallel effects was given in section 1.4.1.6, in the context of the laminar pipe entrance flow, and the level of this non-parallelism was quantified for these flows. The following section is concerned specifically with the effect of non-parallelism on the stability analysis. Some of the previously introduced arguments are repeated here for clarity.

A reservation may be raised about the relevance of a linear *parallel* stability analysis in a pipe entrance, where there is a definite non-zero radial flow component. No direct attempt [except for a proposed model by da Silva (1990)]

[3]The experimental data extend far downstream while the linear theory curve increases abruptly beyond a particular axial station.

It was because of the limitations inherent in the above data that da Silva (1990) undertook an analysis unbound to any approximate base flow system. To obtain an accurate series of pipe entrance profiles for high Reynolds numbers he solved the axisymmetric incompressible Navier-Stokes equations in the high Reynolds number (Re independent) limit as a finite-difference system. The data from this analysis was fed directly into his finite-difference temporal stability analysis. His analysis thus avoided any gross approximations; for this reason his results could be inferred to be the most accurate of the above. Although da Silva's finite difference formulation was implemented with extreme care (high order, a graded mesh system and the use of a vorticity-transport formulation[3]), reservation can be placed on a number of aspects of his study:

(i) The use of a simple and temporally explicit first-order finite-difference base flow model was inappropriate for a stability analysis.

(ii) The use of the finite-difference methodology to solve the badly scaled fourth order Sexl stability equation was subject to the same criticism as in point (i) above.

(iii) The causality problem with the boundary conditions inherent in the vorticity-transport method, as intimated in chapter 10, combined with the physically invalid upwinding discretisation, possibly introduced a systematic error into his base flow model, thus invalidating his stability analysis.

In a recent paper on pipe flow stability, Abbot & Moss (1994) used the spectral base flow model of chapter 14 to generate a highly accurate set of velocity profiles for use in a stability analysis. This stability calculation was simply the implementation the algorithm of section 16.4 on these profiles. The comparison of these data to that of both da Silva and Garg is shown in figure 16.2. As can be seen, the present data are higher than the da Silva data, but align almost perfectly with the results of Garg. This vindicates the results of Garg, especially his use of the Hornbeck approximate velocity profiles. This approximate model is thus accurate enough to be used in a pipe entrance stability analysis. The prime culprit in the deviation of the da Silva model from the present data is thought to be the vorticity-transport formulation. His superficially logical argument, that the benefit of avoiding second derivatives was an advantage of the method, is flawed in that the error introduced by the explicit boundary conditions in vorticity at the wall, swamp any gain in accuracy produced by the elimination of second derivatives. It is quite possible that if da Silva had produced data using a primitive variable approach, his results would have actually been more accurate, not less so. It is interesting that the minimum critical Reynolds number of 11667 obtained in the present study is substantially higher than da Silva's value

[3]Use of the vorticity-transport formulation allows for the solution to be determined directly as a velocity derivative, avoiding any explicit second order differentiation in the base flow solution. While avoiding such operations is important in a finite-difference approach, it is of no consequence in a spectral method, because of the infinite differentiability of the spectral basis functions.

profile occurs; i.e. to the values of these parameters at the nose of the neutral stability curves in the α - Re plane.

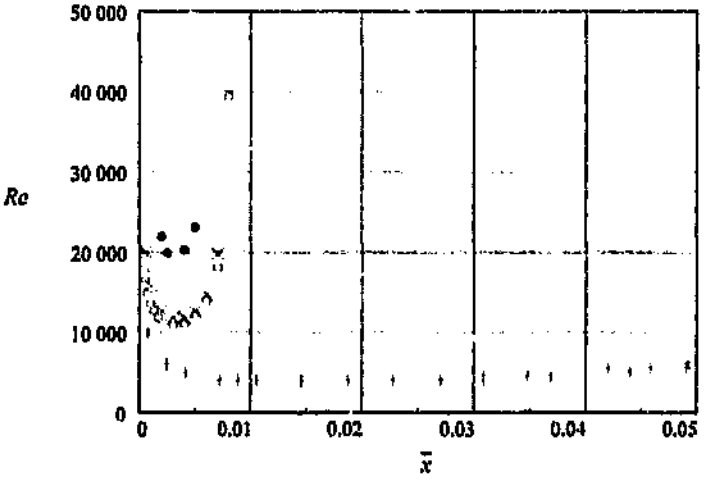

Figure 16.1: The axial variation of the critical Reynolds number for axisymmetric disturbances in steady-state pipe entrance flow, showing the results of various Authors: •, Huang & Chen (1974); ×, Garg (1981); ○, da Silva (1990); +, Sarpkaya (Experimental).

The early results of Tatsumi used a boundary layer-like approximation to the Sexl equation, ing with a set of *almost similar* velocity profiles. Although his results show qualitatively the correct behaviour, they are generally believed to be unreliable. The study by Huang & Chen (1974) investigated the temporal stability behaviour of the entrance. These authors used the Sparrow *et al* (1964) base flow model to generate the velocity profiles used in the stability analysis. While the use of a simplified base flow model might at first seem sensible in order to lessen the calculation burden[1], the sensitivity of the stability results to the base flow profile as demonstrated by Gupta & Garg (1981) places in question *any* stability calculation based on an approximate model.

Gupta & Garg [Gupta & Garg (1981), Garg (1981)] used an approximate base flow solution - the Hornbeck (1963) model - in order to better determine the stability response of the entrance system. This particular model has been shown by *inter alia* Schmidt & Zeldin (1969), Crane & Burley (1976) and Shah (1976) to be more reliable than the earlier Sparrow model. One would thus expect the Garg results to be closer to the actual curves than the earlier data. However, by virtue of the Hornbeck model itself being only approximate, Garg's results are themselves arguably subject to the same criticism levelled at those of Huang & Chen.

[1] While the full axisymmetric laminar pipe entrance flow system was solved in chapter 14, this accurate and economical solution was only possible because of the development of spectral techniques in conjunction with powerful modern computing facilities. Such tools were not available until very recently.

Chapter 16

The stability of steady pipe entrance flows

Theory applicable to the determination of the stability of generally accelerated velocity profiles was developed in chapter 10. No numerical solution of the unsteady stability equation was attempted; however, a similar equation - the Orr-Sommerfeld relation - was solved numerically in chapter 13, for the case of plane Poiseuille flow.

In this chapter, the stability equation (10.55) is cast in a form amenable to solution using the operational-Tau approach. Notably, the regular singular point existing at the pipe origin for this equation is removed by a simple transformation. The resulting equation is then formulated numerically using the tools derived in section 13.1. Although the general unsteady stability equation is discretised here, only the results for the stability of the zero-acceleration pipe entrance flow are presented, in order that comparisons can be drawn to existing stability results in the literature. The base flow velocity profiles used for the stability analysis in this chapter are those calculated previously in chapter 14. The more general accelerating stability results are then presented in chapter 17 that follows.

16.1 General overview

Some numerical study has been directed towards determining the response of pipe entrance flow to linear perturbations. Relevant investigations are notably those by Tatsumi (1952), Huang & Chen (1973, 1974), Gupta & Garg (1981), Garg (1981) and da Silva & Moss [da Silva (1990), Moss & da Silva (1993), da Silva & Moss (1994)]. These data are shown plotted in figure 16.1. The subscripts [crit] here and subsequently refer to the conditions (those particular values of α, Re) at which the lowest unstable Reynolds number for a particular

Chapter 16

The stability of steady pipe entrance flows

Theory applicable to the determination of the stability of generally accelerated velocity profiles was developed in chapter 10. No numerical solution of the unsteady stability equation was attempted; however, a similar equation - the Orr Sommerfeld relation - was solved numerically in chapter 13, for the case of plane Poiseuille flow.

In this chapter, the stability equation (10.55) is cast in a form amenable to solution using the operational-Tau approach. Notably, the regular singular point existing at the pipe origin for this equation is removed by a simple transformation. The resulting equation is then formulated numerically using the tools derived in section 13.1. Although the general unsteady stability equation is discretised here, only the results for the stability of the zero-acceleration pipe entrance flow are presented, in order that comparisons can be drawn to existing stability results in the literature. The base flow velocity profiles used for the stability analysis in this chapter are those calculated previously in chapter 14. The more general accelerating stability results are then presented in chapter 17 that follows.

16.1 General overview

Some numerical study has been directed towards determining the response of pipe entrance flow to linear perturbations. Relevant investigations are notably those by Tatsumi (1952), Huang & Chen (1973, 1974), Gupta & Garg (1981), Garg (1981) and da Silva & Moss [da Silva (1990), Moss & da Silva (1993), da Silva & Moss (1994)]. These data are shown plotted in figure 16.1. The subscripts [crit] here and subsequently refer to the conditions (those particular values of α, Re) at which the lowest unstable Reynolds number for a particular

to the entrance type of flow. This framework of representation was devised to allow direct comparison to, and verification of, the experimental results, which is done later in part IV.

With the base flow comprehensively quantified, the following two chapters are concerned with the linear stability behaviour of these flows.

15.8 Summary

The various aspects of the behaviour of the laminar pipe entrance flow under conditions of exponential acceleration were investigated numerically. In all cases the flow was started impulsively to a high Reynolds number; thereafter it was accelerated exponentially. Eight different accelerations were investigated, starting from the zero (steady) case, and increasing the acceleration parameter in steps of 10 up to $\bar{\Omega} = 70$. A number of issues were considered:

(i) The far downstream, parallel, temporally developing flow was investigated because it simplified substantially the governing equations. Both their transient and limiting behaviour were studied, and the parameters introduced in previous chapters (shape parameter, displacement thickness, scaled displacement thickness) were used successfully to characterise these flows.

(ii) The steady-state (in the normalised co-ordinate system) behaviour of the accelerating pipe entrance was investigated. The flow towards the inlet was shown to approach the Blasius limit, independent of the acceleration parameter. Away from the inlet, the velocity profiles approached the same velocity profile limit as for the temporally developing parallel profiles.

(iii) The full temporal and spatial development of the entire pipe flow, from the impulsive start, to a state of invariance in the normalised basis, was shown to be closely approximated by a combination of the steady entrance model upstream, matched to the simplified parallel model further downstream.

(iv) The effect of the Reynolds number dependent mapping on the data was investigated. The simplicity of the general solution in the normalised basis (much like steady impulsive pipe flow) was shown to yield complex behaviour when transformed into the physical domain. To illustrate this behaviour, sets of curves were generated showing the temporal and spatial (in the normalised framework) variation of displacement thickness from the perspective of the physical co-ordinate system. Two sets of curves were given: firstly, the *temporal* variation of δ^*/R from different fixed physical positions, and secondly, the variation in $\bar{x}$ of δ^*/R for a set of fixed physical stations.

(v) The two representations discussed above in particular allowed data 'measured' from any fixed axial position in the physical co-ordinate system to be compared to both the simpler theoretical models. For a particular acceleration, data from the parallel, temporally developing portion of the flow fell on the single parallel curve in the $\bar{t}$ - δ^*/R framework, while the entrance part of the data aligned with the steady entrance curve in the $\bar{x}$ - δ^*/R system. Only a small portion of the full data did not align with either curves - that portion associated with the transition from the parallel

the critical point of the neutral stability curve is contained in section 13.1. The current section is concerned about the entire neutral curve; its shape indicating the nature of the flow system. Figure 16.7 shows a series of neutral curves for selected velocity profiles between the inlet and the point at which linear instability ceases to occur. The scale is logarithmic in order to show properly the full behaviour of these data. Further to this the wavenumber and Reynolds number in this figure are both scaled with respect to the boundary layer parameters; i.e. the curve is represented in the $\alpha_{\delta^*} - Re_{\delta^*}$ plane. Also shown in this figure is the neutral curve for the Blasius boundary layer. It is clearly evident that this is the limiting behaviour of pipe entrance flow toward the inlet.

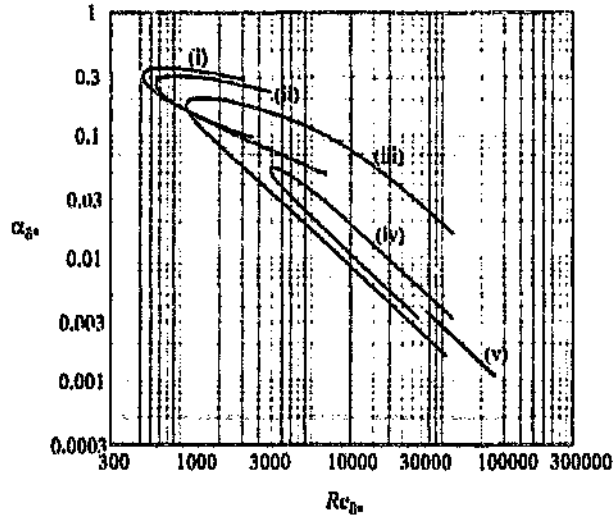

Figure 16.7: Neutral stability curves in the $\alpha - Re$ plane, for selected velocity profiles: (i), $\tilde{x} = 0$ (Blasius boundary layer limit); (ii), $\tilde{x} = 0.000\,197$; (iii), $\tilde{x} = 0.003\,59$ (Minimum critical point); (iv), $\tilde{x} = 0.007\,83$; (v), $\tilde{x} = 0.008\,18$.

The behaviour downstream is also noteworthy. Downstream of the point of minimum critical Re (at $\tilde{x} \approx 0.003\,59$), the curves contract towards, with the upper and lower branches approaching each other until, for $\tilde{x} = 0.00818$, they are virtually concurrent. This strongly indicates that velocity profiles downstream of the latter point *show no linear instability*.

Broadly speaking, these curves show two types of behaviour when moving downstream from the inlet plane. Close to the inlet, successive curves show a 'rotation' away from the Blasius curve. This trend continues until approximately the point of minimum critical Reynolds number, thereafter the curves are successively contained by the ones upstream, until they vanish altogether beyond $\tilde{x} = 0.008\,18$.

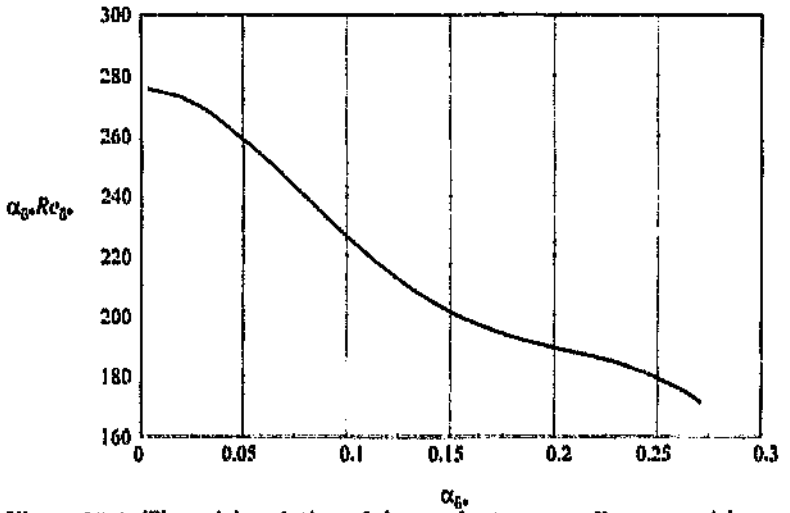

Figure 16.6: The axial variation of the product $\alpha_{\delta^*[\mathrm{crit}]}Re_{\delta^*[\mathrm{crit}]}$ with wavenumber $\alpha_{[\mathrm{crit}]}$ for axisymmetric disturbances in steady-state pipe entrance flow.

effects must be important for the predominance of the pipe entrance. This conclusion overturns the perspective that non-parallel effects have a part to play in pipe stability. The above argument is reflected in the paper by Abbot & Moss (1994).

16.5.5 The point of maximum instability in a pipe

Due to the unbounded behaviour of the critical parameters as the inlet plane is approached, it is sensible to categorise the flow here by scaling the parameters according to the boundary layer dimension. However, the physical flow in a pipe at any one time will possess a fixed Reynolds number based on pipe radius everywhere, and in order to determine which portion of the pipe entrance becomes unstable first in some chosen flow, one needs to re-consider the critical Reynolds number $Re_{[\mathrm{crit}]}$ based on radius and mean cross-sectional velocity. The variation of this parameter was given in figure 16.2 and these data show a minimum value for the critical Reynolds number of 11 667 at an axial position of $\tilde{x} = 0.003\,59$. Table C.17 shows these minimum critical values underlined.

16.5.6 Neutral stability curves

The critical Reynolds number for a particular pipe velocity profile is obtained by determining the point of minimum Re of the $c_i = 0$ curve in the α - Re plane. In fact all the parameters presented previously concerned the fluid quantities corresponding to this point. A detailed description of the method of finding

$c_{[crit]}$ corresponds approximately to the velocity of the critical layer in the pipe boundary layer. Again, considering the boundary-layer like nature of the pipe inlet, it is more appropriate to scale $c_{[crit]}$ according to the boundary layer parameters. The appropriate scaling quantity here is the ratio of the mean velocity to that at the centreline. A new boundary layer celerity can thus be introduced as

$$\tilde{c} = \frac{U}{u_c} c. \tag{16.26}$$

The numerical value of $\tilde{c}_{[crit]}$ is far more stationary than $c_{[crit]}$ for the entire axial domain considered, decreasing only slightly from $\tilde{c}_{[crit]} = 0.396\,64$ (the Blasius limiting value) at the inlet to $\tilde{c}_{[crit]} \approx 0.375\,46$ at the last station considered. The variation of $\tilde{c}_{[crit]}$ is tabulated in table C.17.

16.5.4 Behaviour with increasing x

While the behaviour for decreasing x shows that the system becomes boundary layer-like near the inlet, other perhaps more interesting behaviour is manifest as x increases. Here, at some finite value of $x \approx 0.008\,2$, the value of $\alpha_{\delta^*[crit]}$ rapidly approaches zero. The consequences of the wavenumber approaching zero somewhere in the domain are profound, the implication being that from this point downstream, *no* critical Reynolds number would exist for the flow [Abbot & Moss (1994)].

Leading from the above, it is interesting to investigate the behaviour of the *product* of critical wavenumber and critical Reynolds number as $\alpha_{[crit]} \to 0$. This product strongly effects the structure of the Sexl stability equation (10.55); if the value of this product were to increase unboundedly then the stability at that point would acquire an inviscid nature, however, if it were to approach some finite value (or zero), then no such conclusion could be drawn. Further to this, if the product were to remain non-zero in this limit then $Re_{[crit]}$ at this point would approach infinity at the rate $1/\alpha_{[crit]}$. The variation of the product $\alpha_{\delta^*[crit]} Re_{\delta^*[crit]}$ with $\alpha_{\delta^*[crit]}$ is shown in figure 16.6. Clearly evident here is the approach of the product to a fixed value of ≈ 275 as the wavenumber tends to zero. This indicates that the system indeed has no finite critical Re at this point. However, because the product $\alpha_{\delta^*[crit]} Re_{\delta^*[crit]}$ does not become infinite, the solution to the equation at this point is not simply the inviscid simplification to the Sexl system.

The relative proportion of the entire entrance which exhibits a finite critical Reynolds number is rather small. The linear instability of the flow can only occur for $0 \leq x \leq 0.0034$, whereas the entrance length (see chapter 14) is about 0.221; thus the magnification of infinitesimal disturbances is only possible in the first 3.8 percent of the total pipe entrance. This shows that finite amplitude

the $\bar{x}$ axis near this point. However, as with the critical Reynolds number, the data is unbounded towards the inlet and thus the curve's behaviour for higher values of $\bar{x}$ is obscured by its high numerical value toward the inlet. Again this is simply due to the incorrect choice of reference frame.

If the wavenumber is scaled as

$$\alpha_{\delta^*} = \alpha \frac{\delta^*}{R}, \tag{16.25}$$

then it shows bounded behaviour towards the inlet. Figure 16.5 shows the present data in this framework. Shown also is the inlet asymptotic limiting value of $\alpha_{\delta^*[\mathrm{crit}]} \approx 0.303\,77$ - the Blasius boundary layer value for this parameter.

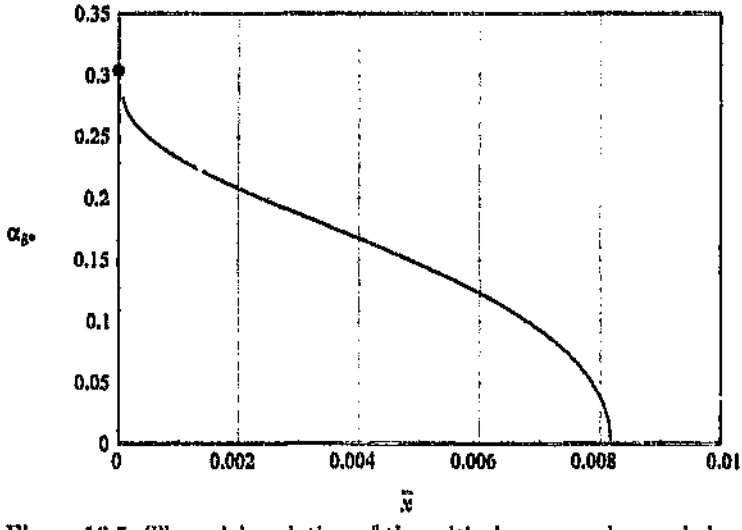

Figure 16.5: The axial variation of the critical wavenumber scaled with respect to displacement thickness, for axisymmetric disturbances in steady-state pipe entrance flow. •, the Blasius boundary layer limit, $\alpha_{\delta^*} = 0.303\,77$.

When scaled according to the boundary layer parameters, the trend towards intersection at the downstream part of the curve becomes marked. This clear limiting tendency here coincides with the vertical asymptotic behaviour of the critical Reynolds number.

16.5.3 Celerity

The celerity or phase speed of the neutrally unstable eigenvalue is designated as $c_{[\mathrm{crit}]}$ and indicates in broad terms the nature of the disturbance. In the current investigation, the most unstable mode is a wall mode with value increasing from $c_{[\mathrm{crit}]} \approx 0.4$ at the inlet to ≈ 0.5 at the last unstable station. The value of

The behaviour of the curves towards the downstream end is notable; both data curve strongly upward here and appear to be asymptotic to a vertical line. The current data however extend da Silva's results by more than an order of magnitude in Reynolds number, the last point on the current data[11] possessing a critical Reynolds number of $Re_{\delta^*[\mathrm{crit}]} = 78\,776$ compared to his value of approximately 5600. Garg again did not take his calculations far enough downstream to indicate any clear limiting behaviour here. This vertical asymptotic behaviour prompted further investigation of the system. The presence of such an asymptote is important; its existence would imply that the remainder of the pipe downstream of this point would not exhibit linear instability. This limiting behaviour is considered in section 16.5.4, but first the variation of the critical wavenumber and celerity are presented.

16.5.2 Wavenumber

The critical wavenumber $\alpha_{[\mathrm{crit}]}$ is the spatial frequency of the most unstable disturbance in the pipe entrance. In the case of the temporal stability analysis used here, this parameter is real-valued. The variation of the critical wavenumber with x is given in figure 16.4.

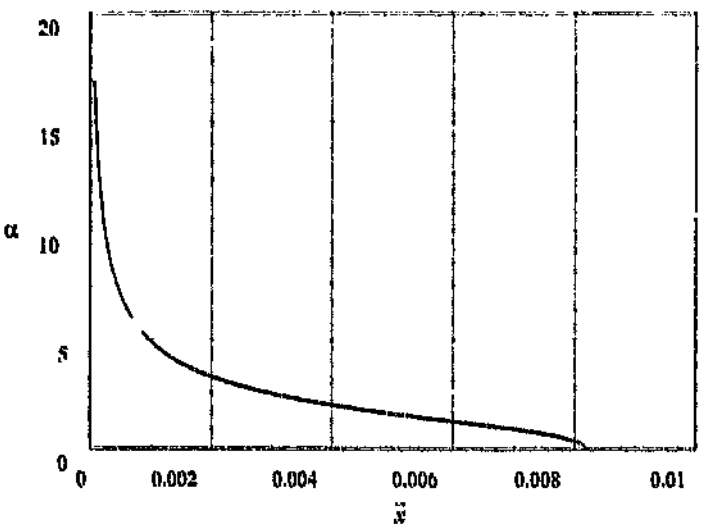

Figure 16.4: The axial variation of the critical wavenumber, for axisymmetric disturbances in steady-state pipe entrance flow.

The critical wavenumber decreases rapidly from infinity at the pipe inlet with a decreasing slope, then gradually approaches zero. For values of x greater than 0.008, the curve again increases in slope, and appears to intersect abruptly with

[11] This final unstable profile was obtained by interpolating between the velocity profiles at the adjoining Gauss-Lobatto points, using a spectral transformation.

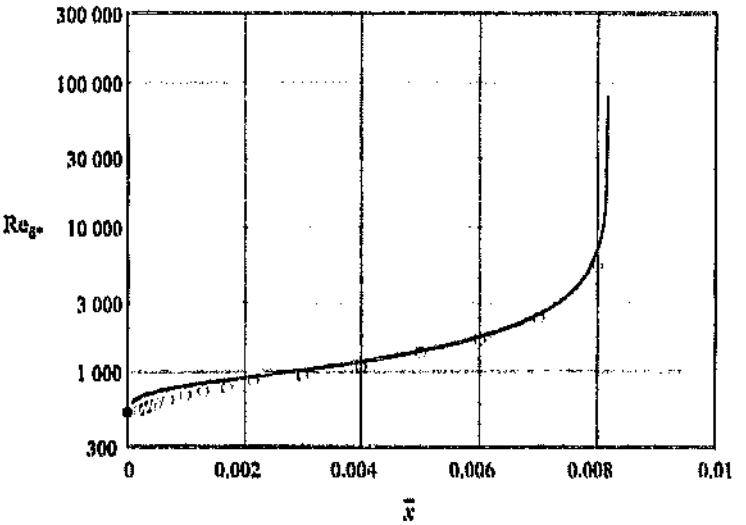

Figure 16.3: The axial variation of the critical Reynolds number based on displacement thickness, for axisymmetric disturbances in steady-state pipe entrance flow: ○, da Silva (1990); ···, Abbot & Moss (1994); ●, Blasius boundary layer limit $Re_{\delta^*[crit]} = 519.06$.

solution however, accuracy was maintained in this limit by increasing the order of solution. This was possible because of the infinite-order convergence behaviour exhibited by the spectral approach.

The Blasius boundary layer stability limit of $Re_{\delta^*[crit]} = 519.06$ is shown on the vertical axis. Both data approach this limit closely; however that of da Silva actually dips slightly below the value of 520 before $\bar{x} = 0$ is approached. The current data initially heads toward a point much higher than this value, curving down to 520 quite abruptly. This abrupt behaviour indicates that the effects of the axisymmetry are still prevalent even when the boundary layer is very thin. Before the current data became available, it was thought that the da Silva data [as contrasted to the Garg (1981) results] was more accurate towards the inlet plane, primarily due its apparent better and more regular convergence to the Blasius stability limit here. The Garg results appeared to be heading to a limiting value much higher than the correct one. This argument was used by da Silva & Moss (1994) to infer the correctness of their data. The present data shows an identical trend to Garg's results for intermediate values of $\bar{x}$, as mentioned dipping to intersect the axis at 520 quite abruptly. The 'incorrect' trend apparent in Garg's data described by da Silva & Moss (1994) was thus only due to his not performing calculations close enough to the pipe inlet[10].

[10]He was possibly unable to obtain critical Reynolds numbers any closer to the inlet due to limitations in his numerical approach.

16.5.1 Displacement thickness Reynolds number

While the $\bar{x}$ - $Re_{[crit]}$ co-ordinate system of figure 16.1 might well indicate the disparities between the different data, there is no means of directly inferring which data is more correct in this framework. This is primarily because both towards the limit $\bar{x} \to 0$, and for increasing $\bar{x}$, the critical Reynolds number of the flow increases without bound. A far more meaningful way of viewing the behaviour of the flow close to the inlet is by transforming the system such that all variables are scaled according to properties of the thin boundary layer. This approach was adopted in the context of the laminar base flow in chapter 14, and was used in the paper by da Silva & Moss (1994), also in the context of the pipe entrance flow. That the boundary layer framework is valid in this context can be shown by simple inference. Consider a pipe entrance velocity profile consisting of a thin boundary layer matched to a uniform core flow. Suppose also that this particular velocity profile possesses a minimum critical Reynolds number $Re_{[crit]} = U_{[crit]}R/\nu$. Such a profile, as the boundary layer thickness approaches zero, will have a value for $Re_{[crit]}$ that increases without bound, simply because the stability behaviour of such a system is a boundary layer phenomenon. If the Reynolds number Re is scaled according to the boundary layer displacement thickness $\delta^*/R = \frac{1}{2}(1 - \frac{U_m}{u_c})$ and the centreline velocity u_c as

$$Re_{\delta^*} = \frac{u_c \delta^*}{\nu} \tag{16.23}$$

then the value of $Re_{\delta^*[crit]}$ should approach the boundary layer stability value of approximately 520 as the boundary layer thickness $\delta^*/R \to 0$. This is because, in this limit, the boundary layer loses knowledge of its pipe-like nature and becomes more like a flat plat flow. Using the definition (16.23), a transformation can be defined to calculate the appropriate value of $Re_{\delta^*[crit]}$ when given $Re_{[crit]}$. This is as follows:

$$Re_{\delta^*} = Re \frac{\delta^*}{R} \frac{u_c}{U}. \tag{16.24}$$

Using equation (16.24), the data of figure 16.2 can be transformed into a boundary-layer like framework. The result of applying this equation to the data is shown in figure 16.3. The data of da Silva (1990) is superimposed for comparison.

As in figure 16.1, the two sets of data shown in the figure agree fairly well. Their deviation from one another is greatest towards the pipe inlet. This would be expected for two reasons. Firstly, the numerical system requires higher accuracy towards the boundary layer limit and the finite-difference scheme of da Silva thus shows its deficiency here. Secondly, the error due to the vorticity transport formulation would also be expected to be higher in this limit, mainly due to the higher spatial rate of change in the flow here. For the current spectral

16.4.3 Method of solution

Equation (16.20) is simply an algebraic matrix eigenvalue problem and is easily solved using standard numerical software. The current problem was solved as before using Matlab standard routines. The relevant Matlab scripts used for the solution are to be found in appendix D. Notably, Matlab provides the QZ algorithm [Wilkinson (1979)] which allows one to obtain directly the eigenvalues and eigenfunctions of the system for the various base flow profiles investigated.

Solution order was taken as $N = 80$ for most of the solutions obtained. Investigation of the limiting behaviour towards the inlet necessitated the use of increased orders of solution. All solutions were of course undertaken on base flows solved in previous chapters, and for this reason the dimension of the base flow coefficient vector $\vec{a}$ was fixed, in most cases also at $N = 80$. The strong advantage of the Tau method was apparent here in that no matching of dimension was necessary between the base flow and stability investigation. Thus it was possible to solve any combination of base flow - stability order[8].

Limiting behaviour of the system for early times and short axial displacements was determined by obtaining stability results for the error function profile and Blasius boundary layer solutions respectively, these being the proper limiting behaviours of the system in these limits[9]. The recent paper by Abbot & Moss (1994) investigated the stability of the steady-state pipe inlet and found that it possessed rather startling stability behaviour commensurate with its becoming Blasius-like. Limiting stability behaviour of the flow as $\hat{t} \to 0$ has, with the exception of the qualitative study by Moss (1985), not been investigated in the literature and will thus be covered here in some detail. What follows is the presentation of the stability data, firstly for the steady-state (impulsively started) systems, and later for the more general exponential cases.

16.5 Comprehensive results

The above section was primarily concerned with comparison of the present data with existing results. What follows is the presentation of the various parameters concerning the stability of the steady pipe entrance.

[8] If the base flow is of a higher order than the stability system, then the extra coefficients of the base flow will simply be ignored by truncation. If the stability is of a greater order than the base flow then the solution will be for a base flow vector with extra zeroes appended up to the order of the stability system.

[9] The investigation of chapter 15 showed that the base-flow behaves like a Blasius or a parallel flat-plate boundary layer in these limits respectively.

namely (16.8). These in the Tau system become

$$\vec{\phi}\hat{B}_L = c\vec{\phi}\hat{B}_R, \tag{16.15}$$

where $\hat{B}_R$ is simply an $N \times 2$ matrix of zeroes and $\hat{B}_L$ is given by

$$\hat{B}_L = \left[\hat{F}|_{\hat{r}=1} \quad \hat{\eta}\hat{F}|_{\hat{r}=1}\right] = \begin{bmatrix} 1 & 0 \\ 1 & 2 \\ 1 & 8 \\ 1 & 18 \\ \vdots & \end{bmatrix}. \tag{16.16}$$

As before, the application of these boundary conditions are carried out by means of a simple augmentation. If the equation (16.12) is represented in a more compact notation as

$$\vec{\phi}\hat{D}_L(\vec{u}) = c\vec{\phi}\hat{D}_R; \tag{16.17}$$

$$\begin{aligned} \hat{D}_L \equiv & \frac{-i}{\alpha Re}\left[\hat{P} + (\bar{\Omega} - 2\alpha^2)\hat{Q} + \alpha^4\hat{\beta}^3\right] \\ & - \left[\hat{Q} - \alpha^2\hat{\beta}^3\right]\cdot\hat{R}(\vec{u}) + \hat{\mathcal{R}}\left(\vec{u}\hat{T}\right), \end{aligned} \tag{16.18}$$

$$\hat{D}_R \equiv \left[\hat{Q} - \alpha^2\hat{\beta}^3\right], \tag{16.19}$$

then the full system to be solved numerically is

$$\vec{\phi}\hat{\Pi}_L = c\vec{\phi}\hat{\Pi}_R \tag{16.20}$$

with

$$\hat{\Pi}_L = \left[\hat{B}_L \vdots \hat{D}_L\right], \tag{16.21}$$

$$\hat{\Pi}_R = \left[\hat{B}_R \vdots \hat{D}_R\right]. \tag{16.22}$$

16.4.1 Basic equations

Consider again equation (16.6), along with the operators (16.7) and boundary conditions (16.8). All the terms in (16.7) are, after multiplication through by r, members of the set $\mathcal{Q}$ of operators with polynomial coefficients (see section 12.2 for a detailed discussion on this family of operators); they can therefore be formulated directly in the Tau system. Using the theory of chapter 12, the analogues of the equation (16.6) and operators (16.7) in the Tau system (after multiplication by $\vec{r}$) are

$$\begin{aligned} &\frac{-i}{\alpha Re}\vec{\phi}\left[\hat{P}+\left(\Omega-2\alpha^2\right)\hat{Q}+\alpha^4\hat{\mu}^3\right]= \\ &\vec{\phi}\left[\hat{Q}-\alpha^2\hat{\mu}^3\right]\left(\hat{\mathcal{R}}(\vec{u})-cI\right)-\vec{\phi}\left[\hat{\mathcal{R}}\left(\vec{u}\hat{T}\right)\right], \end{aligned} \tag{16.12}$$

$$\begin{aligned} \hat{P} &= \hat{\eta}^4\hat{\mu}^3+6\hat{\eta}^3\hat{\mu}^2+3\hat{\eta}^2\hat{\mu}-3\hat{\eta} \\ \hat{Q} &= \hat{\eta}^2\hat{\mu}^3+3\hat{\eta}\hat{\mu}^2 \\ \hat{T} &= \hat{\eta}^2\hat{\mu}^3-\hat{\eta}\hat{\mu}^2. \end{aligned} \tag{16.13}$$

The perturbation streamfunction in the Tau system is defined as

$$\check{\phi}=\vec{\phi}\vec{e} \tag{16.14}$$

where $\vec{\phi}$ is a row vector of unknown coefficients onto the Chebyshev basis vector $\vec{e}$. The infinite matrices $\hat{\eta}$ and $\hat{\mu}$ are the differentiation and polynomial shift operators respectively. These were defined in section 12.2. $\hat{\mathcal{R}}()$ is the polynomial convolution operator. The matrix I is simply the identity matrix; the remaining terms carry their usual meanings.

The matrices in the system (16.12), (16.13) are of course infinite. A solution is now sought in the subspace P_{N-1} of polynomials with order less than N by truncating the assembled system at dimension $N\times N$. The series solution (16.14) would be expected to converge uniformly everywhere to the exact solution at an order greater than any power of N. Before such construction and solution can take place however, the relevant boundary conditions must be augmented to the infinite numerical system (16.12) in order that the resultant solution be unique.

16.4.2 Boundary conditions

The boundary conditions are augmented in an identical fashion to section 13.1; however in the present system there are only two conditions to be applied,

relat ons. If one was interested in the linear growth rate of the disturbance, then he particular nature of the scheme (temporal or spatial) would become impor ant; however such a study would quite probably use a direct simulation and no a linear prediction anyway. Therefore the temporal study of linearised disturba ces in the present context of identifying the inception of transition is a reason ble one.

While the breakdown of real flows is a complicated non-linear process, the simple linear s bility analysis can be used as the leading approximation to a finite amplitude s bility analysis. Direct numerical simulation of transition by *inter alia* Sandha. ı & Kleiser (1992) vindicate linear stability theory as an accurate descripti of the initial stages of transition in an environment where he background d. turbances are small[7]. They show authoritatively that the linear modes are tho selected by the later Tollmein-Schlichting waves that develop on the way to t e formation of Λ vortices in the flow. The secondary stability behaviour of th flow beyond the linear domain is well described in this paper, while the w k by Herbert (1988) affords an excellent summary of recent thinking in this su ject. The parallel linear theory used here is thus directly applicable as a leadi g term to a finite-amplitude study of instability. The parallel results are howeve not useful if non-parallel effects are dominant, and in this case other methods must be used [See for instance Gaster (1974)]. Howeve , it has been shown by Moss & da Silva (1993), and more rigorously in Abbot & Moss (1994) that n n-parallel effects are wholly insignificant in pipe entrance stability. These two studies are in agreement with the numerical simulation of Fasel & Konzelman (1990) which shows, in the context of flat-plate boundary layers, that non-pa allel effects have recently received more prominence than they deserve. This aper shows that the various non-parallel methods' agreement with theory [f instance Bouthier (1972), (1973)] was fortuitous.

In conclusion, the u e of parallel temporal linear stability theory for a pipe entrance region is a v lid approach to adopt, in order to determine the inception of instabilities in thi system in the absence of bypass effects. A subsequent section discusses the near stability of the impulsively started pipe entrance. Results are presented i comparison to existing data, in order that the current approach be verified. I owever the operational-Tau formulation of the unsteady Sexl equation must be rst given.

16.4 Numerica formulation

Numerical formulation of a related eigenvalue problem - the Orr-Sommerfeld equation - was given in section 13.1 of chapter 13. The approach here is equivalent and relevant intermediate stages are given for completeness.

[7]Transition in an environment where the background perturbations are not small is subject to such effects as *bypass* transition [See Morkovin & Reshotko (1989)].

and spatial stability characteristics of the flow respectively. The temporal stability of the flow is determined if the wavenumber α of the disturbance is taken as fixed and real. In this case the above equation reduces to a linear differential eigenvalue problem of the form

$$\mathcal{A}\check{\phi} = c\mathcal{B}\check{\phi} \tag{16.10}$$

with the celerity c the generally complex eigenvalue. If however the spatial stability of the flow is to be investigated, then c is taken as a fixed real parameter, and the spatial behaviour of the flow is determined by a non-linear eigenvalue problem of the form

$$\sum \mathcal{A}_i \alpha^i \check{\phi} = 0. \tag{16.11}$$

By far the easier mode of stability to investigate is the temporal one. Here, equation (16.10), independent of the type of numerical scheme used, reduces to a complex linear algebraic matrix-eigenvalue problem when formulated numerically. As such it can be solved by any one of a number of algorithms suitable to such problems. A standard approach would be to use the QZ algorithm [Wilkinson (1979)] as a 'black-box' routine in some high-level mathematical computer language such as Matlab. Iterative (shooting) techniques could also be employed in such a case [by reformulating (16.10) to resemble an initial-value problem], but with the proliferation of modern direct techniques, such an approach is hardly justified. The multifarious approaches for the solution of this system are interesting from a historical perspective, and the reader is referred to da Silva (1990) or Drazin & Reid (1981) for detailed information.

Numerically, the spatial stability formulation (16.11) becomes an algebraic eigenvalue problem with the eigenvalue α entering in a polynomial manner, and a simple means of solution is not readily apparent. However solution methods have been proposed and successfully implemented for this problem; Watson (1962), Gaster (1965), and more recently Bridges & Morris (1984a, 1984b). Notably the latter authors discuss solution to the spatial stability of a similar boundary layer using a companion-matrix approach. Their numerical scheme uses a Chebyshev method, but the main complexity in all cases lies in the treatment of the non-linearity itself, and thus the difficulty with the spatial problem is independent of the method used. Of course the relationship between temporal and spatial instability is discussed in the well-known paper by Gaster (1962).

The spatial approach has been forwarded as being more representative when used in comparison to experimental results, where for instance a ribbon vibrates at a fixed point and the disturbance grows spatially therefrom. While this is a valid viewpoint, the study of the inception of instability is unaffected by this argument because it is inherently concerned with *neutral* disturbances, at which point the temporal and spatial results are equivalent by virtue of Gaster's (1962)

given by the relation

$$\alpha_{\delta^*} = \alpha \frac{\delta^*}{R}. \tag{17.5}$$

Figure 17.4 shows the variation of this parameter with time, for the full range of acceleration parameters considered.

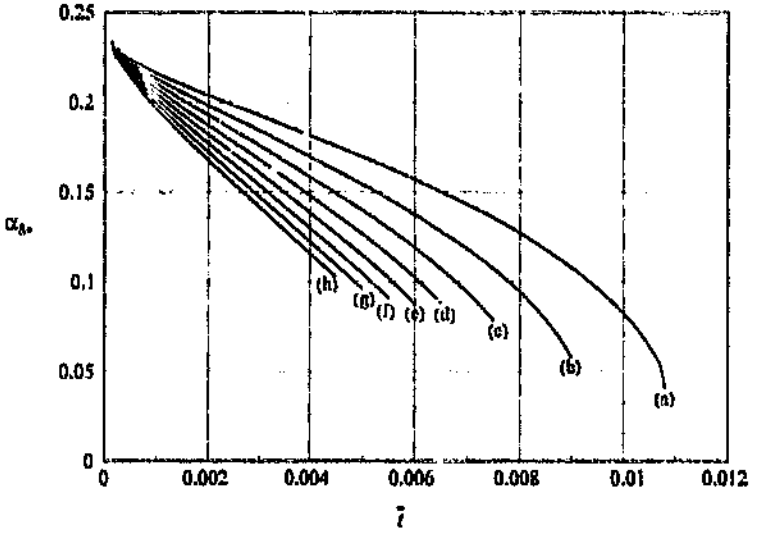

Figure 17.4: The temporal variation of the critical displacement thickness wave number in parallel, temporally developing flow, for discrete values of the acceleration parameter; (a), $\Omega = 0$; (b), $\Omega = 10$; (c), $\Omega = 20$; (d), $\Omega = 30$; (e), $\Omega = 40$; (f), $\Omega = 50$; (g), $\Omega = 60$; (h), $\Omega = 70$.

For time zero, all the data are clearly convergent on the error function limit of $\alpha_{\delta^*} = 0.2401$. As time progresses, all the curves show a consistent decrease in this parameter towards zero as time progresses. For the non accelerating case, the curve bends strongly downwards. This behaviour further strengthens the inference that the critical Reynolds number becomes infinite at a certain time[6]. For the higher acceleration cases, the data does not show as strong a descent to zero, but this is due to the lack of stability data for the further downstream velocity profiles. Again the curves indicate that the final instability time occurs earlier for increasing accelerations.

The stability data presented here are tabulated in appendix C. The tables there show the variation of the relevant critical parameters with time for each value of the acceleration investigated.

[6]See the argument presented in the previous section, and that contained in Arnal et al & Moss (1994) for further explanation.

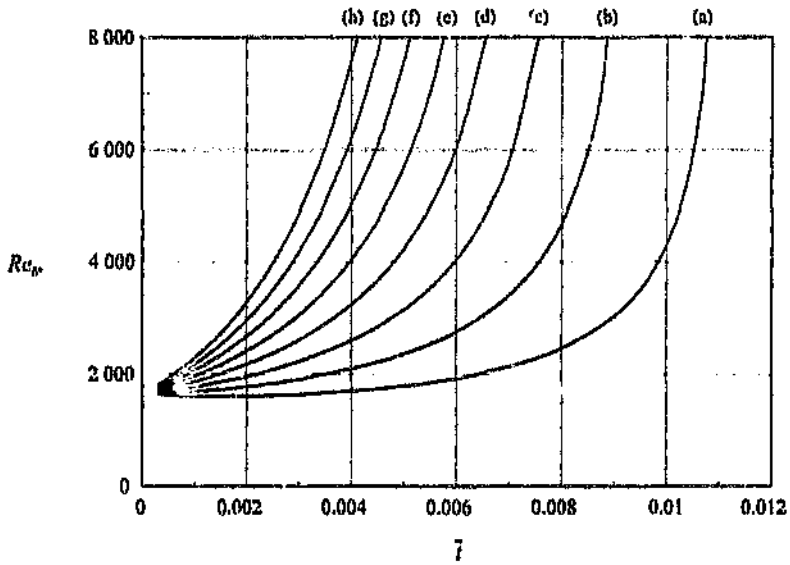

Figure 17.3: The temporal variation of the critical displacement thickness Reynolds number in parallel, temporally developing flow, for discrete values of the acceleration parameter; (a), $\Omega = 0$; (b), $\Omega = 10$; (c), $\Omega = 20$; (d), $\Omega = 30$; (e), $\Omega = 40$; (f), $\Omega = 50$; (g), $\Omega = 60$; (h), $\Omega = 70$.

The critical Reynolds number based on displacement thickness increases away from the error function limit for all values of Ω. The impulsive curve initially shows a very gradual increase then later turns sharply upward. For increasing values of the acceleration parameter the curves show a stronger initial upward trend. All the curves exhibit a slope that increases continually with time; furthermore, they do not intersect each other. This indicates that the flow corresponding to each curve exhibits no linear instability beyond a certain time, and that the value of this time decreases with an increasing acceleration parameter. For the impulsive case, the curve is almost vertical at its downstream end; in fact no instability limit (below $Re = 10^6$) could be found for the velocity profile following that one corresponding to the last point on this curve. For flows with increasing values of the acceleration parameter, the slope of the curves at $Re \approx 10^5$ was still too gradual to allow accurate prediction of their final point of instability[5].

The wavenumber α describes the spatial frequency of the unstable disturbance. As the instability is a boundary layer phenomenon, it is apt to consider the wavenumber with respect to the boundary layer displacement thickness, and

[5]The numerical scheme for Reynolds numbers above 10^5 required increased order of solution to maintain good accuracy. For the higher accelerating flows, the high Reynolds number ($\approx 10^6$) at which this limiting behaviour is shown made calculations unfeasible.

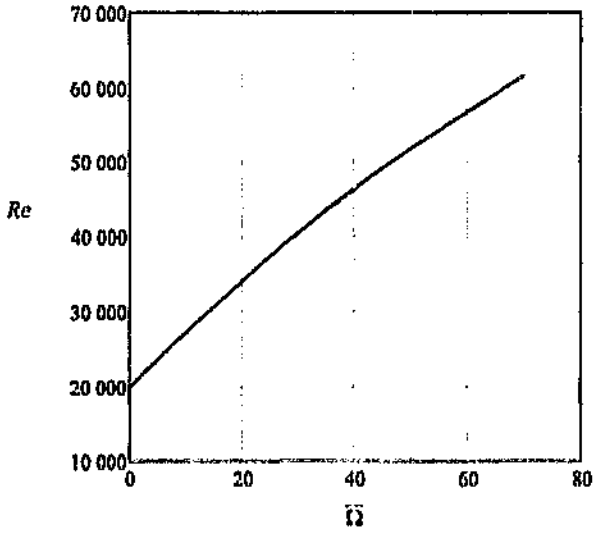

Figure 17.2: The variation of the minimum critical Reynolds number with acceleration parameter in parallel, temporally developing flow.

An interesting comparison can be drawn between the minimum critical Reynolds number for impulsive flow ($\bar{\Omega} = 0$) and the equivalent value of $Re_{[crit]} = 11\,667$ obtained for the steady pipe entrance flow in the previous section. The minimum value for the impulsive parallel flow is $Re_{[crit]} = 19\,879$, approximately twice the magnitude of the former. Thus, generally the impulsively started downstream flow is far more stable than the entrance flow.

As in the case of the pipe entrance flow, the critical Reynolds number for decreasing boundary layer thickness (decreasing time) becomes infinite. This is due to the boundary-layer like nature of the flow in this limit. Instability for all the accelerations occurs only when the boundary layer is thin; thus as before it is appropriate to scale the critical Reynolds number according to the boundary layer as

$$Re_{\delta^*} = Re\frac{\delta^*}{R}\frac{u_e}{U_m}. \tag{17.1}$$

The same data as in figure 17.1 is represented scaled with respect to the boundary layer in figure 17.3.

As in the previous section concerning the pipe entrance system, the use of this ordinate immediately removes the unbounded behaviour in the limit towards $t = 0$. Clearly apparent is that all the curves show as an asymptotic limit the error-function stability value (17.3). Here as before the effect of the acceleration becomes insignificant as δ^* diminishes, with all curves showing the same initial point.

17.1.4 Critical Reynolds number and wavenumber

The variation of the critical Reynolds number in time for each acceleration is shown in figure 17.1. The vertical axis is given using a logarithmic scale, in der to better show the large variation in the critical Reynolds number.

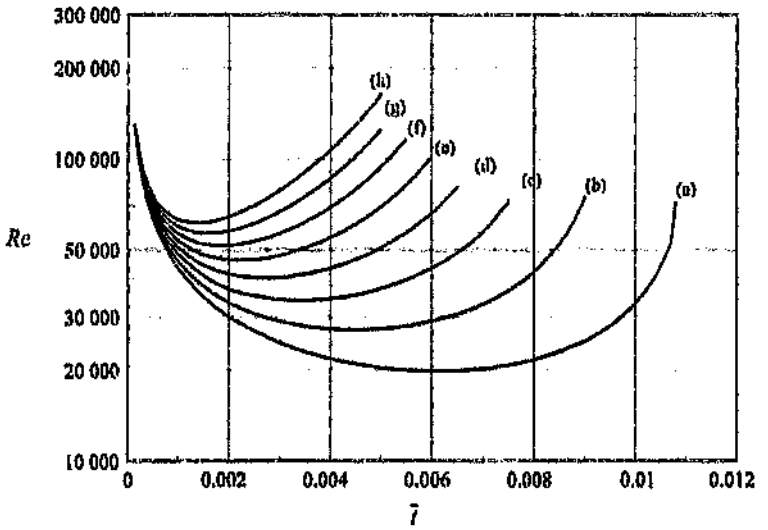

Figure 17.1: The temporal variation of the critical Reynolds number in parallel, temporally developing flow, for discrete values of the acceleration parameter; (a), $\Omega = 0$; (b), $\Omega = 10$; (c), $\Omega = 20$; (d), $\Omega = 30$; (e), $\Omega = 40$; (f), $\Omega = 50$; (g), $\Omega = 60$; (h), $\Omega = 70$.

As time increases from zero, all the curves show a rapid decrease to a minimum point. This minimum point occurs for increasing values of the acceleration parameter at successively earlier times and higher Reynolds numbers. Beyond the point of minimum critical Reynolds number, all curves bend sharply upwards, from which may be inferred that there exists a maximum time for each acceleration beyond which the flow always remains stable. The impulsive flow ($\Omega = 0$) shows the most abrupt behaviour, the rate of increase of the curves becoming gentler with increasing acceleration. It appears as if all the data will show vertical asymptotic behaviour, but at subsequently higher Reynolds numbers for increasing values of the acceleration parameter. Unfortunately numerical limitations prevented the accurate determination of these limits for the higher accelerations.

The lowest point on each curve represents the minimum critical Reynolds number - the lowest Reynolds number at which the flow can becomes unstable. This occurs at a particular time for each value of Ω. The minimum critical Re increases rapidly with increasing acceleration parameter. The variation of this value with acceleration parameter is shown in figure 17.2.

temporal variation for intermediate times is however unknown, and needs to be investigated further.

There is strong similarity between the current flow and the pipe entrance system: in the entrance system, the spatial wavenumber α is a strong function of the axial co-ordinate $\bar{x}$, while in the temporal system, this parameter is, as mentioned, a strong function of time. Thus the applicability of the linear analysis to the temporal system would seem to be qualified to the same level as its for the steady entrance system. As before, the reservations expressed above are not concerned with the flow-rate change in time at all. The renormalisation of the base flow equations performed in chapter 10 places all the flows - those with strong temporal base-flow variations and those without - on an equal footing.

17.1.3 Solution procedure

Sets of highly accurate velocity profiles were generated for the parallel developing flow, in order to extract reliable stability data. These profiles were obtained using the algorithm described in section 13.2. In order to ensure accuracy, the spatial order was increased to $N = 120$, and the time-step reduced to $\Delta t = 1 \times 10^{-6}$. The initial velocity profile was taken as 'top-hat' ($u = 1$ everywhere) and every tenth result was stored. The solution was stopped when t exceeded 0.1. Eight sets of data were produced in total, each for a distinct value of the acceleration parameter - $\bar{\Omega}$ increasing in steps of ten in the range $0 \leq \bar{\Omega} \leq 70$.

The stability properties of the resultant profiles were obtained in an identical fashion to those for the entrance profiles of the preceding section. The stability solutions were mostly developed at solution order $N = 80$; for the thin velocity profiles at early times, solution orders of up to $N = 100$ were employed to ensure accuracy. As before, difference in solution order between the base flow and the stability analysis was not problematic. The higher order coefficients of the base flow velocity profiles were simply ignored by truncation[4].

The critical Reynolds number for selected profiles was obtained as before by finding the point of lowest Re on their respective neutral stability curves in the α - Re plane. For each value of $\bar{\Omega}$, values of $Re_{[crit]}$ were obtained for profiles increasing in time, continuing up to the point at which the flow exhibited no linear instability. The data for the various accelerations are presented on the same sets of axes, both because of their similarity and for the sake of comparison. The order of presentation also follows a path common to the previous section.

[4]The large number of terms ($N = 120$) were retained in the base flow calculations simply to ensure maximum accuracy. This was feasible because the solution procedure was so fast; even at this high order of solution, the full solution for each value of the acceleration parameter was obtained in about half an hour on a 50 MHz '486 computer. For most of the profiles, all the coefficients above $N = 60$ were no larger than the round-off error of $\approx 10^{-14}$.

The incorrect inference of da Silva (1990), that the entrance and downstream velocity profiles were identical, led him to conclude that his entrance stability calculations were applicable far downstream in the parallel region of the pipe. The current study indicates that for impulsively started pipe flow, the downstream flow for early times is in fact far *more* stable than the entrance region. This discrepancy between the stability of the Blasius and error function profiles prompted the investigation of the stability of the parallel impulsively started flow far from the inlet. Results for this system are presented in a following section, but firstly the applicability of the linear stability analysis - that is, the correctness of the pseudo-steady assumption in this case - will be discussed.

17.1.2 Temporal variation of the velocity profile shape

The suitability of the linear stability analysis to the parallel system is based on the assumption of pseudo-steady flow; i.e. that the temporal variation of the base flow is much less than the temporal frequency of the important eigenmodes. The applicability of the normal mode approach here is thus, in a manner analogous to the non-parallel flow situation, qualified. It is not strictly true that the time scales of the variation of the base flow are orders of magnitude less than the temporal frequency of the disturbance. Certainly at early times the spatial wavenumber α is a strong function of time.

However, one must again consider the flow from the perspective of the boundary layer. At early times, the displacement thickness of the boundary layer in a pipe is very small. For the previously considered pipe entrance flow, the shape of the boundary layer approached the Blasius solution, with critical displacement thickness Reynolds number attaining the value of $Re_{\delta^*[\mathrm{crit}]} = 519{,}060$ here. In a similar manner for the present case, the thin boundary layer approaches the error-function shape as the boundary layer thickness decreases. Analogous to the entrance flow mentioned above, the parallel flow for diminishing displacement thickness δ^*/R behaves less like a pipe system and becomes more boundary layer-like[3]. The correctness of the linear analysis applied to this system for early times is thus dependent only on the temporal variation of the boundary layer shape itself, not its change in dimension. The boundary layer retains a high degree of self-similarity here, and becomes invariant in the limit of zero boundary-layer thickness. This infers that a simple linear analysis is appropriate in this limit. The applicability of the linear analysis is however qualified as the boundary layer thickness becomes large; the pipe-like nature of the flow becomes important and the temporal variation of the flow in this region may not be negligible. The rate of change in velocity profile in time however slows dramatically as the boundary layer thickens; in the far time limit when the profiles become invariant (possessing parabolic shape in the impulsive case) the linear analysis again becomes exact. The magnitude of the effect of the

[3]The distance from the edge of the boundary layer to the pipe centre-line for a thin profile is much larger than the boundary layer dimension. In this limit of vanishing boundary layer thickness, the stability behaviour of the flow is a boundary layer phenomenon.

where the independent variable η is given by

$$\eta = \frac{y}{2\sqrt{\nu t}}. \tag{17.2}$$

It was straightforward to obtain a Chebyshev series solution for the error-function (see section 13.2) for various domain extents $[0, \eta_{max}]$. The stability limit of these profiles was thus easily determined using the identical stability algorithm to that used for determining the Blasius stability solution in section 13.3. As with the Blasius stability solution, both domain size η_{max} and solution order N were varied, in order to determine the proper stability solution. The resulting minimum critical Reynolds number of this profile was determined to be

$$Re_{\delta^*[\text{crit}]} = 1\,674.79 \tag{17.3}$$

exact to 6 significant figures. This result was obtained for a solution order of $N = 100$ and corresponding boundary-layer thickness $\delta^*/\eta_{max} = 0.028\,209$. The variation of critical Reynolds number with domain size and order is given in table 17.1. This table is analogous to table 13.9 which concerns the Blasius profile.

Table 17.1: The value for the minimum critical Reynolds number based on displacement thickness Re_{δ^*} for various orders of solution and domain truncation, for the parallel impulsively started boundary layer.

	Minimum critical Re_{δ^*}		
N	$\delta^* = 0.056\,419$	$\delta^* = 0.028\,209$	$\delta^* = 0.018\,806$
50	1 680.476 217		
60	1 672.861 085		
70	1 673.137 828	1 681.534 386	
80	1 673.131 257	1 675.372 170	1 670.450 662
90	1 673.131 305	1 674.817 985	1 672.136 803
100		1 674 785 107	1 674.515 179
110			1 674.799 840
120			1 674.792 654
130			1 674.787 584

The most remarkable property of the parallel boundary layer profile is that its stability limit (17.3) is over three times higher than the Blasius boundary layer value of ≈ 520. Thus the non-parallel nature of the inlet flow has a profound effect on its stability behaviour. Its influence however, is to change the fundamental shape of the velocity profile rather than to modify severely the linear stability analysis[2]

[2]As has been discussed in some detail, the *parallel* linear stability analysis is applicable throughout the pipe. The large disparity in stability between the entrance region and the far downstream flow stems from the fact that two fundamentally different velocity profiles are present in each region, and not due to any non-parallel influence on the stability analysis.

The stability response of generally accelerating parallel flows to infinitesimal disturbances has not been addressed in the literature, due to the lack of any theoretical basis for analysis. However, even the stability of the *steady* ($\bar{U} = 0$) parallel velocity profiles has been neglected, except for a brief analysis by da Silva (1990), where he obtained stability results for a set of parallel temporally developing pipe velocity profiles generated by the simple momentum-integral approach of Moss (1991). He obtained critical Reynolds numbers for this system that were far higher than those for his steady entrance flow system. Unfortunately da Silva had previously incorrectly inferred that the structure of the entrance and parallel boundary layers were identical, and thus summarily dismissed this large discrepancy as being solely due to the simplified nature of Moss' base flow model. It was shown in chapter 14 that the boundary layer structure of the parallel downstream pipe flow was fundamentally different from that of the entrance flow. In particular the parallel model had a boundary layer that was more convex than an equivalent entrance profile. This difference increased with diminishing boundary layer thickness, the limiting shapes being the Blasius solution for the entrance flow, and an error-function shape for the parallel flow. Resulting from this disparity, the stability behaviour of the two types of flow would be expected to be fundamentally different. The stability of the Blasius profile is well known [Drazin & Reid (1981), also see section 13.3]; the previous section demonstrated that the Blasius critical Reynolds number $Re_{\delta^*[\text{crit}]} = 519.060$ was indeed the limiting value for the pipe entrance. However, the stability of the error function limit does not appear to have been studied in the literature.

The error-function limit was discussed in some detail in section 13.1, and a Tau solution to this problem was generated; however no stability analysis was performed there. The section below concerns such a stability analysis on these profiles, and follows a similar approach to the Blasius stability investigation of section 13.3.

17.1.1 Stability of the limiting error function profile

The error function velocity profiles were generated in section 13.2, using a simple Tau approach for the equation (13.63). The analytic derivation of this particular equation was first carried out by Stokes (1851) [see Schlichting (1979)], and describes the flow near a flat plate, impulsively started from rest and moving in its own plane. Alternatively, via a simple Galilean reference frame transformation, it gives the solution for the impulsively started flow surrounding a stationary flat plate. Equation (13.63) has a simple analytic solution; the boundary layer shape is self-similar and is described by the error-function solution

$$\frac{u}{U_\infty} = \text{erf}(\eta) \tag{17.1}$$

Chapter 17

The stability of exponentially accelerating pipe flows

In the previous chapter the general unsteady Sexl stability equation was discretised using the modified operational Tau method, in order to accurately determine the stability behaviour of the laminar velocity profiles generated in chapter 15. However, only stability data for the steady (non-accelerating) flow was presented there. This chapter presents the more general stability results for the exponentially accelerating base flows calculated earlier. The stability behaviour is investigated for the two different asymptotic limits of impulsively started and exponentially accelerated pipe flow: firstly for the parallel temporally developing parallel downstream flow, and secondly for the steady-state inlet system[1]. Results for all the accelerations are presented together in each case, to allow comparisons to be drawn between the data. In the final section the stability of the parallel and entrance flow stability results are compared directly to one another.

17.1 The far-downstream temporally developing flow

A mathematical model to describe the temporal development of flow in a pipe far from the inlet plane was developed in chapter 13. Velocity profiles for the general case of impulsively started and exponentially accelerated pipe flows were subsequently calculated in chapter 15, these profiles developing in time from a 'top-hat' configuration to a steady-state shape for large times. This section is concerned with the linear stability behaviour of these flows, for the chosen rates of acceleration parameter, namely $\Omega \in \{0, 10, 20, 30, 40, 50, 60, 70\}$.

[1] It should be remembered that the exponentially accelerating entrance flows were steady in the transformed solution domain, and that the strong unsteadiness in the physical flow system was primarily due to a simple reference-frame transformation. Unless otherwise indicated, the term *steady* will refer to flows which are steady in this transformed domain.

All data given in the previous figures is tabulated for selected values of the axial displacement $\bar{x}$, in table C.17. This table has as its independent variable the axial displacement $\bar{x}$. Table C.18 contains the correspondence of these axial values with the other base flow variables such as the displacement thickness δ^* and shape parameter S. While this chapter has been primarily concerned with the linear stability steady pipe entrance flow, the following chapter extends the above analysis, and generates results for the more general exponentially accelerating case.

Referring to the figure, it is notable that, despite the large variation in velocity profile shapes, the discrete eigenvalues remain mutually coherent and their arrangement changes little through the entire axial range. The most distinct feature as $\tilde{x}$ increases is the appearance of 'extra' discrete eigenvalues, from 5 in number at the inlet to 7 at the last unstable station - this phenomenon is however commensurate with the increase in Reynolds number at the most downstream station [Grosch & Salwen (1978)]. The continuous eigenvalue spectrum is plotted as a series of loci for the reason that individual members do not retain a strong identity; rather the line defined by their group arrangement remains well structured, migrating from a vertical orientation (Blasius) to an angled placement downstream.

16.6 Summary

The above discussion has centred on the steady-state pipe entrance flow, primarily because it is the only point of comparison with the existing literature. The study undertaken has clarified many uncertain points about this flow, most importantly showing that non-parallel effects are insignificant in the description of such flows. The broad conclusions following from the above discussion are as follows:

(i) In a steady laminar pipe entrance flow, the only region subject to destabilisation by infinitesimal disturbances is $0 \leq \tilde{x} \leq 0.008\,18$, only about 4 percent of the pipe entrance length.

(ii) In this unstable region, non-parallel effects are insignificant, especially towards the point of maximum instability.

(iii) The lowest Reynolds number based on radius at which the pipe entrance will first become unstable to small disturbances is 11667. The corresponding axial station at which this will occur is $\tilde{x} = 0.003\,59$.

(iv) The behaviour of the flow towards the pipe inlet is boundary-layer like, and the correct framework in which to present stability characteristics of the flow here is by using parameters scaled with respect to the boundary layer displacement thickness and pipe centreline velocity.

(v) The structure of the critical eigenvalue spectra and neutral curves vary smoothly and gradually from those corresponding to the Blasius solution near the inlet plane, to the last obtainable results at $\tilde{x} = 0.008\,18$. This is in contrast to the strong variation in velocity profile shape over the range. This indicates that, for most of the range, it is the boundary layer structure that is most important in determining the stability characteristics of the flow.

16.5.7 Eigenvalue spectrum

The neutral curves describe the behaviour of the most unstable eigenvalue in the system. While this behaviour might alone be sufficient for a simple linear analysis, a more general finite-amplitude model would require all the linear eigenvalues as initial perturbations on the system. The full spectrum is also a clear indicator of the nature of the flow behaviour[12]. Figure 16.8 shows the variation of the eigenvalues in $\bar{x}$, all the spectra being for $Re = Re_{[crit]}$. Shown also are the eigenvalues for the Blasius solution, and those from the last station at which stability could be measured.

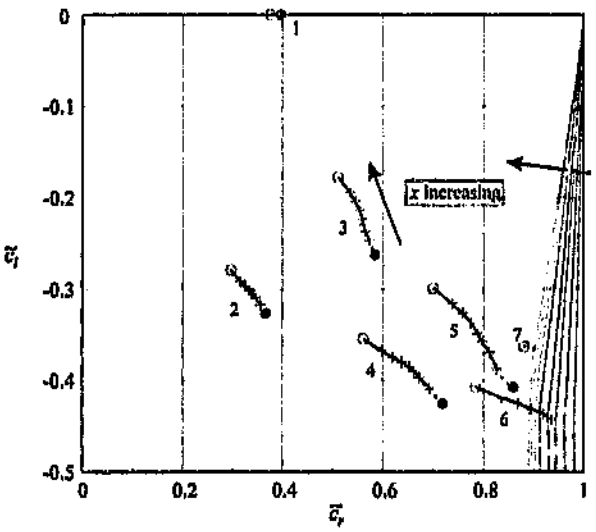

Figure 16.8: Migration of the eigenvalues with axial distance in the range $0 \leq \bar{x} \leq 0.008\ 18$ for the minimum critical Reynolds number at each position. Eigenvalues are numbered according to the scheme of Mack (1976). The continuous spectra are indicated as a series of lines. •, spectrum at $\bar{x} = 0$ (Blasius limit); ○, spectrum at $\bar{x} = 0.008\ 18$; intermediate spectra correspond to $\bar{x} = 0.000\ 071\ 1$, 0.000 634, 0.001 51, 0.002 72, 0.004 55, 0.005 94, 0.007 06.

The structure of the eigenvalue spectrum in the context of Hagen-Poiseuille flow was discussed in section 13.1. The eigenvalues were classified there into wall, median and centre modes respectively. The centre and median modes together correspond to the continuous spectrum of the Blasius boundary layer, while the wall modes form the discrete spectrum [see for instance Antar & Benek (1978), Grosch & Salwen (1978) for a discussion of the continuous and discrete spectra in the context of the Blasius boundary layer].

[12] If the eigenvalue spectrum of a flat-plate boundary layer were markedly different to one for pipe flow near the inlet, then one could safely conclude that the appearance of similarity between these flows was fortuitous; however substantial agreement of structure would strengthen dramatically the conclusion of similarity.

the system is represented *exactly* by a horizontal line moving upward on figu 13. Thus in the exponential case, instability of the pipe entrance will be governed precisely by the steady linear mechanism described in this chapter[9]. This is in contrast to the steady (non-accelerating) system. In this case, the state-line does not move upwards on the figure; thus the transients associated with the initial impulsive start of the flow will occur at the Reynolds number of the final flow. As a result, there is no guarantee in the non-accelerating case that instability will be due to the steady linear mechanism as given by the $\Omega = 0$ curve in figure 17.13. Certainly, in order to attempt to measure linear instability in the steady case, the initial development would have to occur at a linearly unstable Reynolds number, while in the exponentially accelerating system, the initial development can be guaranteed to be linearly stable.

Thus, because of the moving state-line in the exponential system, these flows provide an unique basis for investigating pipe flow stability. An exponentially accelerating entrance flow will always undergo linear destabilisation at some time in its development, due to the fact that the state line will always eventually intersect the relevant stability curve. Furthermore, starting the flow at an initial low Re will ensure a laminar initial development until steady-state is reached.

17.3 Comparison between the spatial and temporal results

Due to the different stability behaviour for the parallel flow and the entrance system, a comparison between the two systems would be useful in quantifying their disparity. To this end, a limited comparison was given in figure 17.10, where the minimum critical values of both flows were shown as a function of the acceleration parameter.

Comparison of the full stability curve is hampered by the fact that the parallel stability behaviour is given as a function of time, whereas the spatial curves are given with respect to axial position. However, in both types of flow there is a strict correspondence between the time (or axial position) and the displacement thickness, thus showing the variation of the critical Reynolds numbers with displacement thickness for both flows is an ideal way of comparing the two sets of results. To this end, the variation of the critical displacement thickness Reynolds number with displacement thickness is shown in figure 17.14 for both the parallel developing system and the entrance flow.

[9] That is, of course, if the level of background disturbance is sufficiently small. The entire discussion is concerned with the linear mechanism alone, and thus finite-amplitude effects are ignored. However, exactly the same argument will apply in a finite-amplitude environment, but in that case, the 'stability' curves shown in figures 17.12 and 17.13 would be the finite-amplitude equivalents of the linear curves.

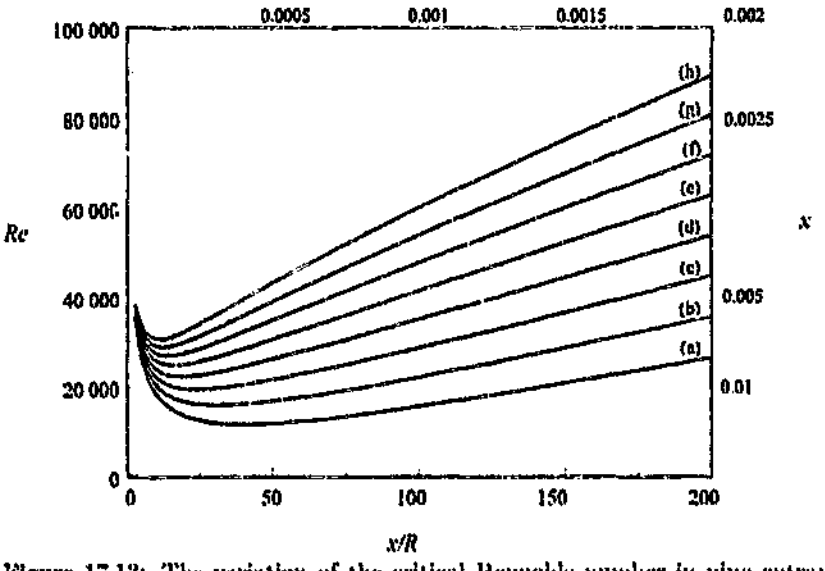

Figure 17.13: The variation of the critical Reynolds number in pipe entrance flow with respect to the physical co-ordinate system, for discrete values of the acceleration parameter; (a), $\Omega = 0$; (b), $\Omega = 10$; (c), $\Omega = 20$; (d), $\Omega = 30$; (e), $\Omega = 40$; (f), $\Omega = 50$; (g), $\Omega = 60$; (h), $\Omega = 70$; superimposed are lines of constant normalised axial position $x = \text{const.}$

The stability behaviour of a particular exponentially accelerating pipe flow at a particular time has a simple interpretation in both figures 17.12 and 17.13; namely its state is represented by a horizontal line. Considering a flow from a *physical* perspective, the most appropriate figure to describe the flow development is figure 17.13. Development of the entrance region of an exponentially accelerating pipe entrance flow would be described by a horizontal line moving upwards in time. For instance, the stability of a flow accelerating at a rate $\Omega = 40$ would be described by a horizontal line moving upward at a rate $Re = Re_0 \exp(40t)$. Initially for low Reynolds numbers (early time), the state-line would not intersect the relevant stability curve - curve (e) in this case. At a later time, intersection at approximately $x/R = 35$ would induce instability at this point. Later, as the state-line continues to move upward, instability would be induced both further upstream and downstream of the initial point of instability.

The above discussion highlights a very important distinction between exponentially accelerating flows and the limiting non-accelerating case; namely that in the latter system the state-line remains fixed at a particular Reynolds number whereas it always moves upward in the former flow. This fixed position of the state-line in the steady flow system represents an innate problem that makes accurate stability measurements in impulsively started flows problematic. In an exponential system, the transients in the entrance flow disappear while the Reynolds number is still low (and the flow is stable); thereafter the stability of

That is, trajectories corresponding to fixed physical axial stations $\tilde{x} = \tilde{x}_a$ are lines given by (17.11) in figure 17.8. To this end, figure 17.12 gives the data of the above mentioned figure again, but with this grid of constant $\tilde{x}$ trajectories superimposed.

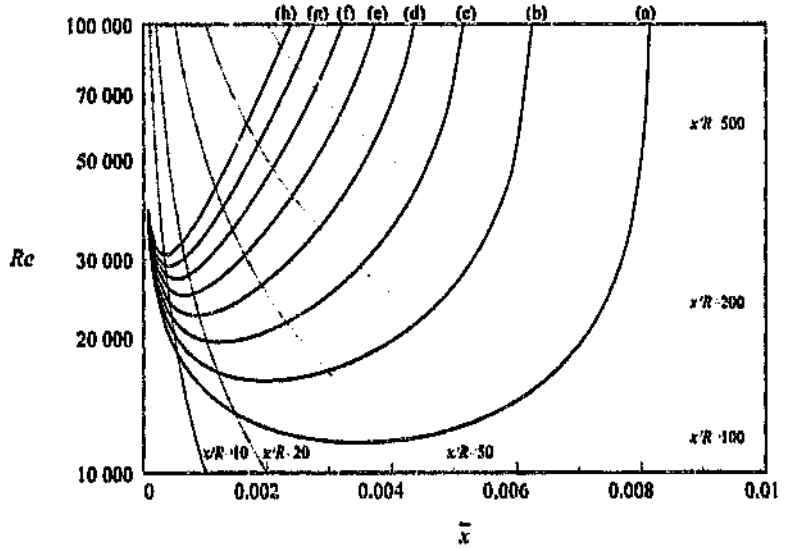

Figure 17.12: The spatial variation of the critical Reynolds number in pipe entrance flow, for discrete values of the acceleration parameter; (a), $\tilde{\Omega} = 0$; (b), $\tilde{\Omega} = 10$; (c), $\tilde{\Omega} = 20$; (d), $\tilde{\Omega} = 30$; (e), $\tilde{\Omega} = 40$; (f), $\tilde{\Omega} = 50$; (g), $\tilde{\Omega} = 60$; (h), $\tilde{\Omega} = 70$; superimposed are lines of constant physical axial position $\tilde{x}$ =const.

To make interpretation easier, the data of this figure can be transformed such that the ordinate is the physical dimensionless co-ordinate system $\tilde{x}$. Graphically, this is achieved simply by distorting the data of figure 17.12 such that the lines of constant $\tilde{x}$ become vertical. The data transformed in such a way is given in figure 17.13. Lines of constant $\tilde{x}$ (corresponding to vertical lines in figure 17.12) are also given in this figure.

The shape of the stability curves as seen from the physical co-ordinate system $\tilde{x}$ are far more extensive than in the normalised basis. As the stability curves become vertical downstream in the normalised system (in particular the zero acceleration curve showed marked behaviour in this regard at a relatively low Reynolds number), their representation in the physical system is to follow the lines of constant x, now given by equations of the form

$$Re = K'\tilde{x} \tag{17.13}$$

where the constant is given by $K' = x^{-1}$.

In a physical experiment, measurements are most usually taken at fixed x stations in the pipe. It was shown in chapter 15 that a physical station in an exponentially accelerating flow corresponds to a station of variable $\bar{x}$ in the normalised system. The variation of the dimensionless position (corresponding to a fixed physical position) for a given acceleration Ω is given by the relation

$$\bar{x} = \frac{x_a}{RRe_0} \exp(-\Omega t) \tag{17.7}$$

where Re_0 is the Reynolds number at time $t = 0$, and x_a denotes a chosen fixed axial position in the physical co-ordinate system. Thus, fixed physical stations correspond to normalised axial positions decreasing in time according to (17.7). This exponential mapping arises out of the more general Reynolds number dependent mapping between the physical and normalised axial systems. The two are related by the simple transformation

$$\bar{x} = \frac{x}{RRe(t)}. \tag{17.8}$$

Thus $\bar{x}$, for a fixed value of x, scales in inverse powers of the Reynolds number; for the current study, the Reynolds number varies in an exponential manner in time, hence the negative exponential behaviour of the $\bar{x}$ ordinate in time. Unfortunately, equation (17.8) defines the mapping in terms of dimensional parameters. An improved representation can be introduced by defining a dimensionless axial system based simply on the ratio of axial position to the pipe radius, given by

$$\tilde{x} = \frac{x}{R}. \tag{17.9}$$

Using (17.9), the variation of a fixed physical station (fixed $\tilde{x}_a$ corresponding to a fixed x_a) in the dimensionless basis x can thus be defined according to

$$\bar{x} = \tilde{x}_a Re(t)^{-1}. \tag{17.10}$$

Equation (17.10) simply describes lines of the form

$$Re = K\bar{x}^{-1} \tag{17.11}$$

in the $Re - \bar{x}$ plane, where K is given by

$$K = \tilde{x}_a = \frac{x_a}{R}. \tag{17.12}$$

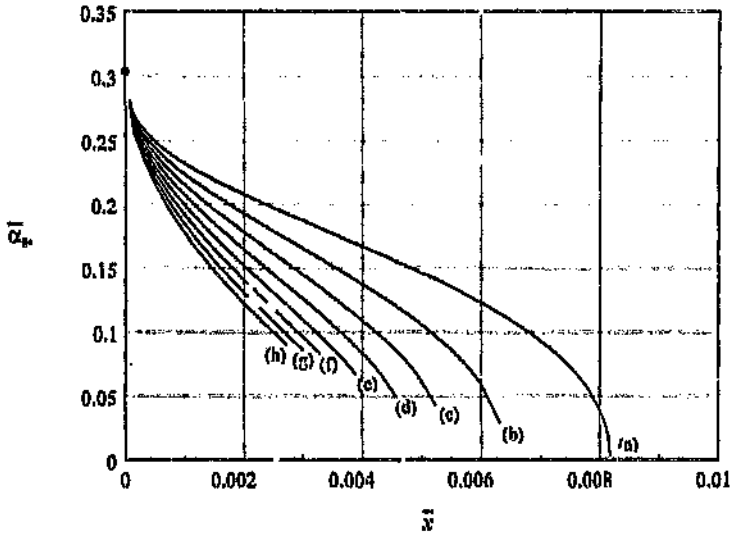

Figure 17.11: The variation of the critical wavenumber based on displacement thickness with acceleration parameter in steady pipe entrance flow; •, Blasius boundary layer limit, $\alpha_{\delta^*[\mathrm{crit}]} = 0.303\,77$; (a), $\Omega = 0$; (b), $\Omega = 10$; (c), $\Omega = 20$; (d), $\Omega = 30$; (e), $\Omega = 40$; (f), $\Omega = 50$; (g), $\Omega = 60$; (h), $\Omega = 70$.

rectly analogous; here the curves approach zero wavenumber at diminishing axial stations for increasing values of Ω. The asymptotic limiting behaviour as $\alpha_{\delta^*[\mathrm{crit}]} \to 0$ was discussed in some detail both in the previous chapter (chapter 16), and in Abbot & Moss (1994). These were both concerned only with the zero acceleration system, and the downstream limit beyond which no instability is possible was found to be $\bar{x} \approx 0.008\,18$. As mentioned above, it is apparent that such behaviour is also evident in the stability data presented here. Unfortunately, the critical Reynolds number at which this asymptote occurs becomes successively higher with Ω. Accurate determination of the limiting points for all the data was thus not attempted, but could be achieved, certainly for the lower accelerations. However, the magnitude of the Reynolds number at which the stability curves began to show such asymptotic behaviour ($> 10^6$) would have placed a severe numerical limitation on determining the asymptotes for the higher values of the acceleration parameter.

17.2.2 The physical co-ordinate system

While the stability data are represented in a simple and uniform manner in the normalised basis, the observation of an actual accelerating flow would be in the physical co-ordinate system. The mapping between the two systems depends on the Reynolds number, thus the variable nature of this transformation confuses the simplicity of representation attainable in the normalised system.

Returning to figure 17.8, the variation of the minimum critical Reynolds number (the 'nose' of the stability curves in that figure) with acceleration parameter Ω is given by figure 17.10. The equivalent data for the parallel flow system, first shown in figure 17.2, are superimposed on this figure.

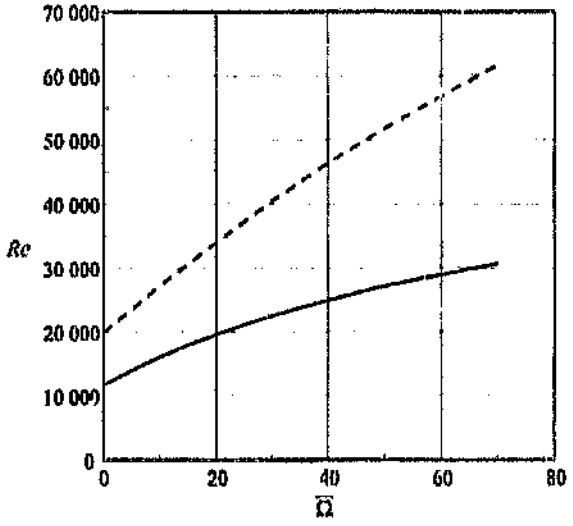

Figure 17.10: The variation of the minimum critical Reynolds number with acceleration parameter in steady pipe entrance flow, compared to the data for the parallel downstream case: ——, entrance; – – –, downstream.

This figure shows that the minimum critical Reynolds number for the parallel downstream flow, and the entrance system differ by an almost constant ratio as the acceleration parameter increases. This indicates that the discrepancy between the two flow systems is essentially independent of the acceleration parameter. A further significant trend in the present data is the flattening off of curves with increasing Ω. Unfortunately no stability results for very high accelerations were obtained. From the present data it can not be inferred whether this trend is asymptotic to a horizontal line or not.

The variation of the critical wavenumber based on displacement thickness α_{δ^*} with dimensionless axial position $\bar{x}$ is shown in figure 17.11. The displacement thickness wavenumber was defined earlier in the chapter, as equation (17.5).

In the boundary layer limit, as $\bar{x} \to 0$, the curves for all the accelerations approach the Blasius boundary layer value of 0.303 77 (see chapter 16). From this point downstream, the wavenumber for each curve diminishes and approaches zero with an increasing slope. This is in qualitative agreement with the behaviour of the parallel critical wavenumber (in that case the variation was with respect to time) shown in figure 17.4, where the curves of $\alpha_{\delta^*[\mathrm{crit}]}$ approached the error-function limit as $\bar{t} \to 0$, and tend to zero at successively smaller times for increasing values of Ω. The behaviour of the present entrance data is di-

Reynolds number, given by equation (17.4). The data plotted according to this ordinate are shown in figure 17.9.

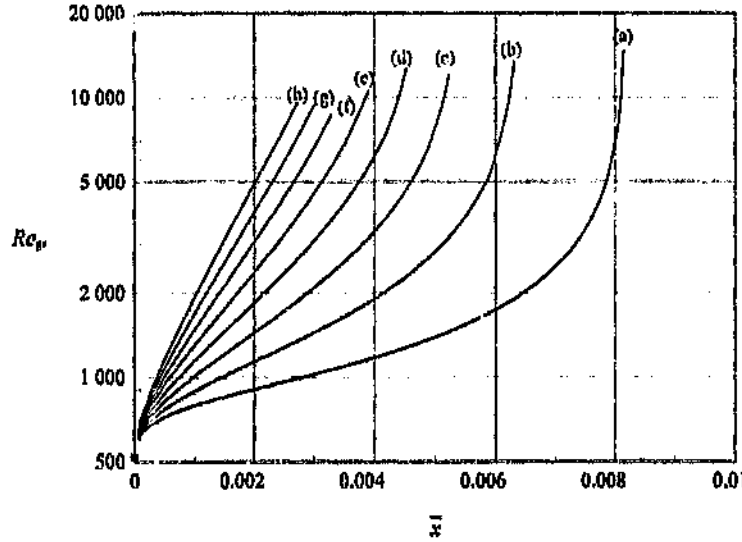

Figure 17.9: The spatial variation of the critical boundary layer displacement thickness Reynolds number in pipe entrance flow, for discrete values of the acceleration parameter; •, Blasius boundary layer limit, $Re_{\delta^*[crit]} = 519.06$; (a), $\bar{\Omega} = 0$; (b), $\bar{\Omega} = 10$; (c), $\bar{\Omega} = 20$; (d), $\bar{\Omega} = 30$; (e), $\bar{\Omega} = 40$; (f), $\bar{\Omega} = 50$; (g), $\bar{\Omega} = 60$; (h), $\bar{\Omega} = 70$.

It is plainly clear here that all curves are convergent on the Blasius limit of $Re_{\delta^*[crit]} = 519.06$ as $\bar{x} \to 0$. The curves for all accelerations show an increase in $Re_{\delta^*[crit]}$ with $\bar{x}$, with the slope of the curves also increasing with acceleration parameter. A clear contrast in shape is evident between these data and the equivalent parallel results shown in figure 17.3; while the current data descend sharply to the Blasius stability limit, the parallel curves (figure 17.3) show a more languid convergence to the higher error function limit as the boundary layer thickness diminishes. The zero acceleration curve increases rapidly from the Blasius limit, then assumes a more gradual slope for intermediate values of $\bar{x}$, followed finally by a region $\bar{x} > 0.008$ in which the curve rapidly approaches a vertical asymptote (see chapter 16). As acceleration increases, the distinction between the 'gradual' and 'asymptotic' sections of the data reduces; and for the highest acceleration of $\bar{\Omega} = 70$ investigated, the stability curve has an almost uniform upward slope within the Reynolds number range considered. The behaviour of all curves with increasing $\bar{x}$ is to become asymptotic to a vertical line. Furthermore, these asymptotes appear to be at reducing values of $\bar{x}$ for increasing values of the acceleration parameter. As before, concerns about numerical accuracy limited the Reynolds number range. The higher acceleration curves tended to become asymptotic at higher values of $Re_{\delta^*[crit]}$ and accurate limiting behaviour could not be deduced at the present order of discretisation.

to the normalised co-ordinate $\bar{x}$ is of great importance. The variation of $Re_{[crit]}$ with $\bar{x}$ is given in figure 17.8. The impulsive entrance data are again reproduced here for purposes of comparison.

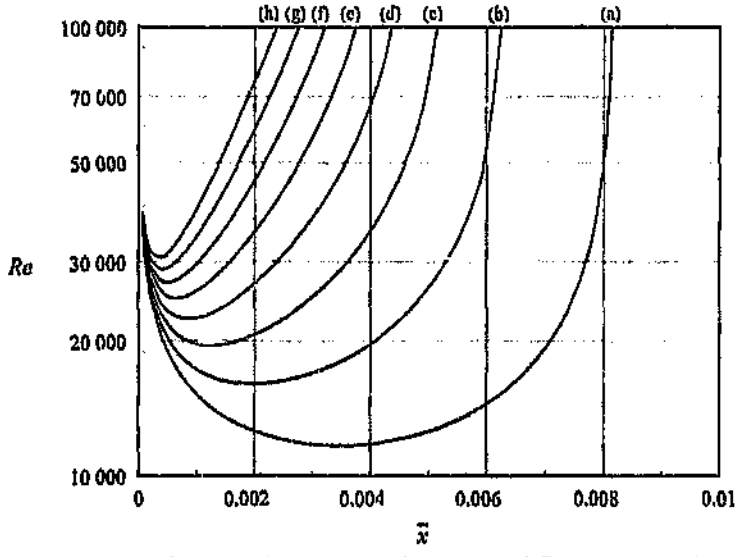

Figure 17.8: The spatial variation of the critical Reynolds number in pipe entrance flow, for discrete values of the acceleration parameter; (a), $\bar{\Omega} = 0$; (b), $\bar{\Omega} = 10$; (c), $\bar{\Omega} = 20$; (d), $\bar{\Omega} = 30$; (e), $\bar{\Omega} = 40$; (f), $\bar{\Omega} = 50$; (g), $\bar{\Omega} = 60$; (h), $\bar{\Omega} = 70$.

As expected, the data show similar structure to the parallel flow of the previous section. The curves descend from infinity at $\bar{x} = 0$, attain a minimum value, and then rapidly increase again. The minimum point for increasing values of the acceleration parameter occurs at successively higher Reynolds numbers, and correspondingly smaller values of $\bar{x}$. Referring back to the parallel stability curves given in figure 17.7, there is, however, a substantial quantitative difference between the stability of the previous parallel flow, and the current entrance system. In the former case, the stability curves generally occur at far higher Reynolds numbers than in the latter. In keeping with the trend for the impulsive pipe flow, the minimum critical point of the current data for all the accelerations are substantially lower than the equivalent parallel data.

Whereas the zero acceleration stability curve is relatively flat, the curves for higher values of the acceleration parameter become more angular with a 'sharp' minimum point. A similar trend was manifest in the temporal flow. As would be expected, all the data approach each other as $\bar{x} \to 0$. As $\bar{x}$ increases, the curves deviate rapidly. The curves approach a common point at $\bar{x} = 0$ because the velocity profiles in this limit approach the common Blasius profile shape. The asymptotic limit at $\bar{x} = 0$ is not apparent in figure 17.8 because of the unbounded behaviour of the stability curves here: as before the correct context to view the data in this limit is according to the boundary layer displacement thickness

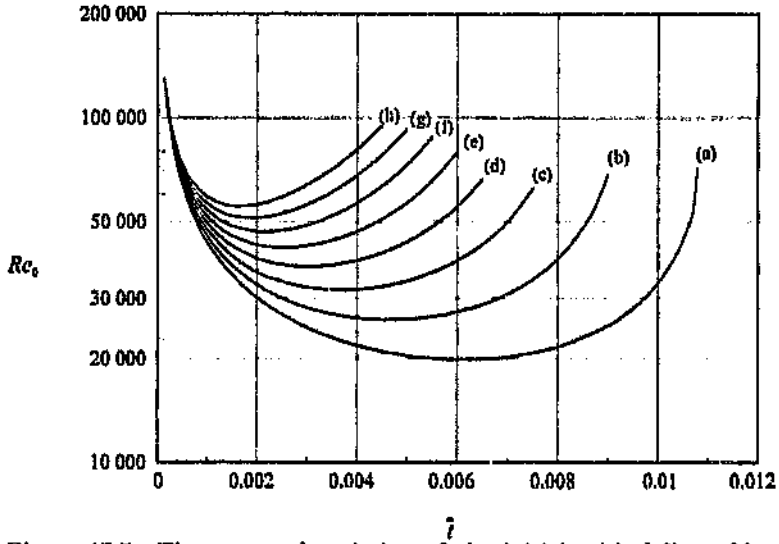

Figure 17.7: The temporal variation of the initial critical Reynolds number in parallel, temporally developing flow, for discrete values of the acceleration parameter; (a), $\bar{\Omega} = 0$; (b), $\bar{\Omega} = 10$; (c), $\bar{\Omega} = 20$; (d), $\bar{\Omega} = 30$; (e), $\bar{\Omega} = 40$; (f), $\bar{\Omega} = 50$; (g), $\bar{\Omega} = 60$; (h), $\bar{\Omega} = 70$.

Regarding the steady nature of the exponentially accelerating pipe entrance flows, chapter 15 showed how such flows were steady with respect to a reference frame that stretches exponentially with time in the axial direction. Both the base flow model and stability equation were developed in this normalised framework. The entrance region for any chosen exponential acceleration approached a steady state limit in the dimensionless co-ordinate system in a manner directly analogous to the truly steady-state flow. Thus the continually varying nature of the physical exponential entrance flow was shown to be due to a co-ordinate stretching effect alone. In this section, the terminology 'steady' will be used to refer to any flow which is invariant in the normalised framework; all the entrance models undergoing exponential acceleration generated in chapter 15 are invariant in their far-time limit. The unsteady Sexl stability equation (10.55) was applied to the general entrance data generated in chapter 15. The solution procedure was identical to that adopted in the previous section (excepting of course the use of the different base flow profiles). The results for all the accelerations will as before be presented together in the same sets of axes to promote easy comparison.

17.2.1 Critical Reynolds number and wavenumber

As before, the primary concern is with the instability of the flow. To this end the variation of the critical Reynolds number in the pipe entrance with respect

curve. Trajectories missing the 'nose' of the stability curve - for instance the lowest exponential path shown in the figure - would never intersect the stability curve. Furthermore, some slightly higher trajectories describe flows that become unstable for only a short while, reverting again to a stable state for later times. This situation would be different if the slopes of the exponential paths were greater than the far-time side of the stability curve. In this case, any path that circumvented the nose would eventually intersect the neutral stability curve, the result being that any flow would become unstable after a suitable period (and at a suitably high Reynolds number). However, the current evidence presented here for parallel flows indicates the opposite - that initially stable impulsively started exponentially accelerating flows far from the inlet will remain stable. Moreover, flows that become unstable (the higher trajectories in the figure) will eventually re-stabilise[8]. The data shown in figure 17.6 is for the highest acceleration investigated. It was used because it represented the most marked deviation away from the impulsive case (figure 17.5).

Due to this trajectory dependence, the superimposition of curves for different acceleration parameters - as in figure 17.1 - is confusing. An advantageous method of presentation would be one in which the curves for all the accelerations possessed the same loci of interpretation. This is easily achieved for the present data, simply by representing it in terms of the initial impulsive Reynolds number Re_0. Practically, this means distorting the data in the Re - $\bar{t}$ plane (see figure 17.6) such that the exponential paths become horizontal. In such a case the development of the flow in time for a particular starting Reynolds number is always given by traversing a horizontal line in the Re_0 - $\bar{x}$ plane. This transformation can be simply attained via application of the the relation (17.6).

Figure 17.7 shows the full data plotted in the R_{δ_0} - $\bar{t}$ plane. Here the neutral stability curves of figure 17.1 for the higher values of the acceleration parameters are shown distorted downward in order that the trajectories of interpretation are horizontal. However, this distortion can be seen to be minor; the general shape of the curves remain similar to the equivalent data in figure 17.1.

17.2 The far-time entrance flow

Stability results for the generally accelerating pipe entrance flows were obtained in an identical manner to the results of the preceding section. The stability results for the steady-state pipe entrance flow were presented separately in chapter 16. The results presented here are for the equivalent 'steady-state' entrance flows with non-zero acceleration parameter.

[8] Of course, if a flow remains unstable for a sufficient time, finite amplitude transition to turbulence will commence. In this case, the linear argument will be invalidated. However the primary concern at the moment is with the inception of instability; the re-stabilisation of the higher Reynolds number flows is considered here for interest only.

The above argument becomes highly important when considering the stability curves of the flows with exponential accelerations. In this case, the flowrate variation of *particular* flows are given by exponential loci in the $Re - \bar{t}$ plane of the form

$$Re(\bar{t}) = Re_0 \exp(\bar{\Omega}\bar{t}) \tag{17.6}$$

where $Re_0 \equiv Re(0)$ is the initial impulsively realised Reynolds number of the flow at $\bar{t} = 0$. As with the impulsive case above, the stability curve for a particular $\bar{\Omega}$ is only valid if interpreted from a valid trajectory; in this case one given by the equation (17.6)[7].

Thus for varying values of the initial impulsive Reynolds number Re_0, the equation (17.6) describes a family of curves which represent valid traversals of the particular stability curve. To illustrate this principle for the accelerating system, figure 17.6 gives the stability curve for $\bar{\Omega} = 70$, superimposed on which are the relevant trajectories as given by (17.6) for different values of Re_0.

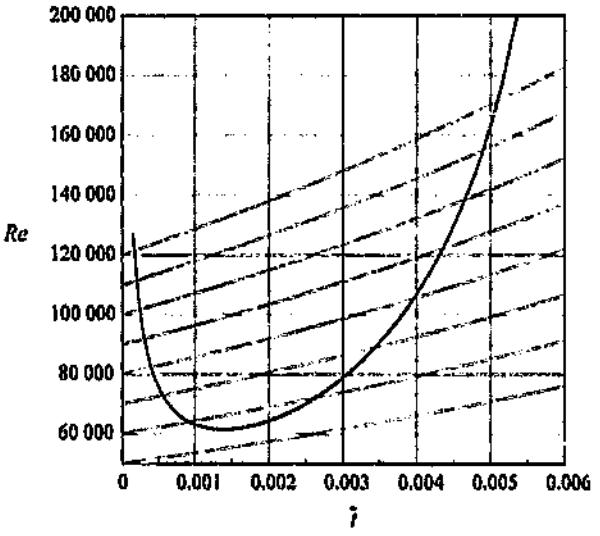

Figure 17.6: The neutral stability curve for $\bar{\Omega} = 70$, showing The trajectories for developing flows in parallel impulsively started accelerating pipe flow, for different values of Re_0.

Of interest in this figure is the presence of trajectories that remain stable for all time. This is mainly due to the limited temporal extent of the stability

[7]The important point here is that the base flow used for the stability analysis is peculiar to the acceleration parameter chosen. Following a different trajectory to that implicit in the base flow model immediately implies a different base flow, and thus a different stability curve in the first place.

17.1.5 Physical interpretation of stability results

Physically, the stability curve for the parallel impulsive ($\bar{\Omega} = 0$) case has a straightforward interpretation - it indicates the values of Reynolds number for which the pipe will become unstable for a particular duration. In this case the stability behaviour of a particular flow is represented by traversing a horizontal line in the Re - $\bar{t}$ plane. Figure 17.5 shows the impulsive parallel stability curve, with three such lines indicated. The lowest line is for $Re = 10\,000$, the intermediate one for $Re = 20\,000$, and the highest represents the development for $Re = 30\,000$.

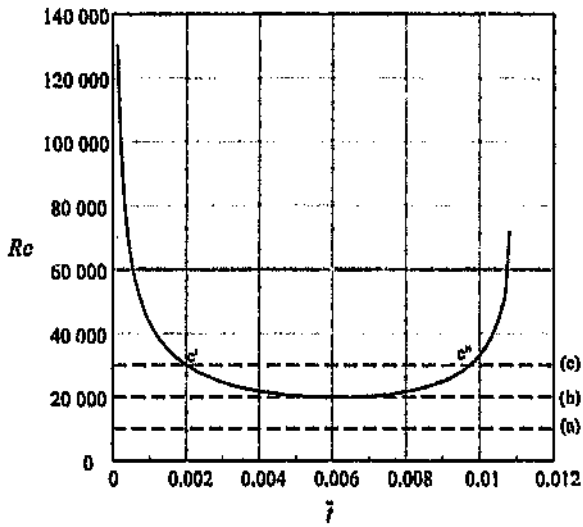

Figure 17.5: The trajectories for various developing flows in parallel impulsively started pipe flow. (a), $Re = 10\,000$; (b), $Re = 20\,000$; (c), $Re = 30\,000$.

For a flow impulsively started to a Reynolds number of 10 000 - line (a) - the stability behaviour in time is represented by traversing the line from left to right. In this case, the flow never becomes unstable. Simply put, line (a) does not intercept the neutral stability curve. For the intermediate flow with a Reynolds number of 20 000, following line (b) along from left to right shows that the system becomes unstable for a very short duration - as the line traverses the unstable region of the plane near the minimum critical point. For the highest Reynolds number considered [line (c), $Re = 30\,000$], traversing the line shows that the system becomes unstable for a far longer duration, commencing at the time corresponding to point c', the flow re-stabilising at time c''. While the above discussion may seem obvious, it highlights an important point; that the impulsive stability curve for the temporal case is only valid for flows that are impulsive, or nearly so. That is the neutral stability curve shown in figure 17.5 gives the correct behaviour if traversed horizontally in time. A trajectory at, say 45° on the current scale of axes would represent a flow in which accelerative effects were large, invalidating the use of the $\bar{\Omega} = 0$ curve.

18.2.2 Flow development from a fixed physical position

Numerically, the full flow development was shown above to consist of first the parallel temporally developing flow, and then the steady entrance region. In order to understand the implications of the variable mappin, on the perception of this data from the physical co-ordinate system, it is worthwhile to consider the temporal flow development from a fixed *physical* position in the pipe entrance. The argument below is concerned with the numerically predicted flow variation in the pipe, and *not* with the experimental results.

For a chosen physical axial position x_i within the pipe, initially the flow will be strictly parallel, and described by the simplified parallel flow model. For this region, stations located at different physical axial positions will show identical boundary layer development, due to the parallel flow not having any axial dependence. As the entrance flow arrives at successive stations, the parallel model will no longer be valid, and the flow will then be described by the steady (in the renormalised system) entrance flow model. There is however a Reynolds number dependent mapping, given by equation (18.1), between the physical and dimensionless axial co-ordinate systems. In the specific case of an exponential flow, a fixed physical axial position x_i relates to a variable normalised axial position $\bar{x}(t)$ as

$$\bar{x}(t) = \frac{x_i}{R\,Re(t)} = \frac{x_i}{R\,Re_0}\exp[-\bar{\alpha}t]. \tag{18.6}$$

Thus a fixed physical station maps to a dimensionless station that diminishes with time in a negative exponential manner. The steady (in dimensionless co-ordinates) entrance solution varies spatially (in $\bar{x}$ - the renormalised axial ordinate) from a thin boundary layer profile at the inlet, to the limiting downstream profile. Traversing this solution in the direction of decreasing dimensionless axial position results in a series of profiles whose temporal development is towards a thinner boundary layer. The result of observing the numerical development from a fixed physical axial position is as follows: first an initial increase in the boundary layer dis.ension is seen, in accordance with the simple parallel development model; subsequently a decrease in the boundary layer thickness is observed, as the fixed physical station 'traverses' upstream in the invariant pipe entrance model.

For any chosen station x_i, equation (18.6) gives a relationship between the time t and the dimensionless axial position $\bar{x}(t)$; thus the variation of a parameter (for instance displacement thickness) in time at a fixed axial position can be given equivalently as its variation in dimensionless axial position. Due to the fact that the time ordinate relates to the dimensionless axial position in inverse proportion, flow development in time is from right to left for the dimensionless axial position. This presents two complementary means of representing data measured at a fixed physical axial position: the variation of a parameter can be

By use of this mapping, the simple numerical solution in the (x, F, t) co-ordinate system could be transformed into the physical domain (x, r, t), with a resultant recovery of the complex flow behaviour similar to that observed experimentally.

18.2.1 Asymptotic approximations to the full numerical solution

The discussion of section 15.5 showed how the development of impulsively started and exponentially accelerated pipe entrance flow could be predominantly described by two simplified asymptotic models: for early times by the parallel, temporally developing flow described in section 15.2, and for later times by the steady (in the dimensionless basis) entrance system, given in section 15.3. The numerical simulation of the development of impulsively started and exponentially accelerated pipe entrance flow, was shown in chapter 15 to follow a well defined pattern in the normalised co-ordinate system:

(i) For early times, the flow developed away from the initial conditions $u = 1$ everywhere, with the boundary layer growing radially with increasing time. The pipe inflow condition was meanwhile maintained as a constant - thin boundary layer - velocity profile.

(ii) Far downstream, the flow remained parallel, and the velocity profiles developed temporally towards a steady state limiting shape. The limiting profiles for increasing acceleration had successively lower centreline velocities, and thus reduced displacement thickness. The time taken to reach the steady limit reduced with increasing acceleration parameter.

(iii) The flow in the entrance also approached a steady state configuration, with the velocity profiles varying spatially from the thin boundary layer inflow condition at the inlet, to the parallel limiting shape of profile, described in point (ii) above, further downstream. The dimensionless length over which this development occurred reduced for increasing values of the acceleration parameter.

The early time, parallel development of the flow was described by the simplified parallel flow model, while the later entrance flow was given exactly by the steady (in the normalised co-ordinate system) entrance flow. The full numerical simulation for the developing entrance flow showed that there was only a small transitional region between the parallel and entrance flow regimes that was not described by either of the two asymptotic models. Thus an accurate description of the full flow was afforded numerically by first considering the parallel flow model, and thereafter the steady entrance flow system.

t was constant (for a particular pipe geometry and fluid) and is given by

$$t = \frac{t}{t_0}, \quad t_0 \equiv \frac{R^2}{\nu}. \tag{18.3}$$

Due to the constant mapping, the difference in the temporal ordinate between the experimental data presented in chapter 8 and the numerical data given in chapter 15 was simply a constant scaling[3] by t_0. The relationship between the physical and dimensionless axial systems was more complicated, due to the Reynolds number dependence of the mapping, and this transformation is given by

$$x = \frac{x}{x_0(t)}, \quad x_0(t) \equiv R\,Re(t). \tag{18.4}$$

The current experimental results were measured at a fixed physical axial station. For an exponentially increasing Reynolds number, the scaling parameter $x_0(t)$ showed an exponential increase in value, and thus, for a fixed physical position, the dimensionless ordinate decreased in a negative exponential manner. While the concept of this variable mapping was extensively covered in section 11.5, it is fundamental to the reconciliation of theory with experiment (presented in section 18.3). Thus for clarity, the various facets of the dimensionless numerical solution and its mapping to the physical domain are revisited below.

The main problem of representing generally accelerating pipe flows is the unbounded behaviour of the dependent variables. In the context of exponentially accelerating flows, the axial velocity term scales exponentially, and the subtleties in the variation of the flow field with time are swamped by the gross integral changes in the axial velocity. From the point of view of the analysis of these flows, the unbounded integral change in the flow properties means that there is no unique universal frame of reference in which to model such systems[4]. The elementary analytical study of chapter 10 renormalised the axial velocity according to its mean cross-sectional value. This resulted in a dimensionless velocity that remained of order unity, regardless of the change in the flowrate over time. A consequence of this renormalisation process was that the axial[5] co-ordinate x mapped to the dimensionless co-ordinate x in a Reynolds number dependent manner as

$$x = x[R \cdot Re(t)]. \tag{18.5}$$

[3]The experimental data were also offset from zero time, due to an experimental start-up delay. It is assumed here that this delay has been removed from the measured data.

[4]In the case of steady flows, the various flow quantities (velocity, pressure) can be scaled by a constant such that their magnitude remains of order one. In the exponential case, scaling the terms by a constant will not eliminate the unboundedness.

[5]The pressure, axial velocity and axial co-ordinate were all subject to a Reynolds number dependent mapping, but the $x \mapsto x$ mapping was the only one that concerned an *independent* variable.

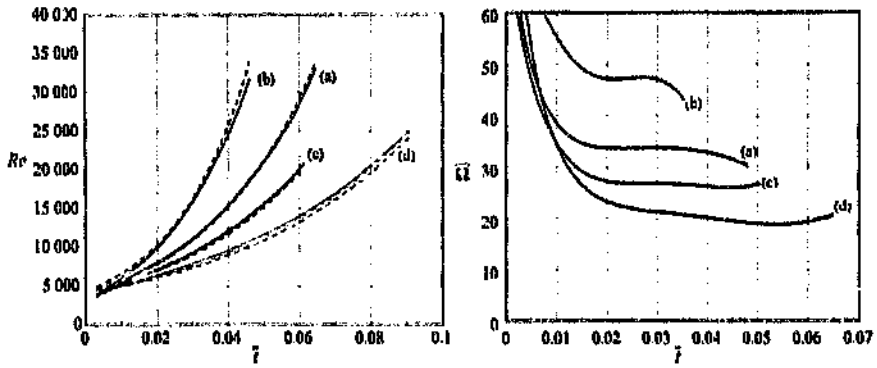

Figure 18.3: The flow variation with time, for the 'G' series of tests. Both the Reynolds number and acceleration parameter variation are shown: (a), GXPA; (b), GXPB; (c), GXPC; (d), GXPD; – – –, expected variation: , actual variation.

tained a fairly constant mean value. The decrease in Ω for the highest tests was expected by the fact that a constant value of acceleration parameter implies an exponentially increasing dQ/dt. Accurate valve control was probably limited at a fixed maximum dQ/dt, thus the higher accelerations would not have been able to maintain constant Ω beyond the point of effective control.

The variation of Ω for the 'G' series of tests is shown in figure 18.3. These tests had the highest initial impulsive Reynolds number, and thus showed the most marked start-up effects. However by time $t = 0.02$, these transients had as before died away, and all data showed similar trends to both the 'E' and 'F' tests.

18.2 Dimensionless co-ordinate system

The experimental base flow data in chapter 8 was presented primarily as the variation of various parameters (displacement thickness, shape parameter, etc.) versus time in seconds. The analysis of part III showed that the appropriate framework of comparison between theory and experiment was the normalised co-ordinate system. This section is concerned with the description of the mapping between these two systems.

In the numerical analysis (part III), the mapping between the physical variables and their dimensionless counterparts was defined. In the case of the time ordinate, the transformation between the physical variable t and dimensionless one

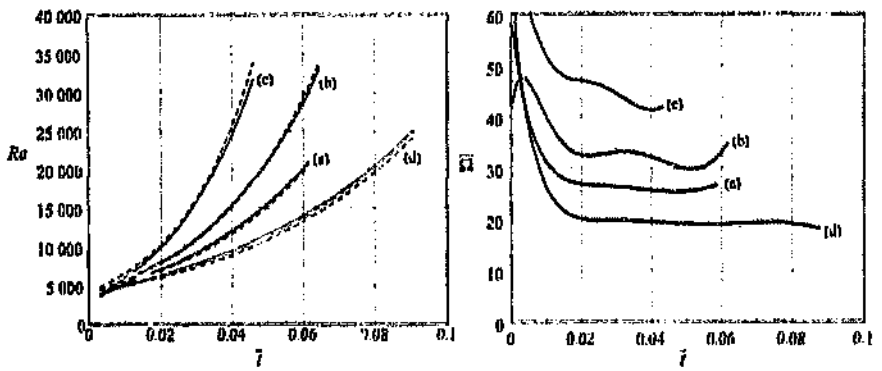

Figure 18.2: The flow variation with time, for the 'F' series of tests. Both the Reynolds number and acceleration parameter variation are shown: (a), FXPA; (b), FXPB; (c), FXPC; (d), FXPD; – – –, expected variation; ——, actual variation.

namely (a) and (d), show the most regular and constant behaviour, while the higher curves, especially (c), are rather more irregular. The variability at higher accelerations was due to the limited response of the flow control system.

The strong variation at the early times was unavoidable, and was due to a combination of factors; the poor response of the valve at low flowrates, combined with the need to avoid valve overshoot. Concerning the latter point, it was seen in chapter 6 that a small amount of overshoot caused large structures to be generated at the pipe inlet, which subsequently convected downstream. For this reason, the avoidance or reduction of the effects caused by overshoot was deemed more important than achieving a constant value of Ω for the early portion of the test. Early variability in the acceleration parameter was acceptable for two main reasons: firstly, the laminar structure of the flow at the start of the flow was less sensitive to the magnitude of the acceleration[3]; secondly, transition to turbulence occurred near the end of each test, where the value of Ω had remained constant for some time.

The 'F' series of tests, whose variation of flowrate and acceleration parameter is given in figure 18.2, show very similar trends to the 'E' series. They show a far stronger initial variability of Ω than the 'E' tests, due to their less 'hard' impulsive start. As before, the start-up transients had died away by $t \approx 0.02$. For the lower accelerations - (a) and (d) in figure 18.2 - the value of Ω remained constant to a high level of approximation, whereas the higher two accelerations showed waviness due to the limited response of the control system. The worst curve in this regard was (c), corresponding to the test FXPC; here the acceleration parameter showed a gradual reduction form a value of $\Omega \approx 47$ at $t \approx 0.02$, to $\Omega \approx 41$ at $t \approx 0.04$. The next lowest curve - curve (b) - was wavy, but main-

[3]It was shown theoretically in chapter 16 that all tests, regardless of acceleration, approached a fixed boundary layer structure in the limit of vanishing boundary layer thickness.

Table 18.1: The values of the parameters Re_0, Ω of the experimental flowrate variations for the separate tests.

Test	Re_0	Ω	Test	Re_0	Ω
EXPE	3018	19.6	FXPD	4143	19.6
EXPF	3018	32.5	GXPA	6510	32.5
EXPG	3018	45.5	GXPB	6510	45.5
FXPA	4143	26.0	GXPC	6510	26.0
FXPB	4143	32.5	GXPD	6510	19.6
FXPC	4143	45.5	HXPA	2959	13.0

A more sensitive way of determining the agreement of the flow variation with exponential, is by extraction of the physical variation of the acceleration parameter itself. This was done by fitting a 9th order least squares polynomial to the flow data, and then analytically determining Ω using relation (18.1). The flowrate varied smoothly, and thus the global curve fit gave an accurate indication of the actual flowrate variation. The experimental variation of the Reynolds number is shown in figures 18.1 to 18.3 that follow, along with the extracted acceleration parameter. The 'E' series of tests (as before including the test HXPA) are shown in figure 18.1, while figures 18.2 and 18.3 gave the results for the 'F' and 'G' tests respectively. The categorisation into the 'E', 'F' and 'G' groups is, as before, according to the impulsive start-up Reynolds numbers (table 18.1).

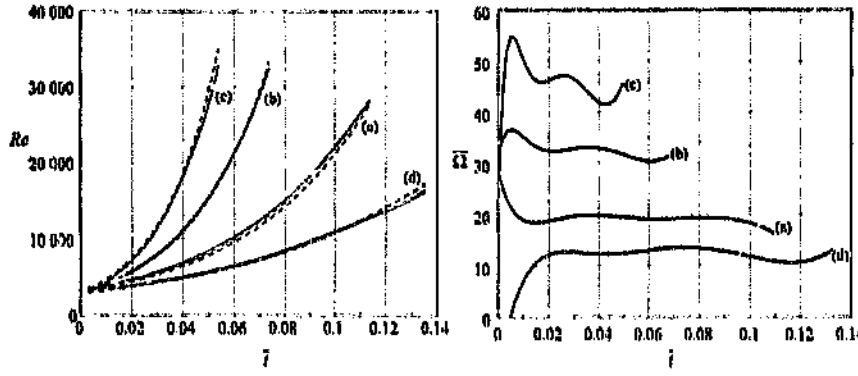

Figure 18.1: The flow variation with time, for the 'E' series of tests. Both the Reynolds number and acceleration parameter variation are shown: (a), EXPE; (b), EXPF; (c), EXPG; (d), HXPA; — — —, expected variation; ——, actual variation.

As can be seen in figures 18.1 to 18.3, while the Reynolds number variation is close to exponential for each test, the acceleration parameter varies quite strongly in some cases. The acceleration parameter thus shows itself to be a very sensitive indicator of the 'exponentiality' of the flow. The variation of the acceleration parameter for the 'E' series of tests is given by figure 18.1. For all four tests Ω is strongly variable in the range $0 < t < 0.02$; thereafter it remains relatively constant until the completion of the test. The lower curves,

18.1 Acceleration parameter

The quantifying parameter for acceleration from the analysis was termed the acceleration parameter. This factor describes the effect of flowrate acceleration, and is defined by

$$\Omega \equiv \frac{1}{U_m}\frac{dU_m}{dt}, \tag{18.1}$$

where U_m is the mean cross-sectional velocity. This parameter is identical to that used by Shen (1961), Moss (1991), and Lefebvre & White (1989, 1991). Shen was concerned with the inviscid limiting stability behaviour of such flows, Moss described the parallel laminar flow in a pipe using a simple integral approach, while Lefebvre & White used this term to describe their constant-acceleration experimental results. It arose naturally from the present analysis, thus revealing itself as the correct parametric group for classifying accelerating flows.

In the numerical model of the flow, the exponential acceleration was consistent with taking Ω to be a constant. Eight different accelerations were investigated in total, corresponding to the following values of the acceleration parameter; $\Omega \in \{0, 10, 20, 30, 40, 50, 60, 70\}$. The effect of increasing the value of the acceleration parameter in the analysis was to produce pipe entrance flows showing progressively shorter development times and suppressed boundary layer development. The theoretical model was Reynolds number independent; thus the eight different cases by implication embraced flows with arbitrary start-up Reynolds numbers.

Experimentally, twelve different exponential accelerations were generated in total, comprising three sets of four tests, each set having a different initial impulsive Reynolds number. The anticipated flow variation for each test was given by

$$Re = Re_0 \exp[\Omega t], \tag{18.2}$$

where the value of the constants Re_0, Ω are given in table 18.1, which is simply table 7.3[1] repeated for convenience.

It was easy to simulate an exponential flow numerically; simply by setting the acceleration parameter to a constant value. However, experimentally, the flow had to be controlled accurately to match the chosen exponential increase using a closed-loop flow control system. Although the resultant experimentally generated flowrate variations were approximately exponential, there were noticeable deviations from those expected, mainly due to non-linearities in the control system, coupled with poor response at the low flow rates.

[1] The acceleration constant k from the early table has been replaced by the acceleration parameter Ω. For exponentially accelerating flow, the two are related according to $\Omega = kR^2/\nu$.

Chapter 18

Laminar base flow

Experimentally measured velocity profiles from the entrance region of impulsively started and exponentially accelerated pipe flows were presented in chapter 8. These flows showed unusual characteristics in their development; notably an initial period of boundary layer development, followed by a flow in which the boundary layer thinned with time. In all cases transition to turbulence subsequently occurred, the discussion of which is the subject of the next chapter. No theoretical explanation was available for the observed flow behaviour, and this motivated a general analytical investigation of the generally accelerating pipe entrance flow.

To this end, an analysis was conducted from first principles, utilising the general incompressible axisymmetric Navier-Stokes relations as a starting point (see part III). Use was made of a dimensionless co-ordinate system to describe the pipe flow, wherein the scaled axial velocity remained bounded and of order unity despite strong variations in the physical value of this parameter. The mapping between this system and the physical co-ordinate system was dependent on the Reynolds number, and thus in an exponentially accelerating pipe flow, this mapping varied exponentially in time. While the analytical solutions were straightforward in the dimensionless co-ordinate system, the variable mapping to the physical domain resulted in a complex flow which emulated all the unusual attributes of the experimentally measured system, for instance the boundary layer thinning phenomenon. The effect of the acceleration was encapsulated in the acceleration parameter, and steady pipe flows were shown to be described by taking its value to be zero. The present chapter is concerned with the reconciling of the numerical and measured laminar flow data, in order to discover the level of *quantitative* agreement between the two.

Preamble

The synthesis represents the culmination of the work carried out. Comparison is made between the theory and the experimental data, and the latter is processed further in the light of insights gained from the former.

As before the laminar base flow and flow breakdown are presented separately, to allow proper discussion of the aspects unique to each. Both chapters concentrate on high-level comparisons between experiment and theory, and are succeeded by the conclusions and recommendations in two subsequent chapters.

Part IV

SYNTHESIS

different to ensure disparate stability behaviour. In contrast, the temporal and spatial curves for the remaining data [(b) to (h) inclusive] converge before becoming vertically asymptotic. This indicates that the velocity profiles from each type of flow (for the same value of δ^* that is) have become indistinguishable in this limit.

17.4 Summary

In the present chapter, the stability of generally accelerating pipe flow has been investigated, both in the far downstream, parallel limit, and in the steady entrance case. These two simple limits have been studied for the main reason that they both embrace the majority of the developing pipe flow. A large disparity was found between the stability of the downstream and entrance regimes, the former revealing itself as being twice as stable as the latter. In both cases, the region of instability was shown to be restricted to a small portion of the entire flow - in the temporal case to early times, and for the entrance flow to a small region near the inlet plane. Generally, acceleration has a stabilising effect on the flow. However, the fundamental behaviour of exponentially accelerating pipe flow has been shown to be similar to its limiting case; the impulsively started pipe entrance flow. All stability data presented here, for both the parallel downstream and the steady entrance flows, are also tabulated in appendix C.

This chapter concludes the presentation of the analytical and numerical data. The following chapters are concerned with the reconciliation of the experimental data - both base-flow and stability - with the theory developed here.

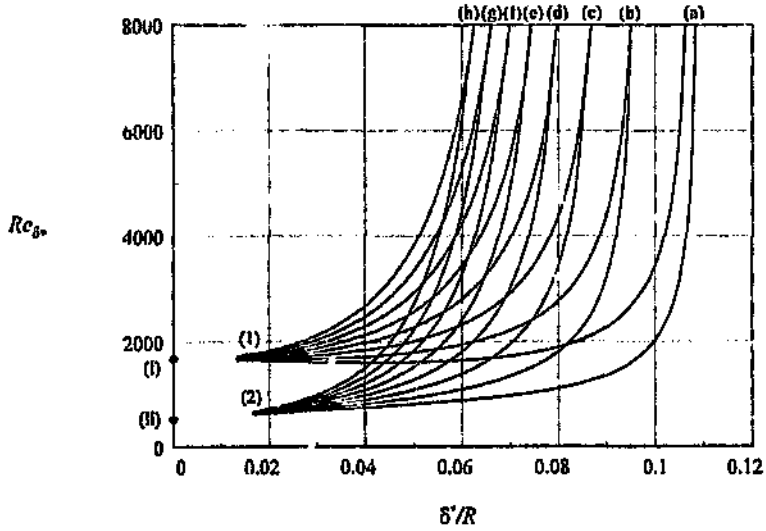

Figure 17.14: The variation of the critical displacement thickness Reynolds number with displacement thickness, for discrete values of the acceleration parameter; (1), parallel developing flow; (2), entrance flow; (i), Error-function stability limit, $Re_{\delta^*[\text{crit}]} = 1675$; (ii), Blasuis stability limit, $Re_{\delta^*[\text{crit}]} = 519.06$; (a), $\Omega = 0$, (b), $\Omega = 10$; (c), $\Omega = 20$; (d), $\Omega = 30$; (e), $\Omega = 40$; (f), $\Omega = 50$; (g), $\Omega = 60$; (h), $\Omega = 70$.

The framework of comparison for the stability data was chosen to be the δ^* - Re_{δ^*} plane, because of the bounded behaviour shown by both parameters as $\delta^* \to 0$. This figure reveals clearly the distinctions and similarities between the two sets of data. As the boundary layer thins, the stability curves for each flow regime approach their respective limits; namely the Blasius stability limit for the entrance flow, and the error-function limit for the parallel, temporally developing system. As was seen with the base-flow representation in the previous chapter, the use of the displacement thickness as the ordinate is advantageous in that it emphasises the thin boundary layer behaviour of the flow; thus the convergence of each data set to their respective limits is clearly seen in this figure.

The stability curves from each type of flow converge to one another as the boundary layer thickens, for each respective value of the acceleration parameter. This behaviour would be expected, due to the fact that the velocity profiles from each type of flow became similar as the boundary layer grows[10]. Simultaneous to the convergent behaviour, the stability curves from each flow show an asymptotic increase in the critical Reynolds number with increasing values of δ^*. For the non-accelerating flow (a), both the temporal and spatial stability curves become vertically asymptotic *before* convergence occurs; thus the two respective limiting velocity profiles at which stability last occurs, are in each case sufficiently

[10]This behaviour was discussed in detail in the previous chapter.

test EXPE, comprising the stations EE1, EE2, EE3 and EE5, was shown. The marked presence of (a) the inlet bump at the parallel-entrance flow interface for each station, combined with (b) variability of Ω, prevented the thinning portion of the data from each station from coinciding. The large waviness in EXPE is thus predominantly due to the combination of these four data (each with its own inlet bump) from different axial positions. Further, the thinning region of the flow was also prone to (c) a general slight lack of repeatability, due to variable inlet effects other than the inlet bump. The above factors [(a), (b) and (c)] were responsible for the large scatter seen. Apart from the effects described above, there is a further cause of *systematic* deviation of the experimental data from the theoretical trends, addressed in section 18.3; namely the mismatch of the simple theoretical and the experimental boundary conditions at the pipe inlet plane. The consequences of this can be seen in the data EXPF in figure 18.9, where the experimental points remain below the theoretical lines with reducing x.

A final, separate, point to be born in mind when considering figure 18.9 is the lack of a time direction in this figure. This is due to the fact that the dimensionless axial position of an experimental data point is a function of both the time and the physical axial station: combination of data from different physical stations of a test renders meaningless the indication of any temporal development on the figure.

Consider now a comparison between the data shown in figure 18.9. For small values of the dimensionless axial position, the variability far exceeds in magnitude the theoretical trends for increasing acceleration. In this region of the figure (approximately for $x < 0.005$), no acceleration dependent trend can be inferred. However, all four data follow in general the asymptotic theoretical variation, indicating strongly that, while the thinning region is substantially disturbed by inlet effects, the mean flow behaviour is close to the simple theoretical model[12]. For dimensionless axial positions greater than about $x \approx 0.005$, the inlet variability becomes small relative to the difference between the theoretical curves for different accelerations, and the experimental effects of acceleration can thus be resolved. The trend is similar to that shown in the temporal comparison in figure 18.8; the lower two accelerations - EXPE and HXPA - are in approximate alignment with the low acceleration theoretical curves, somewhere in the range $0 < \Omega < 30$, whereas the higher two curves - EXPF and EXPG - align somewhere in the range $30 < \Omega < 70$. This is in agreement with the theory, to the level of uncertainty in the data.

[12]Recall that the experimental data has been transformed into the dimensionless co-ordinate system via a variable transformation, and there is consequently no reason why the data should substantially align with each other or the theory; excepting that the theory describes the experimental system accurately.

show distinct trends. However, the experimental variation of the displacement thickness shows the correct qualitative behaviour with increasing acceleration parameter for this region, consistent with the superimposed theoretical results. The lowest acceleration test HXPA ($\Omega \approx 13$) follows approximately the $\Omega = 10$ line; the test EXPE ($\Omega \approx 20$) varies somewhere between $\Omega = 10$ and 20, while the remaining two curves - EXPF and EXPG ($\Omega \approx 33$ and ≈ 45 respectively) are positioned somewhere between $\Omega = 50$ and 70 theoretical curves. Thus although the data show the correct qualitative trends, those for the largest two accelerations seem to be convergent to higher acceleration parameter curves than would be expected. Unfortunately, for the two higher acceleration tests (EXPF and EXPG), measurements were not taken sufficiently far downstream to capture extensive parallel development of the flow, with the result that the full extent of these two data sets are within the region of strong acceleration parameter variability. Referring to figure 18.1, both of these tests showed slightly higher values of the acceleration parameter for early times, and this possibly contributed to their trend towards the higher acceleration parameter theoretical curves here.

The discussion now returns to the lower two acceleration parameter tests, namely HXPA and EXPE. For HXPA, the data in figure 18.8 are in close agreement with the simple theory: the measurements extend only as far as $t \approx 0.025$, and lie between the $\Omega = 0$ and $\Omega = 10$ theoretical curves, approaching the $\Omega = 10$ curve at $t = 0.025$. This is consistent with the measured variation in acceleration parameter shown in figure 18.1, which increases from below zero at start-up, to a value just above 10 for later times. Considering EXPE, the acceleration parameter (figure 18.1) approaches a constant value of about 20 as early as $t \approx 0.01$. Consistent with this the experimental data follow the $\Omega = 20$ theoretical line closely in the range $0.01 \leqslant t \leqslant 0.025$. However, for times greater than 0.025, the data depart from the $\Omega = 20$ line and approach the $\Omega = 10$ curve instead. This trend was seen earlier in figure 18.4, and was ascribed in section 18.3.1 to the presence of the inlet bump in the data EE5[11].

In a manner similar to the temporal comparison above, all four sets of data from the 'E' series of tests were superimposed in the spatial framework. This is shown in figure 18.9. As with the temporal representation (where the boundary layer thinning flow was not shown), the data from the parallel development region of each test have been omitted for clarity in this instance. In general, the deviation of the experiment from the theory shown in this figure is far greater than in the equivalent parallel representation; furthermore, the individual data show a large degree of scatter. Before proceeding with the data comparison, the reason for this strong variability will be explicitly addressed.

The variability of the thinning flow can be understood by considering the manner in which the data of figure 18.9 is derived. For the sake of illustration, the test EXPE will be discussed. In figure 18.5, the spatial development of the single

[11] Remember that each data in figure 18.8 is a combination of data from many tests; in the case of EXPE, is consists of values from EE1, EE2, EE3 and EE5.

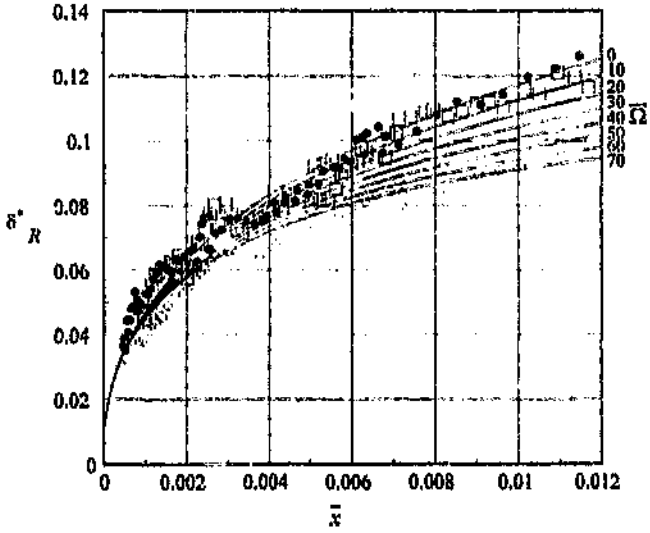

Figure 18.9: The variation of dimensionless displacement thickness with dimensionless axial position, for the boundary layer thinning portion of the 'E' series of tests: •, EXPE ($\bar{\Omega} \approx 20$); ○, EXPF ($\bar{\Omega} \approx 33$); ◇, EXPG ($\bar{\Omega} \approx 45$); ×, HXPA ($\bar{\Omega} \approx 13$); , theoretical curves.

In order of increasing acceleration parameter, the tests are: HXPA, EXPE, EXPF, and EXPG (their variation of $\bar{\Omega}$ in time was given in figure 18.1). Due to the fact that the acceleration parameter did not remain strictly constant in these tests it is not possible to give an exact representative value of this parameter. However, the anticipated value[10] of the acceleration parameter for the various tests was given in table 18.1, and for the four tests presented here the values are: EXPE, $\bar{\Omega} = 19.6$; EXPF, $\bar{\Omega} = 32.5$; EXPG, $\bar{\Omega} = 45.5$; HXPA, $\bar{\Omega} = 13.0$. Although the measured parameter was close to these values for later times, the flow at start-up showed a highly variable value of $\bar{\Omega}$. The reader is referred to the earlier section 18.1 for a detailed discussion on the acceleration parameter for the various tests.

The temporal development given by figure 18.8 will be considered first. As $\bar{t} \to 0$, all the theoretical curves converge towards a single locus. Furthermore, the measured data shows excellent alignment with the theory here, which also approaches a single acceleration-independent curve as $\bar{t} \to 0$. As time increases, the data from the separate tests follow increasingly lower trajectories for increasing acceleration parameter.

Consideration of figure 18.1 shows that the value of $\bar{\Omega}$ for all four tests was highly variable for $\bar{t} < 0.02$. Due to this variability, the measured data would not be expected to follow any one theoretical line for small times, but only the general trend of the data. By about $\bar{t} = 0.005$ the points from the separate tests begin to

[10]The value that the flow control system attempted to achieve.

18.4 Flow development with increasing acceleration

The data presented in the previous section were concerned with the flow development of a single test: also of interest are the more global trends, especially the effect of increasing acceleration parameter on the flow field. The 'E' series of tests was chosen to illustrate the effect of the acceleration parameter on the experimental system, for the reason that it was the most extensive, combined with the fact that it showed the closest to exponential behaviour for early times. The complementary temporal and spatial means of representing the data were chosen, because as before, it allowed a compact comparison with the simple theoretical results for both the early parallel flow, and for the later boundary layer thinning regime. The measured variations of δ^*/R with both t and x from the tests EXPE, EXPF, EXPG and HXPA (see figure 18.1) are given below.

The variation of the dimensionless displacement thickness in time for the 'E' series of tests is given in figure 18.8, while the complementary spatial development is shown in figure 18.9. In these two figures, no discrimination is made between data from the different stations of a test, only between the different tests. That is, the stations EE1, EE2, etc. are all combined to form the single data set EXPE. The thinning portion of each data is omitted from the temporal development, while the early time flow is left off the spatial representation, predominantly for clarity and to avoid cluttering. Superimposed on both figures are the respective theoretical development curves.

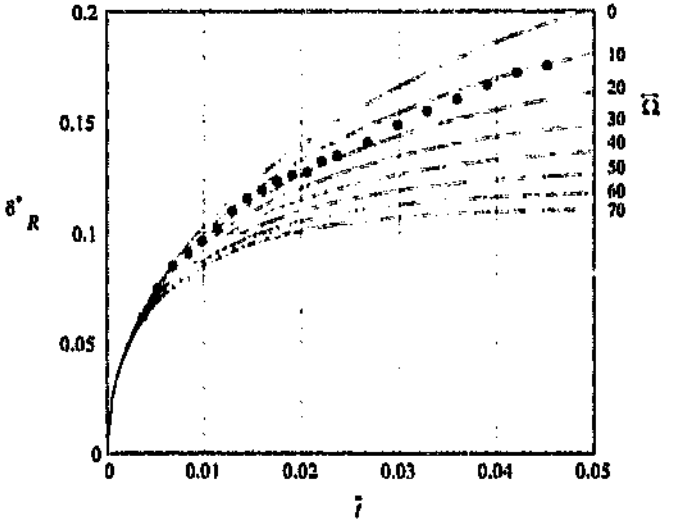

Figure 18.8: The variation of dimensionless displacement thickness with time, for the parallel portion of the 'E' series of tests: •, EXPE ($\bar{\Omega} \approx 20$); ○, EXPF ($\bar{\Omega} \approx 33$); ◇, EXPG ($\bar{\Omega} \approx 45$); ×, HXPA ($\bar{\Omega} \approx 13$); , theoretical curves.

the various curves should be considered when comparing the theory with experiment.

(ii) With reference to the spatial flow development shown in figure 18.7; as before, the data EE5 is not present on this scale of axes. The other three data show acceptable alignment with the $\bar{x} = 20$ spatial development curve. As would be expected, the data from the parallel developing part of the flow - those points which aligned in figure 18.6 - here form distinct lines.

(iii) The inlet bump, present at the interface between the parallel and entrance regions, does not appear to have a significant effect on the shape parameter. In fact the only significant undershoot[9] in the shape parameter can be seen in figure 18.7, for the data EE1 at $\bar{x} \approx 0.003$. This seems to indicate that the inlet effect is associated more with the central core flow of the pipe than with the boundary layer. This behaviour was also noted in the experimental data presented earlier in section 8.6, where the entrance jet seemed to be restricted to the outer edge of the boundary layer and the neighbouring core flow.

(iv) The data for the most upstream station EE1 in figure 18.7 deviate fairly strongly from the theoretical curve as $\bar{x} \to 0$. Mismatch between experimental and theoretical behaviour was also seen in the displacement thickness for this station. As was explained in the prior section concerning the displacement thickness, discrepancies at this station were quite possibly predominantly due to an inconsistency between the simple theoretical inflow conditions at the inlet (constant, thin boundary layer profile), and the boundary conditions existing at the experimental inlet plane.

Despite minor discrepancies, the experimental data, as adjudged by both the shape parameter and the displacement thickness, is in excellent agreement with the simple theoretical results, for the case of the test EXP6.

[9] An overshoot was seen in the displacement thickness when the bump passed. An undershoot would be expected in the shape parameter for the same phenomenon.

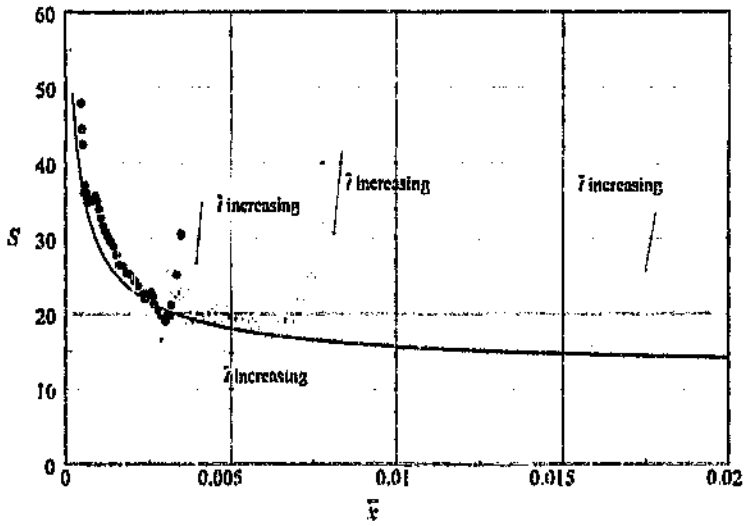

Figure 18.7: The variation of the boundary layer shape param with dimensionless axial position, for the test EXPE: •, EE1 ($x/R = 12.24$); ▫, EE2 ($x/R = 29.25$); ◇, EE3 ($x/R = 64.52$); , theoretical curve for $\Omega = 20$.

As with the displacement thickness, the shape parameter shows qualitative agreement with the predicted patterns. At early times, the shape parameter decreases rapidly from infinity, following the parallel temporal development curves, in this case all the data follow approximately the curve corresponding to $\Omega = 20$. The arrival of the entrance flow sequentially at the various axial stations causes a halt in the temporal decrease of the shape parameter, and its trend reverts to a gradual increase in time. The furthermost upstream stations leave the parallel development curve first, followed later by those at subsequent downstream positions. The increase in the shape parameter with time is commensurate with the boundary layer thinning behaviour of the flow at later times.

It was shown in section 18.3.1, in the context of the displacement thickness, that the boundary layer thinning portion of the experimental data is better described in the spatial framework of figure 18.7. As can be seen in this figure, sets of data that were separate in figure 18.6, converge substantially on each other (and fall close to the theoretical curve) in the dimensionless axial framework. Although all data predominantly follow the correct expected trends, a number of idiosyncrasies are present which are interesting:

(i) Considering the data of figure 18.6; although the approximate value of the acceleration parameter for these data was $\Omega \approx 20$, the furthermost downstream curve - EE5 - is convergent to a slightly lower value. This discrepancy is possibly due to the systematic uncertainty in the shape parameter. Due to this error, not much certainty can be placed on the exact value of the measured parameter; rather the qualitative behaviour of

detailed structure of the inlet flow may have been different from that of the simple theory. Concerning the first point, a finite boundary layer thickness at the pipe inlet would certainly have produced the observed effect. Extrapolation to a 'virtual' inlet plane within the contraction would have necessitated adding some factor to the physical axial location, thus bringing the data closer into line with the theoretical curves. It was, however, unclear whether this factor was to be a constant value of $\tilde{x}$ or x; quite possibly neither simple compensation would have corrected the data properly. For this reason it was decided not to adjust the data.

18.3.2 The velocity profile shape parameter

The experimental variation of δ^*/R discussed above was determined experimentally to a far greater accuracy than was the shape parameter S. It was shown in section 8.5.1 that the shape parameter was prone to a large systematic error, due to the unknown position of the pipe wall relative to the LDV measuring volume. However, consideration of the variation of S with both $\tilde{t}$ and $\tilde{x}$, and its comparison with the theory are given below, as the trends embody useful information. The variation of S with both $\tilde{t}$ and $\tilde{x}$ is given in figures 18.6 and 18.7. As before, only data from the test EXPE is presented. In both figures the experimental data have been compared with the theoretical variation for the acceleration $\tilde{\Omega} = 20$, while the station EE5 has been omitted from figure 18.5 because it does not appear on the scale of axes of the theoretical curves.

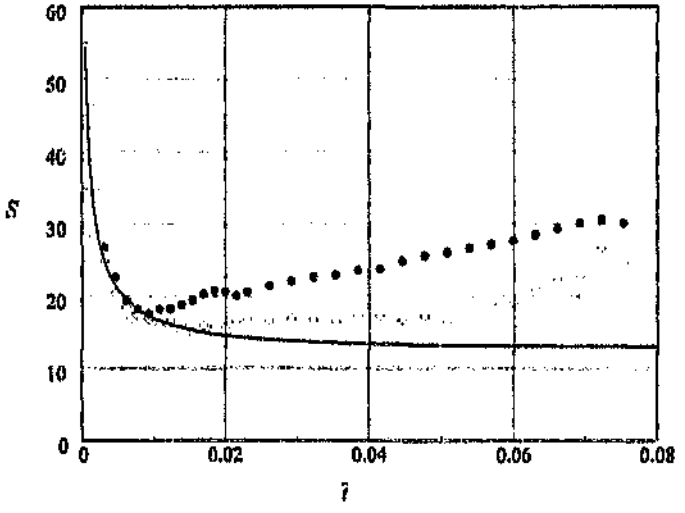

Figure 18.6: The variation of the boundary layer shape parameter with dimensionless time, for the test EXPE: •, EE1 ($\tilde{x}/R = 12.24$); ○, EE2 ($\tilde{x}/R = 29.25$); ◇, EE3 ($\tilde{x}/R = 64.52$); ×, EE5 ($\tilde{x}/R = 320.50$); , theoretical curve for $\tilde{\Omega} = 20$.

trace separate curves in figure 18.5. In contrast, the boundary layer thinning portions for each of the three axial stations, which are widely separate from one another in figure 18.4, align substantially with the simple theoretical steady (in the dimensionless system) entrance curves. A number of important issues arise here, which require detailed discussion:

(i) In general, all the data closely follow the theoretical curves for the later boundary layer thinning regime. The assertion that the boundary layer thinning behaviour is entirely ascribable to the reference frame transformation, is thus largely true. This is a remarkable result, and justifies the use of the simple *steady* entrance flow models to describe the unsteady entrance flow.

(ii) The inlet effects seen in the spatial representation shown in figure 18.5 are more noticeable than in the temporal system given by figure 18.4. All three tests given here overshoot the $\bar{\Omega} = 20$ theoretical curve before converging on it. The region of overshoot is indicated in figure 18.5; as (a) for the data EE1, (b) for EE2, and (c) for EE3. The dimensionless axial extent of this effect can be seen to decrease with diminishing dimensionless axial position. A superficial interpretation of this fact would make it appear as if the structure was growing axially as it convected downstream. However, the overshoot on the left-most data actually occurs at a later time than in the measurements from further downstream. In reality the structure is effectively a 'bump' convecting downstream at the parallel-entrance flow interface, and its decrease in size with decreasing dimensionless axial position is due to the variable scaling of the axial co-ordinate. A more meaningful measure of this structure - its temporal extent - can be inferred from the data. For all three sets of data, the temporal extent of this bump is approximately constant, at about $\Delta\bar{t} \approx 0.016$.

(iii) Data from different stations in figure 18.5 which possess the same value of $\bar{x}$ have differing times. This explains why the overlapping data from different stations should not be expected to align perfectly; due to the variability of $\bar{\Omega}$, the flow will possess a different value of Ω at different times. Whereas the data in the temporal comparison of figure 18.4 would be expected to align with one another, no matter what the variation in $\bar{\Omega}$, for spatial alignment of the thinning flow region it is necessary that Ω remain constant.

(iv) The data for the most upstream station EE1, does not align well with the theory. Although each of the other theoretical data converge to a single line in the limit as $\bar{x} \to 0$, the experimental data of this particular station is offset from all the others, and in fact lies outside their extent. There are two possible reasons for this offset[8]: firstly, the inlet plane was simply taken as the point at which the contraction ended, but this was certainly not the point of zero boundary layer thickness in the pipe; secondly, the

[8]The same effect would apply with less sensitivity to the more downstream data.

to explain the discrepancy from within the confines of the simplified analysis alone. In reality, the mismatch is largely due to differences between the simple numerical inflow boundary conditions and those existing at the pipe inlet experimentally; that is, factors not included in the simple numerical model. This is corroborated by the fact that the maximum deviation from the theory is in all cases associated with the measurements at the interface between the parallel development region and the thinning part of the flow. This portion of the flow was shown in chapter 8 to be affected by inlet variability; in particular by the inlet 'bump', an effect most certainly not incorporated into the simplified numerical model. The effect of the inlet bump is covered later in this section.

Temporal development

First consider the temporal flow development shown in figure 18.4. The mean value of acceleration parameter for this test was just below $\bar{\Omega} = 20$ (figure 18.1) for most of its duration. For the three most upstream stations (EE1, EE2 and EE3), the time period over which the experimental entrance flow shows parallel development is small, confined to the region $0 \leq \bar{t} \leq 0.02$. Unfortunately, this is also the period during which the acceleration parameter shows strong variation (figure 18.1); thus the development curve of the experimental data is not expected to align exactly with any one theoretical value. The variation would be expected to follow the theoretical trend only roughly; in fact for this region the data lies somewhere between the $\bar{\Omega} = 0$ and $\bar{\Omega} = 30$ curves. The far downstream station - EE5 - shows a longer period of initial development; until about $\bar{t} = 0.05$ which is well into the region of constant $\bar{\Omega}$. As a result, one would expect the experimental curve to approach the $\bar{\Omega} = 20$ line, which it does appear to at about $\bar{t} = 0.03$. However, from this time until the occurrence of the inlet front, $0.03 \leq \bar{t} \leq 0.05$, the variation of δ^*/R takes on a slightly larger numerical value than would be expected, causing it to fall on the $\bar{\Omega} = 10$ curve instead. This region of increased boundary layer thickness near the point at which the thinning flow begins was seen in other tests, especially at the far downstream measuring stations. It was associated with in inlet effect: this was a manifestation of the inlet 'bump' prominent in some tests, and associated with the details of the impulsive flow start (see section 6.3).

Spatial development

Consider figure 18.4, the boundary layer thinning region of the flow is indicated by a decrease of displacement thickness with time, with the data in each case diverting from the parallel development curve. However, as discussed earlier, this data in figure 18.4 corresponds to the points *aligned* to the steady entrance data in figure 18.5. For each set of data shown, the points from early times are right-most, and the temporal development proceeds from right to left on the figure. The parallel developing regions that were concurrent in figure 18.4

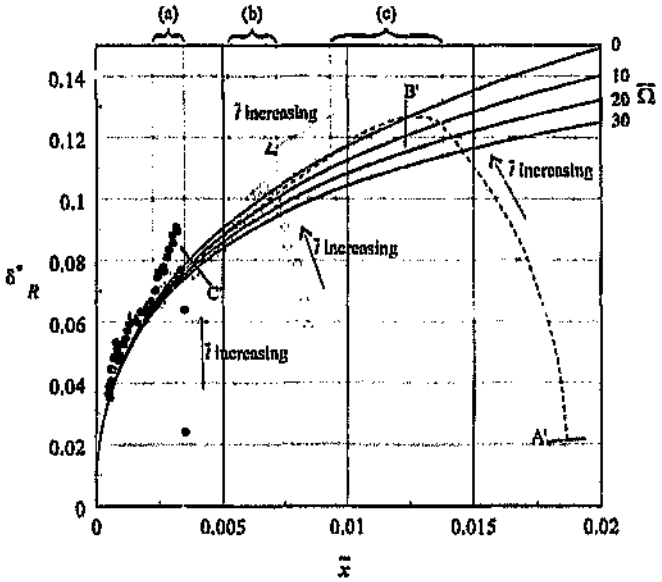

Figure 18.5: The spatial development of δ^*/R for the test EXPE; ···, theoretical results; •, EE1 ($x/R = 12.24$); ○, EE2 ($x/R = 29.25$); ◇, EE3 ($x/R = 64.52$); (a), (b), (c), inlet 'bump'; A', B', C', chosen points of increasing time for EE3.

cated that the two representations given by figures 18.4 and 18.5 respectively were sufficient to show the alignment of the experimental data with the theory. The thinning flow that cuts across the theoretical parallel development curves in figure 18.4 aligns with the theoretical entrance flow curves in figure 18.5, while the converse is true for the early parallel experimental data. Thus in conjunction, both figures give complementary views of the data, allowing verification of most of the measured results. For instance, the line A-B-C in figure 18.4 corresponds to A'-B'-C' in figure 18.5. The segment A-B in the former figure aligns with the theoretical curves there, whereas the corresponding segment A'-B' in the latter figure follows a unique trajectory. The converse is true for the line segment B-C, which follows a unique path in figure 18.4, while B'-C' aligns with the numerical entrance flow curves in figure 18.5.

It should be noted from the outset that in the comparisons which follow, there are dichotomous ways of viewing the correlation between analysis and experiment. In the first instance, the maximum deviation of the measured value of displacement thickness from the theory in figures 18.4 and 18.5 is only 10% - for the data EE5 at $\bar{\tau} = 0.05$ in figure 18.4 - implying good correlation with the simple theory. From another point of view, this small discrepancy in the data EE5 causes it to leave the $\bar{\Omega} = 20$ line and makes it lie on the $\bar{\Omega} = 10$ curve instead. From the latter perspective, a naive interpretation would give a factor of two difference between the theory and measured data - a substantial level of disagreement. The flaw in the latter argument arises from attempting

avoid unnecessary cluttering, only representative results are shown. In this regard the 'E' series of tests is described in detail, for the reason that these had an initial start-up in closest correspondence with the theory, and because they reflected the full range of behaviour of the flow[6].

18.3.1 Displacement thickness

A typical picture of the temporal and spatial development of the flow is given by the test EXPE (see figure 18.1). The variation of displacement thickness δ^*/R with dimensionless time and dimensionless axial position are presented in figures 18.4 and figure 18.5 respectively. In both figures, the experimental data have been mapped to the dimensionless co-ordinate system, and superimposed on the theoretical asymptotic data for the range of accelerations $0 \leq \bar{\Omega} \leq 30$. The data EE5 have been omitted from figure 18.5 because they do not appear on the scale of axes of that figure[7].

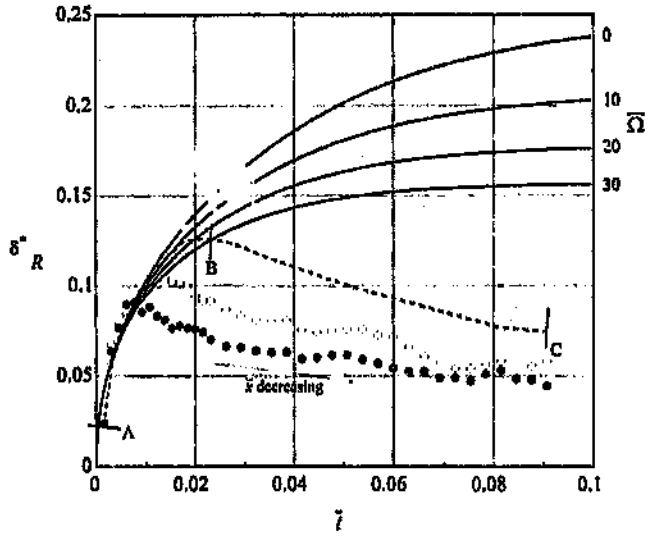

Figure 18.4: The temporal development of δ^*/R for the test EXPE: , theoretical results; •, EE1 ($x/R = 12.24$); ∘, EE2 ($x/R = 29.25$); ◇, EE3 ($x/R = 64.52$); ×, EE5 ($x/R = 320.50$); A, B, C, chosen points of increasing time for EE3.

Lines of theoretical development for the thinning flow are not shown on figure 18.4, while the lines indicating the early temporal development are omitted in figure 18.5, to avoid cluttering. The discussion of the previous section indi-

[6]The other tests were directed more towards the determination of the flow breakdown, and thus were not ideal for showing the laminar flow variation clearly. In contrast, these tests showed marked thickening and thinning regions, and clearly distinguishable patterns of behaviour at the different axial stations.

[7]The numerical results were in this case limited to the range $0 \leq \bar{x} \leq 0.02$.

given with respect to time, or as a function of the dimensionless axial position. In the former case, data from various axial positions will coincide for the parallel developing portion of their flows, while the later thinning behaviour will follow unique trajectories for the different axial positions. Conversely, in the dimensionless axial framework, all the thinning portions of the flow will coincide, while the early temporal development will be unique for differing axial positions.

The arguments presented above were given in greater detail previously in section 15.6, of which the current discussion serves as a summary. There the numerical results for the 'test' acceleration $\bar{\Omega} = 20$ were used to illustrate the principles involved, and the reader is referred to that section for further clarification.

18.2.3 Basis of comparison with experimental data

The above argument was concerned with dimensionless scaling in the context of the numerical system, in order to describe the temporal development of the flow at a fixed physical axial position. In comparing the experimental data with the numerical predictions, two options are available: the measurements may be reduced to the compact dimensionless form of the analysis, or the analysis may be made dimensional according to the parameters of the measurements.

It was decided to use the dimensionless basis, for the reason that it was shown to highlight properties of the flow which could not have been observed from the perspective of the primitive variables. It is central to establish whether the experiment mimics the universality exhibited by the analysis. Further, the important concepts of *steady state flow* with its commensurate *development time*, and *entrance length* only have meaning in the dimensionless framework.

In sections 18.3 and 18.4 that follow, comparison is made between the simple theoretical data and the suitably transformed numerical results. The measured data for the test EXPE($\bar{\Omega} \approx 20$) is first considered in isolation in section 18.3. Measurements from the four axial stations EE1 ($x/R = 12.24$), EE2 ($x/R = 29.25$), EE3 ($x/R = 64.52$ and EE5 ($x/R = 320.50$) are compared to the theoretical curves in the dimensionless framework, both for the displacement thickness and the velocity profile shape parameter. Thereafter the effect of increasing acceleration on the flow is demonstrated in section 18.4, by comparing the full data from the four separate 'E' tests [EXPE ($\bar{\Omega} \approx 20$), EXPF ($\bar{\Omega} \approx 33$), EXPG ($\bar{\Omega} \approx 45$), HXPA ($\bar{\Omega} \approx 13$)] with each other and to the theory.

18.3 Flow development in time and space

The experimental data of part II are re-presented below using the dimensionless framework, in order to allow compact comparison with the numerical data. To

19.2 Comparisons

The results of the surface fitting procedure described above are shown in figure 19.5. The individual experimental points are shown as open circles superimposed on the surface plot.

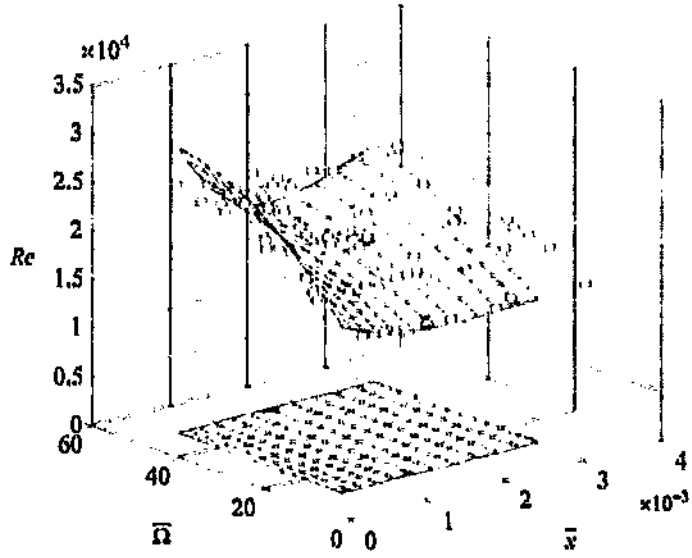

Figure 19.5: The three dimensional fitted surface to the experimental inception data in $(\bar{x}, \bar{\Omega}, Re)$ space, showing the experimental points superimposed. The extent of the surface is indicated on the floor of the plot.

There are two important trends evident in the inception surface shown here. Firstly, the Reynolds number increases in value monotonically with increasing acceleration parameter for all values of x; secondly, for any value of acceleration parameter, the Reynolds number initially decreases in value with axial position, reaches a minimum, and thereafter increases downstream. Both these trends reflect those seen in the theoretical linear stability curves generated in chapter 17. The three-dimensional surface representation of figure 19.5 is only qualitative in nature, and better quantitative comparisons can be obtained by extracting curves from distinct planes of intersection with the surface. Figure 19.10 shows extracted curves for fixed values of the acceleration parameter ($\bar{\Omega} = 10$, $\bar{\Omega} = 20$, $\bar{\Omega} = 30$, $\bar{\Omega} = 40$, $\bar{\Omega} = 50$), superimposed on which are the corresponding theoretical linear stability curves for the pipe entrance region.

Immediately evident is that each curve of the experimental data in figure 19.6 has a lower minimum critical value than the corresponding theoretical curve. As the acceleration parameter increases, the disparity increases. The variation of the minimum critical Reynolds number with acceleration parameter is shown in figure 19.7.

corresponded to a matrix of coefficients F with size 5×3 - a quadratic variatio in $\hat{\Omega}$ and fourth order variation in $\hat{x}$). The standard deviation of the data from the fitted surface was 1.6537×10^3 in Reynolds number. The distribution of the error was close to normal, as evidenced by the histogram of figure 19.4.

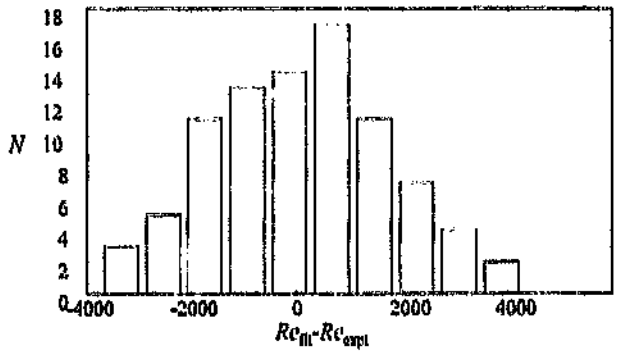

Figure 19.4: The distribution of the experimental data about the fitted surface.

The shape of the histogram seemed to indicate that the surface fit was an accurate representation of the data in the mean. The standard deviation shown by the data from the surface was approximately 8% of the average surface Reynolds number of ≈ 20000. A more appropriate estimation of the accuracy of fit in this case is not the standard deviation, but rather the *standard error of the mean*, given by $\sigma_s = Re'/\sqrt{N}$ where Re' is the standard deviation in Reynolds number, and N is the number of data points. In the current case, $N = 87$, and thus the standard error in terms of Reynolds number is $\sigma_s = 177.3$. For a confidence level of 95%, the uncertainty in the fitted surface would be expected to be $\pm 2 \times \sigma_s$, which amounts to an uncertainty in Reynolds number of $Re \approx 355$. Combining all the inception data to define a single surface holds a number of advantages over considering the stability results from each test individually:

(i) It allows a global correlation, in both $\hat{x}$ and $\hat{\Omega}$, between all the measured data.

(ii) Combining all the data yields a statistically better population of points (15 degrees of freedom for 87 points) for interpolation purposes. Curve fitting to the individual test data would give substantially poorer results, due to the sparse data distribution ($\approx$ 5 degrees of freedom for 8 points on average).

(iii) The resultant surface obtained from the fit allows correlation of the data in any chosen form within the range of the fit. For instance, curves of constant Reynolds number can be extracted with ease, as can Re - $\hat{x}$ curves at arbitrary values of the acceleration parameter.

(iv) A global error estimate could be obtained from observing the statistical deviation of the data from the surface.

where F is a matrix of coefficients, and the vectors e_x^T, e_Ω are polynomial basis vectors in the independent variables x and Ω respectively. These bases were chosen to be the Chebyshev polynomials of the second kind, on the range $[0, 1]$. This choice was made because of the orthogonal properties of these polynomials, and because substantial numerical machinery existed for them, developed in the numerical analysis of the previous chapters. By truncating e_x^T at order N, e_Ω at M, and the coefficient matrix at $N \times M$, the interpolating surface could be restricted to order $(N-1) \times (M-1)$. A solution was then sought in the form of equation (19.2) which interpolated the experimental data in the least-squares sense. Due to the unit range of the Chebyshev polynomials, the experimental data was scaled to the unit square in the x - Ω plane. The full set of data was not used; only those points near the inlet region (data from the region surrounding the minimum critical points of the experimental data) were retained. The reasoning behind this was simple. Firstly, the data in the square domain given by $4.1504 \times 10^{-4} < x < 3.8042 \times 10^{-3}$, $11.442 < \Omega < 49.065$ showed a uniform distribution, whereas points outside this region were located on 'tendrils'; secondly, this area embraced the experimental minimum critical points of all the data. Since a fairly low order fit was desired, the restriction of the region was beneficial in this regard as well. An explicit procedure was not used, rather a global minimisation iterative algorithm was employed. Ideal for this purpose was the supplied Matlab function `fmins`. This function uses a simplex search algorithm, to minimise a function of several variables. Practically, this algorithm minimises any function represented by a Matlab m-file, as long as that function returns a scalar value to be minimised. Since the problem was to minimise the least-squares residual of the polynomial surface fit (19.2) to the discrete data $(\bar{x}_i, \Omega_i, Re_i)$, a function was defined of the form

$$\epsilon = \sum_i \left[Re_i - \hat{Re}(\bar{x}_i, \Omega_i) \right]^2 \tag{19.3}$$

where $\hat{Re}(\bar{x}_i, \Omega_i)$ is defined by equation (19.2). An initial guess for the matrix F was supplied, and the function `fmins` returned the best fit coefficient matrix for the particular order chosen. Solution was initially obtained for low orders (initially a linear fit), and the order was increased in each of the ordinates, simply by augmenting zeroes to the resulting matrices from the previous solution. The resulting matrix was then used as the first iterand for the next solution. The properties of the Chebyshev basis allowed this augmentation; the magnitude of the coefficients of extra terms in a Chebyshev series become rapidly insignificant, while their presence does not affect greatly the value of the already determined lower coefficients [see chapter 12, or Fox & Parker (1968), Rivlin (1990), for a discussion on the properties of the Chebyshev polynomials].

The solution procedure was terminated at an order where the fitted surface was smooth and regular, and where the addition of extra coefficient terms had an insignificant effect on the solution. For the present data, the solution had become invariant to about 100 in Reynolds number at an order of 4×2 (this order

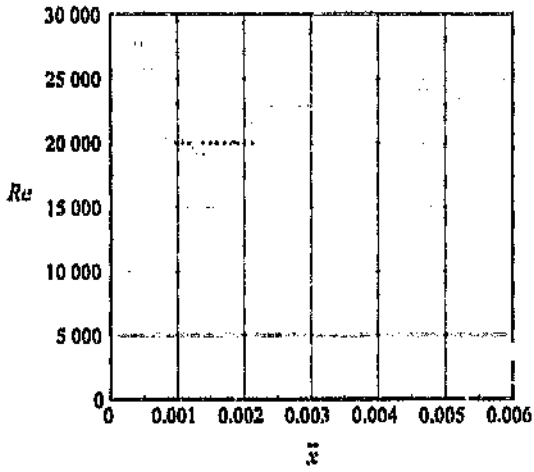

Figure 19.3: The variation of the experimental critical Reynolds number with dimensionless axial position, for the test GXPA ($Re_0 = 0510$, $\tilde{\Omega} = 32.5$).

flow; therefore comparisons will be made between the measured data and the stability results for the steady (dimensionless) pipe entrance flow.

Surface fitting to the experimental data

Theoretical linear stability characteristics were calculated for various constant values of the acceleration parameter. However, in the experimental system the Reynolds number in the pipe was only approximately exponential. Consequently the value of the acceleration parameter did not remain constant during a test. The variation of the acceleration parameter with time was shown in figures 18.1 to 18.3. Due to the fact that the instantaneous value of the experimental acceleration parameter was known, the experimental inception measurements could be given as points in $\tilde{x}$, $\tilde{\Omega}$, Re space. Consideration of all the experimental inception data showed that they approximated a smooth surface in $\tilde{x}$, $\tilde{\Omega}$, Re space. It was therefore decided to fit a *surface* to the entire data set, and to extract data trends therefrom, rather than by fitting curves to the individual tests. The achievement of a surface fit is advantageous for the reason that it allows a multi-dimensional correlation (in $\tilde{x}$ and $\tilde{\Omega}$) between all the inception results, negating the idiosyncrasies of the individual tests and yielding a global 'best-fit'. In contrast, individual curve fitting to the data from each acceleration would necessitate a high order (4th order) interpolation to a sparse (≈ 8 points) set of data. It was chosen to fit a general two-dimensional polynomial surface to the data, of the form

$$\hat{Re}(\tilde{x}, \tilde{\Omega}) = a_x^T F a_{\tilde{\Omega}}, \tag{19.2}$$

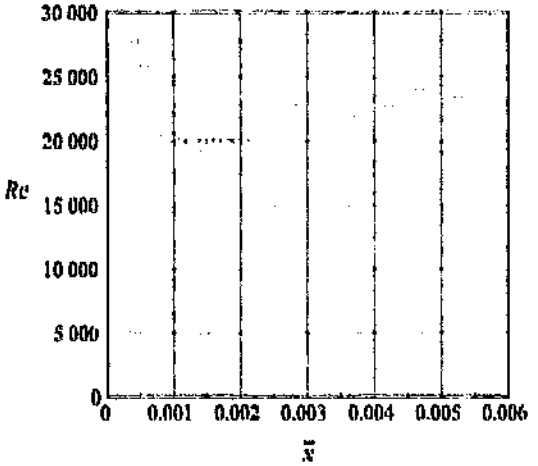

Figure 19.3: The variation of the experimental critical Reynolds number with dimensionless axial position, for the test GXP4 ($Re_0 = 6510$, $\Omega = 32.5$).

flow; therefore comparisons will be made between the measured data and the stability results for the steady (dimensionless) pipe entrance flow.

Surface fitting to the experimental data

Theoretical linear stability characteristics were calculated for various constant values of the acceleration parameter. However, in the experimental system the Reynolds number in the pipe was only approximately exponential. Consequently the value of the acceleration parameter did not remain constant during a test. The variation of the acceleration parameter with time was shown in figures 18.1 to 18.3. Due to the fact that the instantaneous value of the experimental acceleration parameter was known, the experimental inception measurements could be given as points in x, Ω, Re space. Consideration of all the experimental inception data showed that they approximated a smooth surface in x, Ω, Re space. It was therefore decided to fit a *surface* to the entire data set, and to extract data trends therefrom, rather than by fitting curves to the individual tests. The achievement of a surface fit is advantageous for the reason that it allows a multi-dimensional correlation (in x and Ω) between all the inception results, negating the idiosyncrasies of the individual tests and yielding a global 'best-fit'. In contrast, individual curve fitting to the data from each acceleration would necessitate a high order (4th order) interpolation to a sparse (≈ 8 points) set of data. It was chosen to fit a general two-dimensional polynomial surface to the data, of the form

$$\hat{Re}(x,\Omega) = a_{ij}^T Pr_{ij}, \tag{19.2}$$

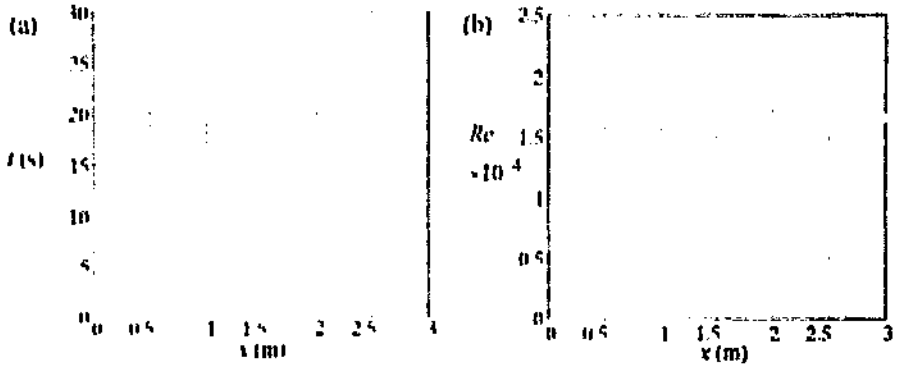

Figure 19.1 The axial variation of the experimental flow breakdown, from the tests (APX Re 6500 to 32500), as a function of time and Reynolds number. The error bars represent one standard deviation.

critical point. The flow breakdown downstream was shown in chapter 9 to be connected with wash-down and growth of disturbances from near the minimum critical point.

19.1 Synthesis of measured data

The data of figure 19.1 is in terms of dimensional variables. Comparison with the theoretical data requires a mapping to the normalised co-ordinate system. In the case of the axial position x, the mapping is given by

$$x' = \frac{x}{R\,Re} \tag{19.1}$$

where R is the pipe radius, and Re is the Reynolds number. Each point from figure 19.2b represents a co-ordinate pair in the x - Re plane; thus the dimensionless axial position corresponding to each point on this graph can be calculated directly from equation (19.1). Figure 19.3 below shows the inception data from figure 19.2b represented in the normalised axial ordinate.

The figure shows that there is no substantial qualitative difference between this representation and the dimensional one given in figure 19.2 earlier. However, the normalisation of the axial ordinate allows comparisons to be made, both between the results for different exponential accelerations, and directly with the numerical models. In part III the stability characteristics of the two asymptotic descriptions of the pipe entrance flow were obtained: firstly for the temporally developing, parallel flow, and secondly for the steady (in dimensionless terms) entrance model. It was stated earlier that all the flow breakdown and subsequent transition phenomena occurred in the boundary layer thinning portion of the

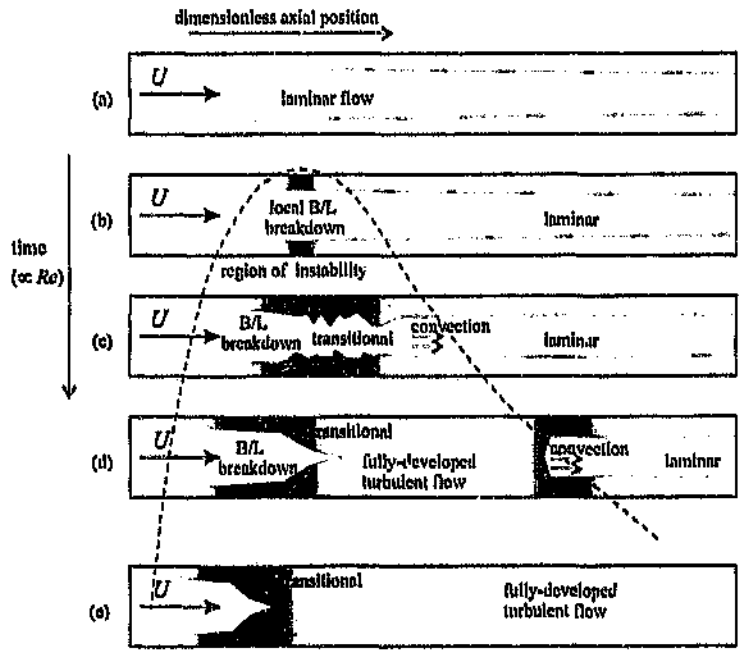

Figure 19.1: The schematic depiction of the transition to turbulence in the entrance region of an exponentially accelerating pipe flow: (a), laminar flow; (b), local boundary layer breakdown; (c), transitional flow convects downstream, local boundary layer breakdown persists near the inlet; (d), local breakdown upstream, turbulent front convects downstream; (e), local breakdown upstream, pipe-wide turbulent flow downstream; – – –, region of inception.

Measurements of the flow breakdown in the pipe entrance were made at various axial positions, by placing the LDV measuring volume within the boundary layer at various axial stations. The radial position at each station was chosen to be that point within the boundary layer that showed maximum sensitivity to flow breakdown. Twelve runs were made at each station, and the results were stored. For each run, the first identifiable time of flow deviation from the laminar state was measured, and the mean value of the twelve times was taken as the time of flow breakdown at that axial station. The Reynolds number variation with time was known (from the flowmeter data), and consequently the critical Reynolds number at each axial station could be ascertained. Figure 19.2 below repeats the experimental transition data for the test GXPA ($Re_0 \approx 6510$, $\Omega \approx 32.5$), first given as figure 9.9, and embodying 17 axial stations.

The two representations of the data in this figure are equivalent; the critical Reynolds number was simply determined from the time of transition, by using the flowmeter data. Breakdown first occurs at an intermediate axial station, in this case $x \approx 0.6$ m. As time progresses (and the Reynolds number increases), breakdown is observed both upstream and downstream of the original minimum

Chapter 19

Stability and inception

In this chapter, the basic experimental inception data of chapter 9 is further processed in the light of the theoretical framework emergent from the analysis. The earlier experimental inception results, given in that chapter in terms of the dimensional co-ordinate system, are transferred into the normalised co-ordinates, to allow direct comparison with the simple linear stability theory results from chapter 17 of the analysis. The current study was concerned with the behaviour of impulsively started and exponentially accelerated pipe entrance flows. From the perspective of a fixed axial position in the pipe, a clear pattern of behaviour was shown in all of the flows measured in this work. Initially the flow remained laminar, with breakdown and transition occurring later, when the Reynolds number was high. The early laminar development consisted of two phases: initially, boundary layer growth occurred at the measuring station, thereafter a region of boundary layer thinning ensued. The first phase of the laminar development was shown in the previous chapter to be accurately described by a simple parallel base flow model. The ostensibly complex behaviour of the second thinning phase was shown to be given by a steady numerical solution in the normalised co-ordinate system[1].

In all the flows measured, the breakdown of the laminar state was seen to occur during the later boundary layer thinning portion of the flow. Flow breakdown began as a laminar 'waviness' within the boundary layer in the pipe entrance, which subsequently developed into turbulent flow behaviour. These disturbances were subsequently observed both upstream and downstream of the initial inception point. They also grew in extent radially in the downstream direction, and pipe-wide turbulent flow was noted in the system far downstream. Near the inlet, while the boundary layer was disturbed, the central 'core' flow always remained laminar. Figure 19.1 below illustrates the general sequence of transition events seen in the flow.

[1]The previous chapter contained a detailed description and summary of the co-ordinate systems and the variable mapping between them, and they will not be discussed further here.

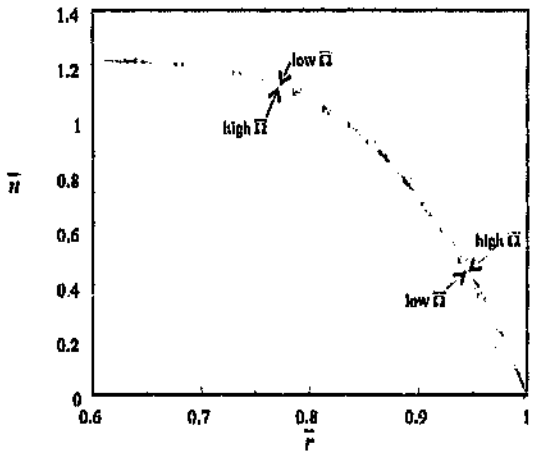

Figure 18.12: The variation in the shape of the velocity profile with acceleration parameter in the parallel developing region for the 'E' series of tests: ∘, station EE2, $\bar{t} = 7.685 \times 10^{-3}$, $\bar{\Omega} \approx 20$; ×, station EG3, $\bar{t} = 1.261 \times 10^{-2}$, $\bar{\Omega} \approx 45$; the two solid lines represent the equivalent numerical velocity profiles for $\bar{\Omega} = 20$ and $\bar{\Omega} = 50$.

Here the trends shown by the experimental data are both qualitatively and quantitatively correct. The higher acceleration profile EG3 has a higher value of velocity near the wall, and a correspondingly lower value near the edge of the boundary layer. The difference between the two experimental profiles was close to the discrepancy between the theoretical curves. Furthermore each of the theoretical profiles correlates substantially with its experimental counterpart.

function profiles were plotted against one another. In both cases, the entrance profile is less convex or curved near the wall than the equivalent parallel velocity profile. This results in the entrance profile having lower values of velocity near the boundary, and by way of compensation, higher velocities towards the outer edge of the boundary layer.

Referring now to the experimental data, the measured values for the parallel part of the flow show a good match with the theoretical curve. The experimental profile is even more convex than its theoretical counterpart. This is consistent with the predictions of chapter 15 that increased acceleration causes a more convex velocity profile: the start-up value of acceleration parameter was higher than the nominal value ($\Omega \approx 20$) for this test (figure 18.1). The entrance data shows a lot of variability, due to the non-repeatable entrance effects in this region of the flow, but in the mean the correlation with the theory appears to be moderately good. Comparing the two experimental results with each other, the anticipated trend is evident - the entrance profile has a lower velocity near the wall, and a higher velocity elsewhere. The observed discrepancy is, however, far too large to be caused by the difference in flow regimes alone, a conclusion supported by the tiny difference between the theoretical curves. The observed large experimental discrepancy is thus possibly due to the initial variation in the acceleration parameter, combined with the innate uncertainty associated with the later entrance flow.

18.5.2 The effect of acceleration on the velocity profile

As mentioned, it was shown in chapter 15 that increasing the acceleration parameter caused the velocity profile to adopt an increasingly convex shape. Unlike the comparison of the previous section, the effect of acceleration on the profile became *more* marked with increasing displacement thickness[15]. Thus in the case of discerning the effects of the acceleration it was straightforward to find appropriate velocity profiles.

The value of displacement thickness chosen was the same as in the previous section ($\delta^*/R = 0.091$). Profiles were taken from the parallel developing flow alone, in order to minimise experimental uncertainty. It was shown earlier in the chapter (for instance in figure 18.8) that the parallel temporally developing flow was highly repeatable and subject to minimal variability. Two profiles were obtained, each with the same displacement thickness, but originating from flows possessing different values of the acceleration parameter. The first profile was taken to be the parallel profile from figure 18.11 above (EE2; $\Omega \approx 20$ - axial position irrelevant due to parallel flow), and the second was extracted from the data EG2 ($\Omega \approx 45$). These two profiles are shown in figure 18.12 below. Superimposed are the equivalent theoretical profiles for $\Omega = 20$ and $\Omega = 50$ respectively.

[15]This was ascertained by informal numerical experimentation.

18.5.1 Parallel developing and steady entrance velocity profiles

It was shown theoretically in chapter 14 that profiles from the parallel developing and boundary layer thinning regions of the pipe flow had significantly different velocity profile shapes for the same value of any chosen parameter such as the displacement thickness. In order to see if this was so experimentally, it was decided to compare the theoretical profiles directly to measured ones. For this purpose two profiles were extracted from the data EE2 ($x/R = 29.25$, $\bar{\Omega} \approx 20$) for $\delta^*/R = 0.091$ - one from the early parallel developing region and one from the boundary layer thinning region (see figure 18.4). The equivalent theoretical profiles for the same values of displacement thickness and mean acceleration parameter were obtained from the numerical analysis. These experimental and theoretical data are shown superimposed in figure 18.11.

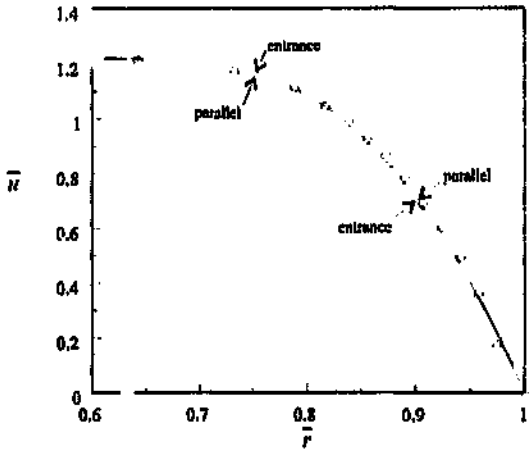

Figure 18.1 : Experimental velocity profiles from the parallel and entrance regions of the flow, for the station EE2 ($x/R = 29.25$, $\bar{\Omega} \approx 20$): o, $\bar{f} = 7.685 \times 10^{-3}$ (parallel development); ×, $\bar{f} = 2.152 \times 10^{-2}$ (entrance flow); the two solid lines represent the equivalent numerical parallel and entrance flow profiles.

The choice of displacement thickness to provide an appropriate comparison was not easy. An ideal choice would have been profiles with very thin boundary layers, for the reason that they would show the most marked difference in regard to structure. Unfortunately, this choice was not possible for several reasons: firstly, the very early (parallel) velocity profiles were not very regular, mainly as a result of poor placement of radial measuring stations (station positioning was optimised for the later profile development); secondly, in the boundary layer thinning (entrance) portion of the flow, the profiles underwent transition to turbulence before attaining a very thin boundary layer. It was for these reasons that the profiles shown in figure 18.11 were chosen to have a relatively thick boundary layer. As can be seen, the expected theoretical discrepancy (between the solid lines) is very small indeed for these profiles. The theoretical trend is the same as that shown in figure 14.7 of chapter 14, where the Blasius and error-

18.5 Velocity profiles

This chapter has been concerned up until now with comparison between theory and experimental data using two parameters - the displacement thickness and the velocity profiles shape parameter. The parametric nature of the displacement thickness allowed direct and full superimposition of theory and experiment using a pair of two-dimensional plots; versus $\bar{t}$ for the parallel flow and with respect to $\bar{x}$ for the thinning flow. Due to the fact that a velocity profile represe a radial variation of the velocity, a full comparison between the measured theoretical profiles is only possible using two three-dimensional representati embodying $\bar{u}(\bar{r},\bar{t})$ for the temporally developing flow, and $\bar{u}(\bar{r},\bar{x})$ for the boundary layer thinning region. However, due to the inherently qualitative nature of a surface plot comparison[13], it was decided to effect only a comparison between individual selected velocity profiles.

The primary aim of the velocity profile comparison was to ascertain the agreement between theory and experiment. Furthermore, it was important to observe whether the numerically predicted trends in velocity profile structure - due to acceleration and non-parallel effects - were present in the experimental data[14]. As before, data were taken from the 'E' series of tests. A fixed value of the displacement thickness was chosen, and two phenomena were investigated: firstly a comparison was made between a parallel developing velocity profile and its steady entrance counterpart for a fixed value of the acceleration parameter (figure 18.10a); secondly, the effect of the acceleration parameter on the structure of the parallel developing velocity profiles was observed (figure 18.10b). These two comparisons are given below.

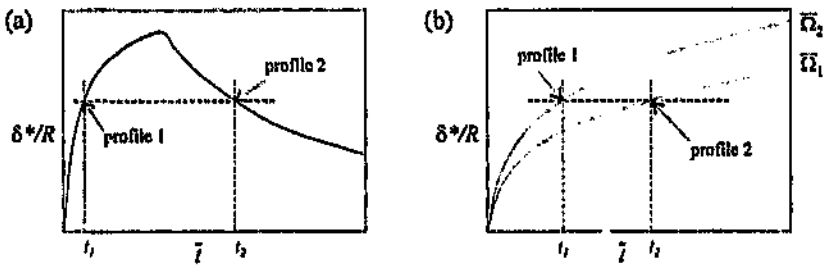

Figure 18.10: A schematic representation of the portions of the flow from where velocity profiles were obtained: (a) profiles from the parallel and thinning flow; (b) profiles from the parallel flow region - different acceleration parameters.

[13]Two widely disparate surfaces can be made to look indistinguishable by judicious choice of view point, while identical surface plots can seem different due to differing display grids.

[14]It was shown in chapter 14 that the parallel and entrance flow velocity profiles had fundamentally different shapes, in the limit as the boundary layer thickness approached zero. The steady entrance flow was convergent to a Blasius structure, whereas the parallel flow became of an error function shape in this limit. In a similar manner, the presence of acceleration was shown to produce more 'convex' velocity profiles, than for steady flow.

14. Arising from point 13, it is clear that the velocity profile shape parameter of Moss (1985) is not a unique quantifier of velocity profiles for any class of unsteady pipe entrance flows. This negates the conclusion of da Silva (1990), that this parameter uniquely characterises velocity profiles for the impulsively started steady flow rate case.

15. The overall effect of increasing the acceleration parameter in the dimensionless system is to (a) increase the value of the velocity profile shape parameter throughout the pipe; (b) correspondingly lower the value of the displacement thickness everywhere; (c) cause the system to attain steady-state in a shorter time; and (d) produce a more convex shaped velocity profile.

16. In general, the numerical base flow model reproduces all of the features of the measured system. The observed boundary layer thinning behaviour is produced by projecting the numerical solution into the physical space. The only substantial laminar features not explained by theory are 'bumps', observed at the interface between the entrance and parallel flow regions, and thought to arise from experimental pipe inlet effects at start-up.

17. The minimum critical Reynolds number for the classical zero-acceleration pipe entrance flow case was determined to be $Re = 11\,667$, while critical Reynolds numbers in excess of 500 000 were obtained at the last unstable downstream station, an order of magnitude greater than that achieved by previous researchers. Steady pipe entrance flows were shown to be linearly unstable to axisymmetric disturbances for only a small region of the pipe entrance, namely $0 < x \leq 0.081\,9$. The present stability results agree substantially with those of Garg (1981), and show the study of da Silva (1990) to be inaccurate. The error in da Silva's analysis is thought to arise from the use of a temporally explicit finite-difference scheme, combined with the physically incorrect and controversial upwinding technique used to describe the diffusion terms in his base flow model.

18. In the case of the zero-acceleration impulsively started pipe entrance flow, the stability behaviour of the two regions described in point 13 are substantially different, in accordance with the differences between their velocity profiles. The minimum critical Reynolds number of the parallel flow ($Re = 19\,885$) was shown to be approximately twice as high as the equivalent value for the entrance system ($Re = 11\,667$). Furthermore, as the boundary layer thickness reduces, the parallel system approaches a critical displacement thickness Reynolds number about three times larger than the equivalent limit for the entrance system ($Re_{\delta^*} = 1675$; 519 respectively).

19. The non-parallel nature of the pipe entrance flow has an insignificant effect on its stability behaviour. Non-parallel effects, quantified by the parallel parameter κ, are maximum at the inlet plane, where the velocity profiles approach the Blasius limit. Downstream the non-parallelism reduces rapidly, and formally disappears at $x = 0.008\,19$, that axial station beyond which no critical Reynolds numbers exist.

10. An operational numerical approach was developed, allowing the general solution of the equations of fluid mechanics, for both linear and non-linear problems, encompassing both boundary value and eigenvalue systems. The approach of Ortiz [Ortiz & Samara (1981, 1983)] was extended by eliminating the inversion of a badly scaled transformation matrix, inherent to their method. Consequently this modified technique was used to solve high order problems accurately. The commonality of the operational philosophy with both collocation and simple finite-difference methods was demonstrated, as was its equivalence to Orszag's (1971a) Tau method.

11. Numerical models were successfully developed, both for high Reynolds number accelerating pipe entrance flows, and for their linear stability:
(a) In the case of the base flow model, the pressure term was eliminated analytically from the governing equations, and the resulting system was formulated using the operational Tau method radially, and collocation axially. The unusual integral and limit terms arising from the elimination of the pressure were treated uniformly with the other terms by the Tau discretisation. The temporal discretisation was fully implicit for the linear terms, and explicit for the non-linear ones.
(b) The unsteady stability equation was an extension of the Sexl stability relation. The singularity present at the origin was eliminated analytically by transforming the radial ordinate, in order to ensure spectral convergence of the resultant operation Tau system.

12. The velocity profile shape parameter of Moss (1985), in conjunction with the displacement thickness, were both used as scalar parametric representations of the numerical velocity profiles. The *scaled* shape parameter was introduced: in contrast to the velocity profile shape parameter this shows bounded behaviour as the boundary layer thickness approaches zero, allowing the quantification of the velocity profile structure in this limit.

13. It was shown that the velocity field in the dimensionless co-ordinate system is comprehensively described by two simple models: the first being parallel, temporally developing and linear, and the second spatially developing, steady and non-linear. At any chosen time there exists a dimensionless axial position, downstream and upstream of which the former and latter models are valid, respectively. The spatial extent of the interface between the two regions was shown to be small at all times during the flow development. Towards the plane of the pipe inlet, the spatially developing velocity profile approaches the Blasius limit in shape, while the downstream parallel velocity profiles become error function-like in shape for small times. These two asymptotic limits are independent of the acceleration parameter.

4. For each test, there existed an axial position near the inlet at which the flow first destabilised, denoted the minimum critical point. As time progressed, the flow was destabilised both upstream and downstream of this point. The flow breakdown in the region of this point was characterised by the development of laminar 'wiggles' within the boundary layer, while the flow near the centreline remained laminar. Moving downstream, the radial extent of the instability increased, until far downstream, flow breakdown occurred by means of a convected turbulent slug. All the flows measured were prone to eventual instability and finally transition to turbulence.

5. The exponential flow is an ideal system in which to measure experimental inception behaviour, as the flow breakdown data for a *single* test traces out an entire experimental stability curve in the x - Re plane. In contrast a steady pipe flow would have to be started to many different Reynolds numbers to extract the axial variation of the critical Reynolds number.

6. The experimentally observed effect of the exponential acceleration was to stabilise the flow; the minimum critical Reynolds number increased with higher rates of acceleration. This is consistent with the observations of, amongst others, Shen (1961) and da Silva (1990).

7. The behaviour of pipe entrance flow under conditions of arbitrary acceleration is governed by two parameters; the Reynolds number defined by $Re \equiv \frac{RU}{\nu}$, and the acceleration parameter $\Omega \equiv \frac{1}{Re}\frac{dRe}{dt}$. In the context of exponentially accelerating flows, the acceleration parameter remains constant.

8. The development of the generally unsteady pipe boundary layer equations involved no quasi-steady assumptions, and contain the zero-acceleration pipe flow equations as a special case. A single term in the equations governs the effect of acceleration on the pipe flow.

9. The analytic model describes the accelerating pipe entrance flow in a set of dimensionless co-ordinates. The values of the dependent variables remain bounded, despite unbounded changes in their physical counterparts. A Reynolds number-dependent mapping exists between the dimensionless and physical axial positions. In contrast to the unbounded behaviour of the physical system, the numerical model develops toward an invariant state as time increases.

Chapter 20

Conclusions

A comprehensive study of exponentially accelerating pipe flows has been undertaken, embracing analytical, numerical and experimental components. A set of differential equations was developed to describe pipe flows varying generally with time; their numerical solution yielded results in substantial agreement with measurements conducted on a specially developed test facility. The specific conclusions that follow will show that the work has contributed to an enhanced understanding of such systems.

1. An integrated flow control and data acquisition system was successfully developed, for producing and measuring pipe flows undergoing arbitrary accelerations. The apparatus was used to generate a family of impulsively st[illegible]ed, exponentially accelerated pipe flows. The laminar development and subsequent breakdown of twelve different exponentially varying flows was investigated using a laser Doppler velocimeter.

   Velocity profiles were measured at discrete axial positions in the pipe, from which values of displacement thickness and velocity profile shape parameter [Moss (1985)] could be successfully extracted. The shape parameter was subject to a systematic error, due to the unknown position of the pipe wall relative to the LDV measuring volume. For this reason displacement thickness was chosen as the primary means of comparison between the measurements and the analysis. Flow breakdown occurred in a repeatible and coherent fashion. This was determined by monitoring the flow at a number of evenly spaced axial positions, each at a single radial position within the boundary layer.

3. The measured velocity profiles were scaled with respect to the mean cross-sectional velocity obtained from the flowmeter. The resulting normalised profiles showed distinct behaviour: an initial period of boundary layer growth was followed by a region of flow in which the boundary layer thinned with time. Eventually flow breakdown took place within this boundary layer thinning portion of the flow.

low about 1%, the linear theory is applicable for the prediction of the instability. The expected trend in the data is illustrated in figure 19.13 below, where the data of figure 19.12 are hypothetically extrapolated to zero disturbance size.

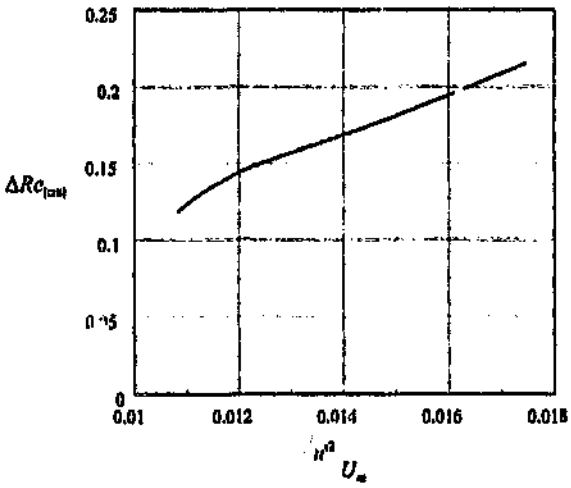

Figure 19.12: The reduction in experimental minimum critical Reynolds number with respect to the linear theory, with disturbance amplitude.

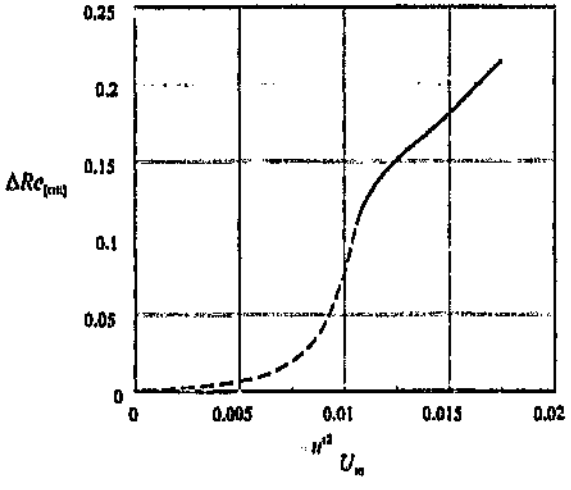

Figure 19.13: The expected reduction in the minimum critical Reynolds number with respect to the linear theory, as the disturbance amplitude approaches zero.

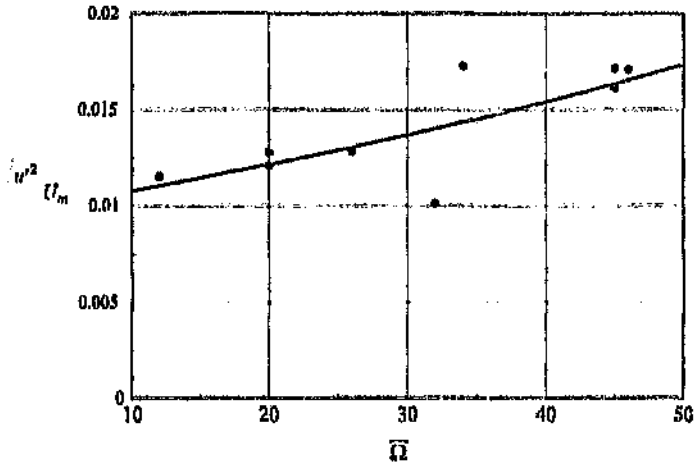

Figure 19.11: The variation of the RMS background disturbance magnitude with acceleration parameter, measured at centreline near the pipe inlet.

Herbert (1988). For this range of amplitudes, non-linear effects are dominant, but the disturbance magnitude is still too small to invoke by-pass mechanisms. This is consistent with the present results: what was seen experimentally was a gradual, flow breakdown within the thin boundary layer present within the pipe entrance, indicating a 'conventional' cascade of instabilities towards turbulence, rather than a sudden by-pass transition. Unfortunately the point measurement nature of the LDV precluded the determination of the global structure of the flow breakdown mechanism, and for this reason it was decided rather to conduct simple inception measurements. A crude yet useful measure of the quantitative effect of the disturbances is the percentage reduction in the minimum critical Reynolds number (relative to the linear theory) with increasing RMS amplitude. The discrepancy between theory and experiment can be defined as

$$\Delta Re_{[\text{crit}]} \equiv \frac{Re_{[\text{crit}]\text{theory}} - Re_{[\text{crit}]\text{expt}}}{Re_{[\text{crit}]\text{theory}}} \tag{19.6}$$

where $Re_{[\text{crit}]\text{theory}}$ represents the theoretical minimum critical Reynolds number, while $Re_{[\text{crit}]\text{expt}}$ is the experimentally obtained value. The variation of $\Delta Re_{[\text{crit}]}$ with RMS disturbance magnitude is given in figure 19.12 and represents a correlation of data from figures 19.7 and 19.11. The increase in $\Delta Re_{[\text{crit}]}$ with increasing disturbance magnitude is almost linear for the range of magnitudes $0.012 \lesssim \overline{(u'^2)}^{\frac{1}{2}}/U_m \lesssim 0.017$, the maximum reduction in the critical Reynolds number being about 22% for the high amplitude perturbations. For values of the RMS amplitude below about 0.012, the curve begins to turn downward, indicating that below this amplitude the effect of the disturbance size becomes increasingly unimportant. This is consistent with other observations [Kachanov (1987), Herbert (1988)] which indicate that for disturbance levels be-

wavenumber of $n = 1$ [Huang & Chen (1974)][5]. The use of the axisymmetric disturbance was used for the sake of simplicity: as the stability of accelerating flows was virtually unknown, the most economical means of investigating them was by using the simplest approximation to their behaviour. A logical extension to the current analysis would be the determination of the non-axisymmetric stability behaviour of exponentially accelerating flows. The stability curve for the non-axisymmetric disturbance in the case of the steady entrance flow has both a slightly lower critical Reynolds number, and a greater axial extent than the axisymmetric one. Use of a non-axisymmetric analysis should thus reduce the current differences between the theoretical and measured results. However it is highly unlikely that incorporation of this effect would contribute significantly towards reducing the discrepancy.

A more likely cause of the major difference between the linear theory and experiment is the presence of finite-amplitude disturbances within the pipe entrance flow. Unfortunately, the theoretical finite-amplitude response of even the steady pipe entrance flow is unknown [see Abbot & Moss (1994)]. In the context of the Blasius boundary layer, finite-amplitude effects are known to reduce substantially the minimum critical Reynolds number [see Herbert (1988) for a relevant overview of finite-amplitude stability], and by inference this is almost certainly true in the present case as well. Determination of the level of finite amplitude disturbances present in the experiment was undertaken in chapter 8, where the RMS disturbance magnitude was established at centreline near the pipe inlet. The magnitude of the disturbance relative to the mean cross-sectional velocity was shown to remain approximately constant within a test. Comparing the different tests, the value of the disturbance magnitude increased with acceleration parameter from just above 1%, to a maximum of 1.7%. The RMS data of figure 8.12 is re-presented below in figure 19.11 with the average value of the measured acceleration parameter for each test being used in place of the acceleration constant k of the previous figure[6].

Evident in this figure is the clear increase in the level of finite amplitude perturbations with acceleration parameter. Such an increase in the background environment would be expected to cause an increasing deviation between the theoretical and experimental minimum critical Reynolds numbers. Exactly this effect was seen in the data of figure 19.7. Thus the discrepancy between the theory and experiment is qualitatively accounted for by the presence of these finite-amplitude disturbances. As mentioned in chapter 8, the perturbation magnitude in the present case is within the region described as *medium amplitude* by

[5]This has been formally demonstrated only for the Hagen-Poiseuille flow. While Huang and Chen showed that the $n = 1$ disturbance is more unstable than the axisymmetric case in the pipe entrance, it is possible that a disturbance possessing an azimuthal wavenumber greater than unity might be the most unstable here.

[6]The acceleration parameter had not yet been defined in chapter 8, and thus the experimental exponential constant k was used to represent the magnitude of the acceleration there. In the present context, the measured acceleration parameter was initially variable, thereafter settling down to a more-or-less constant value. The average value taken for Ω was actually the mean from the latter, constant portion of the flow.

Numerical values of δ^* and u_e were used to transform the experimental data, for the reason that no measured variations of the parameters were obtained at the stations where the inception measurements were conducted[3]. Nevertheless, the comparisons of chapter 18 suggested that experimental and theoretical values of displacement thickness were correlated to within 5% of one another.

Of primary interest in figure 19.10 is the trend for decreasing axial position. Whereas the theoretical curves converge on a single point in the limit as $\tilde{x} \to 0$, the curves obtained from the fitted surface remain approximately parallel. This trend is probably due to the low order of fit, combined with the sparseness of experimental data in the limit of decreasing $\tilde{x}$. Considering all the experimental curves together, their mean trend is in the general direction of the Blasius limit: all the experimental curves are convergent to values of Re_{δ^*} between 400 and 900. The only manner of resolving the question of behaviour in the pipe inlet limit is to conduct more measurements there.

Two distinct sources of discrepancy are evident between the theory and experiment. On the one hand, sparseness of measured points towards the pipe inlet exacerbates uncertainty in the measured value here. On the other hand, if the uncertainty was hypothetically eliminated, a fundamental disagreement would still be expected for the full range of axial positions, due to fundamental differences between the assumptions of the analysis and the conditions present in the physical system. The possible major causes of the latter disagreement are considered in the section that follows.

19.3 Effects of non-axisymmetry and finite-amplitude disturbances

It was argued above that, apart from uncertainties in measurements, there remains a discrepancy between the theory and experiment due to differences between the simple analytical model and the physical system. If non-parallel effects are disregarded *ab initio*[4], there remain two major reasons for the inherent disagreement that appears to exist between theory and experiment: namely *non-axisymmetric effects* and the presence of *finite-amplitude disturbances* within the experimental system.

Considering non-axisymmetric effects, the entire discussion thus far has concerned the comparison of the measured inception data with *axisymmetric* linear stability results, even though in the context of steady pipe entrance flows the most dangerous disturbances are *non*-axisymmetric, with an azimuthal

[3]Measurements of the displacement thickness were required at each station where the inception measurements were conducted. In order to achieve this, it would have been sufficient to measure the centreline velocity at those positions. Unfortunately, this was not done, and thus no experimental variation of displacement thickness was available.

[4]This effect was shown to be important in the context of pipe flows by Abbot & Moss (1994).

curve is the most shallow, and the uncertainty in Reynolds number of $\delta Re = 350$ translates to an uncertainty in position of $\delta\bar{x} \approx 0.002$; while for the steeper curve $\bar{\Omega} = 50$ the axial uncertainty is $\delta\bar{x} \approx 0.001$.

Referring back to figure 19.6, both the theoretical and experimental curves increase in magnitude for reducing axial position. While the theoretical data increase rapidly towards infinity in the limit as $\bar{x} \to 0$, the fitted data show a more gradual increase, especially for the lower acceleration parameter curves. The use of the Reynolds number to study the flow behaviour in this limit is not ideal, due to its unbounded behaviour. However, it was shown in chapter 17 that the displacement thickness Reynolds number approached the value $Re_{\delta^*} = 519.060$ as $\bar{x} \to 0$. To explore this limiting behaviour the stability data of figure 19.6 were transformed into the $\bar{x}$ - Re_{δ^*} framework according to

$$Re_{\delta^*} = Re \frac{\delta^*}{R} \frac{u_e}{U_m}, \tag{19.5}$$

the result of which is shown in figure 19.10.

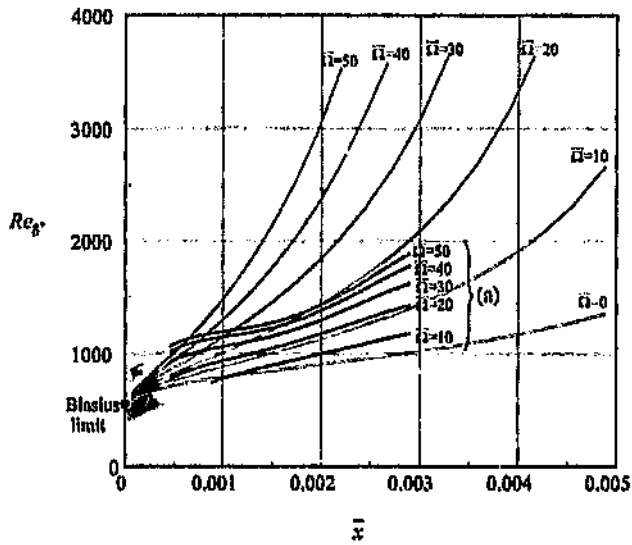

Figure 19.10: The variation of critical displacement thickness Reynolds number with axial position, for various values of the acceleration parameter: (a), curves extracted from the fitted experimental surface; thin lines, theoretical stability curves.

While the experimental curve would not be expected to follow the linear stability variation exactly, the behaviour of each data with $\bar{x}$ might be expected to be qualitatively similar. Thus the stationary behaviour of the experimental curve in figure 19.8 is possibly spurious, and related to inadequacies in the surface fit. Determination of derivative information is prone to a much higher inaccuracy than the extraction of the actual surface values, and the strong variability in the position of the minimum critical value can be inferred by a simple sensitivity analysis. All the experimental curves shown in figure 19.6 have single minimum points, and the uncertainty in the position of this point is directly related to the shallowness of the curve nearby. Figure 19.9 illustrates this principle.

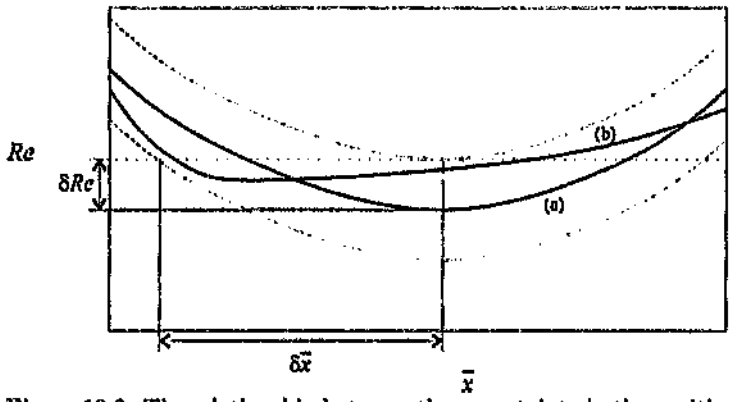

Figure 19.9: The relationship between the uncertainty in the position of a curve, and the uncertainty in the position of its minimum point: (a), fitted curve; (b), possible valid variation of Re.

Here curve (a) represents a section through the surface fit. The dotted lines bracketing curve (a) represent the error bounds of the data, positioned at $Re + \delta Re$ and $Re - \delta Re$ respectively. Any curve remaining within these bounds, for instance curve (b), represents a valid variation of the Reynolds number with axial position, to the level of certainty given by these bounds. As can be seen, while curve (b) remains entirely within the bounding lies, its turning point is far from that of the fitted data (a). This sensitivity can be quantified by a simple consideration of the figure. Any valid curve must have a turning point positioned within the error bounds, under the horizontal dotted line[2]. An uncertainty in Reynold number δRe results in a commensurate uncertainty $\delta\bar{x}$ in the position of the minimum value. The ratio $\delta\bar{x}/\delta Re$ increases in proportion to the shallowness of the curve near the critical point. The axial region of uncertainty can be stated in a compact form as

$$\delta\bar{x} = [\bar{x} \mid Re(\bar{x}) < Re_{\min} + 2\delta Re] \tag{19.4}$$

where $Re_{\min}$ is the minimum critical value. In the current context the $\Omega = 10$

[2]Any curve with a turning point above this line would have to pass outside of the error bounds.

By extrapolating the experimental curve to zero acceleration parameter, the experimental value of minimum critical Reynolds number for steady entrance flow can be estimated, shown as a dotted line in figure 19.7. In the present case this estimation is significantly closer to the theoretical linear stability minimum critical Reynolds number of 11 667 [Abbot & Moss (1994)] than that obtained in any previous study [c.f. Sarpkaya (1975)]. The convergent trend between the two curves is consistent with the results of the finite-amplitude measurements of section 8.4. In that section, a reduction in the level of finite-amplitude disturbance was seen with decreasing acceleration parameter, and thus convergence between the linear theory and experimental inception results would be expected as disturbance intensity reduces. This point is taken further in section 19.3.

The leeward (downstream) side of the experimental data shown in figure 19.6 remains lower in slope than the equivalent portion of the numerical curves, especially for the curves possessing higher values of the acceleration parameter. This is due to the fact that the measured data define the loci of disturbance *inception* in the flow, while the theoretical data represent the *linear stability* response of the flow. The leeward side of the experimental curves define that region destabilised by finite amplitude disturbances convected downstream from near the critical point. This issue was discussed previously in section 9.3.

In the theoretical curves of figure 19.6, the axial position of the minimum critical point migrates rapidly towards the inlet plane with increasing acceleration parameter. In the experimental data, its position remains fairly constant with acceleration. The variation of the minimum critical axial position with acceleration parameter is shown in figure 19.8.

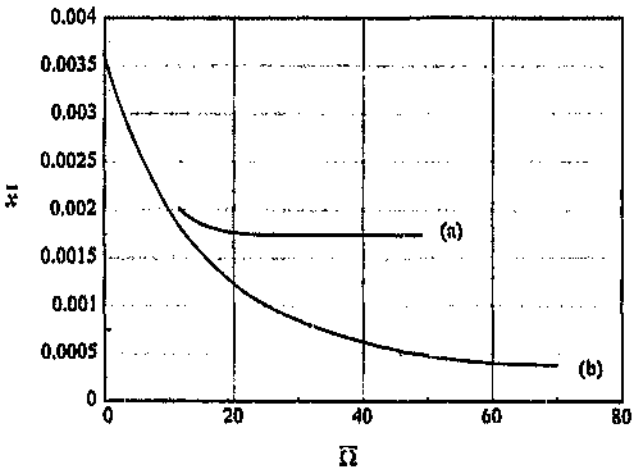

Figure 19.8: The variation of the minimum critical axial position with acceleration parameter: (a), curve extracted from experimental data surface fit; (b), theoretical pipe entrance minimum critical curve.

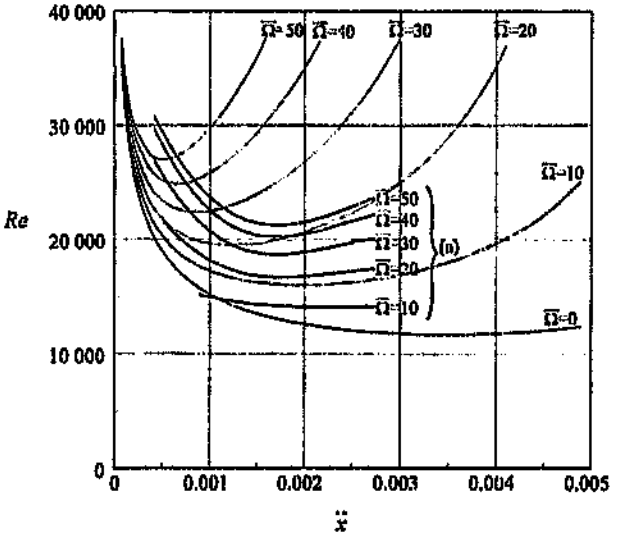

Figure 19.6: The variation of critical Reynolds number with axial position, for various values of the acceleration parameter: (a), curves extracted from the fitted experimental surface; thin lines, the theoretical stability curves.

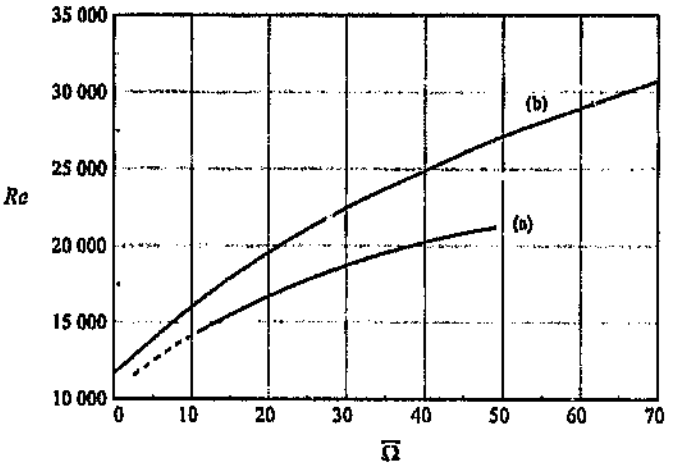

Figure 19.7: The variation of the minimum critical Reynolds number with acceleration parameter: (a), curve extracted from experimental data surface fit; (b), theoretical pipe entrance minimum critical curve; – – –, extrapolation to zero acceleration.

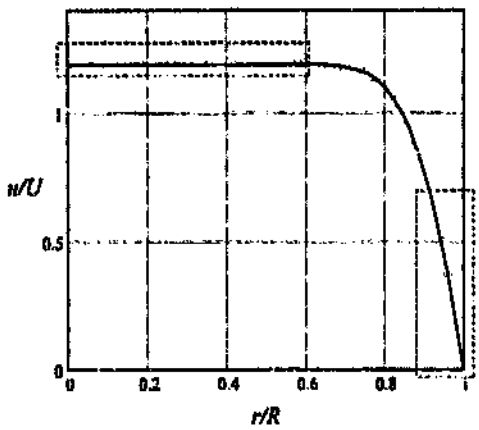

Figure A.5: Numerical velocity profile with noise of magnitude 1% added: o, noisy data; , exact curve.

Integration of the velocity profile yielded an error in the mean flow rate of

$$\epsilon'_U = 2.360 \times 10^{-4}. \tag{A.10}$$

Different points to the previous ones were chosen for the derivative and centreline fit, notably more points were required to achieve an accurate centreline determination, but the number of wall points was identical. The chosen points were again indicated by means of dotted rectangles in figure A.5.

The error in the shape parameter was relatively unaffected by the noise; in fact its value decreased slightly, to

$$\epsilon'_N = 4.64 \times 10^{-3}. \tag{A.11}$$

The centreline determination was markedly affected by the noise, its error increasing drastically to

$$\epsilon'_{u_c} = 5.64 \times 10^{-3}, \tag{A.12}$$

but the previous highly accurate value was due to the almost exact linearity o the data there - the current value was more like the real measurements.

In conclusion, the mean flow determination was least affected by noise, the error being 0.02% for 1% normal noise. Both wall derivative and centreline approximation were equivalently affected, their uncertainty being about 0.5% for the same noise level. In reality, most of the measured profiles were *less* noisy

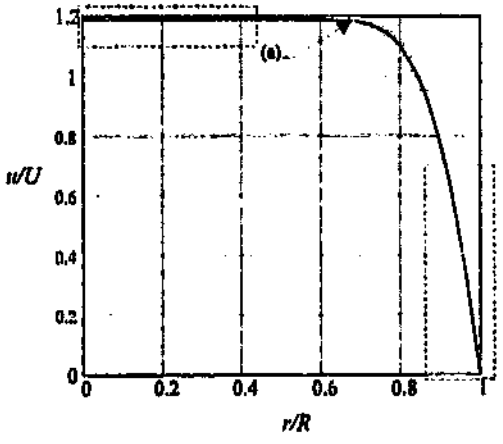

Figure A.4: Numerical velocity profile, showing sampled points to be used for the estimation of the integration error.

Using the same velocity profile as above, the procedure to establish centreline velocity and the velocity derivative at the wall was applied. The dotted rectangles in figure A.4 contain the points used to determine these two parameters.

The actual shape parameter of the velocity profile was $S = 19.990\,118$. Using a second order interpolation to the boundary layer points within the dotted rectangle, the error in the shape parameter was

$$\epsilon_S = 7.786 \times 10^{-3}. \tag{A.8}$$

Due to the flatness of the current profile, the estimation of the centreline velocity (actual value $u_c = 1.189\,843$) was extremely accurate. A linear interpolation resulted in the error being

$$\epsilon_{u_c} = 9.25 \times 10^{-8}. \tag{A.9}$$

A.4.2 Effect of noise

The profile integrated above was not very realistic in that the velocity values at the points were exact. Data from an LDV is subject to some uncertainty, typically it can resolve to about 1% of the flow range. In order to measure the effects of random noise on the velocity profiles, noise with a zero mean and standard deviation of 1% of the mean velocity was added to the profile above. The interpolations above were repeated and values compared. Figure A.5 shows the noisy profile superimposed on the exact curve.

which, with the typical values given earlier was approximately

$$\epsilon_U \approx 6.3 \times 10^{-4}$$

or about 0.06%.

A.4 Errors in experimental velocity profiles

There were two major sources of error associated with the extraction of parameters from experimental velocity profiles: one concerning determination of the mean cross-section velocity (by integration of the velocity profile), and one relating to the extraction of the centreline and wall derivative parameters. The *systematic* error associated with the wall derivative was discussed in section A.3; the current discussion concerns the random error in the extraction of this parameter.

A.4.1 Velocity profile integration error

This error was difficult to estimate, but concerned the mismatch between the fitted curve and the experimental data defining the velocity procedure. This analysis is not concerned with errors introduced by variability of the individual velocity-time traces due to inlet effects.

The best way of determining this error was by estimating the mean cross-sectional velocity of an *numerical* velocity profile: since the actual properties of the numerical profile, were accurately known, such a test would serve to highlight errors introduced by the curve fitting profile. The test profile that was selected was one from the parallel developing flow, with an acceleration parameter $\Omega = 30$ - an intermediate acceleration - and with shape parameter $S \approx 20$. The data was sampled at radial intervals similar to those used in the experimentation. The resultant 'experimental' profile was then integrated using the curve fitting routine described in section 7.6.3. Since the mean cross-sectional flow rate of the numerical profile was unity, the measured mean velocity would serve directly as the error estimate. Figure A.4 shows the selected profile, plus the discrete selected points.

The boundary layer fit shown was of fourth order, while the centreline fit was third order. The mean flow rate estimated by the boundary layer fit was $U_{fit} = 0.999\,980$, the interpolation procedure thus produced an error of only

$$\epsilon_U = 1.990 \times 10^{-5}. \tag{A.7}$$

Thus for small errors in positioning of the wall, the error in the derivative at the wall was simply the quantity $u_r \frac{\delta r}{r'}$. The radial quantity r' was hard to estimate; to simplify matters equation (A.4) could be rearranged as follows:

$$\hat{u}_r = u_r - (u_r)^2 \left(\frac{\delta r}{u'}\right). \tag{A.5}$$

Equation (A.5) was in terms of the actual slope and the quantities u' and δr. The error in the estimation of the slope was thus

$$\epsilon_{u_r} = (u_r)^2 \left(\frac{\delta r}{u'}\right) \tag{A.6}$$

Typical uncertainties in the wall position were around $\delta r = 0.002$; on average the velocity value u' was approximately 0.1. With the wall gradient being of the order 10, the systematic uncertainty in velocity derivative at the wall was approximately

$$\epsilon_{u_r} \approx 2.$$

The velocity shape parameter was defined as -2 times the dimensionless velocity profile derivative at the wall. Thus the variability in the shape parameter was about

$$\epsilon_S \approx 4.$$

As mentioned, this error was systematic: all the gradients measured from a set of profiles from a particular station would show the same discrepancy. This effect was in addition to normal errors associated with the velocity profiles, which are discussed in the following section.

A.3.1 Error in the mass flow rate due to wall error

The estimation of the area under the velocity profile was also subject to uncertainty in the wall position; however the discrepancy in this case was minute. The 'extra' flow entailed by the wall moving a distance δr outward was approximately

$$\epsilon_U \approx 2\pi\left(\frac{1}{2}u'\delta r\right)$$

A.3 Systematic error in the profile wall slope due to uncertainty in the wall position

Assume a group of three velocity points from the inner boundary layer of a velocity profile, plus a wall position that is subject to some uncertainty. A quadratic least-squares fit is made through all four data and from the slope of this curve at the intersection with the radial axis the velocity derivative at the pipe wall is inferred. Figure A.3 illustrates this process.

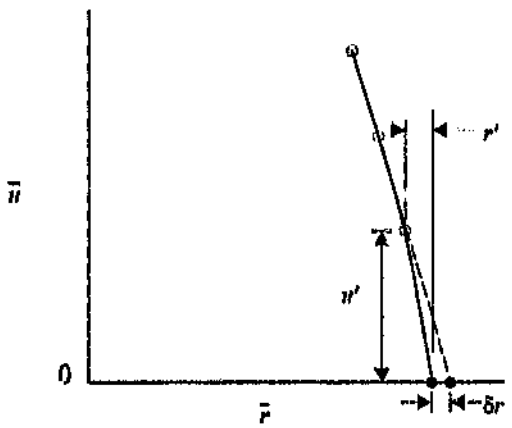

Figure A.3: The effect of wall variability on the estimation of the velocity derivative at the pipe wall.

Here u' is the velocity value of the point closest to the wall. It is assumed that the profile is normalised in radius and velocity; thus the mean cross-sectional velocity of the profile is unity. The quantity r' represents the distance of the innermost measuring station from the wall. The small term δr is an uncertainty in the wall position.

Let the slope of the solid line at the wall be $u_r = \left.\frac{\partial u}{\partial r}\right|_{u=0}$. This slope can be approximated by the ratio $u_r \approx \frac{u'}{r'}$. If the wall co-ordinate shifts by the amount δr, then the slope at the wall can be approximated as

$$\hat{u}_r = \frac{u'}{r' + \delta r}$$

which by a binomial expansion for δr small becomes

$$\hat{u}_r = u_r \left(1 - \frac{\delta r}{r'} + \cdots\right). \tag{A.4}$$

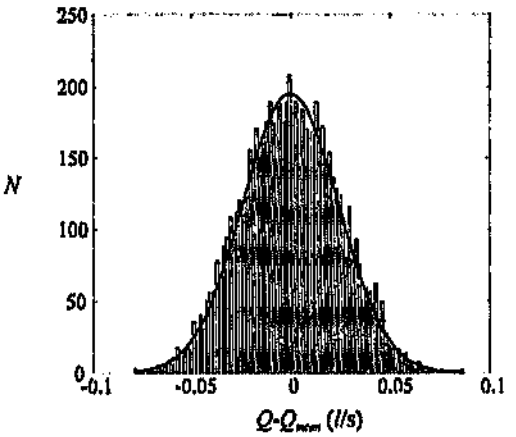

Figure A.2: The distribution of the flowmeter data about the mean. The horizontal scale is normalised with respect to the full range (in this case 4 l/s). A model Gaussian distribution is shown superimposed.

$$\begin{aligned} \sigma_{l/s} &= 0.024\,02\ l/s; \\ \sigma_{Re} &= 355.4\ . \end{aligned} \tag{A.2}$$

Thus at a Reynolds number of 20 000, the percentage variation was 1.8%, while at the maximum range of 60 000, this related to a variation of 0.6%.

The flowmeter was measuring a smooth variation on the flowrate, thus the uncertainty to which the flowrate was ascertained from the noisy data above was given by the standard error of the mean [Brinkworth (1973)], given by

$$\epsilon_{Re} = \frac{\sigma_{Re}}{\sqrt{N}}$$

where N is the number of data realisations. The average number of points for a single flowmeter trace - such as that in figure A.1 - was ≈ 4000; thus the error to which the flow variation was obtained on average, was about

$$\epsilon_{Re} = 5.6\ . \tag{A.3}$$

This error analysis concerned only the scatter of the flowmeter data, not its linearity. The calibration of the flowmeter was discussed in detail in section 7.5.3 on page 124.

A.2 Scatter in the flowmeter data

Data was acquired from the flowmeter at a rate of 100 Hz, in the form of an analogue signal. This signal was sampled using 12 bit precision at effectively 10 bit resolution - see section A.1 above. However, the analogue signal was actually derived from a digital signal - the serial communication link between the flowmeter proper and the control head. While this analogue signal was steady to within the 10 bits being measured, the digital signal it encoded - as a stepped-wave sample-and-hold type signal - was *far* more noisy than this. The analogue noise could thus be neglected in comparison to the innate noise in the signal from the proprietary flowmeter unit.

The scatter inherent in the signal was as a ratio of the full-scale range of the unit: it thus became relatively worse at the lower flowrates. Data for the test EXPE is shown in figure A.1.

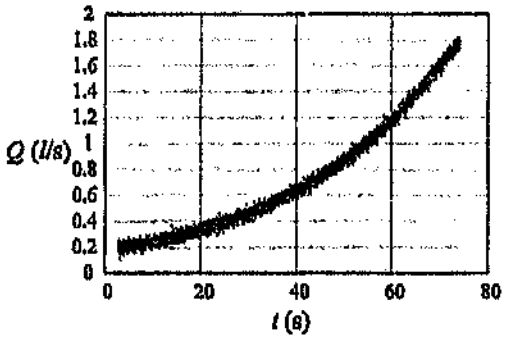

Figure A.1: Unsmoothed flowmeter data from the test EXPE, showing the innate broadening in the data. The full range is 4 *l/s*.

In order to ascertain the scatter, a polynomial was fitted to the data, and this mean value was subtracted from the raw data. The resultant data was centred around zero, and showed no increase in broadening with range - the scatter was constant for the entire data. The distribution of the resultant data about the mean could thus be ascertained. This distribution is given in figure A.2.

The normal distribution calculated using the mean and standard deviation of the data is shown superimposed as a solid curve. It is immediately evident that the distribution is Gaussian; thus the simple mean calculation can be used, and the standard deviation will give an indication of the variability. The ordinate is presented in *l/s*; the error is given as a ratio of the maximum flowrate and therefore has units.

The maximum flowrate through the flowmeter related to a Reynolds number. The equivalent standard deviation could thus also be given in terms of Reynolds number. The standard deviations are as follows.

Appendix A

Error and sensitivity analysis

A.1 Analogue acquisition

Many data such as the flowmeter and tank pressure were measured using an analogue-to-digital converter card mounted in the PC. Furthermore the electromagnetic valves were controlled by analogue output lines from the same card.

The card used was a PC30B analogue/digital card, made by Eagle Electronics, Cape Town. The input and output was to 12 bits precision on some lines, and 8 bits on others. A properly shielded junction box and coaxial cables were used to connect the card to the controlled and measured items.

Measurements at the ends of the shielded cables showed that the 12 bit channels gave repeatable results to 10 bits precision, the last bit being noise. This was true of both input and output channels. The 8 bit channels were repeatable to the full 8 bits.

Thus for the 12 bit channels, the innate error was

$$\begin{aligned} \epsilon &= \frac{4}{4096} \\ &= 0.098\%. \end{aligned} \tag{A.1}$$

The accuracy in the 8 bit channels was assumed to be the resolution of those channels, namely 0.39%.

Part V

APPENDICES

of wall shear stress probes mounted throughout the length of the pipe; alternatively a movable probe might be employed to reduce expense.

4. A higher data density of stability measurements in the $\tilde{\Omega} - \tilde{x}$ plane would have allowed a more detailed and accurate surface fit to the experimental inception data. Detailed measurements closer to the inlet plane, impossible in the current rig due to restricted optical access, would have further clarified the experimental stability behaviour of the flow in this limit.

5. A small oversight of important consequence was neglecting to obtain the centreline velocity at the axial stations where inception data was measured. It was shown in section 8.4 that knowledge of the dimensionless centreline velocity is sufficient to determine the displacement thickness. This omission resulted in the displacement thickness being unknown for the inception measurements. Leading from the above, an economical method of obtaining both the velocity profile shape parameter and the displacement thickness in a pipe flow would be to measure the centreline velocity with an LDV while simultaneously capturing the wall shear stress directly with a wall-mounted probe.

6. The observed boundary layer flow breakdown, although statistically coherent in broad structure, was random in detail. This, in combination with the point measurement nature of the LDV did not allow the instantaneous behaviour of this phenomenon to be captured throughout the pipe. A more suitable method of capturing such information would be via global velocimetry approaches such as light-sheet tomography, or general flow visualisation techniques.

7. The stability behaviour of the flow was investigated numerically using a simple linear stability analysis, whereas in reality the mechanism of flow breakdown in the measured system involved finite-amplitude effects. A means of obtaining better correlation between theory and the current experimentation would be to conduct a finite amplitude analysis of the accelerating pipe entrance flow. No detailed finite-amplitude stability analysis exists, even for steady pipe entrance flows. Possible methods to be employed in such an investigation would be either a weakly non-linear theory [see Herbert (1988)] or a full numerical simulation. Although the latter approach is computationally intensive, the advent of fast modern machines and economical new numerical techniques would make such a goal attainable.

8. Before attempting a complicated finite-amplitude analysis of the pipe flow, it would first be worthwhile to conduct a simple non-axisymmetric linear stability investigation. It is well known [see Huang & Chen (1974)] that the non-axisymmetric stability curve (with an azimuthal wavenumber of one) is slightly lower than its symmetrical counterpart, and more importantly has a greater *axial* extent. By inference the same trends would apply to the present stability data, which might account for at least some of the observed discrepancies.

Chapter 21

Recommendations

The investigation into the stability and other behaviour of exponentially accelerating pipe entrance flows was successful in achieving most of its set objectives. The current study did, however, show some deficiencies and these are described below, together with possible future extensions.

1. There is a fundamental lack of understanding concerning the behaviour of pipe inlet contractions in general, with most designs utilising simple rules-of-thumb combined with potential flow theory. Further, no literature exists for the design of contractions in the context of unsteady flows. While the present pipe inlet contraction has been used successfully in other applications, it led to a number of undesirable effects; (a) the observed inlet 'bump' at the interface between the parallel and entrance flow regions; (b) the slight variability of the entrance flow region; and (c) the level of finite-amplitude disturbances in the flow field. A more controlled experimental investigation into unsteady pipe flows would thus first require the detailed investigation (possibly a combination of numerical and experimental) of inlet contractions under unsteady conditions.

2. In the current system, the dynamic control of the flow was optimal only for the higher range of Reynolds numbers. Deficiencies in the control system at low Reynolds numbers aggravated the inlet effects described in point 1, and caused the measured flow rate to deviate noticeably from the expected variation. The use of adaptive control algorithms, combined with a more accurate flowmeter, would alleviate this problem. A more complete solution would however also require the replacement of the existing electro-pneumatic valve with a more sensitive and responsive device, possibly a tailored ball valve driven by a stepper or DC motor.

3. While the LDV proved itself in most areas to be an optimum measurement tool, it had deficiencies. In particular it was only able to achieve a relatively poor estimation of the wall shear stress. To overcome this, it is recommended that this parameter be measured directly, using a battery

20. The predicted minimum critical Reynolds number increases with acceleration parameter, both for the parallel downstream profiles, and for the entrance flow. In the case of the entrance flow, the linear stability curves for increasing acceleration are successively contained within their lower acceleration counterparts, and all curves approach each other with reducing boundary layer thickness. Further, the value of the critical displacement thickness Reynolds number for each curve approaches the Blasuis stability limit as the boundary layer thickness approaches zero. The axial extent of the unstable region reduces with increasing acceleration parameter. The parallel downstream flow shows analogous behaviour to the entrance system, except that the critical displacement thickness Reynolds number approaches the error-function stability limit as the boundary layer reduces in thickness. The stability curves for the parallel downstream flows are generally much higher than for the entrance flows possessing the same acceleration parameter.

21. All the experimentally observed instability occurred in the entrance region of the pipe, corresponding to the steady numerical entrance model in the dimensionless co-ordinate system. This allowed the measured inception data to be compared directly to the steady entrance stability analysis.

22. A least-squares surface was fitted through all the measured inception data in the $\bar{x} - \bar{\Omega} - Re$ space. The fitting procedure yielded good results for the experimental minimum critical Reynolds number, and gave an indication of the experimental pipe entrance stability behaviour. However, the low order of fit, combined with the relatively few experimental inception points for the smaller axial positions, gave a less accurate fit toward the inlet. This resulted in both the position of the minimum critical point, and the asymptotic behaviour of the surface as $\bar{x} \to 0$, being inaccurately represented.

23. The magnitude of the dimensionless free stream disturbance $[\sqrt{(\overline{u'^2})}/U]$ measured at centre-line near the pipe inlet plane was constant for the duration of a test, while its value increased linearly with acceleration parameter, from a value of about 1.1% at the lowest acceleration, to about 1.7% for the highest. Discrepancies between the measured minimum critical Reynolds numbers and the linear theory increased with acceleration parameter. The experimental minimum critical Reynolds number was about 22% lower than the theory for the high disturbance tests, reducing to a discrepancy of 12% for the lowest disturbance magnitude. The differences between theory and experiment are consistent with the presence of small finite-amplitude disturbances, of insufficient magnitude to cause by-pass transition. Nevertheless, on the basis of minimum critical Reynolds number the current work shows a substantially closer correlation than previous studies between linear stability predictions and measured deviations from laminar flow.

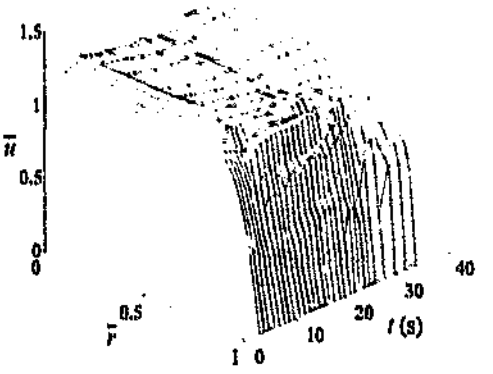

Figure B.29: Velocity profiles for the test GCG ($x/R = 41.29$), represented as a surface.

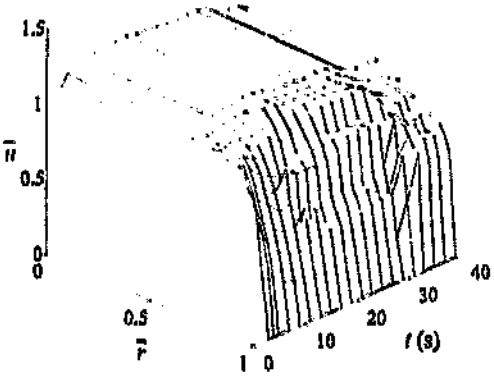

Figure B.30: Velocity profiles for the test GDF ($x/R = 67.01$), represented as a surface.

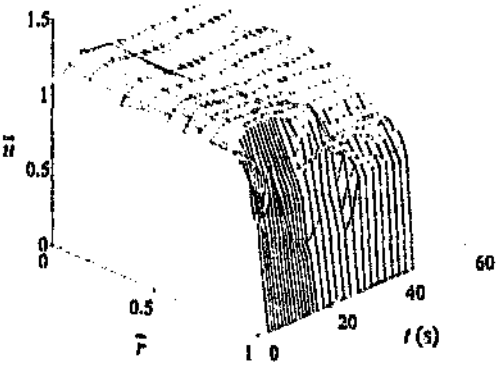

Figure B.31: Velocity profiles for the test GDG ($x/R = 30.91$), represented as a surface.

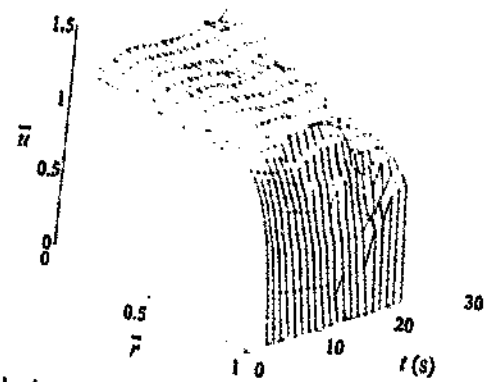

Figure B.26: Velocity profiles for the test GBJ ($x/R = 99.35$), represented as a surface.

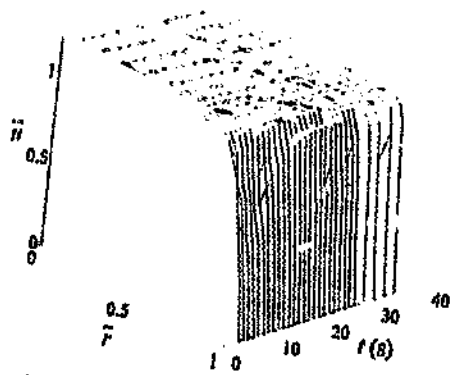

Figure B.27: Velocity profiles for the test GCE ($x/R = 11.49$), represented as a surface.

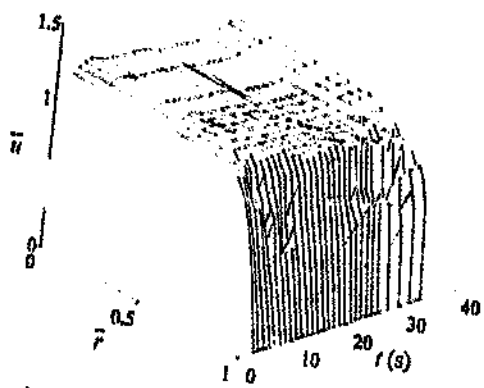

Figure B.28: Velocity profiles for the test GCF ($x/R = 24.69$), represented as a surface.

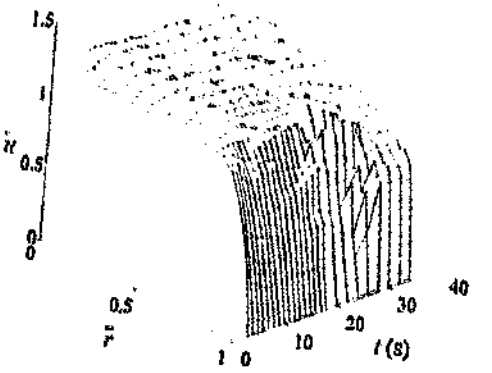

Figure B.23: Velocity profiles for the test GAA ($x/R = 44.40$), represented as a surface.

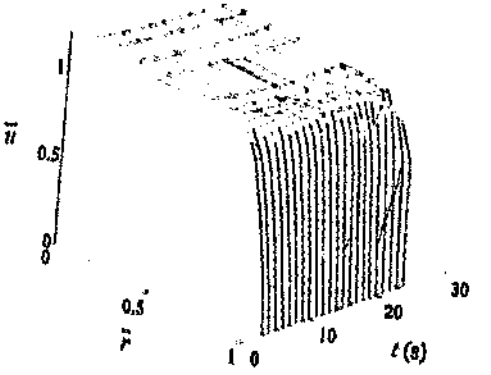

Figure B.24: Velocity profiles for the test GBH ($x/R = 11.74$), represented as a surface.

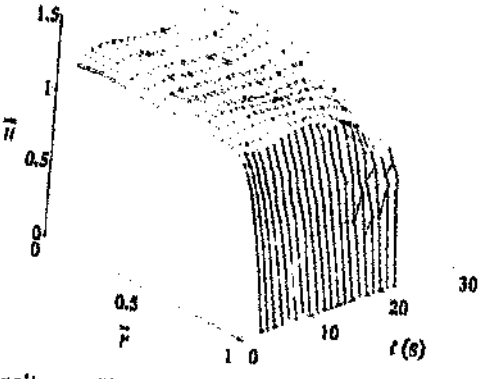

Figure B.25: Velocity profiles for the test GBI ($x/R = 41.01$), represented as a surface.

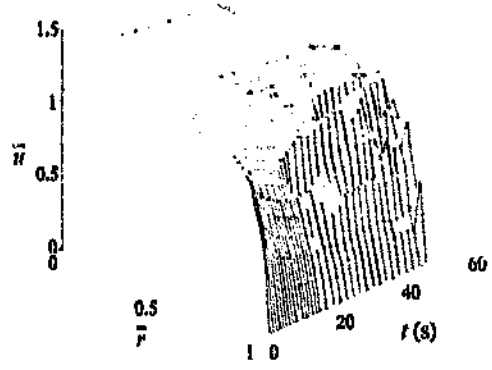

Figure B.20: Velocity profiles for the test FD2 ($x/R = 79.54$), represented as a surface.

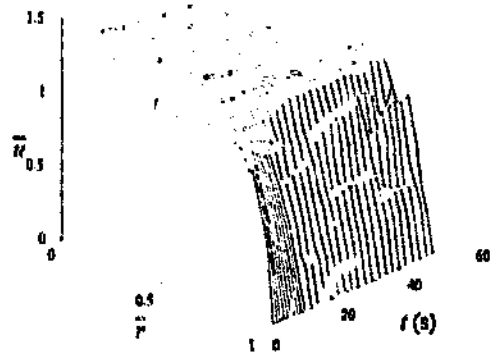

Figure B.21: Velocity profiles for the test FD3 ($x/R = 36.31$), represented as a surface.

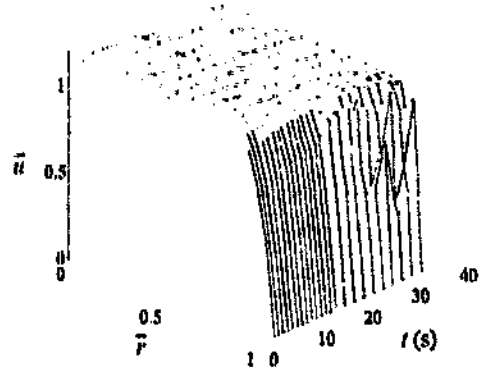

Figure B.22: Velocity profiles for the test GA6 ($x/R = 11.51$), represented as a surface.

Figure B.17: Velocity profiles for the test FB5 ($x/R = 90.54$), represented as a surface.

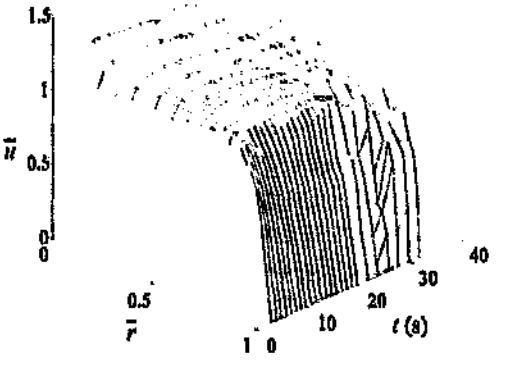

Figure B.18: Velocity profiles for the test FC3 ($x/R = 38.38$), represented as a surface.

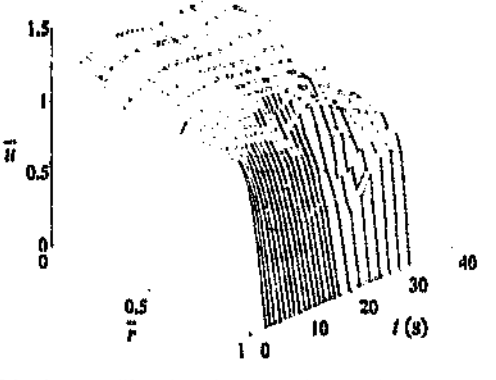

Figure B.19: Velocity profiles for the test FC4 ($x/R = 79.96$), represented as a surface.

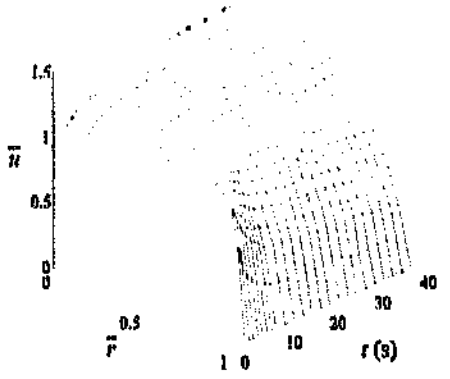

Figure B.14: Velocity profiles for the test FA3 ($x/R = 67.84$), represented as a surface.

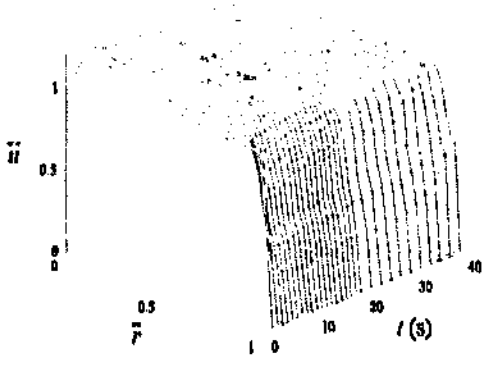

Figure B.15: Velocity profiles for the test FB3 ($x/R = 13.69$), represented as a surface.

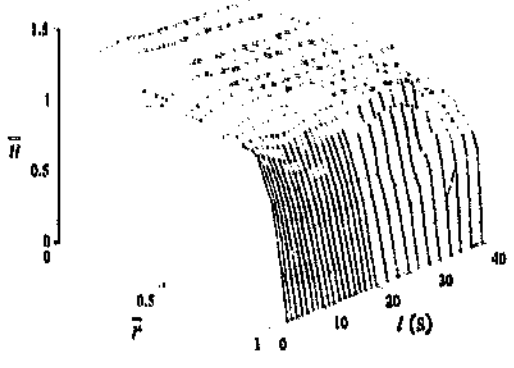

Figure B.16: Velocity profiles for the test FB4 ($x/R = 44.61$), represented as a surface.

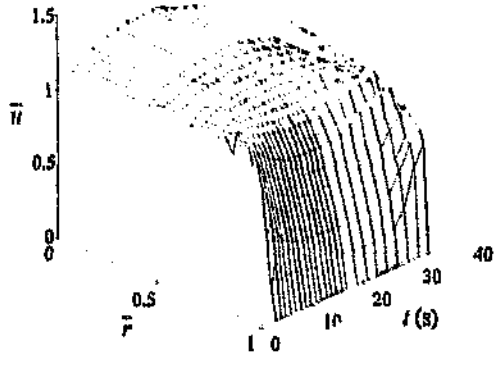

Figure B.11: Velocity profiles for the test EG3 ($x/R = 169.63$), represented as a surface.

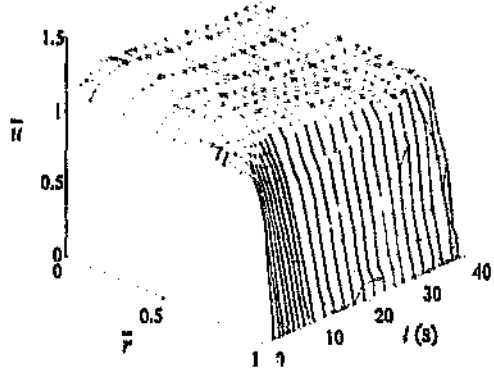

Figure B.12: Velocity profiles for the test FA0 ($x/R = 25.52$), represented as a surface.

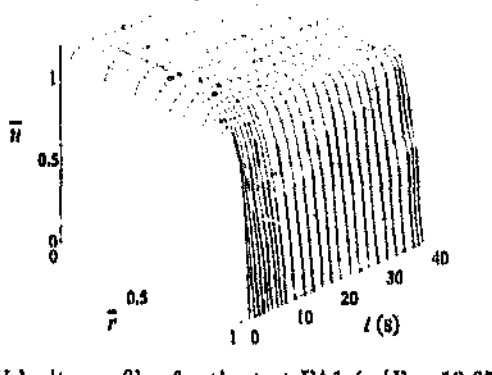

Figure B.13: Velocity profiles for the test FA1 ($x/R = 13.07$), represented as a surface.

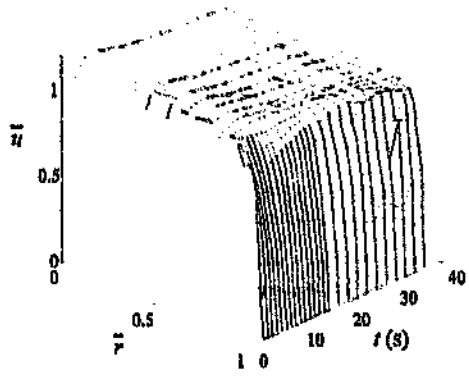

Figure B.8: Velocity profiles for the test EG0 ($x/R = 13.49$), represented as a surface.

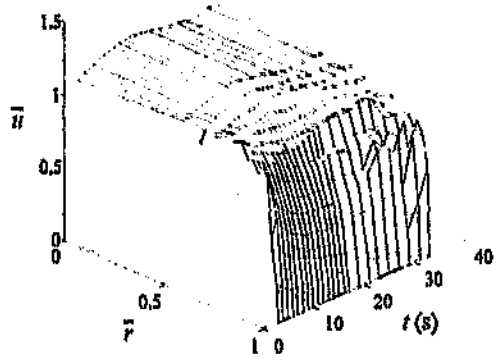

Figure B.9: Velocity profiles for the test EG1 ($x/R = 64.52$), represented as a surface.

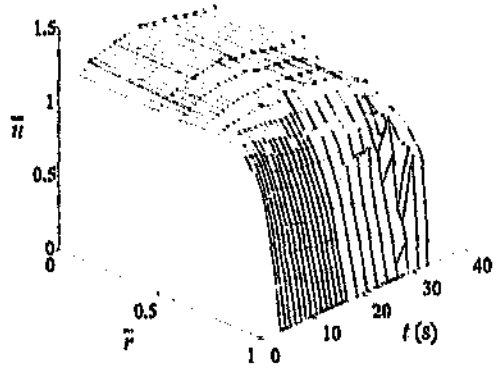

Figure B.10: Velocity profiles for the test EG2 ($x/R = 105.06$), represented as a surface.

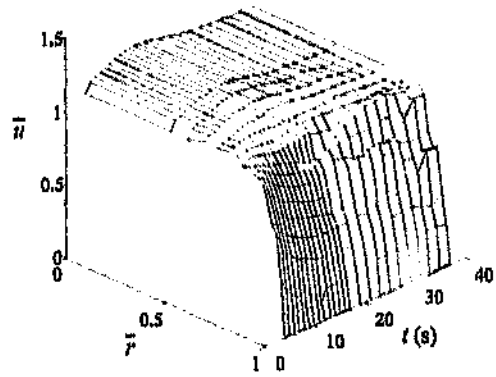

Figure B.5: Velocity profiles for the test EF1 ($x/R = 03.09$), represented as a surface.

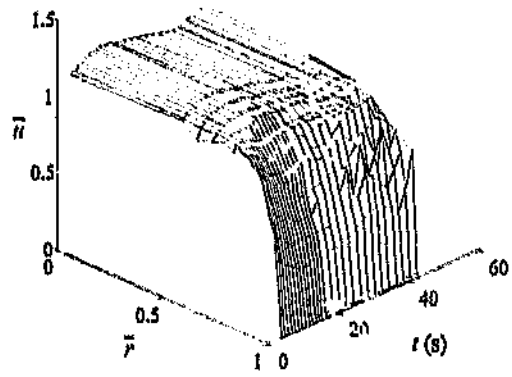

Figure B.6: Velocity profiles for the test EF2 ($x/R = 40.01$), represented as a surface.

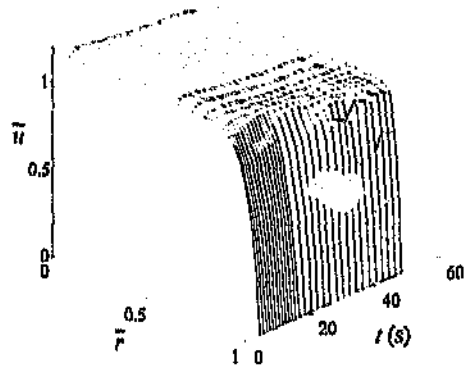

Figure B.7: Velocity profiles for the test EF3 ($x/R = 13.49$), represented as a surface.

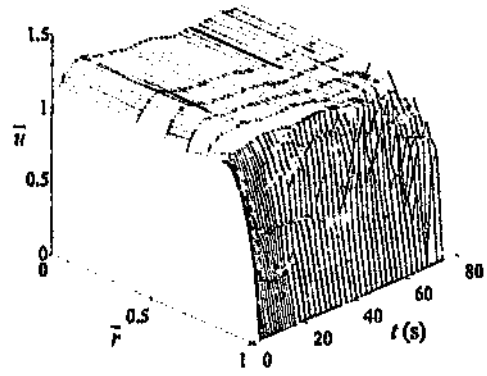

Figure B.2: Velocity profiles for the test EE2 ($x/R = 20.25$), represented as a surface.

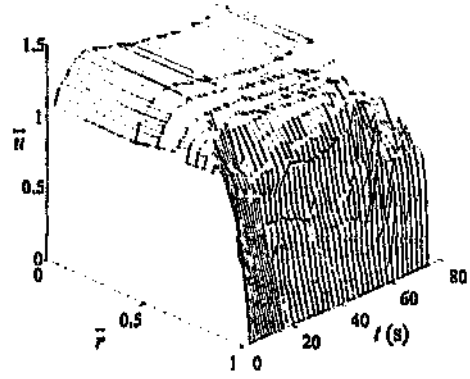

Figure B.3: Velocity profiles for the test EE3 ($x/R = 64.52$), represented as a surface.

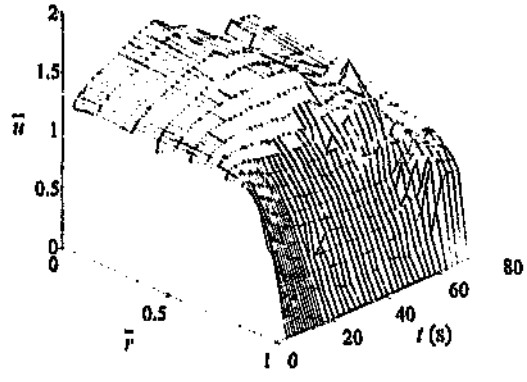

Figure B.4: Velocity profiles for the test EE5 ($x/R = 320.50$), represented as a surface.

Appendix B

Base flow data

This appendix contains all the experimental velocity profile data, given as a three dimensional surface plots. The data is non-dimensionalised with respect to radius, and normalised by its mean velocity. It is ordered sequentially. This profile data represents a coarse sampling of the raw traces, points being taken every one or two seconds.

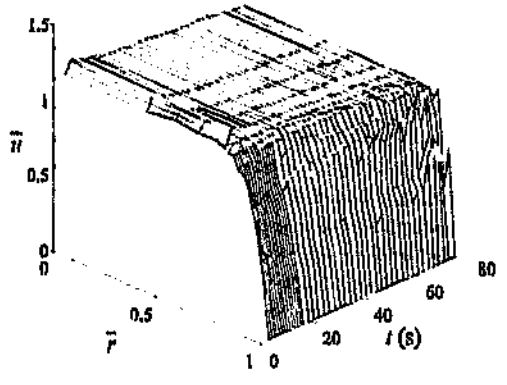

Figure B.1: Velocity profiles for the test EE1 ($x/R = 12.24$), represented as a surface.

than the artificially generated one here; thus the present error estimate is a conservative one. However the variability due to inlet effects at times produced much larger variability in the boundary layer than shown here. Errors due to these effects were extremely difficult to quantify: the distribution of these events was not normal (in most traces they were absent, only appearing at some stations).

The above analysis assumed no bias in the velocity data. Bias would obviously affect the mean velocity profoundly:- if all the traces were to show a systematic 1% error in velocity, the mean velocity would also show the same error. Optimal placing of the sampled points also maintained the level of accuracy. In some profiles, traces were missing or badly displaced, and this would have severe consequences on the error estimate.

A.4.3 Verification of the mean flow accuracy

The only means of verifying the accuracy of the profile integration was using the flowmeter calibration, conducted in section 7.5.3 on page 124. Here mean flow data obtained from integration of all the velocity profiles w. compared to measured flowmeter d' 'a; figure 7.15 gave this calibration data graphically.

Referring to the figure 7.15 on page 125, the lower part of the curve was obtained from integration of velocity profiles from the parallel part of the flow, whereas the upper portion was derived from the entrance part of the flow - the flow subject to the large variability. Consideration of the variability of the more accurate parallel region was undertaken to test the correctness of the error estimates contained above.

The variability of the 'parallel' data was 1.0%. However these data also depended on the accuracy of the flowmeter, whose variability was of the order of one percent. Thus the only conclusion drawn from this comparison was that the variability introduced by the integration was better than one percent.

Table C.9: Critical parameters at discrete times in the far-downstream impulsively started pipe flow, for the case $\bar{\Omega} = 40$. The underlined data are the values of the parameters at the minimum critical Reynolds number.

t ($\times 10^5$)	α[crit]	α_{δ^*}[crit] ($\times 10^3$)	Re_{R}[crit] ($\times 10^{-3}$)	Re_{δ^*}[crit]	c[crit]	$\tilde{c}$[crit]
15	17.560	231.45	124.05	1679.3	0.32530	0.31673
20	14.825	227.07	108.31	1711.4	0.32601	0.31603
25	13.177	226.33	96.295	1712.8	0.32789	0.31663
30	11.910	224.41	88.359	1730.1	0.32887	0.31648
40	10.158	221.11	77.237	1757.8	0.33081	0.31641
50	8.9686	218.07	69.992	1788.8	0.33231	0.31615
60	8.0923	215.21	64.823	1820.8	0.33358	0.31584
70	7.4110	212.48	60.961	1854.2	0.33464	0.31545
80	6.8601	209.84	57.975	1888.9	0.33553	0.31501
90	6.4028	207.29	55.608	1924.9	0.33630	0.31453
100	6.0145	204.80	53.700	1962.2	0.33696	0.31402
125	5.2518	198.82	50.370	2053.1	0.33815	0.31255
150	4.6804	193.05	48.245	2148.9	0.33905	0.31108
<u>200</u>	<u>3.8619</u>	<u>181.97</u>	<u>46.399</u>	<u>2413.9</u>	<u>0.33978</u>	<u>0.30770</u>
250	3.2826	171.17	46.492	2706.6	0.33960	0.30418
300	2.8361	160.41	47.989	3060.6	0.33875	0.30043
350	2.4709	149.53	50.772	3495.5	0.33734	0.29651
400	2.1594	138.42	54.960	4041.0	0.33543	0.29243
450	1.8834	126.91	60.012	4743.8	0.33303	0.28815
500	1.6313	114.86	69.345	5683.3	0.33006	0.28358
550	1.3927	101.98	81.080	7007.5	0.32641	0.27861
600	1.1571	87.768	101.02	9033.0	0.32185	0.27302

Table C.8: The correspondence between t and the other velocity profile parameters at discrete times in the pipe entrance, for the case ($\Omega = 30$).

t ($\times 10^5$)	S	δ^*/R ($\times 10^3$)	U_c/U
15	98.842	13.186	1.0271
20	85.402	15.326	1.0316
25	76.438	17.190	1.0356
30	69.918	18.860	1.0392
40	60.895	21.796	1.0456
50	54.821	24.353	1.0512
60	50.382	26.645	1.0563
70	46.958	28.734	1.0610
80	44.216	30.665	1.0653
90	41.959	32.466	1.0694
100	40.059	34.157	1.0733
125	36.390	38.004	1.0823
150	33.696	41.438	1.0904
200	29.983	47.408	1.1047
250	27.497	52.538	1.1174
300	25.695	57.068	1.1288
350	24.320	61.141	1.1393
400	23.232	64.852	1.1490
450	22.346	68.264	1.1581
500	21.610	71.427	1.1667
550	20.987	74.376	1.1747
600	20.455	77.139	1.1824
650	19.992	79.739	1.1897

Table C.7: Critical parameters at discrete times in the far-downstream impulsively started pipe flow, for the case $\bar{\Omega} = 30$. The underlined data are the values of the parameters at the minimum critical Reynolds number.

$\bar{t}$ ($\times 10^5$)	$\alpha_{[\mathrm{crit}]}$	$\alpha_{\delta^*[\mathrm{crit}]}$ ($\times 10^3$)	$Re'_{R[\mathrm{crit}]}$ ($\times 10^{-3}$)	$Re_{\delta^*[\mathrm{crit}]}$	$c_{[\mathrm{crit}]}$	$\bar{c}_{[\mathrm{crit}]}$
15	17.583	231.85	123.17	1668.1	0.3257	0.31712
20	14.854	227.06	107.19	1694.7	0.32661	0.31661
25	13.209	227.07	95.066	1692.3	0.32863	0.31734
30	11.944	225.26	87.002	1705.2	0.32977	0.31733
40	10 198	222.27	75.637	1723.7	0.33204	0.31757
50	9.0132	219.50	68.175	1745.3	0.33387	0.31761
60	8.1413	216.92	62.799	1767.4	0.33547	0.31759
70	7.4636	214.46	58.740	1790.8	0.33686	0.31750
80	6.9164	212.09	55.560	1815.0	0.33810	0.31736
90	6.4622	209.80	53.002	1840.2	0.33921	0.31718
100	6.0769	207.57	50.905	1866.3	0.34021	0.31697
125	5.3211	202.22	47.100	1937.2	0.34226	0.31624
150	4.7559	107.07	44.488	2010.1	0.34404	0.31553
200	3.9482	187.18	41.595	2178.5	0.34655	0.31360
250	3.3787	177.51	40.484	2376.7	0.34817	0.31158
300	2.9412	167.85	40.549	2612.2	0.34912	0.30927
350	2.5850	158.05	41.569	2895.7	0.34952	0.30678
400	2.2820	147.99	43.515	3242.6	0.34941	0.30409
450	2.0153	137.57	46.502	3676.3	0.34882	0.30119
500	1.7729	126.64	50.811	4234.1	0.34769	0.29803
550	1.5466	115.03	56.903	4979.6	0.34597	0.29450
600	1.3277	102.42	66.141	6032.7	0.34348	0.29049
650	1.1062	88.205	80.708	7656.7	0.34002	0.28579

Table C.6: The correspondence between $\bar{t}$ and the other velocity profile parameters at discrete times in the pipe entrance, for the case $\Omega = 20$.

$\bar{t}$ ($\times 10^5$)	S	δ^*/L ($\times 10^3$)	U_c/U
15	98.708	13.192	1.0271
20	85.247	15.336	1.0316
25	76.264	17.203	1.0356
30	69.726	18.878	1.0392
40	60.673	21.823	1.0456
50	54.573	24.392	1.0513
60	50.109	26.695	1.0564
70	46.664	28.798	1.0611
80	43.902	30.742	1.0655
90	41.625	32.557	1.0696
100	39.707	34.264	1.0736
150	33.267	41.630	1.0908
200	29.489	47.698	1.1055
250	26.947	52.936	1.1184
300	25.096	57.582	1.1301
350	23.676	61.778	1.1410
400	22.546	65.618	1.1511
450	21.622	69.165	1.1605
500	20.850	72.466	1.1695
525	20.509	74.036	1.1738
550	20.194	75.558	1.1780
560	20.074	76.153	1.1797
600	19.630	78.466	1.1861
650	19.137	81.215	1.1939
700	18.704	83.823	1.2014
750	18.320	86.304	1.2086

Table C.5: Critical parameters at discrete times in the far-downstream impulsively started pipe flow, for the case $\Omega = 20$. The underlined data are the values of the parameters at the minimum critical Reynolds number.

t ($\times 10^5$)	$\alpha_{[\mathrm{crit}]}$	$\alpha_{\delta^*[\mathrm{crit}]}$ ($\times 10^3$)	$Re_{R[\mathrm{crit}]}$ ($\times 10^{-3}$)	$Re_{\delta^*[\mathrm{crit}]}$	$c_{[\mathrm{crit}]}$	$\tilde{c}_{[\mathrm{crit}]}$
15	17.606	232.26	122.30	1657.1	0.32611	0.31751
20	14.883	228.25	106.07	1678.2	0.32722	0.31719
25	13.242	227.81	93.856	1672.1	0.32938	0.31805
30	11.977	226.10	85.667	1680.6	0.33067	0.31819
40	10.239	223.44	74.073	1690.2	0.33327	0.31873
50	9.0580	220.94	66.409	1702.9	0.33542	0.31906
60	8.1906	218.65	60.844	1715.8	0.33735	0.31934
70	7.5167	216.46	56.607	1729.8	0.33908	0.31955
80	6.9731	214.37	53.254	1744.4	0.34065	0.31971
90	6.5224	212.35	50.528	1759.6	0.34210	0.31983
100	6.1402	210.39	48.267	1775.5	0.34345	0.31992
150	4.8331	201.20	41.042	1863.7	0.34903	0.31997
2 ·	4.0432	192.85	37.038	1952.9	0.35381	0.32006
2.0	3.4789	184.16	35.277	2088.6	0.35680	0.31903
300	3.0522	175.75	34.284	2231.1	0.35963	0.31822
350	2.7066	167.21	34.047	2399.9	0.36194	0.31722
400	2.4147	158.45	34.452	2602.1	0.36370	0.31605
450	2.1697	149.37	35.480	2847.9	0.36519	0.31467
500	1.9304	139.80	37.197	3152.4	0.36613	0.31307
525	1.8228	134.95	38.350	3333.6	0.36642	0.31216
550	1.7187	129.86	39.764	3539.3	0.36657	0.31118
560	1.6779	127.78	40.403	3629.6	0.36660	0.31076
600	1.5183	119.13	43.497	4048.4	0.36643	0.30893
650	1.3224	107.40	48.995	4750.9	0.36561	0.30622
700	1.1235	94.173	57.552	5795.8	0.36389	0.30289
750	0.9085	78.407	72.503	7562.6	0.36005	0.29864

Table C.4: The correspondence between $\bar{t}$ and the other velocity profile parameters at discrete times in the pipe entrance, for the case $\bar{\Omega} = 10$).

$\bar{t}$ ($\times 10^5$)	$\bar{S}$	δ^*/R ($\times 10^3$)	$\bar{U}_c/\bar{U}$
15	98.575	13.198	1.0271
20	85.092	15.345	1.0316
25	76.089	17.217	1.0356
30	69.534	18.895	1.0393
40	60.451	21.850	1.0457
50	54.324	24.430	1.0514
60	49.836	26.745	1.0565
70	46.369	28.861	1.0612
80	43.586	30.819	1.0657
90	41.290	32.649	1.0699
100	39.354	34.371	1.0738
115	36.958	36.784	1.0794
150	32.836	41.823	1.0913
200	28.992	47.992	1.1062
250	26.393	53.339	1.1194
300	24.490	58.104	1.1315
350	23.024	62.427	1.1427
400	21.851	66.400	1.1531
450	20.886	70.085	1.1630
500	20.077	73.531	1.1724
550	19.386	76.772	1.1814
600	18.788	79.834	1.1900
650	18.265	82.740	1.1983
700	17.801	85.509	1.2063
750	17.388	88.152	1.2140
800	17.017	90.685	1.2215
850	16.683	93.115	1.2288
875	16.527	94.295	1.2324
900	16.378	95.453	1.2359
925	16.236	96.589	1.2394

Table C.3: Critical parameters at discrete times in the far-downstream impulsively started pipe flow, for the case $\tilde{\Omega} = 10$. The underlined data are the values of the parameters at the minimum critical Reynolds number.

$\tilde{t}$ ($\times 10^5$)	$\alpha_{[\mathrm{crit}]}$	$\alpha_{\delta^*[\mathrm{crit}]}$ ($\times 10^3$)	$Re_{R[\mathrm{crit}]}$ ($\times 10^{-3}$)	$Re_{\delta^*[\mathrm{crit}]}$	$c_{[\mathrm{crit}]}$	$\tilde{c}_{[\mathrm{crit}]}$
15	17.629	232.67	121.43	1643.1	0.32651	0.31790
20	14.913	228.84	104.97	1661.8	0.32783	0.31777
25	13.274	228.54	92.664	1652.2	0.33012	0.31876
30	12.011	226.96	84.354	1656.5	0.33157	0.31904
40	10.279	224.61	72.546	1657.6	0.33449	0.31988
50	9.1032	222.39	64.694	1661.7	0.33697	0.32051
60	8.2403	220.39	58.957	1665.9	0.33924	0.32109
70	7.5703	218.49	54.559	1671.1	0.34129	0.32160
80	7.0304	216.67	51.053	1676.8	0.34321	0.32205
90	6.5832	214.93	48.181	1682.9	0.34500	0.32247
100	6.2043	213.25	45.778	1689.6	0.34668	0.32285
110	5.7337	210.91	42.777	1698.5	0.34911	0.32342
150	4.9118	205.43	37.884	1729.1	0.35402	0.32440
200	4.1289	198.15	33.499	1778.3	0.36013	0.32556
250	3.5825	191.09	30.782	1837.9	0.36545	0.32647
300	3.1678	184.06	29.039	1909.2	0.37019	0.32718
350	2.8345	176.95	27.952	1993.9	0.37447	0.32772
400	2.5552	169.67	27.359	2094.8	0.37834	0.32810
450	2.3136	162.15	27.182	2215.6	0.38183	0.32831
500	2.0991	154.35	27.390	2361.3	0.38496	0.32835
550	1.9040	146.18	27.997	2539.3	0.38770	0.32817
600	1.7225	137.51	29.057	2760.5	0.39003	0.32776
650	1.5504	128.28	30.689	3042.7	0.39188	0.32704
700	1.3827	118.23	33.088	3413.0	0.39323	0.32598
750	1.2152	107.12	36.676	3925.1	0.39389	0.32445
800	1.0407	94.377	42.291	4684.8	0.39375	0.32234
850	0.84809	78.970	52.142	5966.3	0.39246	0.31938
875	0.73754	69.546	60.580	7041.1	0.39125	0.31746
900	0.60839	58.072	74.762	8820.0	0.38951	0.31515
925	0.44074	42.571	106.06	12697	0.38704	0.31227

Table C.2: The correspondence between $\tilde{t}$ and the other velocity profile parameters at discrete times in the pipe entrance, for the zero acceleration ($\tilde{\Omega} = 0$) case.

$\tilde{t}$ ($\times 10^5$)	S	δ^*/R ($\times 10^3$)	U_c/U
13	106.09	12.234	1.0251
14	102.04	12.729	1.0261
15	98.442	13.204	1.0271
16	95.207	13.662	1.0281
17	92.281	14.105	1.0290
20	84.936	15.355	1.0317
25	76.017	17.223	1.0357
30	69.342	18.913	1.0393
40	60.228	21.878	1.0457
50	54.074	24.469	1.0514
60	49.563	26.796	1.0566
80	43.287	30.893	1.0659
100	39.000	34.479	1.0741
140	33.437	40.631	1.0885
200	28.491	48.268	1.1069
90	23.870	58.635	1.1328
400	21.146	67.198	1.1553
500	19.292	74.023	1.1754
600	17.930	81.242	1.1940
700	16.877	87.251	1.2114
800	16.033	92.778	1.2278
900	15.337	97.911	1.2435
950	15.032	100.35	1.2511
970	14.918	101.30	1.2541
980	14.861	101.78	1.2556
990	14.806	102.25	1.2571
1000	14.752	102.71	1.2585
1020	14.645	103.64	1.2615
1040	14.542	104.55	1.2644
1050	14.492	105.01	1.2658
1060	14.442	105.46	1.2673
1070	14.393	105.91	1.2687
1080	14.297	106.80	1.2702

Table C.1: Critical parameters at discrete times in the far-downstream impulsively started pipe flow, for the zero-acceleration case ($\Omega = 0$). The underlined data are the values of the parameters at the minimum critical Reynolds number.

$\tilde{t}$ ($\times 10^5$)	$\alpha_{[\mathrm{crit}]}$	$\alpha_{\delta^*[\mathrm{crit}]}$ ($\times 10^3$)	$Re_{R[\mathrm{crit}]}$ ($\times 10^{-3}$)	$Re_{\delta^*[\mathrm{crit}]}$	$c_{[\mathrm{crit}]}$	$\tilde{c}_{[\mathrm{crit}]}$
13	20.023	244.75	128.07	1604.6	0.32765	0.31964
14	18.727	238.17	126.94	1656.7	0.32558	0.31730
15	17.643	232.78	124.56	1688.0	0.32453	0.31596
16	16.805	229.44	120.78	1695.3	0.32458	0.31571
17	16.194	228.26	116.08	1683.7	0.32548	0.31631
20	15.016	230.44	103.36	1636.4	0.32884	0.31875
25	13.340	239.75	92.187	1644.3	0.33030	0.31892
30	12.004	226.95	83.895	1648.5	0.33171	0.31917
40	10.334	226.02	71.243	1629.5	0.33555	0.32088
50	9.1473	223.78	63.256	1627.1	0.33827	0.32171
60	8.2921	222.16	57.272	1621.2	0.34095	0.32268
80	7.0889	219.00	49.050	1615.1	0.34561	0.32425
100	6.2699	216.16	43.498	1610.7	0.34979	0.32567
140	5.1925	210.98	36.335	1606.9	0.35719	0.32817
200	4.2228	203.90	30.137	1610.7	0.36682	0.33140
300	3.2874	192.75	24.681	1639.3	0.38067	0.33603
400	2.7015	181.53	21.860	1697.0	0.39282	0.34002
500	2.2749	169.76	20.402	1789.5	0.40373	0.34347
<u>600</u>	<u>1.9339</u>	<u>157.11</u>	<u>19.885</u>	<u>1928.0</u>	<u>0.41352</u>	<u>0.34633</u>
700	1.6410	143.17	20.231	2138.3	0.42212	0.34846
800	1.3718	127.27	21.654	2466.7	0.42932	0.34966
900	1.1040	108.10	24.939	3036.4	0.43468	0.34956
950	0.96088	96.424	27.996	3514.8	0.43643	0.34884
970	0.89972	90.718	29.715	3753.0	0.43691	0.34880
980	0.86785	88.328	30.732	3927.2	0.43710	0.34813
990	0.83524	85.401	31.880	4097.6	0.43723	0.34782
1000	0.80137	82.312	33.187	4290.1	0.43734	0.34749
1020	0.72949	75.605	36.439	4764.0	0.43739	0.34673
1040	0.64992	67.952	40.988	5418.6	0.43723	0.34580
1050	0.60617	63.653	44.046	5854.8	0.43706	0.34527
1060	0.55880	58.931	47.928	6407.6	0.43682	0.34469
1070	0.50667	53.660	53.075	7131.7	0.43650	0.34404
1080	0.37937	40.515	71.719	9728.7	0.43557	0.34292

Appendix C

Tabulated velocity profile and stability data

C.1 The far-downstream parallel developing flow

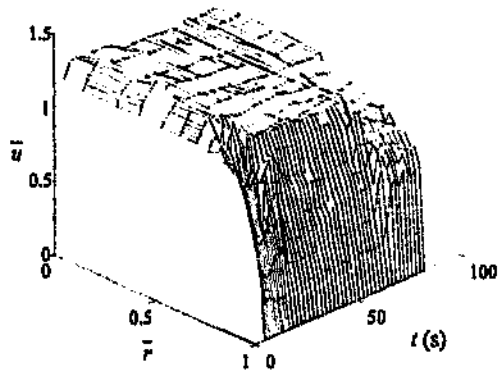

Figure B.35: Velocity profiles for the test HAJ ($x/R = 32.99$), represented as a surface.

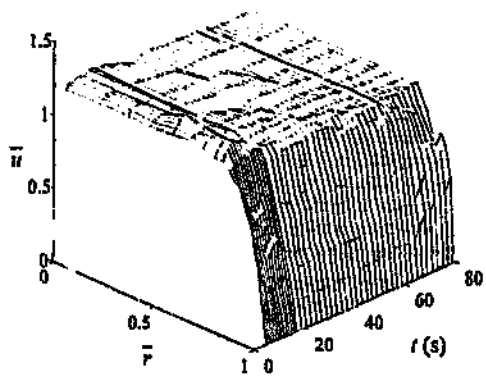

Figure B.36: Velocity profiles for the test HAK ($x/R = 11.41$), represented as a surface.

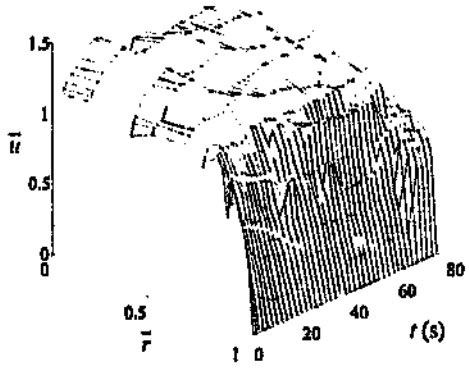

Figure B.32: Velocity profiles for the test HAG ($x/R = 113.57$), represented as a surface.

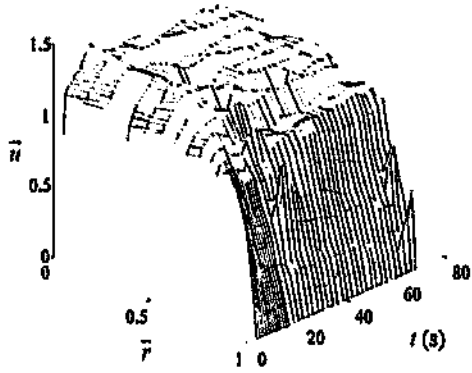

Figure B.33: Velocity profiles for the test HAH ($x/R = 81.62$), represented as a surface.

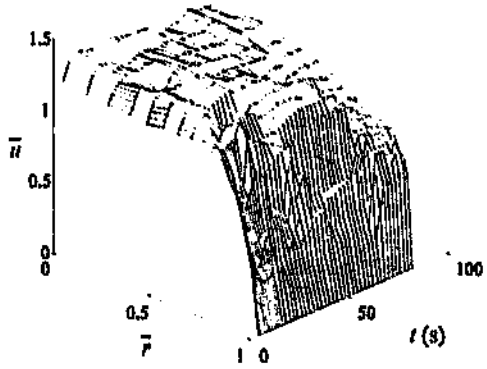

Figure B.34: Velocity profiles for the test HAI ($x/R = 54.56$), represented as a surface.

Table C.21: Variables and parameters at discrete points in the pipe entrance, for the case $\bar{\Omega} = 20$. The underlined data are the values of the parameters at the minimum critical Reynolds number.

$\bar{x}$ ($\times 10^5$)	$\alpha_{[crit]}$	$\alpha_{\delta^*[crit]}$ ($\times 10^3$)	$Re_{R[crit]}$ ($\times 10^{-3}$)	$Re_{\delta^*[crit]}$	$c_{[crit]}$	$\hat{c}_{[crit]}$
0	∞	303.77	∞	519.06	0.39664	0.39664
7.1079	16.809	279.99	36.218	624.08	0.40258	0.38017
12.625	13.190	267.44	31.126	657.80	0.40251	0.38619
19.703	10.880	261.09	27.493	692.99	0.40326	0.38301
28.331	9.1273	253.02	25.060	735.47	0.40343	0.38106
38.495	7.8653	246.99	23.033	771.79	0.40457	0.37916
50.180	6.8201	239.13	21.809	821.21	0.40463	0.37629
63.367	6.0241	232.23	20.821	869.72	0.40503	0.37380
78.034	5.3560	224.93	20.180	925.19	0.40518	0.37115
94.160	4.7987	217.62	19.779	986.44	0.40513	0.36839
111.72	4.3267	210.34	19.562	1053.4	0.40508	0.36570
<u>130.68</u>	<u>3.9177</u>	<u>202.88</u>	<u>19.546</u>	<u>1129.1</u>	<u>0.40480</u>	<u>0.36288</u>
151.02	3.5606	195.35	19.690	1213.4	0.40448	0.36009
172.70	3.2426	187.61	20.015	1309.6	0.40398	0.35723
195.68	2.9573	179.69	20.519	1419.2	0.40339	0.35437
219.94	2.6973	171.49	21.226	1546.1	0.40264	0.35144
245.44	2.4579	162.99	22.169	1694.9	0.40177	0.34848
272.12	2.2349	154.12	23.397	1871.7	0.40072	0.34545
299.96	2.0245	144.82	24.991	2086.2	0.39949	0.34233
328.90	1.8236	135.00	27.068	2352.1	0.39801	0.33908
358.91	1.6289	124.52	29.835	2692.4	0.39622	0.33564
389.92	1.4368	113.21	33.630	3145.3	0.39401	0.33192
421.91	1.2424	100.71	39.136	3786.2	0.39121	0.32779
454.81	1.0379	86.420	47.840	4779.1	0.38756	0.32302
488.56	0.80662	68.880	64.205	6612.0	0.38256	0.31722
523.13	0.49363	43.173	113.29	12000	0.37512	0.30951

Table C.20: The correspondence between x and the other velocity profile parameters at discrete points in the pipe entrance, for the case $\Omega = 10$.

x ($\times 10^5$)	S	δ^*/R ($\times 10^3$)	U_c/U
0	∞	0	1
7.1079	72.372	16.675	1.0345
12.625	60.147	20.308	1.0423
19.703	51.388	24.050	1.0505
28.331	44.988	27.803	1.0589
38.495	40.141	31.520	1.0673
50.180	36.384	35.177	1.0757
63.367	33.383	38.761	1.0840
78.034	30.951	42.266	1.0923
94.160	28.933	45.689	1.1006
111.72	27.242	49.027	1.1087
130.68	25.801	52.281	1.1168
151.02	24.564	55.451	1.1247
172.70	23.487	58.540	1.1326
195.68	22.548	61.547	1.1404
219.91	21.716	64.475	1.1480
245.44	20.980	67.324	1.1556
272.12	20.321	70.098	1.1631
299.96	19.731	72.796	1.1704
328.90	19.197	75.422	1.1776
358.91	18.716	77.976	1.1848
389.92	18.276	80.461	1.1918
421.91	17.877	82.876	1.1987
454.81	17.510	85.226	1.2055
488.56	17.175	87.510	1.2122
523.13	16.865	89.730	1.2187
558.45	16.580	91.888	1.2252
594.47	16.316	93.984	1.2315
631.14	16.073	96.021	1.2377

Table C.19: Variables and parameters at discrete points in the pipe entrance, for the case $\bar{\Omega} = 10$. The underlined data are the values of the parameters at the minimum critical Reynolds number.

$\bar{x}$ ($\times 10^5$)	$\alpha_{[crit]}$	$\alpha_{\delta^*[crit]}$ ($\times 10^3$)	$Re_{R[crit]}$ ($\times 10^{-3}$)	$Re_{\delta^*[crit]}$	$c_{[crit]}$	$\hat{c}_{[crit]}$
0	∞	303.77	∞	519.06	0.39664	0.39664
7.1079	16.829	280.62	35.774	617.11	0.40329	0.38984
12.625	13.263	269.35	30.424	644.03	0.40401	0.38760
19.703	10.949	263.32	26.656	673.47	0.40526	0.38577
28.331	9.2171	256.26	23.998	706.50	0.40632	0.38373
38.495	7.9601	250.90	21.800	733.37	0.40825	0.38252
50.180	6.9376	244.04	20.323	769.00	0.40943	0.38063
63.367	6.1423	238.08	19.099	802.51	0.41096	0.37910
78.034	5.4849	231.83	18.177	839.20	0.41243	0.37757
94.160	4.9380	225.61	17.470	878.43	0.41381	0.37599
111.72	4.4766	219.47	16.916	919.49	0.41529	0.37457
130.68	4.0780	213.20	16.518	964.40	0.41667	0.37310
151.02	3.7315	206.92	16.235	1012.5	0.41810	0.37173
172.70	3.4249	200.49	16.069	1065.4	0.41947	0.37036
195.68	3.1510	193.93	16.009	1123.6	0.42083	0.36903
219.94	2.9034	187.19	16.055	1188.4	0.42214	0.36771
245.44	2.6770	180.23	16.213	1261.4	0.42341	0.36640
272.12	2.4681	173.01	16.488	1344.3	0.42462	0.36509
299.96	2.2732	165.48	16.901	1440.0	0.42573	0.36375
328.90	2.0898	157.62	17.471	1551.7	0.42673	0.36236
358.91	.9150	149.32	18.230	1684.9	0.42758	0.36090
389.92	1.7469	140.56	19.256	1846.5	0.42823	0.35932
421.91	1.5828	131.18	20.617	2048.1	0.42862	0.35757
454.81	1.4203	121.04	22.463	2307.8	0.42866	0.35559
488.56	1.2555	109.87	25.063	2658.6	0.42824	0.35329
523.13	1.0838	97.253	28.942	3164.9	0.42718	0.35052
558.45	0.89575	82.308	35.384	3983.5	0.42521	0.34706
594.47	0.66986	62.956	48.736	5640.6	0.42181	0.34253
631.14	0.30727	29.504	113.04	13434	0.41587	0.33601

Table C.18: The correspondence between x and the other velocity profile parameters at discrete points in the pipe entrance, for the case of zero acceleration ($\Omega = 0$).

x ($\times 10^5$)	S	δ^*/R ($\times 10^3$)	U_c/U
0	∞	0	1
7.1079	72.166	16.693	1.0345
12.625	59.895	20.341	1.0424
19.703	51.093	24.103	1.0506
38.495	39.759	31.638	1.0676
50.180	35.960	35.339	1.0761
63.367	32.920	38.976	1.0845
78.034	30.449	42.542	1.0930
94.160	28.393	46.034	1.1014
130.68	25.180	52.790	1.1180
151.02	23.917	56.054	1.1263
195.68	21.835	62.360	1.1425
245.44	20.204	68.376	1.1584
272.12	19.515	71.270	1.1663
328.90	18.334	76.881	1.1817
358.91	17.824	79.582	1.1893
389.92	17.358	82.218	1.1968
454.81	16.540	87.302	1.2115
488.56	16.179	89.751	1.2188
523.13	15.845	92.130	1.2259
594.47	15.250	96.740	1.2399
631.14	14.984	98.953	1.2467
706.15	14.503	103.21	1.2601
725.27	14.395	104.24	1.2634
763.70	14.185	106.26	1.2699
783.02	14.084	107.25	1.2731
802.51	13.988	108.22	1.2762
814.21	13.931	108.80	1.2781
818.10	13.912	109.00	1.2788
818.60	13.910	109.03	1.2788

C.2 The steady pipe entrance flow

Table C.17: Variables and parameters at discrete points in the pipe entrance, for the zero acceleration case ($\Omega = 0$). The underlined data are the values of the parameters at the minimum critical Reynolds number.

x^* ($\times 10^5$)	v_0[crit]	v_{δ^*}[crit] ($\times 10^3$)	Re_{η}[crit] ($\times 10^{-3}$)	Re_{δ^*}[crit]	ζ[crit]	ζ[crit]
0	∞	303.77	∞	519.06	0.39664	0.39664
7.1079	16.849	281.26	35.332	610.16	0.40400	0.39051
12.625	13.335	271.25	20.747	630.74	0.40549	0.38809
19.703	11.018	265.58	25.818	654.59	0.40726	0.38763
38.495	8.0546	254.83	20.649	697.41	0.41188	0.38582
50.180	7.0463	249.01	18.961	721.05	0.41415	0.38488
63.367	6.2601	243.99	17.551	741.90	0.41677	0.38428
78.034	5.6140	238.83	16.414	763.23	0.41951	0.38381
94.160	5.0777	233.75	15.484	785.07	0.42225	0.38338
130.68	4.2391	223.80	14.042	828.78	0.42818	0.38208
151.02	3.9041	218.84	13.488	851.50	0.43130	0.38205
195.68	3.3475	208.75	12.638	900.38	0.43773	0.38313
245.44	2.9003	198.31	12.069	955.96	0.44441	0.38363
272.12	2.7063	192.90	11.877	987.38	0.44781	0.38397
328.90	2.3615	181.55	11.675	1060.7	0.45467	0.38476
<u>358.91</u>	<u>2.2062</u>	<u>175.57</u>	<u>11.667</u>	<u>1104.2</u>	<u>0.45809</u>	<u>0.38518</u>
389.02	2.0598	169.35	11.725	1153.7	0.46146	0.38558
454.81	1.7873	156.04	12.075	1277.2	0.46798	0.38027
488.50	1.6584	148.84	12.395	1355.8	0.47106	0.38051
523.13	1.5325	141.21	12.841	1450.5	0.47396	0.38662
594.47	1.2834	124.15	14.289	1713.9	0.47904	0.38636
631.14	1.1560	114.39	15.453	1906.4	0.48108	0.38587
706.15	0.8782	90.638	19.741	2567.5	0.48363	0.38380
725.27	0.7991	83.299	21.675	2854.5	0.48374	0.38289
763.70	0.6135	65.190	28.398	3831.8	0.48337	0.38065
783.02	0.4828	51.770	35.517	4849.5	0.48276	0.37921
802.51	0.3344	36.184	53.333	7366.3	0.48150	0.37728
814.21	0.1709	18.599	105.56	14080	0.48051	0.37504
818.10	0.0321	3.4965	565.11	78766	0.48012	0.37546
≈ 818.60	0	0	∞	∞	≈ 0.48007	≈ 0.37540

Table C.16: The correspondence between $\tilde{t}$ and the other velocity profile parameters at discrete times in the pipe entrance, for the case $\tilde{\Omega} = 70$).

$\tilde{t}$ ($\times 10^6$)	S	δ^*/R ($\times 10^3$)	U_c/U
15	99.374	13.162	1.0270
20	86.022	15.289	1.0315
25	77.134	17.137	1.0355
30	70.682	18.789	1.0390
40	61.780	21.686	1.0453
50	55.812	24.201	1.0509
60	51.467	26.445	1.0558
70	48.129	28.484	1.0604
80	45.467	30.361	1.0646
90	43.284	32.104	1.0686
100	41.454	33.737	1.0723
125	37.944	37.423	1.0809
150	35.393	40.684	1.0886
200	31.926	46.278	1.1020
250	29.652	50.997	1.1136
300	28.037	55.090	1.1238
350	26.829	58.704	1.1330
400	25.891	61.939	1.1414
450	25.143	64.862	1.1491
500	24.534	67.523	1.1561
550	24.029	69.962	1.1627

Table C.15: Critical parameters at discrete times in the far-downstream impulsively started pipe flow, for the case $\Omega = 70$. The underlined data are the values of the parameters at the minimum critical Reynolds number.

$\hat{t}$ ($\times 10^5$)	$\alpha_{\text{[crit]}}$	$\alpha_{\delta^*\text{[crit]}}$ ($\times 10^3$)	$Re_{H\text{[crit]}}$ ($\times 10^{-3}$)	$Re_{\delta^*\text{[crit]}}$	$c_{\text{[crit]}}$	$\tilde{c}_{\text{[crit]}}$
15	17.400	230.21	126.75	1713.3	0.32408	0.31556
20	14.740	225.35	111.76	1762.5	0.32419	0.31428
25	13.078	224.11	100.10	1776.2	0.32564	0.31449
30	11.810	221.91	92.564	1807.1	0.32617	0.31392
40	10.037	217.67	82.270	1865 1	0.32710	0.31292
50	8.8369	213.86	75.765	1926.9	0.32763	0.31178
60	7.9477	210.18	71.332	1991.7	0.32789	0.31056
70	7.2561	206.68	68.187	2059.5	0.32796	0.30928
80	6.6958	203.29	65.921	2130.8	0.32784	0.30794
90	6.2294	199.99	64.280	2205.2	0.32760	0.30657
100	5.8329	196.78	63.108	2283.1	0.32724	0.30510
125	5.0528	189.09	61.685	2495.2	0.32588	0.30149
<u>150</u>	<u>4.4659</u>	<u>181.69</u>	<u>61.605</u>	<u>2728.4</u>	<u>0.32421</u>	<u>0.29783</u>
200	3.6230	167.66	64.413	3284.9	0.31988	0.29027
250	3.0249	154.26	70.186	3985.8	0.31482	0.28271
300	2.5635	141.23	78.802	4878.7	0.30934	0.27526
350	2.1872	128.40	90.735	6035.1	0.30359	0.26795
400	1.8666	115.61	107.06	7569.0	0.29764	0.26077
450	1.5836	102.71	129.84	9677.0	0.29144	0.25363
500	1.3239	89.393	163.14	12735	0.28485	0.24639
550	1.0732	75.082	216.26	17592	0.27764	0.23879

Table C.14: The correspondence between $\tilde{t}$ and the other velocity profile parameters at discrete times in the pipe entrance, for the case $\bar{\Omega} = 60$.

$\tilde{t}$ ($\times 10^5$)	S	δ^*/R ($\times 10^3$)	U_c/U
15	99.241	13.168	1.0270
20	85.868	15.208	1.0315
25	76.960	17.150	1.0355
30	70.492	18.807	1.0391
40	61.559	21.714	1.0454
50	55.565	24.239	1.0509
60	51.196	26.495	1.0559
70	47.837	28.546	1.0605
80	45.156	30.436	1.0648
90	42.954	32.194	1.0688
100	41.107	33.841	1.0726
125	37.558	37.567	1.0812
150	34.972	40.870	1.0890
200	31.445	46.556	1.1027
250	29.120	51.375	1.1145
300	27.460	55.573	1.1250
350	26.212	59.297	1.1345
400	25.230	62.645	1.1432
450	24.458	65.684	1.1512
500	23.819	68.463	1.1586
550	23.287	71.021	1.1656

Table C.13: Critical parameters at discrete times in the far-downstream impulsively started pipe flow, for the case $\tilde{\Omega} = 60$. The underlined data are the values of the parameters at the minimum critical Reynolds number.

$\tilde{t}$ ($\times 10^5$)	$\alpha_{[\mathrm{crit}]}$	$\alpha_{\delta^*[\mathrm{crit}]}$ ($\times 10^3$)	$Re_{R[\mathrm{crit}]}$ ($\times 10^{-3}$)	$Re_{\delta^*[\mathrm{crit}]}$	$c_{[\mathrm{crit}]}$	$\tilde{c}_{[\mathrm{crit}]}$
15	17.514	230.62	125.84	1701.9	0.32449	0.31595
20	14.768	225.92	110.60	1745.3	0.32480	0.31486
25	13.111	224.85	98.811	1754.8	0.32639	0.31520
30	11.843	222.74	91.139	1781.0	0.32707	0.31477
40	10.077	218.81	80.553	1828.5	0.32834	0.31408
50	8.8805	215.25	73.786	1879.6	0.32919	0.31324
60	7.9955	211.84	69.087	1932.8	0.32979	0.31232
70	7.3071	208.59	65.681	1988.5	0.33018	0.31134
80	6.7499	205.44	63.151	2046.7	0.33041	0.31030
90	6.2863	202.38	61.241	2107.2	0.33050	0.30922
100	5.8924	199.40	59.794	2170.4	0.33047	0.30811
125	5.1176	192.25	57.649	2341.6	0.32996	0.30516
150	4.5352	185.36	56.781	2527.2	0.32912	0.30222
200	3.6989	172.21	57.762	2965.3	0.32641	0.29602
250	3.1053	159.53	61.261	3507.7	0.32288	0.28970
300	2.6466	147.08	66.987	4188.1	0.31878	0.28335
350	2.2713	134.68	75.168	5056.9	0.31427	0.27700
400	1.9507	122.20	86.479	6193.4	0.30941	0.27065
450	1.6665	109.46	102.25	7731.8	0.30418	0.26422
500	1.4053	96.213	125.09	9922.6	0.29846	0.25759
550	1.1542	81.960	160.74	13306	0.29204	0.25056

Table C.12: The correspondence between $\bar{t}$ and the other velocity profile parameters at discrete times in the pipe entrance, for the case $\bar{\Omega} = 50$).

$\bar{t}$ ($\times 10^5$)	S	δ^*/R ($\times 10^3$)	U_c/U
15	99.108	13.174	1.0270
20	85.713	15.307	1.0316
25	76.786	17.163	1.0355
30	70.300	18.825	1.0391
40	61.338	21.741	1.0454
50	55.317	24.277	1.0510
60	50.925	26.545	1.0561
70	47.545	28.609	1.0607
80	44.844	30.512	1.0650
90	42.623	32.284	1.0690
100	40.759	33.946	1.0728
125	37.170	37.712	1.0816
150	34.549	41.058	1.0895
200	30.961	46.837	1.1033
250	28.583	51.757	1.1155
300	26.877	56.063	1.1263
350	25.588	59.901	1.1361
400	24.578	63.366	1.1451
450	23.764	66.524	1.1535
500	23.094	69.426	1.1612
550	22.534	72.109	1.1685

Table C.11: Critical parameters at discrete times in the far-downstream impulsively started pipe flow, for the case $\tilde{\Omega} = 50$. The underlined data are the values of the parameters at the minimum critical Reynolds number.

$\tilde{t}$ ($\times 10^5$)	$\alpha_{[\mathrm{crit}]}$	$\alpha_{\delta^*[\mathrm{crit}]}$ ($\times 10^3$)	$Re_{R[\mathrm{crit}]}$ ($\times 10^{-3}$)	$Re_{\delta^*[\mathrm{crit}]}$	$c_{[\mathrm{crit}]}$	$\tilde{c}_{[\mathrm{crit}]}$
15	17.537	231.04	124.94	1690.5	0.32490	0.31634
20	14.796	226.49	109.45	1728.3	0.32540	0.31544
25	13.144	225.59	97.544	1733.0	0.32714	0.31592
30	11.877	223.57	89.738	1755.3	0.32797	0.31563
40	10.117	219.96	78.876	1792.8	0.32957	0.31525
50	8.9244	216.66	71.862	1833.6	0.33075	0.31470
60	8.0437	213.52	66.918	1875.9	0.33168	0.31408
70	7.3588	210.53	63.274	1920.0	0.33241	0.31339
80	6.8047	207.63	60.504	1966.1	0.33297	0.31265
90	6.3441	204.81	58.352	2013.9	0.33340	0.31188
100	5.9529	202.08	56.661	2063.5	0.33372	0.31106
125	5.1840	195.50	53.882	2197.7	0.33405	0.30885
150	4.6068	189.15	52.335	2341.0	0.33407	0.30664
200	3.7786	176.98	51.773	2675.5	0.33306	0.30186
250	3.1913	165.17	53.389	3082.3	0.33115	0.29687
300	2.7377	153.48	56.755	3583.7	0.32860	0.29176
350	2.3661	141.73	61.900	4212.5	0.32555	0.28655
400	2.0484	129.80	69.175	5019.4	0.32205	0.28124
450	1.7666	117.52	79.337	6087.8	0.31808	0.27576
500	1.5080	104.70	93.861	7567.1	0.31357	0.27003
550	1.2610	90.932	115.82	9759.0	0.30834	0.26387

Table C.10: The correspondence between $\bar{t}$ and the other velocity profile parameters at discrete times in the pipe entrance, for the case $\bar{\Omega} = 40$.

$\bar{t}$ ($\times 10^5$)	S	δ^*/R ($\times 10^3$)	U_c/U
15	98.975	13.180	1.0271
20	85.558	15.317	1.0316
25	76.612	17.177	1.0356
30	70.109	18.842	1.0391
40	61.117	21.768	1.0455
50	55.070	24.315	1.0511
60	50.654	26.594	1.0562
70	47.252	28.671	1.0608
80	44.530	30.588	1.0652
90	42.292	32.375	1.0692
100	40.410	34.051	1.0731
125	36.781	37.857	1.0819
150	34.124	41.247	1.0899
200	30.473	47.121	1.1040
250	28.042	52.145	1.1164
300	26.289	56.562	1.1275
350	24.958	60.515	1.1377
400	23.909	64.101	1.1470
450	23.060	67.384	1.1558
500	22.358	70.414	1.1639
550	21.767	73.227	1.1716
600	21.264	75.850	1.1788

Appendix D

Matlab m-files

This appendix contains listings of the basic Matlab m-files used in the solution of the numerical systems in this work. The first section lists the basic or generic operators, and the subsequent ones are concerned with the m-files for the solution of the particular mathematical problems.

D.1 The basic operators

The m-files contained in this section comprise the basic Matlab 'toolbox' for solving all the numerical problems in this work. They represent all the algorithms and operator matrices, etc. developed throughout this work.

D.1.1 muhat.m

```
%
% muhat constructs the shift matrix in Chebyshev space of order n
%
% function [mu]=muhat(n);
%
function [m]=muhat(n);
m=zeros(n,n);
m(1,1)=2;
m(1,2)=2;
for i=2:n-1
  m(i,i-1)=1;
  m(i,i)=2;
  m(i,i+1)=1;
end
```

Table C.32: The correspondence between $\tilde{x}$ and the other velocity profile parameters at discrete points in the pipe entrance, for the case $\Omega = 70$.

$\tilde{x}$ ($\times 10^5$)	S	δ^*/R ($\times 10^3$)	U_c/U
0	∞	0	1
7.1079	73.600	16.568	1.0343
12.625	61.644	20.117	1.0419
19.703	53.141	23.735	1.0498
28.331	46.906	27.326	1.0578
38.495	42.390	30.838	1.0657
50.180	38.869	34.247	1.0735
63.367	36.093	37.540	1.0812
78.034	33.879	40.711	1.0886
94.160	32.068	43.759	1.0959
111.72	30.578	46.682	1.1030
130.68	29.328	49.484	1.1098
151.02	28.277	52.166	1.1165
172.70	27.377	54.732	1.1229
195.68	26.608	57.186	1.1291
219.94	25.940	59.530	1.1352
245.44	25.362	61.770	1.1410
272.12	24.855	63.909	1.1465

Table C.31: Variables and parameters at discrete points in the pipe entrance, for the case $\bar{\Omega} = 70$. The underlined data are the values of the parameters at the minimum critical Reynolds number.

$\bar{x}$ ($\times 10^5$)	α[crit]	α_*[crit] ($\times 10^3$)	Re_R[crit] ($\times 10^{-3}$)	Re_{δ^*}[crit]	$\bar{c}$[crit]	$\bar{c}$[crit]
0	∞	303.77	∞	519.06	0.39664	0.39664
7.1079	16.721	277.05	38.474	659.30	0.39917	0.38595
12.625	12.819	257.88	35.043	734.50	0.39466	0.37878
19.703	10.536	250.08	32.159	801.34	0.39308	0.37442
28.331	8.6848	237.32	31.367	906.68	0.38838	0.36715
<u>38.495</u>	<u>7.3781</u>	<u>227.53</u>	<u>30.714</u>	<u>1008.4</u>	<u>0.38520</u>	<u>0.36144</u>
50.180	6.3014	215.80	31.527	1159.1	0.37962	0.35362
63.367	5.4474	204.50	32.840	1332.9	0.37390	0.34582
78.034	4.7291	192.53	35.178	1559.1	0.36709	0.33720
94.160	4.1407	181.19	38.191	1831.6	0.36006	0.32855
111.72	3.6326	169.58	42.333	2170.7	0.35243	0.31952
130.68	3.1988	158.29	47.544	2611.1	0.34462	0.31051
151.02	2.8156	146.88	54.250	3159.7	0.33665	0.30153
172.70	2.4792	135.69	62.600	3851.1	0.32873	0.29274
195.68	2.1757	124.42	73.435	4741.8	0.32091	0.28420
219.94	1.9027	113.27	87.254	5890.3	0.31324	0.27594
245.44	1.6495	101.89	105.64	7445.4	0.30568	0.26792
272.12	1.4145	90.402	130.77	9582.2	0.29815	0.26004

Table C.30: The correspondence between $\bar{x}$ and the other velocity profile parameters at discrete points in the pipe entrance, for the case $\Omega = 60$.

$\bar{x}$ ($\times 10^5$)	S	δ^*/R ($\times 10^3$)	U_c/U
0	∞	0	1
7.1079	73.396	16.586	1.0343
12.625	61.396	20.148	1.0420
19.703	52.851	23.786	1.0499
28.331	46.664	27.404	1.0580
38.495	42.020	30.948	1.0660
50.180	38.461	34.397	1.0739
63.367	35.649	37.736	1.0816
78.034	33.400	40.959	1.0892
94.160	31.557	44.065	1.0966
111.72	30.036	47.052	1.1039
130.68	28.756	49.922	1.1109
151.02	27.677	52.678	1.1178
172.70	26.750	55.322	1.1244
195.68	25.956	57.857	1.1309
219.94	25.263	60.287	1.1371
245.44	24.662	62.616	1.1432
272.12	24.132	64.846	1.1490
299.96	23.667	66.981	1.1547

Table C.29: Variables and parameters at discrete points in the pipe entrance, for the case $\Omega = 60$. The underlined data are the values of the parameters at the minimum critical Reynolds number.

x ($\times 10^3$)	$\alpha_{\text{[crit]}}$	$\alpha_{\delta^*\text{[crit]}}$ ($\times 10^3$)	$Re_{R\text{[crit]}}$ ($\times 10^{-3}$)	$Re_{\delta^*\text{[crit]}}$	$c_{\text{[crit]}}$	$c_{\text{[crit]}}$
0	∞	303.77	∞	519.06	0.39664	0.39664
7.1079	16.738	277.62	38.018	652.20	0.39984	0.38658
12.625	12.894	259.78	34.202	718.05	0.39628	0.38031
19.703	10.606	252.28	31.156	778.10	0.39514	0.37634
28.331	8.7708	240.35	29.965	868.75	0.39144	0.36999
<u>38.495</u>	<u>7.4778</u>	<u>231.43</u>	<u>28.941</u>	<u>954.78</u>	<u>0.38921</u>	<u>0.36512</u>
50.180	6.4049	220.31	29.236	1079.9	0.38472	0.35825
63.367	5.5581	209.74	29.907	1220.7	0.38023	0.35154
78.034	4.8495	198.63	31.368	1399.4	0.37485	0.34414
94.160	4.2651	187.94	33.372	1612.6	0.36913	0.33660
111.72	3.7606	176.94	36.171	1878.7	0.36287	0.32872
130.68	3.3260	166.04	39.771	2205.7	0.35628	0.32070
151.02	2.9427	155.02	44.374	2612.8	0.34949	0.31267
172.70	2.6028	143.99	50.203	3122.8	0.34254	0.30464
195.68	2.2964	132.86	57.598	3768.5	0.33560	0.29677
219.94	2.0175	121.63	67.124	4601.5	0.32860	0.28898
245.44	1.7597	110.18	79.624	5699.4	0.32165	0.28137
272.12	1.5181	98.439	96.660	7202.0	0.31457	0.27377
299.96	1.2847	86.048	121.15	9370.2	0.30730	0.26614

Table C.28: The correspondence between $\bar{x}$ and the other velocity profile parameters at discrete points in the pipe entrance, for the case $\bar{\Omega} = 50$.

$\bar{x}$ ($\times 10^5$)	S	δ^*/R ($\times 10^3$)	U_c/U
0	∞	0	1
7.1079	73.192	16.604	1.0343
12.625	61.147	20.180	1.0421
19.703	52.560	23.838	1.0501
28.331	46.332	27.482	1.0582
38.495	41.648	31.060	1.0662
50.180	38.051	34.549	1.0742
63.367	35.203	37.935	1.0821
78.034	32.918	41.212	1.0898
94.160	31.042	44.377	1.0974
111.72	29.489	47.420	1.1048
130.68	28.178	50.371	1.1120
151.02	27.070	53.203	1.1191
172.70	26.115	55.928	1.1259
195.68	25.294	58.549	1.1326
219.94	24.576	61.069	1.1391
245.44	23.950	63.491	1.1455
272.12	23.397	65.817	1.1516
299.96	22.910	68.052	1.1575
328.90	22.475	70.197	1.1633

Table C.27: Variables and parameters at discrete points in the pipe entrance, for the case $\tilde{\Omega} = 50$. The underlined data are the values of the parameters at the minimum critical Reynolds number.

$\tilde{x}$ ($\times 10^5$)	$\alpha_{[crit]}$	$\alpha_{\delta^*[crit]}$ ($\times 10^3$)	$Re_{R[crit]}$ ($\times 10^{-3}$)	$Re_{\delta^*[crit]}$	$c_{[crit]}$	$\hat{c}_{[crit]}$
0	∞	303.77	∞	519.06	0.39664	0.39664
7.1079	16.755	278.19	37.564	645.13	0.40052	0.38722
12.625	12.968	261.69	33.391	702.17	0.39787	0.38181
19.703	10.675	254.47	30.190	755.70	0.39719	0.37825
28.331	8.8585	243.45	28.634	832.70	0.39449	0.37280
38.495	7.5763	235.32	27.298	904.05	0.39315	0.36873
50.180	6.5092	224.89	27.133	1007.0	0.38978	0.36284
63.367	5.6719	215.16	27.260	1119.0	0.38655	0.35722
78.034	4.9737	204.97	28.007	1257.9	0.38258	0.35105
94.160	4.3938	194.98	29.192	1421.6	0.37823	0.34466
111.72	3.8945	184.71	30.923	1620.3	0.37344	0.33802
130.68	3.4623	174.40	33.224	1861.0	0.36826	0.33116
151.02	3.0821	163.98	36.167	2153.3	0.36289	0.32428
172.70	2.7427	153.39	39.033	2514.7	0.35723	0.31727
195.68	2.4368	142.67	44.675	2962.6	0.35149	0.31033
219.94	2.1563	131.68	50.774	3532.1	0.34555	0.30335
245.44	1.8969	120.44	58.660	4266.1	0.33956	0.29645
272.12	1.6522	108.75	69.261	5249.6	0.33335	0.28947
299.96	1.4183	96.518	84.032	6619.4	0.32691	0.28242
328.90	1.1865	83.287	106.30	8680.7	0.31993	0.27501

Table C.26: The correspondence between $\bar{x}$ and the other velocity profile parameters at discrete points in the pipe entrance, for the case $\Omega = 40$.

$\bar{x}$ ($\times 10^5$)	S	δ^*/R ($\times 10^3$)	U_c/U
0	∞	0	1
7.1070	72.987	16.621	1.0344
12.625	60.898	20.212	1.0421
19.703	52.269	23.891	1.0502
28.331	45.098	27.561	1.0583
38.495	41.274	31.173	1.0665
50.180	37.638	34.703	1.0746
63.367	34.753	38.137	1.0826
78.034	32.433	41.468	1.0904
94.160	30.522	44.695	1.0982
111.72	28.936	47.815	1.1057
130.68	27.594	50.831	1.1132
151.02	26.455	53.742	1.1204
172.70	25.472	56.553	1.1275
195.68	24.622	59.263	1.1345
219.94	23.878	61.877	1.1412
245.44	23.227	64.397	1.1478
272.12	22.649	66.826	1.1543
299.96	22.138	69.166	1.1605
328.90	21.681	71.420	1.1666
358.91	21.273	73.591	1.1726
389.92	20.905	75.682	1.1784

Table C.25: Variables and parameters at discrete points in the pipe entrance, for the case $\bar{\Omega} = 40$. The underlined data are the values of the parameters at the minimum critical Reynolds number.

$\bar{x}$ ($\times 10^5$)	$\alpha_{\text{[crit]}}$	$\alpha_{\delta^*\text{[crit]}}$ ($\times 10^3$)	$Re_{R\text{[crit]}}$ ($\times 10^{-3}$)	$Re_{\delta^*\text{[crit]}}$	$c_{\text{[crit]}}$	$\bar{c}_{\text{[crit]}}$
0	∞	303.77	∞	519.06	0.39664	0.39664
7.1079	16.360	271.93	37.604	646.53	0.39977	0.38648
12.625	13.084	264.45	32.651	687.73	0.39946	0.38331
19.703	10.736	256.48	29.381	737.16	0.39894	0.37988
28.331	8.9374	246.33	27.535	803.16	0.39710	0.37521
38.495	7.6626	238.87	25.964	863.19	0.39651	0.37179
50.180	6.6026	229.13	25.436	948.56	0.39415	0.36679
63.361	5.7882	220.74	24.879	1027.1	0.39280	0.36284
78.034	5.1000	211.49	25.054	1132.9	0.39024	0.35787
94.160	4.5259	202.28	25.580	1255.5	0.38729	0.35267
111.72	4.0341	192.89	26.472	1399.6	0.38407	0.34734
130.68	3.6076	183.38	27.761	1570.8	0.38045	0.34178
151.02	3.2333	173.77	29.450	1773.3	0.37667	0.33619
172.70	2.8983	163.90	31.656	2018.6	0.37256	0.33042
195.68	2.5963	153.86	34.438	2315.3	0.36832	0.32466
219.94	2.3186	143.47	38.002	2683.6	0.36382	0.31880
245.44	2.0618	132.77	42.554	3145.5	0.35919	0.31292
272.12	1.8195	121.59	48.541	3744.2	0.35429	0.30694
299.96	1.5884	109.86	56.610	4544.0	0.34914	0.30084
328.90	1.3619	97.270	68.118	5675.7	0.34353	0.29446
358.91	1.1339	83.448	85.831	7406.5	0.33727	0.28763
389.92	0.88842	67.237	117.64	10491	0.32982	0.27990

Table C.24: The correspondence between $\bar{x}$ and the other velocity profile parameters at discrete points in the pipe entrance, for the case $\bar{\Omega} = 30$.

$\bar{x}$ ($\times 10^5$)	S	δ^*/R ($\times 10^3$)	U_c/U
0	∞	0	1
7.1079	72 782	16.639	1.0344
12.625	60.648	20.244	1.0422
19.703	51.976	23.943	1.0503
28.331	45.663	27.641	1.0585
38.495	40.898	31.287	1.0668
50.180	37.222	34.859	1.0749
63.367	34.299	38.342	1.0831
78.034	31.943	41.730	1.0911
94.160	29.997	45.019	1.0989
111.72	28.377	48.210	1.1067
130.68	27.003	51.302	1.1143
151.02	25.833	54.296	1.1218
172.70	24.819	57.195	1.1292
195.68	23.941	60.000	1.1364
219.94	23.169	62.713	1.1434
245.44	22.491	65.337	1.1503
272.12	21.887	67.874	1.1571
299.96	21.351	70.326	1.1637
328.90	20.870	72.696	1.1701
358.91	20.439	74.986	1.1764
389.92	20.049	77.198	1.1826
421.91	19.697	79.335	1.1886
454.81	19.376	81.400	1.1945

Table C.23: Variables and parameters at discrete points in the pipe entrance, for the case $\bar{\Omega} = 30$. The underlined data are the values of the parameters at the minimum critical Reynolds number.

$\bar{x}$ ($\times 10^6$)	α[crit]	α_{δ^*}[crit] ($\times 10^3$)	Re_R[crit] ($\times 10^{-3}$)	Re_{δ^*}[crit]	c[crit]	$\tilde{c}$[crit]
0	∞	303.77	∞	519.06	0.39664	0.39664
7.1079	16.790	279.38	36.664	631.07	0.40189	0.38851
12.625	13.117	265.53	31.854	672.06	0.40099	0.38476
19.703	10.812	258.87	28.360	713.19	0.40125	0.38203
28.331	9.0372	249.80	26.184	766.12	0.40049	0.37835
38.495	7.7699	243.10	24.355	812.87	0.40083	0.37574
50.180	6.7213	234.30	23.432	878.05	0.39974	0.37187
63.367	5.9059	226.44	22.740	944.32	0.39897	0.36838
78.034	5.2276	218.15	22.460	1022.6	0.39778	0.36458
94.160	4.6611	209.84	22.403	1111.3	0.39628	0.36060
111.72	4.1787	201.45	22.717	1212.1	0.39465	0.35660
130.68	3.7602	192.91	23.248	1329.1	0.39260	0.35240
151.02	3.3937	184.27	24.028	1463.6	0.39061	0.34819
172.70	3.0660	175.36	25.116	1622.1	0.38824	0.34383
195.68	2.7709	166.25	26.526	1808.6	0.38575	0.33946
219.94	2.5004	156.81	28.348	2032.7	0.38302	0.33498
245.44	2.2504	147.04	30.669	2305.0	0.38012	0.33045
272.12	2.0156	136.81	33.663	2643.7	0.37699	0.32581
299.96	1.7926	126.07	37.582	3075.5	0.37360	0.32105
328.90	1.5769	114.63	42.872	3646.8	0.36985	0.31608
358.91	1.3641	102.29	50.358	4442.3	0.36562	0.31079
389.02	1.1468	88.527	61.788	5640.8	0.36067	0.30498
421.91	0.91247	72.392	81.816	7715.0	0.35456	0.29830
454.81	0.62472	50.852	130.14	12653	0.34639	0.29000

Table C.22: The correspondence between $\bar{x}$ and the other velocity profile parameters at discrete points in the pipe entrance, for the case $\bar{\Omega} = 20$.

$\bar{x}$ ($\times 10^5$)	S	δ^*/R ($\times 10^3$)	U_c/U
0	∞	0	1
7.1079	72.577	16.657	1.0345
12.625	60.398	20.276	1.0423
19.703	51.683	23.996	1.0504
28.331	45.326	27.722	1.0587
38.495	40.520	31.403	1.0670
50.180	36.804	35.017	1.0753
63.367	33.843	38.550	1.0835
78.034	31.449	41.996	1.0917
94.160	29.467	45.351	1.0997
111.72	27.813	48.614	1.1077
130.68	26.405	51.785	1.1155
151.02	25.203	54.866	1.1235
172.70	24.158	57.857	1.1309
195.68	23.250	60.761	1.1383
219.94	22.448	63.578	1.1457
245.44	21.742	66.312	1.1529
272.12	21.111	68.963	1.1600
299.96	20.549	71.535	1.1670
328.90	20.042	74.028	1.1738
358.91	19.587	76.446	1.1805
389.92	19.173	78.789	1.1871
421.91	18.798	81.060	1.1935
454.81	18.455	83.261	1.1998
488.56	18.143	85.394	1.2060
523.13	17.856	87.460	1.2120

```
utemp(1,:)=u;
utemp(2,:)=u;
utemp(3,:)=u;
tpointer=2;
M=(dt(dtmark,2)*dt(dtmark,4)).*L+muhat(1:n,1:n);
OP=mu(n)^2*inv_N;
%
% start the loop ...
%
for t=1:tn,
  if t==1,
R=utemp(3,:)*M+K;
  else,
R=utemp(3,:)*M + (dt(dtmark,2)*dt(dtmark,5)).*...
  utemp(2,:)*L+K;
  end;
  utemp(4,:)=R*OP;
  utemp(1:3,:)=utemp(2:4,:);
  % rotate the data in the temporary buffer

  if rem(t,tsave)==0, % save the data into output array
disp('saving data to output array');
disp(t);
disp(shape(utemp(4,:)));
disp(utemp(4,:)*chebvec(0,n));
u(tpointer,:)=utemp(4,:);
tpointer=tpointer+1;

% Draw the thing
ur=realprof(30,u);
mesh(ur,[34,40]);
clear ur
drawnow;
  end;
  if (dt(dtmark,1)<=t & dtsize>dtmark),
disp('changing discretisation');
dtmark=dtmark+1;
K=kmat(1,n,omega,muhat).*dt(dtmark,2);
N=(muhat(1:n,1:n)-(dt(dtmark,3)*dt(dtmark,2))*L);
N=N*mu(n)^2;
N(:,1)=chebvec(1,n);
N(:,2)=etahat(1:n,1:n)*chebvec(0,n);
[ll,uu]=lu(N);
inv_N=inv(uu)*inv(ll);

M=(dt(dtmark,2)*dt(dtmark,4)) .*L+muhat(1:n,1:n);
```

D.3 The one-dimensional base flow equation

This section contains the one-dimensional base-flow script, for the initial value problem for accelerating pipe flow far away from the inlet.

D.3.1 base1d.m

```
% base1d.m
%
% this script generates the parallel base flow model
% using the pressure-integral approach
%
% set parameters ...
%
n=100;
%dt= [ti dt   a0  a1  a2 ...
dt=  [100000 1e-5 1 0 0; ...
  10000  1e-7 0.5 0.5 0];
[dtsize,y]=size(dt);
dtmark=1;

omega=0;      % Acceleration parameter
tn=4000;      % Maximum time step
tsave=20;     % save every tsave timestep

%
% set global matrices ...
%
[etahat,muhat]=etamu(n+10);  % the global shift matrices.
[L]=l_oper(n,omega,etahat,muhat);
[K]=kmat(1,n,omega,muhat).*dt(dtmark,2);

N=(muhat(1:n,1:n)-(dt(dtmark,2)*dt(dtmark,3)).*L);
N=N*mu(n)^2;  % shift the matrix right 2 to augment BC's
N(:,1)=chebvec(1,n)./n;
N(:,2)=etahat(1:n,1:n)*chebvec(0,n)./n;
[l1,uu]=lu(N);
inv_N=inv(uu)*inv(l1);
u=[1 0 0]/cheb2(3);  %Uinit;
[x,y]=size(n);
if y >= n,
  u=u(:,1:n);
else,
  u(x,n)=0;
end;
```

```
LHS=LHS+bcblas(n,etahat);

[LL,UU]=lu(LHS);
invLHS=inv(UU)*inv(LL);

F=RHS*invLHS;
```

D.2.3 g_of_f.m

```
%
% g_of_f.m calculates the value of the Blasuis equation
%
% This function is used by blasius.m
%
% [G]=g_of_f(n,z_max,etahat,f);
%
function [G]=g_of_f(n,z_max,etahat,f);
P=polyr(n,f);
etahat=etahat(1:n,1:n);
G=etahat^2*(2*etahat + z_max^2 .* P);
G=f*G;
```

D.2.4 bcblas.m

```
%
% bcblas.m calcs the BC's for Blasius
%
% Used by blasius.m
%
% [B]=bcblas(n,etahat);
%
function [B]=bcblas(n,etahat);

etahat=etahat(1:n,1:n);
B=zeros(n,n);
v0=chebvec(0,n);
v1=chebvec(1,n);
B(:,1)=v1;
B(:,2)=etahat*v1;
B(:,3)=etahat*v0;
```

```
  delf=delf(1,1:n); delf(1,n)=0;

  error=max(abs(delf));

  LHS=bcblas(n,etahat)+eye(n)*shift;
  RHS=(f+omega*delf)*shift; RHS(3)=1;
  f=RHS*inv(LHS);

  f=f(1,1:n); f(1,n)=0;
  f_rd=realprof(20,f(1:n)*etahat(1:n,1:n));
  f_r=realprof(20,f(1:n));
  f_delf=realprof(20,delf);
  plot(x,f_r,x,f_rd,'w',x,f_delf); grid;
  drawnow;
  disp('error is:');
  disp(error);
  disp('change is:');
  disp(max(oldf-f));

  oldf=f;
end;
save __temp;
```

D.2.2 frechet.m

```
%
% Frechet.m calculates the new guessstimate
%
% This function is used by blasius.m
%
% [F]=frechet(n,z_max,omega,etahat,f,shift);
%
function [F]=frechet(n,z_max,omega,etahat,f,shift);

etahat=etahat(1:n,1:n);
LHS=2*etahat^3 ...
+ (etahat^2*polyr(n,f))*z_max^2 ...
+ (polyr(n,(f*etahat^2)))*z_max^2;
RHS=-g_of_f(n,z_max,etahat,f);
LHS=LHS*shift;
RHS=RHS*shift;
RHS(1)=-f*chebvec(1,n);
RHS(2)=-f*etahat*chebvec(1,n);
RHS(3)=-f*etahat*chebvec(0,n)+1;
```

D.2 The Blasius solution

This script (and subsidiary m-files) calculate the Blasius boundary layer solution using a highly accurate non-linear iterative method.

D.2.1 blasius.m

```
%
% blasius.m This is a script that returns Blasius
%
%%%%%%%%%%%%%%%%%%%%%%%%%%%%%%%%%%%%%%%%%%%%%%%%%%%%%
% First set up parameters ...                       %
%%%%%%%%%%%%%%%%%%%%%%%%%%%%%%%%%%%%%%%%%%%%%%%%%%%%%
if (exist('n') ==0),
   n=20;
end;            % The order
if (exist('z_max') ==0),
  z_max=100;        % Axis stretching
end;
errlimit=1e-13;     % Convergence criterion
omega=0.5;      % relaxation parameter

%%%%%%%%%%%%%%%%%%%%%%%%%%%%%%%%%%%%%%%%%%%%%%%%%%%%
% Calculate the necessary matrices                 %
%%%%%%%%%%%%%%%%%%%%%%%%%%%%%%%%%%%%%%%%%%%%%%%%%%%%
k=n+10;
etahat=makeetahat(k);

%%%%%%%%%%%%%%%%%%%%%%%%%%%%%%%%%%%%%%%%%%%%%%%%%%%%
% Set the initial guess                            %
%%%%%%%%%%%%%%%%%%%%%%%%%%%%%%%%%%%%%%%%%%%%%%%%%%%%
f(1,n)=0;
f=f(1,1:n);

%%%%%%%%%%%%%%%%%%%%%%%%%%%%%%%%%%%%%%%%%%%%%%%%%%%%
% Start iterating!                                 %
%%%%%%%%%%%%%%%%%%%%%%%%%%%%%%%%%%  %%%%%%%%%%%%%%%%
error=1;  % Otherwise we fall through the while loop
shift=mu(n)^3;
oldf=0;
x=(0:19)/19;

while (abs(error)>errlimit),

  [delf]=frechet(n,z_max,omega,etahat,f,shift);
```

```
  error('row vectors please.');
end;
M=A'*B;
M(1,1)=M(1,1).*2;
C(1,1)=sum(diag(M));
for i=2:ya+yb-1,
  C(1,i)=sum(diag(M,i-1))+sum(diag(M,1-i))+...
 sum(diag(fliplr(M),yb-i));
end;
C=C./2;
```

D.1.14 eta

```
%
% The function eta(n) returns a square matrix which is the
% derivative operator for the operational tau approach
% in the canonical basis
% n is the order of the matrix
function [a]=eta(n)
a=zeros(n);
for j=1:n-1
a(j+1,j)=j;
end
```

D.1.15 mu

```
% The function mu(n) returns a square matrix that is the
% shift matrix operator representing premultiplixation by
% x in the canonical basis. n is the order of the matrix
function [a]=mu(n)
a=zeros(n);
for j=1:n-1
a(j,j+1)=1;
end
```

Particular functions

The above m-files comprised a generic numerical toolbox; the following sections contain m-files that calculate specific results contained in this study.

```
% need to call directly!!
%
% NB!!! Construct C, Cinv as [C,Cinv]=transops(3*n/2); !!!!
%
% [S]=coef2pts(V,C,Cinv);
%
function [S]=coef2pts(V,C,Cinv);
[x,y]=size(V);
V(x,3*y/2)=0;
S=V*Cinv;
```

D.1.12 transops

```
%
% transops makes the arrays necessary to evaluate the
% transforms from Chebyshev space to real space and back
%
% [C,Cinv]=transops(n);
%
function [C,Cinv]=transops(n);
for k=1:n,
  for j=1:n,
C(k,j)=2/(n-1)*cos(pi*(j-1)*(k-1)/(n-1));
Cinv(j,k)=cos(pi*(j-1)*(k-1)/(n-1));
  end;
end;
C(:,1)=C(:,1)/2;
C(:,n)=C(:,n)/2;
C(1,:)=C(1,:)/2;
C(n,:)=C(n,:)/2;
```

D.1.13 convcheb

```
%
% convcheb returns the convolution in Chebyshev form
%
% function [C]=convcheb(A,B);
% A,B are the chebyshev coefficient (row) vectors.
% Matrix returned is of order size(A)+size(B)-1;
%
function [C]=convcheb(A,B);
[xa,ya]=size(A);
[xb,yb]=size(B);
if xa~=1 | xb~=1,
```

D.1.10 poly2d

```
%
% poly2d generates the product matrix of the convolution of
% u and v. If supplied with four arguments, it uses the
% pseudo-spectral transform, if given 2 arguments, convolves
% directly.
% C, Cinv, if supplied, are respectively, the Tau to Collocation
% projection operator, and its inverse. They are given by
% transops.m
%
% C=poly2d(u,v{,C,Cinv});
function [C]=poly2d(u,v,C,Cinv);
if (nargin==4),  % transform then multiply
  [m,n]=size(u);
  U=coef2pts(u,C,Cinv);
  V=coef2pts(v,C,Cinv);
  W=U.*V;
  C=pts2coef(W,C,Cinv);
elseif (nargin==2),  % convolve directly
  [m,n]=size(u);
  v(m+1,n+1)=0;
  v=v(1:m,1:n);
  C=zeros(m,2*n-1);
  for i=1:m,
if max(abs(v(i,:))) ~= 0,
  C(i,:)=convcheb(u(i,:),v(i,:));
else,
  C(i,:)=zeros(1,2*n-1);
end;
  end;
else,
  error('Wrong arguments');
end;
```

D.1.11 coef2pts

```
%
% coef2pts converts the discrete chebyshev coefficients
% to their space values at the Gauss-Lobatto points.
% It projects to a grid 3/2 times the subspace dimension
% (by adding zero coefficients to the coefficient vector)
% to avoid aliasing.
%
% This m-file is used exclusively by poly2d.m - no
```

```
function [j]=intmat(n);
j=zeros(n,1);
j(1)=1;
for i=3:2:n,
  j(i)=-i/((i-2)*(i));
end
```

D.1.8 lobgrid

```
%
% lobgrid returns the Gauss-Lobatto grid in x
% in the range [0,1]
%
% [L]=lobgrid(n);
%
function [L]=lobgrid(n);
i=(0:n-1)  * (pi/(n-1));
L=0.5*(cos(i)+1);
```

D.1.9 prodmat

```
%
% prodmat returns the p'th product matrix for Chebyshev products
% of order n * n
%
% [P]=prodmat(n,p);
%
function [P]=prodmat(n,p);
if round(p)-p ~=0,
  error('p must be an integer >=0');
end;
if p>=1 & p<n,
  P=diag(ones(n-p,1),p)+diag(ones(n-p,1),-p) ...
+fliplr(diag(ones(p+1,1),n-p-1));
  P(p+1,1)=1;
  P=P .* (1/2);
elseif p == 0,
  P=eye(n);
elseif p>=n & p<2*n-1,
  P=fliplr(diag(ones(2*n-p-1,1),-p+n-1));
  P=P .* (1/2);
else,
  error('P must be >= 0 and <=2*n');
end;
```

D.1.6 collder

```
%
% collder is the collocation first derivative for the system
% u =(u(x0),u(xi), ... ,u(xN))'.
% It utilises the Gauss-Lobatto points
%
% [C]=collder(n);
%
function [C]=collder(n);
C=zeros(n,n);
for l=1:n,
  xl=cos(pi*(l-1)/(n-1));
  if l==1 | l == n,
cl=2;
  else,
cl=1;
  end;
  for j=1:n,
xj=cos(pi*(j-1)/(n-1));
if j==1 | j==n,
  cj=2;
else,
  cj=1;
end;
if l ~= j,
  C(l,j)=(cl/cj)*((-1)^(l+j-2)/(xl-xj));
elseif l ==j & l==1,
  C(l,j)=(2*(n-1)^2+1)/6;
elseif l ==j & l==n,
  C(l,j)=-(2*(n-1)^2+1)/6;
else
  C(l,j)=-xj/(2*(1-xj^2));
end;
  end;
end;
C=2*C';
```

D.1.7 intmat.m

```
%
% intmat returns the definite integral vector for a polynomial
% in Chebyshev basis (2nd kind)
% function [j]=intmat(n);
%
```

D.1.4 chebvec.m

```
%
% chebvec generates a n dim' column vector containing the
% values for T=(T0,T1,T2,T3,...)' at x=a
% for 0<x<1 for second type Chebyshev
%
% function [T]=chebvec(a,n);
%
function [T]=chebvec(a,n);
T=zeros(n,1);
T(1)=1;
T(2)=2*a-1;
for i=3:n
  T(i)=2*(2*a-1)*T(i-1)-T(i-2);;
end
```

D.1.5 col2cheb

```
%
% col2cheb generates the transformation matrix for transforming
% the values at the Gauss-Lobatto points to discrete Chebyshev
% coefficients
%
% [C]=col2cheb(n);
%
function [C]=col2cheb(n);
C=zeros(n,n);
for k=1:n,
  if k==1 | k==n,
ck=2,
  else,
ck=1;
  end;
  for j=1:n,
if j==1 | j==n,
  cj=2;
else,
  cj=1;
end;
C(k,j)=(2/((n-1)*cj*ck))*cos(pi*(j-1)*(k-1)/(n-1));
  end;
end;
```

D.1.2 etahat.m

```
%
% etahat constructs the diff' matrix in chebyshev space of
% order n
%
% function [eta]=etahat(n);
%
function [m]=etahat(n);
m=zeros(n,n);
for i=2:2:n
  m(i,1)=2*(i-1);
  for j=3:2:i
m(i,j)=4*(i-1);
  end
end
for i=3:2:n
  for j=2:2:i
m(i,j)=4*(i-1);
  end
end
```

D.1.3 cheb2.m

```
%
% The function cheb2(n) returns the Chebyshev mapping V of order
% n, that transforms the polynomial vector into the Chebyshev
% vector of coefficients.
% This is the transformation for Chebyshev polynomials of the
% second kind, on the range 0<x<1
%
% [V]=cheb2(n);
%
function [V]=cheb2(n)
V=zeros(n);
V(1,1)=1;
V(2,1)=-1;
V(2,2)=2;
for j=3:n
  V(j,1)=-2*V(j-1,1)-V(j-2,1);
  for k=2:j
V(j,k)=4*V(j-1,k-1)-2*V(j-1,k)-V(j-2,k);
  end
end
```